

Josef Kulmer

High-Accuracy Positioning Exploiting Multipath for Reducing the Infrastructure

DOCTORAL THESIS

to achieve the university degree of
Doktor der technischen Wissenschaften
submitted to

Graz University of Technology

Supervisor

Assoc.Prof Dipl.-Ing. Dr. Klaus Witrissal

Signal processing and speech communication laboratory

Abstract

Positioning systems using wideband radio signals are able to maintain centimeter-level accuracy if clear line-of-sight measurements to several base stations are available. Obstructed or blocked paths in addition to harsh multipath propagation limit the achievable accuracy. As a remedy, numerous base stations are employed which are associated with increased deployment costs.

In this thesis we tackle localization using radio signals with a minimum amount of available infrastructure, e.g. limited or no access to base stations. To remedy a potential performance loss, three research directions are identified. First, we formulate a site-specific double-directional channel model to enhance the potential of exploiting multipath propagation for localization. We examine propagation mechanisms like path reflections or diffuse multipath with respect to their contained position information. Available prior knowledge of the surrounding environment enables to predict the distributions of both specular reflections as well as diffuse multipath in angle-delay domain. This enables to perform localization using a single base station even in environments with a considerable large amount of path blocking.

The second research direction treats exploitation of measurements with respect to angle and delay information using directive antennas and non-phase-coherent transceivers. Directive antennas attenuate radio signals as function of their transmitting/receiving angles. Having a number of directive antennas, the antennas' directivity enables to exploit multipath angle information without the need of cost-intensive, coherent multi-antenna transceivers. In comparison to an antenna, radiating in an isotropic manner, our theoretic analysis demonstrates the advantage of directive antennas to separate multipath in angle-delay domain, by reducing multipath interference.

The third research direction points to cooperative localization. We demonstrate that a site-specific multipath channel model provides global position coordinates. The users' position coordinates are estimated from specular reflections originating at reflective surfaces. Prior knowledge of the surface location enables to determine the users' positions without requiring a base station at all.

Kurzfassung

Funkortungssysteme ermöglichen eine erreichbare Genauigkeit im Bereich von Zentimetern, gegeben ungestörter Messungen zu mehreren Basisstationen. Blockierte Funksignale sowie deren Mehrwegeausbreitung begrenzen die erreichbare Genauigkeit. Als Abhilfe böte sich die Erhöhung der Anzahl der Basisstationen an, was allerdings mit erhöhten Bereitstellungskosten einhergeht.

Diese Arbeit behandelt Funkortung und dessen Funktionstüchtigkeit bei eingeschränkter Erreichbarkeit von wenigen oder keinen Basisstationen. Zur Verhinderung möglicher Leistungseinbußen werden drei Fragestellungen formuliert. Zunächst betrachten wir ein standortspezifisches und richtungsabhängiges Kanalmodell für die Nutzung von Ortungsinformation in Mehrwegeausbreitung. Wir untersuchen Ausbreitungsmechanismen wie Reflexionen oder diffuse Mehrwegeausbreitung hinsichtlich ihrer enthaltenen Positionsinformationen. Vorhandenes Vorwissen über die Umgebung ermöglicht eine Berechnung der Parameter von Spiegelreflexionen als auch der diffusen Mehrwegeausbreitung. Dies ermöglicht eine Ortung unter Verwendung einer einzelnen Basisstation, selbst in Umgebungen mit beträchtlichen Ausmaßen an blockierten Pfaden.

Die zweite Fragestellung behandelt die Zugänglichkeit von Winkel- und Verzögerungsinformation unter Verwendung von Richtantennen und nicht phasenkohärenten Signalketten. Richtantennen dämpfen Funksignale in Abhängigkeit ihrer Sende- und Empfangswinkeln. Anbringen mehrere Richtantennen ermöglicht die Nutzung der Winkelinformation von Mehrwegeausbreitung ohne Erfordernis der kostenintensiven, Mehrantennen-Systeme. Im Vergleich zu isotropischen Strahlern zeigt unsere theoretische Analyse den Vorteil von Richtantennen, Multipfade im Winkelbereich voneinander zu trennen.

Die dritte Fragestellung zielt auf kooperative Funkortung. Wir zeigen, dass ein standortspezifisches Mehrwegeausbreitungsmodell globale Positionskordinaten liefern kann. Des Benutzers Positionskordinaten werden anhand von Spiegelreflexionen geschätzt, welche an reflektierenden Oberflächen entstehen. Die Kenntnis ebendieser Oberflächenpositionen ermöglicht eine Positionsbestimmung mit globalen Koordinaten ohne Zuhilfenahme von Basisstationen. Basisstationen werden obsolet.

Contents

Abstract	iii
Kurzfassung	v
Acknowledgments	xi
List of acronyms	xiii
List of symbols	xiv
I Introduction to Researched Topics	1
1 Introduction	3
1.1 Research hypotheses	4
1.1.1 Towards a site-specific channel model for localization . . .	4
1.1.2 Localization using a single base station	4
1.1.3 Avoiding base stations through cooperation	5
1.2 Contributions and outline	5
2 Problem formulation	11
2.1 Measurements at signal level	13
2.1.1 Relation between MPC parameters and position parameters	13
2.1.2 Description of additive noise	14
2.2 Measurements at parameter level	14
2.2.1 Estimation and characterization of multipath parameters	14
2.2.2 Representation of delay uncertainty	16
2.3 Remarks and outlook	16
3 Towards a site-specific channel model for localization	17
3.1 Deterministic model	19
3.2 Stochastic modeling of dense multipath	20
3.2.1 Empirical descriptions of dense multipath	20
3.2.2 Theoretic modeling of dense multipath	21
3.2.3 Further considerations and relation to literature	27
3.3 Concluding remarks	32

4	Localization using a single base station	35
4.1	Measurement model in angle-delay domain	36
4.2	Information contained in measurements	37
4.2.1	Position error bound considering path overlap	37
4.2.2	Position error bound neglecting path overlap	37
4.2.3	Numeric evaluation	39
4.3	Algorithms for non-phase-coherent measurements	42
4.3.1	Measurement model for non-phase-coherent measurements	42
4.3.2	Discussion and comparison of algorithms	42
4.3.3	Towards a real-time positioning system	43
4.4	Concluding remarks and outlook	45
5	Avoiding base stations through cooperation	47
5.1	Introduction to Bayesian position estimation	48
5.1.1	Estimation in a Bayesian framework	49
5.1.2	Approximations	49
5.2	Assembling the posterior distribution	50
5.2.1	Impact of agent uncertainty	52
5.2.2	Impact of measurement noise	52
5.2.3	Impact from uncertainty in the surrounding environment	53
5.2.4	Mutual dependencies	55
5.3	Concluding remarks and outlook	55
6	Conclusion	57
	Appendices	58
	Appendix A Derivation of angular and delay power spectrum in far-field, related to Chapter 3.2	61
A.1	Angular delay power spectrum in far-field conditions	61
A.2	Angular power spectrum	62
A.3	Delay power spectrum	62
	Appendix B Derivation of the position error bound, related to Chapter 4	65
B.1	Likelihood function for MPC parameters	66
B.2	Fisher information for MPC parameters	66
B.3	Fisher information for agent position	67
B.4	Position error bound considering path overlap	67
B.5	Position error bound neglecting path overlap	68
	Appendix C Characterization of wideband, directional antenna, related to Chapter 4	71
C.1	Measurement setup	71
C.2	Experiment 1: Beampattern	71
C.3	Experiment 2: Distortions in time and frequency domain	72
C.4	Experiment 3: Diversity in delay and angle domains	72
7	Bibliography	77

<i>CONTENTS</i>	ix
II Included Papers	89
Impact of Rough Surface Scattering on Stochastic Multipath Component Models	91
Using DecaWave UWB Transceivers for High-accuracy Multipath-assisted Indoor Positioning	107
On the Unimportance of Phase-Coherent Measurements for Beampattern-Assisted Positioning	125
Cooperative Multipath-assisted Navigation and Tracking: A Low-Complexity Approach	141
Cooperative Localization and Tracking using Multipath Channel Information	149
Anchorless Cooperative Tracking Using Multipath Channel Information	165

Acknowledgments

First and foremost, I want to announce my honest thankfulness to my advisor Assoc.Prof. Dipl.-Ing. Dr. Klaus Witrissal for the continuous support of my PhD study, for his inspiration, patience, and his considerable knowledge. His passionate guidance during the time of research has given me continual pleasure. I could not imagine having a better advisor.

My sincere thanks go to Erik and Stefan for guiding me down the rabbit hole of communications. Your immense expertise in the literature and your deep understanding of estimation theory have inspired me to constantly reconsider half-baked ideas. Not sure to what extent our bakeries are superior, but thanks to you, they became tasty.

It was a great pleasure to visit Prof. Henk Wymeersch's group at Chalmers University. The warm welcome at cold Gothenburg inspired me to fight against snow storms, spare time and integral equations. Your hard questions but motivating comments and proposals boosted my research in so many perspectives. Thank you for giving me this opportunity.

Last but by no means least I would like to thank my fellows at SPSC, notably Michael, Johannes, Christian and Jamilla for our joint wandering in teaching affairs and gaining insights in operating systems. It was our collaboration, confrontation and lively debate culture which constantly disclosed my passion for linear algebra, exploration of space, and microwaves.

List of Acronyms

3GPP	3rd generation partnership project
ADPS	angle-delay power spectrum
APS	angle power spectrum
DM	dense (diffuse) multipath
DPS	delay power spectrum
EFIM	equivalent Fisher information matrix
ER	effective roughness
FIM	Fisher information matrix
GNSS	global navigation satellite systems
GO	geometrical optics
KL	Kullback Leibler
LOS	line-of-sight
LTE	long term evolution
ML	maximum likelihood
MPC	multipath component
NPC	non-phase-coherent
SINR	signal-to-interference-plus-noise ratio
SNR	signal-to-noise ratio
SPEB	squared position error bound
S-V	Saleh-Valenzuela
TOA	time-of-arrival
UWB	ultrawide-band
WLAN	wireless local area network
WPAN	wireless personal area network

List of Symbols

α_k	amplitude of k th specular reflection
α_R	roughness parameter
$b_m^{(i)}(\cdot)$	beam pattern of m th antenna at node i
$\delta(\cdot)$	Dirac-delta
$f_k(\cdot)$	image-source of k th specular reflection
$f_{\text{meas}}(\cdot)$	measurement function
$h(\cdot)$	spreading function
\mathbf{I}	identity matrix
i, j	index of nodes, agents or anchors
k	index of specular reflection or of its associated surface
k_{α_R}	normalization constant
m	index of antenna
$\mathbf{n}^{(i,j)}$	noise vector for measurements between nodes i and j
$\nu_k(\cdot)$	measurement of dense multipath associated to k th specular reflection
$\mathbf{p}^{(i)}$	position of node i in two or three coordinates
\mathcal{P}	squared position error bound considering path overlap
$\tilde{\mathcal{P}}$	squared position error bound neglecting path overlap
$p_{\text{DM},k}(\cdot)$	angle-delay power spectrum of dense multipath associated to k th specular reflection
ϕ	generic angle
$\phi^{a,(i)}$	azimuth angle at node i
$\phi_k^{a,(i)}$	azimuth angle of k th specular reflection at node i
$\phi^{e,(i)}$	elevation angle at node i
$\phi_k^{e,(i)}$	elevation angle of k th specular reflection at node i
$s(\cdot)$	transmitted signal
S	scatter attenuation
t	time
τ	delay
τ_k	delay of k th specular reflection
$\boldsymbol{\theta}$	parameter vector
$\boldsymbol{\theta}_k$	parameter vector of k th specular reflection
$\mathbf{u}^{(i)}$	direction at node i
$\mathbf{u}_k^{(i)}$	direction of k th specular reflection at node i
\mathbf{x}	state vector
$\mathbf{z}^{(i,j)}$	vector of measurements between nodes i and j

AFFIDAVIT

I declare that I have authored this thesis independently, that I have not used other than the declared sources/resources, and that I have explicitly indicated all material which has been quoted either literally or by content from the sources used. The text document uploaded to TUGRAZonline is identical to the present doctoral thesis.

Date

Signature

Part I

Introduction to Researched
Topics

Chapter 1

Introduction

Radio localization, the desire for localization using radio propagation, has become an integral part of everyday life. The rise of geolocation services such as global navigation satellite systems (GNSS) culminates in location-based services able to guide autonomous vehicles [80], support augmented reality [55] or enhance site-specific communication [106]. While GNSS provides remarkable localization accuracy in rural areas, its performance is rapidly decreasing in urban areas caused by obstructed and reflected signal paths to the satellites [123].

To circumvent these deteriorated connections, one may consolidate terrestrial signals as provided by long term evolution (LTE) [23], wireless local area networks (WLAN) or ultrawide-band (UWB) [138, 17]. Both LTE and WLAN are attractive due to their extensive deployment of base stations especially in urban regions. Nevertheless, the achievable localization accuracy is limited, due to their poor temporal resolution.

Large signal bandwidths, as provided by UWB or fifth-generation cellular (potentially), enable a temporal resolution sufficient to achieve a centimeter-level accuracy [114]. However, to ensure this accuracy in urban areas, a large number of base stations is required [1]. This requirement is a major drawback in high-accuracy localization. Despite the costs of each assembled base station, the stations need to be installed, calibrated and synchronized. Considering the scarce nature of available radio spectrum, the required signal bandwidth is allocated to users competitively and thus, each additional radio measurement also adds some costs.

This thesis tackles high-accuracy localization using radio signals. The particular interest is set on reducing the number of base stations. A decreased number of base stations will degrade the localization performance. Traditionally, this degradation may be counteracted by sensor fusion, for example, with inertial measurement units, odometers or light detection and ranging [11, 127, 129]. While sensor fusion requires additional measurement capabilities, in this theses, we propose to exploit the available radio measurements in a more elaborated way. Tying a site-specific channel model [112] to radio measurements enables to utilize location information contained in reflected signal paths [141]. Their utilization, rather than mitigation, improves the location accuracy and remedies a potential performance loss caused by missing base stations. Employing a site-specific channel model discloses new challenges, as discussed in the following.

1.1 Research hypotheses

In this thesis, three research topics are formulated. The first topic targets on modeling a site-specific propagation channel in order to describe simultaneously position-related information as well as interfering diffuse multipath. The second topic tackles exploration of the angle-delay domain of multipath components in order to reduce the number of base stations to a single one. The third topic treats cooperation among the nodes where a site-specific channel model offers to restrain from the need of base stations at all.

1.1.1 Towards a site-specific channel model for localization

Position estimation achieving high accuracy relies on model-based exploration of the angle-delay domain. Based on geometrical optics [6, 112, 58], the line-of-sight (LOS) to each base station is described using angle measurements or delay measurements or both.

Recent studies have demonstrated that position-related information is also contained in reflections from flat surfaces [141, 113, 116]. While standard systems rely on the angle-delay information of the LOS only, the exploration of reflections adds additional information, potentially allowing to reduce the number of required base stations to a single one. Moreover, exploiting reflections enables to determine the position even in non-LOS conditions where the direct path is blocked by obstacles.

However, it is not clear to what extent the information regarding a reflection enables a deduction of the user positions and the geometry of the surrounding environment. Furthermore, the access to parameters of the reflections is limited due to undesired diffuse multipath. Diffuse multipath denotes closely arriving multipath components which overlap with each other and as a consequence, they cannot be resolved in angle-delay domain (given by the measurement equipment capabilities). Diffuse multipath stems from the interaction of the radio signal with small objects or rough surfaces or both, and is inevitable in real channels. Due to its overlapping nature it limits the accessible position-related information contained in specular components. Research Hypothesis 1 targets at an appropriate site-specific channel model, and is defined as:

Hypothesis 1

A site-specific channel model describes the propagation mechanisms as function of the surrounding environment. A detailed understanding of the propagation mechanisms enlightens the relation between reflections, useful for positioning, and diffuse multipath, acting as self-interference.

1.1.2 Localization using a single base station

Exploiting the angle-delay domain of radio signal measurements enables localization using a single base station [46]. Moreover, using position information contained in scatter points enables localization even in non-LOS conditions [92, 113, 3]. However, exploiting the angle domain poses additional challenges on the measurement equipment capabilities typically achieved by employing

phase-coherent antenna arrays. This rather expensive hardware hinders the exploitation of angle measurements using low-cost transceivers.

As an alternative, the angle domain may be established using directive antennas. Directive antennas weigh the radio signals as function of their arriving angle. Using several directive antennas, angle information gets accessible without the need for phase-coherent antenna arrays which yields the second research Hypothesis as:

Hypothesis 2

The number of base stations can be reduced dramatically by exploiting the angle-delay domain. Using directive antennas, radio signals get accessible in angle-delay domain which avoids the need for coherent multi-antenna transceivers.

1.1.3 Avoiding base stations through cooperation

Providing superior measurement capabilities and introducing cooperation among the users has the potential to circumvent the requirement for numerous base stations. However, lacking base stations, a frame-of-reference is missing which prevents localization using global coordinates.

In absence of a base station, a site-specific channel model can re-establish the missing global coordinates. The site-specific channel model describes multipath propagation as a function of the surrounding environment. This offers the opportunity to exploit the surrounding environment as a frame-of-reference and thus, the users can determine their global coordinates without requiring any base stations at all. Deployment costs drop to zero.

Exploiting the surrounding environment as a frame-of-reference demands a high-precision site-specific channel model. The channel model is exploited by cooperating users, provoking rising complexity of localization algorithms. Research Hypothesis 3 tackles localization avoiding base stations by stating:

Hypothesis 3

Cooperation among the users enables their localization without any need of base stations. The site-specific channel model can be refined using cooperative measurements.

1.2 Contributions and outline

The contributions of this thesis may be summarized as localization achieving high-accuracy while limiting the need for fixed infrastructure (i.e. base stations or anchors). Based on the stated research hypotheses the contributions target on an appropriate site-specific channel model for localization, the limitation of required base stations using angle-delay measurements and avoiding base stations by introducing cooperation.

The thesis consists of two parts. The introduction is captured in Part 1, representative publications are attached in Part 2. In order to clarify the bibliography, attached publications [T#] are denoted by an additional T.

- [T1] J. Kulmer, F. Wen, N. Garcia, H. Wymeersch, and K. Witrisal. Impact of rough surface scattering on stochastic multipath component models. In *Personal, Indoor, and Mobile Radio Communication (PIMRC), 2018 IEEE 29th Annual International Symposium on*. IEEE, 2018.

Propagation models for localization provide a site-specific description of reflections but not of dense multipath. This paper examines a site-specific characterization of dense multipath using the effective roughness (ER) approach. The ER is adapted in order to maintain reciprocity as well as a smooth transition between Lambertian and directional scattering. The derived angle-delay power spectrum is verified using empiric descriptions stemming from measurement campaigns.

- [T2] J. Kulmer, S. Hinteregger, B. Großwindhager, M. Rath, M. Bakr, E. Leitinger, and K. Witrisal. Using DecaWave UWB Transceivers for High-accuracy Multipath-assisted Indoor Positioning. In *IEEE ICC 2017 Workshop on Advances in Network Localization and Navigation (ANLN)*, 2017.

Localization using a single base station demands for high-quality radio transceivers. This paper compares a low-cost transceiver with laboratory grade equipment for the task of multipath-assisted localization. In comparison to uncertainty of the provided floorplan, additional errors originating from clock offsets and measurement noise demonstrate to be negligible. A simple positioning algorithm is derived which evaluates a likelihood function at a number of possible user positions.

- [T3] J. Kulmer, S. Grebien, M. Rath, and K. Witrisal. On the unimportance of phase-coherent measurements for beampattern-assisted positioning. In *2018 IEEE Wireless Communications and Networking Conference (WCNC)*, pages 1–6, April 2018.

The angle-delay domain bears important position information but its exploitation typically requires phase-coherent measurements. In this paper, an algorithm is derived for exploiting the angle-delay domain using directive antennas. Non-linearities originating at the multipath amplitude estimation are approximated to obtain closed-form solutions. The evaluation of the derived estimator shows strong attenuation of local modes in comparison to antennas radiating in an isotropic manner.

- [T4] J. Kulmer, E. Leitinger, P. Meissner, and K. Witrisal. Cooperative Multipath-assisted Navigation and Tracking: A Low-Complexity Approach. In *1st EAI International Conference on Future access enablers of ubiquitous and intelligent infrastructures, 2015*. EAI, 2015.

Cooperative localization has the potential to increase both accuracy and robustness at the cost of increased computational complexity. This paper examines a low complexity approach for cooperative, multipath-assisted localization. Arising non-linearities in delay measurements and non-parametric error distributions are tackled using local linearizations and Gaussian descriptions. Based on numeric evaluations a strong reduction of channel utilization as well as computational complexity is shown at the cost of a minor performance loss.

- [T5] J. Kulmer, E. Leitinger, P. Meissner, S. Hinteregger, and K. Witrissal. Cooperative localization and tracking using multipath channel information. In *2016 International Conference on Localization and GNSS (ICL-GNSS)*, June 2016.

A tracking filter is presented capable to localize two users without any usage of base stations. The users sense their multipath environment and weigh the measured multipath delays for positioning using (low complexity) linearized filters. Performance analysis using synthetic and real data demonstrates a position accuracy in low centimeter-level range on cost of the requirement of highly accurate floorplans.

- [T6] J. Kulmer, E. Leitinger, S. Grebien, and K. Witrissal. Anchorless cooperative tracking using multipath channel information. *IEEE Transactions on Wireless Communications*, 17(4):2262–2275, April 2018.

The performance of cooperative, multipath-assisted localization is strongly dependent on the precision of the provided floorplan. In this paper, an algorithm is proposed for joint localization of at least two users and the simultaneous updating of the floorplan information. A measurement campaign exemplifies the impact of the number of users and the radio-frequency bandwidth. The rearrangement of the floorplan is shown for selected reflective surfaces.

Publication [T1] refers to research Hypothesis 1, publications [T2,T3] refer to Hypothesis 2 and publications [T4-T6] refer to Hypothesis 3.

List of contributions not included in this thesis

There seems to be a common acceptance to emphasize additional scientific contributions with only loose connections to the researched topics. To this end, a list of additional contributions shall be appended, limited to publications reviewed or in review.

- [1] M. Bakr, B. Grosswindhager, M. Rath, J. Kulmer, I. Hunter, R.A. Abd-Alhameed, K. Witrissal, C. Boano, K. Römer, W. Bösch. A Compact Broadband Frequency Selective Microstrip Antenna and Its Application to Indoor Positioning Systems for Wireless Networks. In *IET Microwaves Antennas and Propagation (accepted for publication)*, 2019.
- [2] S. Grebien, J. Kulmer, F. Galler, M. Goller, E. Leitinger, H. Arthaber, and K. Witrissal. Range Estimation and Performance Limits for UHF-RFID Backscatter Channels. *IEEE Journal of Radio Frequency Identification*, 1(1):39–50, March 2017.
- [3] B. Großwindhager, M. Rath, J. Kulmer, M. S. Bakr, C. A. Boano, K. Witrissal, and K. Römer. SALMA: UWB-based Single-Anchor Localization System using Multipath Assistance. In *Proceedings of the 16th ACM Conference on Embedded Networked Sensor Systems*, pages 132–144. ACM, 2018.

- [4] B. Großwindhager, M. Rath, J. Kulmer, S. J. Grebien, M. S. A. Bakr, C. A. Boano, K. Witrival, and K. U. Römer. Demo Abstract: UWB-based Single-anchor Low-cost Indoor Localization System. In *15th ACM International Conference on Embedded Networked Sensor Systems (SenSys)*, 2017.
- [5] B. Großwindhager, M. Rath, J. Kulmer, S. Hinteregger, M. Bakr, C. A. Boano, K. Witrival, and K. Römer. UWB-based single-anchor low-cost indoor localization system. In *Proceedings of the 15th ACM Conference on Embedded Network Sensor Systems*, page 34. ACM, 2017.
- [6] S. Hinteregger, J. Kulmer, M. Goller, F. Galler, H. Arthaber, and K. Witrival. UHF-RFID backscatter channel analysis for accurate wide-band ranging. In *2017 IEEE International Conference on RFID (RFID)*, pages 117–123, May 2017.
- [7] S. Hinteregger, E. Leitinger, P. Meissner, J. Kulmer, and K. Witrival. Bandwidth dependence of the ranging error variance in dense multipath. In *2016 24th European Signal Processing Conference (EUSIPCO)*, pages 733–737, Aug 2016.
- [8] A. N. Hong, M. Rath, J. Kulmer, S. Grebien, K. N. Van, and K. Witrival. Gaussian Process Modeling of UWB Multipath Components. In *2018 IEEE Seventh International Conference on Communications and Electronics (ICCE)*, pages 291–296, July 2018.
- [9] J. Kulmer and P. Mowlae. Harmonic phase estimation in single-channel speech enhancement using von Mises distribution and prior SNR. In *2015 IEEE International Conference on Acoustics, Speech and Signal Processing (ICASSP)*, pages 5063–5067, April 2015.
- [10] J. Kulmer and P. Mowlae. Phase Estimation in Single Channel Speech Enhancement Using Phase Decomposition. *IEEE Signal Processing Letters*, 22(5):598–602, May 2015.
- [11] J. Kulmer and S. Grebien and E. Leitinger and K. Witrival. Delay Estimation in Presence of Dense Multipath. *IEEE Wireless Communication letters*, (in review).
- [12] J. Kulmer, P. Mowlae, and M. K. Watanabe. A probabilistic approach for phase estimation in single-channel speech enhancement using von Mises phase priors. In *2014 IEEE International Workshop on Machine Learning for Signal Processing (MLSP)*, pages 1–6, Sep. 2014.
- [13] J. Kulmer and K. Witrival. Revisiting the image source model: Towards geometry-based modeling of agent-to-agent channels. In *Workshop on Dependable Wireless Communications and Localization for the IoT*, September 2017.
- [14] P. Mowlae and J. Kulmer. Harmonic Phase Estimation in Single-Channel Speech Enhancement Using Phase Decomposition and SNR Information. *IEEE/ACM Transactions on Audio, Speech, and Language Processing*, 23(9):1521–1532, Sep. 2015.

- [15] P. Mowlae and J. Kulmer. Phase Estimation in Single-Channel Speech Enhancement: Limits-Potential. *IEEE/ACM Transactions on Audio, Speech, and Language Processing*, 23(8):1283–1294, Aug 2015.
- [16] P. Mowlae, J. Kulmer, J. Stahl, and F. Mayer. *Single Channel Phase-Aware Signal Processing in Speech Communication: Theory and Practice*. John Wiley & Sons, 2016.
- [17] P. Mowlae, J. Stahl, and J. Kulmer. Iterative joint MAP single-channel speech enhancement given non-uniform phase prior. *Speech Communication*, 86:85 – 96, 2017.
- [18] M. Rath, J. Kulmer, M. Bakr, G. B., and K. Witrals. Indoor Localization and Communication Enhanced by Directional UWB Antennas. In *Workshop on Dependable Wireless Communications and Localization for the IoT*, September 2017.
- [19] M. Rath, J. Kulmer, M. S. Bakr, B. Großwindhager, and K. Witrals. Multipath-assisted indoor positioning enabled by directional UWB sector antennas. In *18th IEEE International Workshop on Signal Processing Advances in Wireless Communications, SPAWC 2017, Sapporo, Japan, July 3-6, 2017*, pages 1–5, 2017.
- [20] J. Stahl, P. Mowlae, and J. Kulmer. Phase-processing for voice activity detection: A statistical approach. In *2016 24th European Signal Processing Conference (EUSIPCO)*, pages 1202–1206, Aug 2016.
- [21] F. Wen, N. Garcia, J. Kulmer, K. Witrals, and H. Wymersch. Tensor Decomposition Based BeamSpace ESPRIT for Millimeter Wave MIMO Channel Estimation. In *IEEE Global Telecommunications Conference (GLOBECOM)*, 2018.
- [22] K. Witrals, S. Hinteregger, J. Kulmer, E. Leitinger, and P. Meissner. High-accuracy positioning for indoor applications: RFID, UWB, 5G, and beyond. In *2016 IEEE International Conference on RFID (RFID)*, pages 1–7, May 2016.

Chapter 2

Problem formulation

This thesis treats the estimation of node positions using radio channel measurements. Let i and j denote two nodes located at positions $\mathbf{p}^{(i)}$ and $\mathbf{p}^{(j)}$. The nodes are able to perform radio channel measurements between each other, yielding the measurement vector $\mathbf{z}^{(i,j)}$. The nodes aim at estimating their positions given the measurements. Formulating a measurement function f_{meas} according to

$$\mathbf{z}^{(i,j)} = f_{\text{meas}}(\mathbf{p}^{(i)}, \mathbf{p}^{(j)}) + \mathbf{n}^{(i,j)} \quad (2.1)$$

the measurement function relates positions $\mathbf{p}^{(i)}$ and $\mathbf{p}^{(j)}$ to the measurement vector $\mathbf{z}^{(i,j)}$ where $\mathbf{n}^{(i,j)}$ describes additive measurement noise.

The representation of f_{meas} depends on the desired level of position accuracy and available measurement capabilities and will be elaborated throughout this thesis. In this problem formulation we introduce f_{meas} using a toy-example presented in Fig. 2.1: two nodes are located in an indoor environment at positions $\mathbf{p}^{(i)}$ and $\mathbf{p}^{(j)}$. Both nodes are equipped with a single antenna, radiating in an isotropic manner. The nodes perform radio channel measurements between each other and aim at estimating their positions using an appropriate f_{meas} . In classic TOA localization, f_{meas} describes the line-of-sight (LOS) distance between both nodes, depicted as Path 1 in Fig. 2.2. In multipath-assisted localization, f_{meas} describes the LOS and in addition, it describes multipath components (MPCs) (Paths 2 - 5 in Fig. 2.2) arising from the interaction of the radio signal with the surrounding environment. If knowledge of the surrounding environment (i.e. the locations of reflective surfaces such as 'window' or 'plaster board west') is available, f_{meas} can utilize this information for positioning.

To further confine f_{meas} , we may distinguish whether $\mathbf{z}^{(i,j)}$ is described at signal level (e.g. the base-band equivalent channel response) or it is described at parameter level (in our toy example, e.g. the estimated multipath delays). The advantage of processing at the signal level, often denoted as *direct* positioning, is direct access to unprocessed data which contains a maximum amount of information, at the cost of increased computational demands [132, 18, 33]. On the contrary, using estimated (multipath) parameters, the dimensions of the measurement model can be reduced, but this approach requires to model the parameters' uncertainty which may be challenging [91].

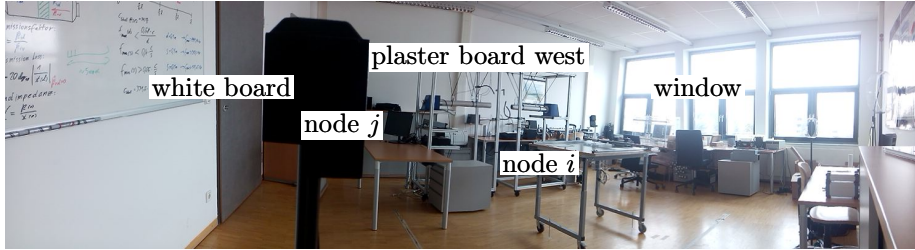


Figure 2.1: Placement of both nodes i and j . 'White board', 'window', 'plaster board west' define the surrounding environment (compare to Fig. 2.2).

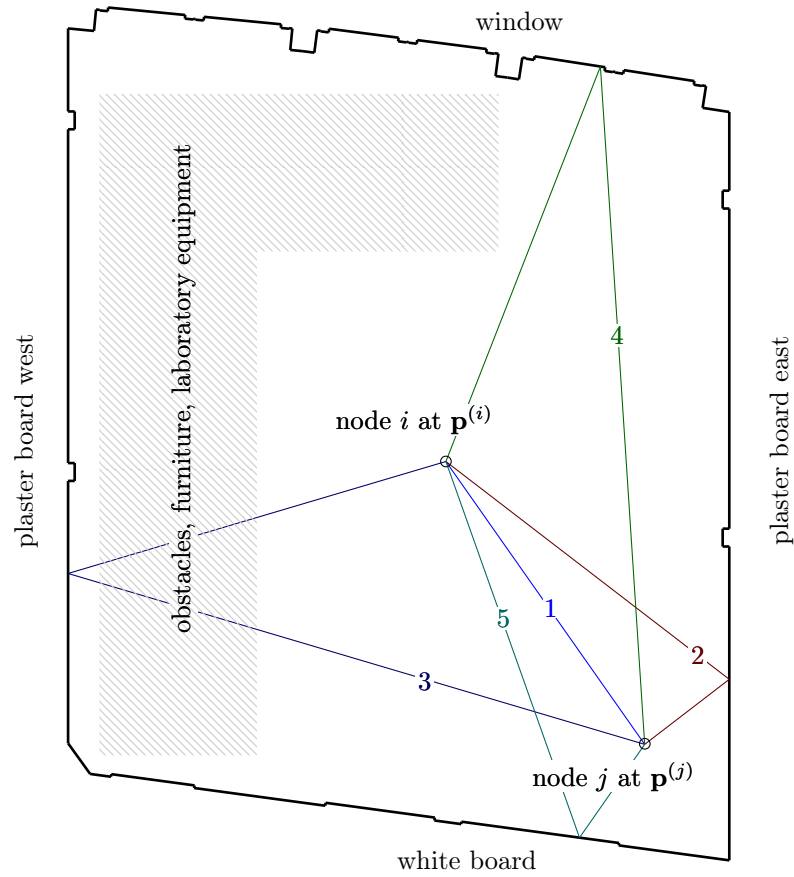


Figure 2.2: Illustration of the setup from Fig. 2.1 showing two nodes i and j . Surrounding environment is labeled by surfaces 'window', 'plaster board west', 'white board' and 'plaster board east' (compare to Fig. 2.1).

2.1 Measurements at signal level

Having measurements available at signal level, a prominent way to describe the measurement model follows as

$$f_{\text{meas}}(\mathbf{p}^{(j)}, \mathbf{p}^{(i)}) = \sum_{k=1}^K \alpha_k \mathbf{s}(\tau_k) \quad (2.2)$$

where the measurement function f_{meas} describes the measurement vector as sum of K MPCs. Each MPC is described by amplitude α_k and delay τ_k , and $\mathbf{s}(\tau_k) = [s(0-\tau_k), s(T_s-\tau_k), s(2T_s-\tau_k), \dots]^T$ denotes the transmitted signal $s(t)$ delayed by τ_k and sampled at period T_s . This representation is often denoted as *tapped delay line model* [93] where the measurement vector $\mathbf{z}^{(i,j)} \in \mathbb{C}^N$ consists of N sampling points. Coming back to the example provided in Fig. 2.2 we incorporate the LOS ($k = 1$) and four reflections ($k = 2 \dots 5$) in f_{meas} . Figure 2.3 illustrates an acquired measurement $\mathbf{z}^{(i,j)}$ (top) in comparison to the modeled one (bottom) using (2.2). We can observe that $\mathbf{z}^{(i,j)}$ presents peaks which may be assigned to the LOS and the reflections. The function f_{meas} models these reflections as function of the nodes' positions, showing that parameters α_k and τ_k bear position information of interest.

2.1.1 Relation between MPC parameters and position parameters

To relate position parameters to MPC parameters, in classic TOA the delay of the LOS ($k = 1$ in Fig. 2.2) can be modeled as geometric distance

$$\tau_{\text{LOS}} = \|\mathbf{p}^{(j)} - \mathbf{p}^{(i)}\|/c \quad (2.3)$$

with $\|\mathbf{x}\|$ as ℓ^2 -norm of vector \mathbf{x} and c as propagation speed (e.g. speed of light). To continue with our toy-example (Fig. 2.2) the remaining paths $k = 2 \dots 5$ describe specular reflections. An elegant way to describe the specular reflections' delays τ_k is elaborated by the concept of *image-sources* [5, 12], resulting in

$$\tau_k = \|f_k(\mathbf{p}^{(j)}) - \mathbf{p}^{(i)}\|/c \quad (2.4)$$

with $f_k(\mathbf{p}^{(j)})$ as image-source of $\mathbf{p}^{(j)}$ at surface k , defined as

$$f_k(\mathbf{p}^{(j)}) = \mathbf{A}_k \mathbf{p}^{(j)} + \mathbf{b}_k \quad (2.5)$$

where \mathbf{A}_k and \mathbf{b}_k depend on the surface normal \mathbf{e}_k and any point \mathbf{p}_k on the surface k as $\mathbf{A}_k = \mathbf{I} - 2\mathbf{e}_k \mathbf{e}_k^T$ and $\mathbf{b}_k = 2\mathbf{e}_k \mathbf{e}_k^T \mathbf{p}_k$. Obviously, (2.4) is capable to describe the LOS path by setting $\mathbf{e}_k = \mathbf{0}$.

Modeling of MPC amplitudes α_k as a function of node positions is not straight-forward. While the LOS path may be described using a free-space path loss model, the reflections are affected additionally by a certain attenuation loss due to the interaction with the surrounding environment. The attenuation loss depends on material specific properties and thus, a proper model of amplitudes requires an accurate characterization of the surrounding environment including surface locations as well as surface properties [39]. In this thesis, we refrain from modeling the amplitudes and instead, treat them as nuisance parameters [141, 113].

The presented toy-example illustrates delay measurements only. In Chapter 3 the delay measurements are extended to path directions at both nodes i and j in order to exploit the position information within MPC directions and delays.

2.1.2 Description of additive noise

Of particular interest is the additive noise, captured in $\mathbf{n}^{(i,j)}$ in (2.1). Additive noise deteriorates the access to position information in f_{meas} which gives importance to its description. In the literature, it is commonly accepted [132, 18, 33],[T2,T3] to treat $\mathbf{n}^{(i,j)}$ as zero-mean, complex-valued Gaussian process with variance σ^2 , written as

$$\mathbb{E}[\mathbf{n}^{(i,j)}] = \mathbf{0} \quad (2.6)$$

$$\mathbb{E}[\mathbf{n}^{(i,j)}(\mathbf{n}^{(i,j)})^H] = \sigma^2 \mathbf{I}. \quad (2.7)$$

This choice is motivated by its simplicity and supported by the algorithms' remarkable performance based on real data [108]. However, the assumption of a constant power in (2.6) has the consequence that each reflection in f_{meas} faces an equal noise power. Considering the example from Fig. 2.1 and Fig. 2.2, notable levels of diffuse multipath originate from objects in the environment (e.g. the laboratory equipment) which are not modeled by f_{meas} . This can be observed in Fig. 2.3 (top) where $\mathbf{z}^{(i,j)}$ contains regions (marked with a question mark ?) which are not explained by f_{meas} (bottom).

2.2 Measurements at parameter level

Equivalent to the signal level, the measurement function f_{meas} can be formulated at parameter level, for example as

$$f_{\text{meas}}(\mathbf{p}^{(j)}, \mathbf{p}^{(i)}) = [\tau_1, \dots, \tau_k, \dots, \tau_K]^T. \quad (2.8)$$

In contrast to the description at signal level, function f_{meas} returns multipath parameters (our toy-example treats delays only but can be extended to other parameters, e.g. direction of departure, arrival or amplitudes) which reduces the dimensions of the observation vector $\mathbf{z}^{(i,j)}$. Considering the toy-example from Fig. 2.2, at parameter level, f_{meas} returns $K = 5$ MPC delays resulting in $\mathbf{z}^{(i,j)} \in \mathbb{R}^5$ while at signal level (see Fig. 2.3), $\mathbf{z}^{(i,j)} \in \mathbb{C}^{50}$. This reduction in dimensions of $\mathbf{z}^{(i,j)}$ simplifies the inverse problem of estimating the node positions $\mathbf{p}^{(i)}$ and $\mathbf{p}^{(j)}$ using measurements $\mathbf{z}^{(i,j)}$. The challenge moves to another abstraction level, the estimation of multipath parameters and their characterization.

2.2.1 Estimation and characterization of multipath parameters

Estimation of multipath parameters in presence of diffuse multipath is a notoriously challenging task. Overlapping DM leads to ambiguous solutions [137, 26, 29] giving importance to the estimation procedure (in Fig. 2.3 there is a path overlap between multipath $k = 2$ and $k = 5$ as well as between $k = 3$ and $k = 4$). Based on an energy criterion, global search [137, 29], iterative search [28, 90]

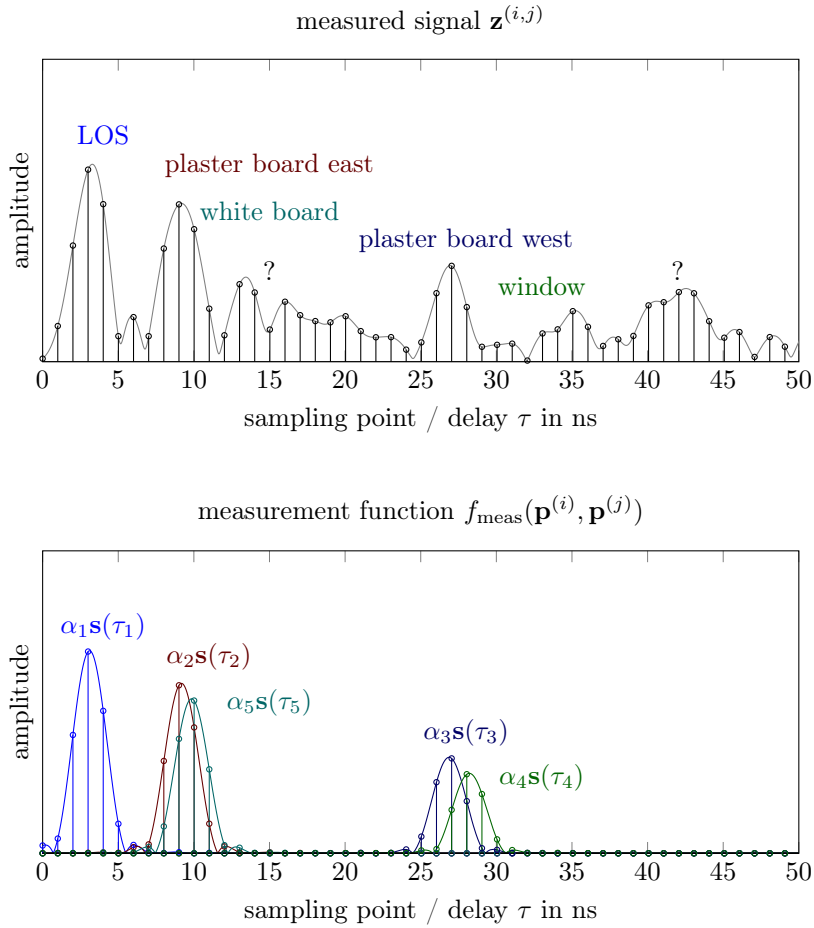


Figure 2.3: Top: measured signal $\mathbf{z}^{(i,j)}$ (dots) acquired from a DecaWave DW1000 transceiver with sampling period $T_s \approx 1$ ns (see [T2]). The continuous gray line indicates an interpolation. Bottom: Outcome of f_{meas} intending to describe $\mathbf{z}^{(i,j)}$ using a sum of multipath components with amplitudes α_k and delays τ_k .

or expectation-maximization algorithms [29] have been proposed. Having delay estimates, a proper uncertainty measure is vital for the measurement model. An uncertainty measure provides information to what extent a specific measurement parameter is reliable. At parameter level, for example, the uncertainty of each multipath delay can be considered by stating [91]

$$\mathbb{E}[\mathbf{n}^{(i,j)}] = \mathbf{0} \quad (2.9)$$

$$\mathbb{E}[\mathbf{n}^{(i,j)}(\mathbf{n}^{(i,j)})^H] = \begin{bmatrix} \sigma_1^2 & & 0 \\ & \ddots & \\ 0 & & \sigma_K^2 \end{bmatrix}. \quad (2.10)$$

The zero-mean property claims that the delay estimation error is unbiased. Furthermore, the second moment exemplifies independence of reflections, indicated by zeros in the off-diagonal elements in (2.10). These assumptions may be violated if different (higher order) reflections share the same reflective surface, as demonstrated empirically in [41].

2.2.2 Representation of delay uncertainty

In what follows is assessing multipath uncertainty σ_k^2 . In [91] a relation between MPC delay uncertainty and MPC signal-to-interference-plus-noise-ratio (SINR) is established by calculating a delay error bound [62, Section 3.11]. The SINR relates the MPC amplitudes to the effects of interfering diffuse multipath and additive noise [141].

2.3 Remarks and outlook

Coming back to the defined research hypothesis, the first hypothesis (Chapter 3, paper [T1]) tackles the formulation of f_{meas} . While standard methods [141] describe f_{meas} as sum of MPCs in the delay domain (as illustrated in our toy-example), in this thesis we aim at extending f_{meas} to a double-directional model (see (3.1)). Moreover, efforts are undertaken for a better description of the measured signal such that f_{meas} (Fig. 2.3 bottom) approaches $\mathbf{z}^{(i,j)}$ (Fig. 2.3 top).

The second hypothesis treats localization using the angle-delay domain (see Chapter 4, papers [T2,T3]). Keeping the toy-example in our mind, we assume node j is fixed at a known position and equipped with several, directive antennas. The moving node i infers its position from radio measurements to each directive antenna at j , exploiting the multipath propagation.

The third hypothesis aims at localization avoiding base stations at all (Chapter 5, papers [T4-T6]). Both nodes i and j are mobile and equipped with a single antenna, radiating in an isotropic manner. Assuming some prior knowledge of the surrounding environment is provided (e.g. the location of reflected surfaces \mathbf{p}_k) the nodes are able to determine their position and simultaneously correct errors in the environment model (e.g. if the provided location of a reflective surface does not fit to the radio signal measurements).

Chapter 3

Towards a site-specific channel model for localization

The channel model describes the interaction between the electromagnetic wave and its surrounding environment. A proper model yields insights in the propagation mechanisms. The question arises to what extent propagation effects need to be explained by the model. In the literature, one may find huge differences in channel models determined by individual demands: The interest in a highly accurate description of wave propagation is satisfied by solving Maxwell's equations which requires an accurate three dimensional environment model to define the boundary conditions. On the contrary, in the field of communications often a few parameters like path loss or delay spread suffice as proper description.

In this thesis, we divide the channel model into a deterministic and a stochastic part [120]. The deterministic part is composed of propagation effects which can be calculated using relations between the geometric setup of both transceivers and the surrounding environment. These relations carry position-related information which can be employed for positioning. It will be further discussed in Section 3.1.

The stochastic part includes propagation effects which are described in a statistical manner [110, 122, 15]. Rather than an exact representation as provided by the deterministic part, the stochastic part aims at representing *average* propagation effects. The propagation effects are described using statistical characteristics which can be calculated analytically from a provided geometric setup or can be estimated from extensive channel measurements. In contrast to the deterministic part, the stochastic part contains position information hidden in its statistical characteristics. To exploit this information for positioning, many observations are required, as further illustrated in Section 3.2.

We define the channel model as [30]

$$r(t) = \int_{\mathbb{S}^2} \int_{\mathbb{S}^2} \int_0^T b^{(i)}(\mathbf{u}^{(i)}) b^{(j)}(\mathbf{u}^{(j)}) s(t-\tau) h(\mathbf{u}^{(i)}, \mathbf{u}^{(j)}, \tau) d\tau d\Omega(\mathbf{u}^{(i)}) d\Omega(\mathbf{u}^{(j)}) + w(t) \quad (3.1)$$

where $b^{(i)}(\mathbf{u}^{(i)}) \in \mathbb{C}$ and $b^{(j)}(\mathbf{u}^{(j)}) \in \mathbb{C}$ describe the complex-valued antenna's beampattern (equivalent to the square-root of the antenna's gain function) of node i and j as function of the unit-length direction $\mathbf{u}^{(i)} \in \mathbb{R}^3$ and $\mathbf{u}^{(j)} \in \mathbb{R}^3$.

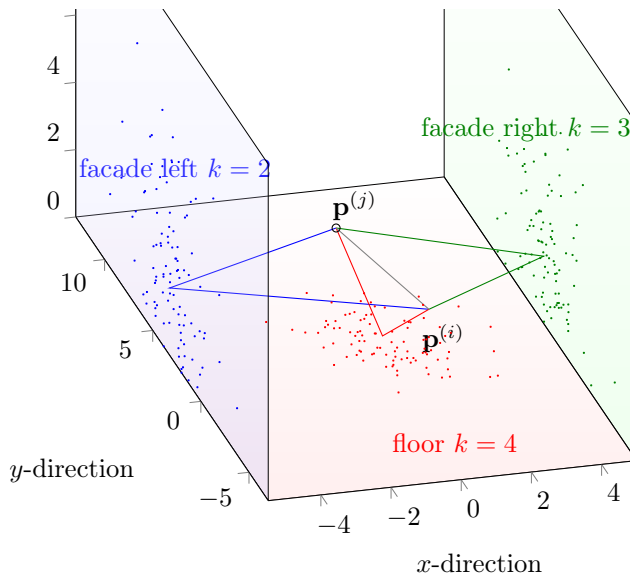


Figure 3.1: Illustration of multipath propagation between node i and j demonstrating the deterministic and stochastic part. The deterministic part describes the LOS ($k = 1$) and 3 specular reflections ($k = 2, 3, 4$) originating from both facades and from the floor. The stochastic part considers additional random reflections which originate from scatter points.

Directions $\mathbf{u}^{(i)}$ and $\mathbf{u}^{(j)}$ are defined on the 2-sphere \mathbb{S}^2 [63] with azimuth $\phi^a \in [0, 2\pi)$ and elevation $\phi^e \in [0, \pi]$ as

$$\mathbf{u} = [\cos(\phi^a) \sin(\phi^e), \sin(\phi^a) \sin(\phi^e), \cos(\phi^e)]^T$$

which may also be represented as $\mathbf{u} \equiv [\phi^a, \phi^e]^T$. The differential solid angle element $d\Omega(\mathbf{u})$ for direction \mathbf{u} is defined as $d\Omega(\mathbf{u}) = \sin \phi^e d\phi^e d\phi^a$. The band-limited transmitted signal is denoted as $s(t)$, T is the length of the received signal $r(t)$ and $w(t)$ denotes additive, white Gaussian noise. Note that, in (3.1) we drop the node indexes i and j unless explicitly required.

Finally, $h(\mathbf{u}^{(i)}, \mathbf{u}^{(j)}, \tau)$ defines the *spreading function* [30] (sometimes denoted as *propagation model* [125, 50, 47]). The spreading function characterizes the input-output relation of the channel and can be modeled as sum of the deterministic and the stochastic part, according to

$$h(\mathbf{u}^{(i)}, \mathbf{u}^{(j)}, \tau) = \sum_k \underbrace{\alpha_k \delta(\mathbf{u}^{(i)} - \mathbf{u}_k^{(i)}) \delta(\mathbf{u}^{(j)} - \mathbf{u}_k^{(j)}) \delta(\tau - \tau_k)}_{\text{deterministic}} + \underbrace{\nu_k(\mathbf{u}^{(i)}, \mathbf{u}^{(j)}, \tau)}_{\text{stochastic}} \quad (3.2)$$

equivalent to

$$h(\boldsymbol{\theta}) = \sum_k \alpha_k \delta(\boldsymbol{\theta} - \boldsymbol{\theta}_k) + \nu_k(\boldsymbol{\theta}) \quad (3.3)$$

with $\boldsymbol{\theta} = [(\mathbf{u}^{(i)})^T, (\mathbf{u}^{(j)})^T, \tau]$ and $\boldsymbol{\theta}_k = [(\mathbf{u}_k^{(i)})^T, (\mathbf{u}_k^{(j)})^T, \tau_k]$. The deterministic part is composed of multipath components (MPCs) with index k , each described

by a parameter vector $\boldsymbol{\theta}_k$ containing position-related information (compare to Chapter 2). The Dirac-delta $\delta(\cdot)$ ensures that the multipath component exists for a unique combination of directions and delay.

The stochastic part is described by $\nu_k(\boldsymbol{\theta}) \equiv \nu_k(\mathbf{u}^{(i)}, \mathbf{u}^{(j)}, \tau)$ and is often denoted as *dense multipath* or *diffuse multipath*. This terminology stems from the observation that in channel measurements, several MPCs arrive closely in the angle-delay domain. Considering the limited resolution determined by the measurement equipment, the arriving MPCs cannot be separated (they are *dense*) and appear as random fluctuations. The random fluctuations are described in a statistical manner.

Figure 3.1 exemplifies a street canyon scenario consisting of two nodes facing multipath propagation. A proper spreading function aims at describing $h(\boldsymbol{\theta})$ based on the floorplan in Fig. 3.1 as illustrated in the following. In Section 3.1 the description of deterministic MPCs is reviewed using the image-source model, demonstrating that angular information of specular reflections can be mapped between both transceivers determined by geometric relations. Section 3.2 reviews the characterization of stochastic multipath showing that its site-specific modeling results in similar angle-delay patterns as observed by cluster-based channel descriptions [110].

3.1 Deterministic modeling of position-related information

The deterministic part of (3.3) represents the relation between MPC parameters $\boldsymbol{\theta}_k$ and both node positions as well as the surrounding environment.

Among different representations of the electromagnetic waves, including Maxwell's equations [87], physical optics [142] or ray tracing [39], its representation using geometrical optics (GO) [6, 58] seems to be promising. At GO the propagation mechanisms are described similar to visible light. It represents the electromagnetic wave as rays which allows simple geometric relations between node positions and propagation parameters. Complex effects like diffraction or penetration are neglected. These rather strong approximations may be cumbersome at low carrier frequencies where the wavelength is in a similar range than the surrounding object sizes. With increasing carrier frequencies, e.g. mm-frequency bands, the impact from diffraction and penetration gets less important [120].

In this work, deterministic relations are gathered using geometric relations solely. Seeking for position-related information in channel measurements, in the literature, two phenomena of propagation are employed commonly, namely reflections from flat surfaces and reflections from scatter points. Reflections at flat surfaces [90, 5, 25] are characterized by an equal impinging and reflected angle, denoted as *specular reflections*. Specular reflections originate at surfaces whose surface roughness is small in comparison to the signal's wave length. Moreover, the surface dimension is required to be large in comparison to the signal's wave length, explained by the Fresnel zones [100, 120]. Considering wavelengths in the order of centimeters, many environments [5] fulfill the requirements of specular components which explains its applicability for the use of positioning.

The second phenomenon of reflections carrying position information stems

from scatter points [56]. Illuminated scatter points spread the impinging power in various directions and parts of the power radiate along the receiver. Prominent examples are street signs or pillars.

Motivated by radio channel measurements in [83, 82, 89], we limit the deterministic part to specular reflections, as shown in the following.

In (3.3) we have defined the parameter vector $\boldsymbol{\theta}_k$ as

$$\boldsymbol{\theta}_k = \begin{bmatrix} \mathbf{u}_k^{(i)} \\ \mathbf{u}_k^{(j)} \\ \tau_k \end{bmatrix} \begin{array}{l} \text{direction at node } i \\ \text{direction at node } j \\ \text{delay} \end{array} \quad (3.4)$$

In order to establish relations between $\boldsymbol{\theta}_k$ and the node positions $\mathbf{p}^{(i)}$ and $\mathbf{p}^{(j)}$, we employ the image-source model f_k , already introduced in Sec. 2.1.1. The MPC parameters result as simple geometric relationships, according to

$$\mathbf{u}_k^{(i)} = \frac{\bar{\mathbf{u}}_k^{(i)}}{\|\bar{\mathbf{u}}_k^{(i)}\|}, \quad \bar{\mathbf{u}}_k^{(i)} = \frac{f_k(\mathbf{p}^{(j)}) - \mathbf{p}^{(i)}}{\|f_k(\mathbf{p}^{(j)}) - \mathbf{p}^{(i)}\|} \quad (3.5)$$

$$\mathbf{u}_k^{(j)} = \frac{\bar{\mathbf{u}}_k^{(j)}}{\|\bar{\mathbf{u}}_k^{(j)}\|}, \quad \bar{\mathbf{u}}_k^{(j)} = \frac{f_k(\mathbf{p}^{(i)}) - \mathbf{p}^{(j)}}{\|f_k(\mathbf{p}^{(i)}) - \mathbf{p}^{(j)}\|} \quad (3.6)$$

and

$$\tau_k = \frac{\|f_k(\mathbf{p}^{(j)}) - \mathbf{p}^{(i)}\|}{c} \quad (3.7)$$

with propagation speed c . Here, directions $\mathbf{u}_k^{(i)}$ and $\mathbf{u}_k^{(j)}$ of node i and j point along the image-sources of node j and i .

In contrast to reflections from scatter points, specular reflections have the remarkable property of $\mathbf{u}_k^{(i)} = -\mathbf{A}_k \mathbf{u}_k^{(j)}$ with Householder matrix \mathbf{A}_k (see Section 2.1.1). Hence, knowledge of the surrounding environment (\mathbf{A}_k is known) enables to calculate $\mathbf{u}_k^{(i)}$ from $\mathbf{u}_k^{(j)}$ as well as $\mathbf{u}_k^{(j)}$ from $\mathbf{u}_k^{(i)}$. This property will be exploited in Chapter 4.

3.2 Stochastic modeling of dense multipath

While the deterministic part describes position-related information, the stochastic part covers random fluctuations appearing in the spreading function. These random fluctuations may have different sources, e.g. they stem from materials with random surface structure (potentially subject to strong variations in time, e.g. leaves of trees) or the reflection's position-related information is arguable negligible (tiny objects located on a desk). Everything not contained in the deterministic part is assumed to be described by the stochastic part.

3.2.1 Empirical descriptions of dense multipath

Research on an empirical description of dense multipath is performed usually in the context of communications culminating in standardized channel models [82, 145, 2], as highlighted in the following.

Empirical descriptions considered in communications

One prominent example of a stochastic channel model is widely known as Saleh-Valenzuela (S-V) model [110]. Originally introduced for indoor propagation considering the delay domain only, it was extended to the angle domain [122] and finally acknowledged as channel model suitable for both indoor and outdoor scenarios in the standards IEEE 802.11ad [82] (60 GHz WLAN), IEEE 802.15.3c [145] (60 GHz WPAN) or 3GPP TR38.901 [2] (0.5-100 GHz). The (extended) S-V model is purely stochastic and it assumes that the receiving power arrives in cluster. In delay domain, the arrival of clusters is described using empirical distributions, e.g. a Poisson distribution is identified for the arrival rate and an exponential distribution for the cluster power. These parameters are denoted as *inter*-cluster parameters [47]. The rays within a cluster are described using the *intra*-cluster parameters. Again a Poisson distribution is employed for rays and an exponential distribution for the decay. In the angular domain, a uniform distribution is used for clusters [145, 2] and a Gaussian or Laplacian or both for the rays within a cluster.

The distributions as well as parameters of the S-V model are identified empirically using extensive measurement campaigns. Although channel standards [82, 145, 2] provide collected parameters for a number of scenarios, like *street canyon* or *rural*, methods for describing DM as function of the geometric setup are missing.

Empirical descriptions considered in localization

In the context of UWB localization, in the delay domain, DM is often characterized using a concatenation of rising and decreasing DM power (denoted as *double exponential DM power*) [79, 140],[T4]. The rising power is considered as *soft onset* [61] of DM. Subsequently the DM power decreases again. The origin of this DM behavior was identified in [61] based on measurements in non-LOS conditions.

3.2.2 Theoretic modeling of dense multipath

In [T1] we propose a site-specific approach in order to model dense multipath. The model describes the surrounding environment using planar surfaces. At each surface k , DM occurs due to a certain roughness. The roughness describes variations in the surface, including small variations stemming from rough cast as well as strong variations originating at balconies or book shelves.

Perceiving DM as realization $\nu_k(\boldsymbol{\theta})$ of a random process, the assumptions on its first and second moment are

$$\mathbb{E}[\nu_k(\boldsymbol{\theta})] = 0 \quad (3.8a)$$

$$\mathbb{E}[\nu_k(\boldsymbol{\theta})\nu_k^*(\boldsymbol{\theta}')] = p_{\text{DM},k}(\boldsymbol{\theta})\delta(\boldsymbol{\theta} - \boldsymbol{\theta}') \quad (3.8b)$$

$$\mathbb{E}[\nu_k(\boldsymbol{\theta})\nu_{k'}^*(\boldsymbol{\theta}')] = 0. \quad (3.8c)$$

Motivated by [8], DM is a zero-mean process (3.8a), uncorrelated between two different angle-delay parameters $\boldsymbol{\theta}$ and $\boldsymbol{\theta}'$ (3.8b) and uncorrelated across different surfaces $k \neq k'$ (3.8c) and thus, solely described by the second moment $\mathbb{E}[|\nu_k(\boldsymbol{\theta})|^2]$. The DM angle-delay power spectrum (ADPS) $p_{\text{DM},k}(\boldsymbol{\theta})$ describes the power spectrum of the DM as function of the parameters $\boldsymbol{\theta}$ and subsequently

as function of the geometric relationships between nodes and surrounding environment. To calculate its impacts, it is worth to analyze DM originating from a single surface before composing the spreading function consisting of several reflections.

At this point a refreshment of the definitions of the spreading function and the channel model may be vital. The spreading function is able to characterize the propagation effects using *infinite* resolution, mathematically depicted by the Dirac delta in the deterministic part. The considered infinite resolution of the DM's stochastic process accompanies with infinite spectral bandwidth which consequences in a non-converging second moment of DM. This non-convergence is depicted mathematically by the Dirac delta in (3.8b).

The ADPS $p_{\text{DM},k}(\boldsymbol{\theta})$ may be interpreted as weighing constant to the (non-converging) second moment. Unfortunately, there is no clear terminology to be found in literature. To be precise, the ADPS is a *power spectral density* but often it is denoted as a power profile (e.g. the power delay profile) [93]. We follow the definition of [30] where the term *density* is dropped.

Isolated DM from a single planar surface

In order to calculate the ADPS $p_{\text{DM},k}(\boldsymbol{\theta})$ for a single reflection k , we assume that the impinging ADPS at the rough surface is scattered back along the direction of the specular component but also in *other* directions. To calculate the power spectrum as function of the scatter directions one may explore the *effective roughness* (ER) approach [20, 21]. Let $\mathbf{q} \in \mathcal{S}_k$ be an arbitrary point with differential area dA , located on the reflective surface k with boundaries \mathcal{S}_k . Assuming node j radiates in an isotropic manner, then the ER $f_{\text{ER}}(\boldsymbol{\theta}_{\text{DM},k})$ describes the differential received power spectrum dP_r at node i arriving from \mathbf{q} , according to

$$dP_r = f_{\text{ER}}(\boldsymbol{\theta}_{\text{DM},k})dA \quad (3.9)$$

with parameters

$$\boldsymbol{\theta}_{\text{DM},k} = \left\{ \underbrace{S, \alpha_R}_{\text{scatter parameters}}, \underbrace{\mathbf{p}^{(i)}, \mathbf{p}^{(j)}, \mathcal{S}_k}_{\text{geometric setup}} \right\} \quad (3.10)$$

Its beauty is its simplicity. The ER depends on two scatter parameters which describe the reflective material properties:

$$\begin{array}{l} S \text{ scatter attenuation} \\ \alpha_R \text{ roughness parameter} \end{array} .$$

The scatter attenuation quantifies the relative amount of total scattered amplitude (similar to the reflection coefficient of the deterministic components). The roughness parameter α_R denotes the level of roughness. For very high roughness (larger than the signal's wavelength) it becomes $\alpha_R = 0$. Reduced levels of roughness are described by an increased α_R . The remaining parameters in $\boldsymbol{\theta}_{\text{DM},k}$ define the geometric setup, consisting of node positions $\mathbf{p}^{(i)}$, $\mathbf{p}^{(j)}$ and surrounding environment \mathcal{S}_k (the boundaries of the reflective surface k).

As shown in [T1], $f_{\text{ER}}(\boldsymbol{\theta}_{\text{DM},k})$ can be written as

$$f_{\text{ER}}(\boldsymbol{\theta}_{\text{DM},k}) = \frac{S^2}{k_{\alpha_R}} \frac{\cos \theta^{(i)}}{(d^{(i)})^2} \frac{\cos \theta^{(j)}}{(d^{(j)})^2} \left(\frac{1 + \cos \psi}{2} \right)^{\alpha_R} \quad (3.11)$$

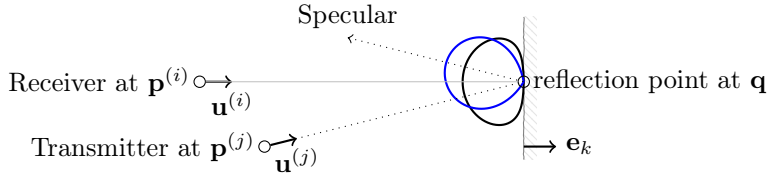


Figure 3.2: Illustration of scattered power at reflection point \mathbf{q} for strong roughness ($\alpha_R = 0$) — and reduced roughness ($\alpha_R = 10$) — in dB scale.

where $\cos \theta^{(i)} = \mathbf{e}_k^T \mathbf{u}^{(i)}$ and $\cos \theta^{(j)} = \mathbf{e}_k^T \mathbf{u}^{(j)}$ denote the angles between directions $\mathbf{u}^{(i)}$, $\mathbf{u}^{(j)}$ and surface orientation \mathbf{e}_k ; and $d^{(i)} = \|\mathbf{q} - \mathbf{p}^{(i)}\|$ and $d^{(j)} = \|\mathbf{q} - \mathbf{p}^{(j)}\|$ are the corresponding distances. Finally, ψ denotes the angle between the specular and scattering path and k_{α_R} acts as normalization factor (defined in [T1]).

Figure 3.2 illustrates the impact of the roughness parameter α_R by exemplifying a *scatter lobe* arising from an impinging ray bouncing at a reflection point \mathbf{q} . Considering large roughness $\alpha_R = 0$, the scatter lobe — corresponds to the *Lambertian* cosine law where the majority of power is scattered along the surface normal. At reduced roughness $\alpha = 10$, the scatter lobe — shifts in the direction of the specular ray. The scatter attenuation acts as scaling factor for the scattering lobe.

It is worth noting that the concept of ER stems from the research field *ray-tracing* [39] with the objective of an accurate simulation of the propagation of electromagnetic waves. Improved accuracy goes hand in hand with increased computational demands. To reduce complexity, one may reduce the number of rays to be traced which results in missing rays in the angle-delay domain. Hence, in [22, 84, 85], the ray-tracer was extended by a stochastic component using the ER approach. This component fills the gaps in the angle-delay domain. Due to its simplicity the ER is employed in quite a number of applications, including point cloud scattering [60, 57, 133, 134, 102] or propagation graph theory [131, 130]. For a compact notation, we assume that each reflective surface is equipped with constant scatter parameters ($S \triangleq S_k$ and $\alpha_R \triangleq \alpha_{R,k}$). Across different materials, these parameters will change [34, 102, 101] which needs to be considered in the further calculations.

In the following, we transform the ER to the ADPS of the DM. While f_{ER} explains dP_r from a specific dA we are interested in the ADPS for the desired propagation parameter vector $\boldsymbol{\theta} = [(\mathbf{u}^{(i)})^T, (\mathbf{u}^{(j)})^T, \tau]$. This requires a variable change from dA to $d\boldsymbol{\theta}$. Figure 3.3 illustrates several scattering lobes arising at reflection points on a rough surface, drawn for two cases of surface roughness. At a very rough surface — the majority of impinging intensity is scattered normal to the surface (and independent on the impinging angle). At smooth surfaces — the majority of power is scattered along the specular reflection direction

The received scattering power from a reflection point with differential area dA depends on (i) the impinging intensity at dA , (ii) the scattering lobe and (iii) the observed intensity from dA . Note, the transmitter radiates with constant

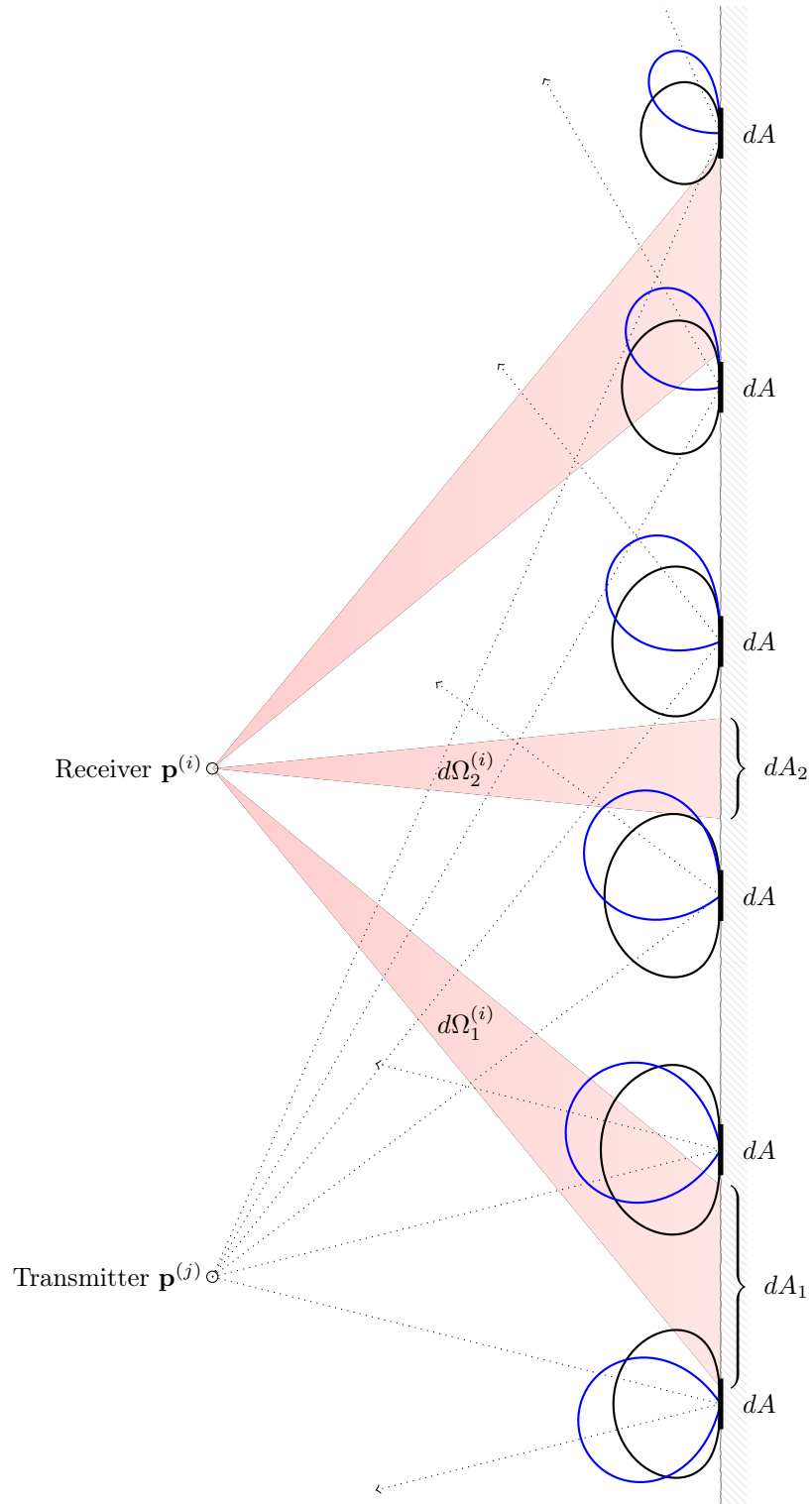


Figure 3.3: The received ADPS of dense multipath is determined by the scattering lobes (--- $\alpha_R = 0$) and (--- $\alpha_R = 10$) as well as the illuminated and observed differential areas dA .

power per differential solid angle $d\Omega^{(j)} \equiv d\Omega^{(j)}(\mathbf{u}^{(j)})$. Hence, the impinging intensity at the rough surface scales as function of impinging angle and distance to the reflection point. This is illustrated in Fig. 3.3 where the scattering lobe is larger for reflection points close to the transmitter. Equivalently, the receiver observes with constant differential solid angle $d\Omega^{(i)} \equiv d\Omega(\mathbf{u}^{(i)})$. Again, the observed dA scales as function of scattering angle and distance; in Fig. 3.3, it is shown that the constant solid angles $d\Omega_1^{(i)} = d\Omega_2^{(i)}$ observe non-equal differential areas $dA_1 \neq dA_2$.

The function f_{ER} describes the spreading of receiving power along the surface, summarizing these effects. Transforming to the spreading along the propagation parameters in $\boldsymbol{\theta}$ yields the desired ADPS $p_{\text{DM},k}(\boldsymbol{\theta})$ according to

$$f_{\text{ER}}(\boldsymbol{\theta}_{\text{DM},k})dA = p_{\text{DM},k}(\boldsymbol{\theta})d\boldsymbol{\theta}. \quad (3.12)$$

Figure 3.4 illustrates the received ADPS $p_{\text{DM},k}(\boldsymbol{\theta})$ evaluated for the azimuth angle for various levels of roughness. The lobes at $\mathbf{p}^{(i)}$ and $\mathbf{p}^{(j)}$ show the ADPS if node j or i transmits in an isotropic manner, respectively. At high levels of roughness $\alpha_R = 0$ the nodes are confronted with a large angular spread. Decreasing the roughness, the angular spread decreases as well.

These plots uncover some non-obvious results worth to be highlighted.

- At large levels of roughness $\alpha_R = 0$ the peak of scattering power is received from a point which is closest to the transmitting node; the direction is indicated as $---$ in Fig. 3.4 corresponding to the peak of the ADPS. This may be counter-intuitive since the scattering lobe has its maximum normal to the surface, as shown in Fig. 3.3 and thus, scattering power along the direction $---$ is strongly attenuated. The reason for the maximum is justified by the larger observation area dA_1 (Fig. 3.3) which counteracts the attenuation from the scattering lobe (e.g. compare dA_1 to dA_2).
- The peak of scattering power is not received from the direction of the specular component $\cdots\cdots\cdots$. This gap is largest at high levels of roughness (see difference between $\cdots\cdots\cdots$ and the direction of the peak of $---$) and gets reduced at lower levels of roughness $\alpha_R \gg$ (see Fig. 3.4).

The derived $p_{\text{DM},k}(\boldsymbol{\theta})$ is valid for a single surface. In the following we assemble the impact from several reflective surfaces.

Composition of DM from multiple planar surfaces

Having the ADPS $p_{\text{DM},k}(\boldsymbol{\theta})$ for a single reflection k , the ADPS $p_{\text{DM}}(\boldsymbol{\theta})$ of the sum of reflections is written as

$$p_{\text{DM}}(\boldsymbol{\theta}) = \sum_k p_{\text{DM},k}(\boldsymbol{\theta}) \quad (3.13)$$

using the assumption of independent DM across different surfaces (3.8c). Finally, the outcome $p_{\text{DM}}(\boldsymbol{\theta})$ for the scenario illustrated in Fig. 3.1 (page 18) is presented. Figure 3.5 exemplifies the ADPS $p_{\text{DM}}(\phi^{a,(i)}, \tau)$, resolved in azimuth-delay domain and Fig. 3.6 depicts $p_{\text{DM}}(\phi^{a,(i)}, \phi^{e,(i)})$, resolved in azimuth-elevation domain. The scatter parameters are set to $S = 0.3$ and $\alpha_R = 4$ [T1]. Darker shading means more DM. The corresponding specular components are shown as crosses.

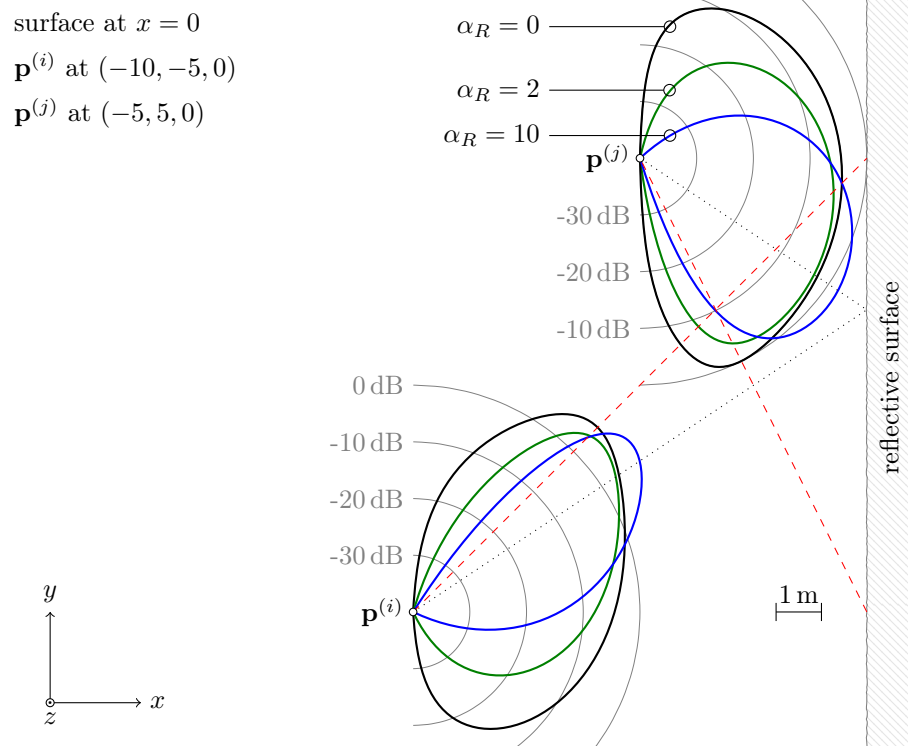


Figure 3.4: Illustration of received ADPS for various levels of roughness $\alpha_R = 0$ —, $\alpha_R = 2$ — and $\alpha_R = 10$ — with specular reflection as

We can observe that the specular components $k = 2, 3$ and 4 are embedded in DM. In the delay domain (Fig. 3.5), the earliest ADPS rises along with the specular component and diminishes with rising delay time. Its shape depends strongly on the geometric setup, e.g. DM originating from the floor ($k = 4$) corresponds to a large angular spread while at $k = 2, 3$, corresponding to the walls, the angular spread is narrower. This effect is also observed in Fig. 3.4 where a reflective surface located close to the node (where the node j is closer than i) is attributed with increased angular spread.

The illustration in Fig. 3.6 depicts the ADPS in azimuth-elevation domain. The maxima of DM (dark regions) are closely located to the specular reflections but there remains a gap, also identified in Fig. 3.4. Furthermore, the reflections are concentrated in the elevation domain conditioned by the geometric setup. These concentrations limit the accessible information in the specular components.

Finally, Fig. 3.7 presents the ADPS separately in the delay (top), azimuth (middle) and elevation domains (bottom). Starting with the delay domain we can observe that the DM ADPS rises simultaneously with the arrival of the specular components $k = 2, 3$ and 4. The paths are well resolved in the delay domain. This is different in the azimuth and elevation domains where several reflections arrive equally. In the azimuth domain, the reflection from the floor overlaps with the LOS. In the elevation domain the equal height of both transceivers results in equal elevation angles of the LOS and components $k = 2, 3$.

3.2.3 Further considerations and relation to literature

A visual comparison between the derived theoretic description of DM to empirical characteristics described by the Saleh-Valenzuela model shows strong similarities [109, 105]. In the following we focus on a quantitative comparison between the parameters of the empirical characteristics summarized in Section 3.2.1 to the derived theoretic distributions from Section 3.2.2.

Angular power spectrum and delay power spectrum

The considered inter-cluster parameters of the Saleh-Valenzuela model depend on the geometric setup, i.e. the placement of both transceivers in the surrounding environment as shown in [82] using ray-tracing. More interesting are the intra-cluster parameters, i.e. the distribution of paths within a single cluster. S-V based channel standards [82, 145, 2] specify the parameters independently for the domains azimuth, elevation and delay; c.f. [51]. This is different at the derived ADPS $p_{\text{DM},k}(\boldsymbol{\theta})$ which shows clearly correlations across the domains (see Fig. 3.5 and Fig. 3.6). For a fair comparison we calculate the angular power spectrum (APS) in azimuth $p_{\text{DM},k}(\phi^{\text{a},(i)})$, the APS in elevation $p_{\text{DM},k}(\phi^{\text{e},(i)})$ and the delay power spectrum (DPS) $p_{\text{DM},k}(\tau)$ [30]

$$p_{\text{DM},k}(\phi^{\text{a},(i)}) = \int p_{\text{DM},k}(\boldsymbol{\theta}) d\sim \phi^{\text{a},(i)} \quad (3.14)$$

$$p_{\text{DM},k}(\phi^{\text{e},(i)}) = \int p_{\text{DM},k}(\boldsymbol{\theta}) d\sim \phi^{\text{e},(i)} \quad (3.15)$$

$$p_{\text{DM},k}(\tau) = \int p_{\text{DM},k}(\boldsymbol{\theta}) d\sim \tau \quad (3.16)$$

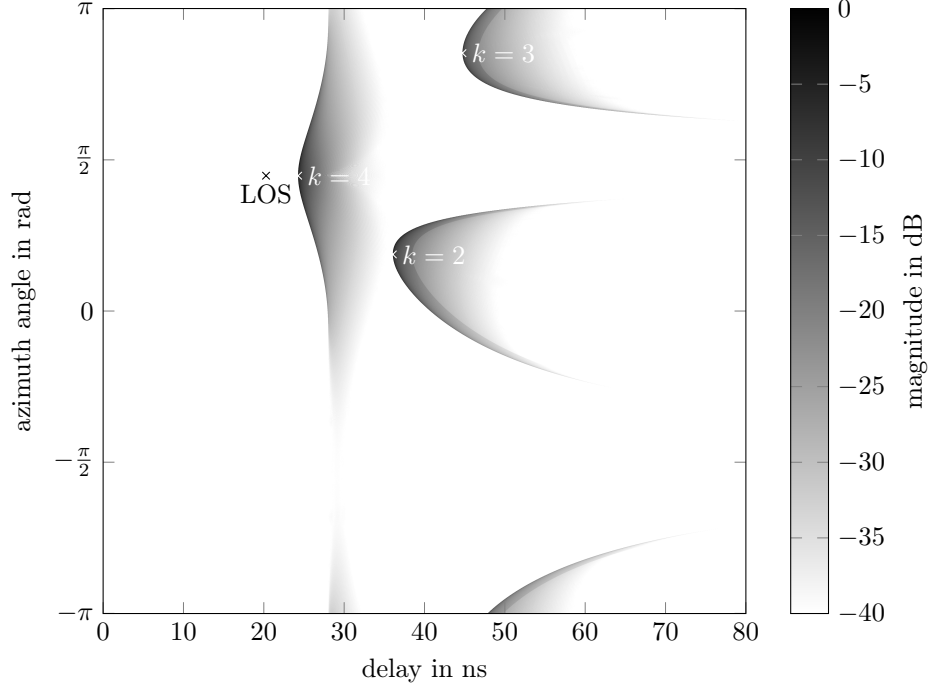


Figure 3.5: The ADPS resolved in azimuth-delay domain at i for the geometric setup provided in Fig. 3.1. The specular components are shown as crosses. The magnitude is normalized to 0 dB.

where the definite integral operator is applied to all variables in $\boldsymbol{\theta}$ except θ' denoted by $d\sim\theta'$. The APS at node j follow equivalently to (3.14) and (3.15).

Non-linearities in $p_{\text{DM},k}(\boldsymbol{\theta})$ prevent closed-form solutions for (3.14)-(3.16). Numerical approximations are derived in [T1].

Under certain assumptions of the geometric setup, i.e. the distance between both transceivers is small compared to the distance between transceivers and reflective surface, and assuming the reflective surface has infinite dimensions, the calculation of the APS and DPS is simplified. Denoting these assumptions *far-field* (ff), one obtains the compact solutions (derived in Appendix A)

Angular power spectrum in azimuth

$$p_{\text{DM},k}^{\text{ff}}(\phi^{\text{a}}) = 4\sqrt{\pi} \frac{S^2 \Gamma(\alpha_R + \frac{5}{2})}{k_{\alpha_R} \Gamma(\alpha_R + 3)} \frac{1}{(c\tau_k)^2} \cos^{2\alpha_R+3}(\phi^{\text{a}} - \phi_k^{\text{a}}) \quad (3.17)$$

Angular power spectrum in elevation

$$p_{\text{DM},k}^{\text{ff}}(\phi^{\text{e}}) = 4\sqrt{\pi} \frac{S^2 \Gamma(\alpha_R + 2)}{k_{\alpha_R} \Gamma(\alpha_R + \frac{5}{2})} \frac{1}{(c\tau_k)^2} \cos^{2\alpha_R+4}(\phi^{\text{e}} - \phi_k^{\text{e}}) \quad (3.18)$$

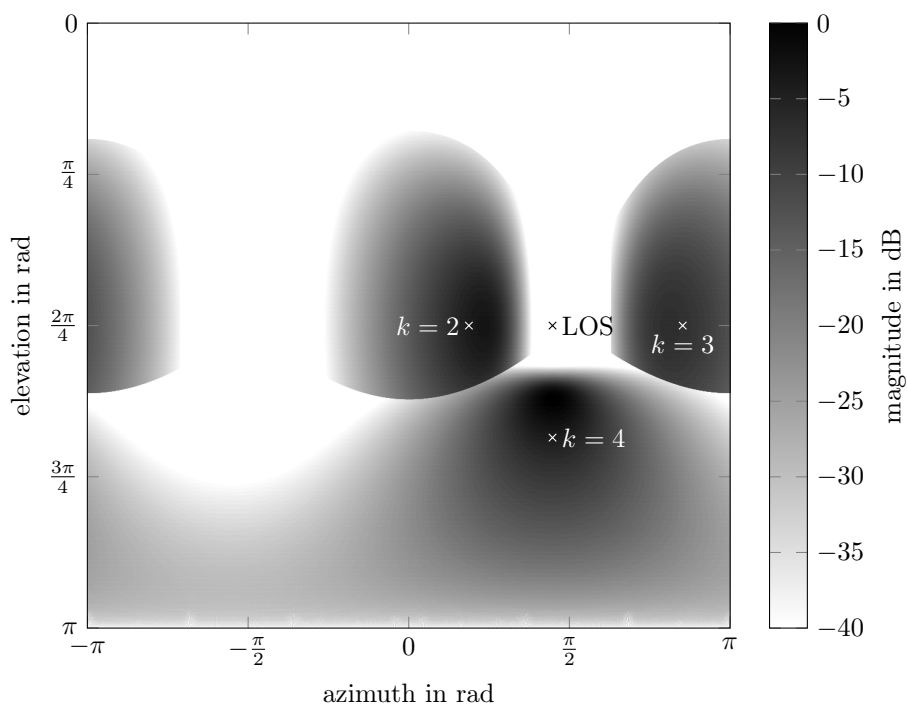


Figure 3.6: The ADPS resolved in azimuth-elevation domain at node i for the geometric setup illustrated in Fig. 3.1. The specular components are shown as crosses. The magnitude is normalized to 0 dB.

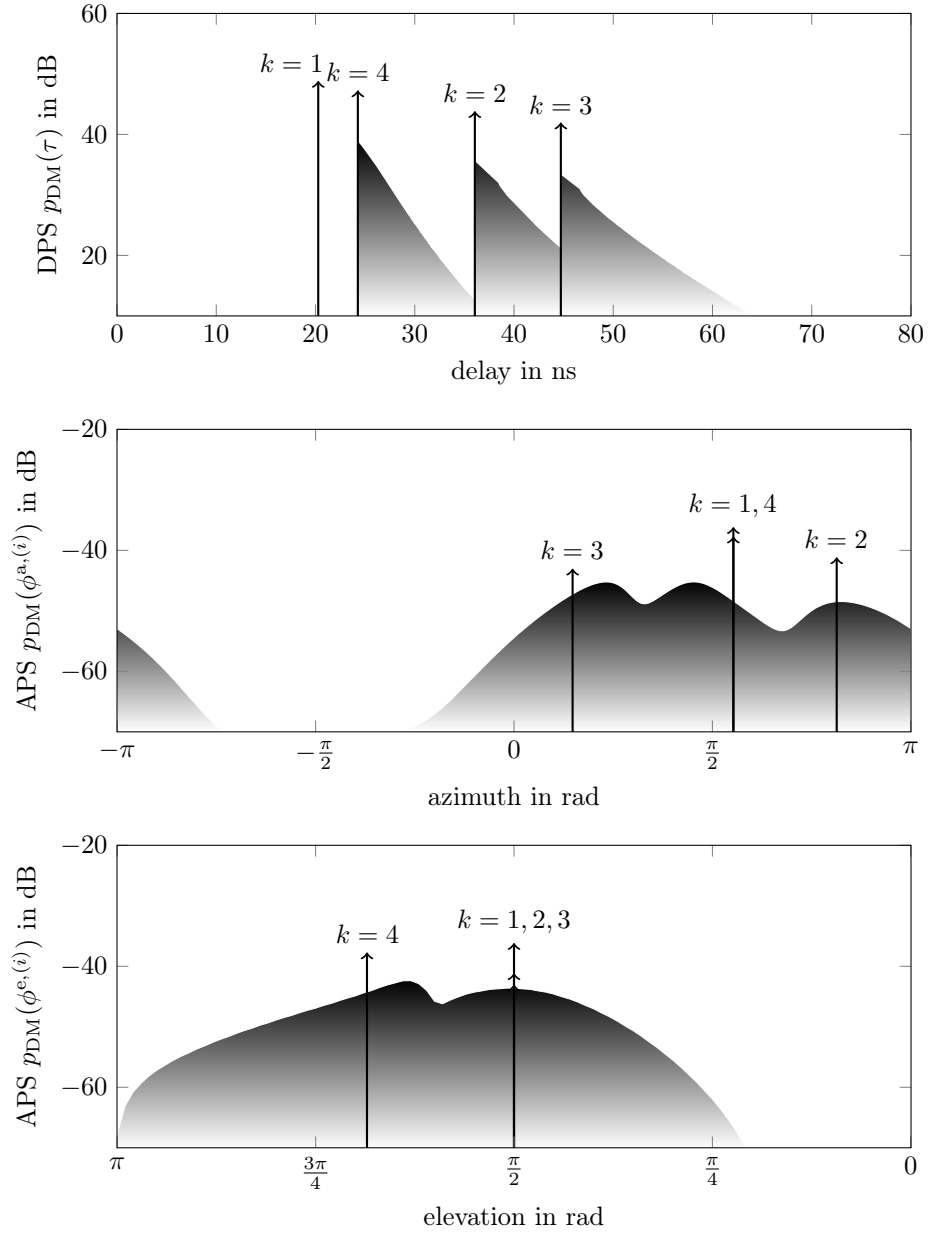


Figure 3.7: Illustration of the ADPS presented in delay $p_{\text{DM}}(\tau)$ (top), azimuth $p_{\text{DM}}(\phi^{a, (i)})$ (middle) and elevation domain $p_{\text{DM}}(\phi^{e, (i)})$ (bottom). The specular components are draw as arrows.

Delay power spectrum

$$p_{\text{DM},k}^{\text{ff}}(\tau) = \frac{S^2 8\pi}{k_{\alpha_R} c^2} \frac{\tau_k^{2\alpha_R+2}}{t^{2\alpha_R+5}} u(\tau - \tau_k) \quad (3.19)$$

with Gamma function $\Gamma(\cdot)$ and unit-step (Heaviside) function $u(t)$. Note that, the APS and DPS in far-field conditions depend on the corresponding specular component, namely its azimuth (3.17), elevation (3.18) and delay parameters (3.17)-(3.19), while the general APS and DPS from (3.14)-(3.16) still depend on the geometric setup contained in $\theta_{\text{DM},k}$. Moreover, in far-field conditions the APS gets equivalent at both nodes i and j and thus, we drop their indices in (3.17) and (3.18).

The obtained analytic solutions for the APS and DPS motivate for a quantitative comparison between the derived and empirical characterizations.

Relation to condensed parameters identified in the literature

In azimuth domain, Gaussian [82] or Laplacian [64, 48] or both power spectra [145] have been identified. In general, measurement-based models have access to the sum of both specular plus dense components only, and thus, a strong specular reflection yields concentrated arriving power from the direction of the specular component which is in favor for the description using a Laplacian distribution. In contrast, at weak specular reflections, the DM gets more importance, resulting in an increased spread in the angular domain. However, as shown in [9], the estimated shape of a cluster is affected heavily by estimation procedure artifacts. This limits the explanatory power of the reported values in literature.

In this work, we aim at parameterizing contributions from DM only, making a Gaussian distribution more attractive. The Gaussian distribution $q_G(\phi; \mu_k, \sigma_k^2)$ is parameterized by its mean μ_k and variance σ_k^2 . To calculate its parameters as function of the parameters of the APS $p_{\text{DM},k}(\phi^a)$ we minimize the Kullback Leibler (KL) divergence between the Gaussian distribution

$$q_G(\phi^a; \mu_k^a, (\sigma_k^a)^2) \propto \frac{1}{\sigma_k^a} \exp\left(-\frac{(\phi^a - \mu_k^a)^2}{2(\sigma_k^a)^2}\right) \quad (3.20)$$

and the APS $p_{\text{DM},k}(\phi^a)$ resulting in

$$\text{first moment: } \mu_k^a = \frac{\int \phi^a p_{\text{DM},k}(\phi^a) d\phi^a}{\int p_{\text{DM},k}(\phi^a) d\phi^a} \quad (3.21)$$

$$\text{square-root second central moment: } \sigma_k^a = \sqrt{\frac{\int (\phi^a - \mu_k^a)^2 p_{\text{DM},k}(\phi^a) d\phi^a}{\int p_{\text{DM},k}(\phi^a) d\phi^a}} \quad (3.22)$$

where the support of the definite integrals is dropped. The identified relations hold equivalent for the elevation angle. Substituting the APS $p_{\text{DM},k}(\phi^a)$ to $p_{\text{DM},k}^{\text{ff}}(\phi^e)$ from (3.17) the Gaussian parameters in the azimuth domain result in

$$\mu_k^{\text{a,ff}} = \phi_k^a \quad (3.23)$$

$$\sigma_k^{\text{a,ff}} = \frac{1}{\sqrt{4 + 2\alpha_R}}. \quad (3.24)$$

Repeating the steps in elevation domain yields equivalent results. The analytic solutions provided in far-field conditions enable some insights,

- the mean value of DM arrives along the specular component's angle (3.23)
- with rising levels of roughness (α_R gets smaller), the standard deviation $\sigma_k^{\text{a,ff}}$ (and $\sigma_k^{\text{e,ff}}$) (3.24), equivalent to the definition of the root-mean-squared (rms) angular spread (3.22), gets wider
- the rms angular spread is independent of the path distance

In delay domain, [110] as well as [145, 2] identify an exponential decay $q_E(\tau; \gamma_k)$ parameterized by decay rate γ_k , according to

$$q_E(\tau; \gamma_k) \propto \frac{1}{\gamma_k} \exp\left(-\frac{\tau - \tau_k}{\gamma_k}\right) u(\tau - \tau_k) \quad (3.25)$$

Minimizing the KL divergence between the exponential decay and the derived DPS with respect to γ_k results in

$$\text{first central moment (decay rate): } \gamma_k = \frac{\int (\tau - \tau_k) p_{\text{DM},k}(\tau) d\tau}{\int p_{\text{DM},k}(\tau) d\tau}. \quad (3.26)$$

Substitution with the DPS $p_{\text{DM},k}^{\text{ff}}(\tau)$ in far-field conditions yields

$$\gamma_k^{\text{ff}} = \frac{\tau_k}{2\alpha_R + 3} \quad (3.27)$$

Similar to the angular domain, some conclusive remarks can be drawn from the observations in far-field, including

- the decay rate rises at increasing path delay, as insinuated in [121, 110]
- rising levels of roughness (α_R gets smaller) increase the decay rate

Figure 3.8 presents the relation between α_R and the rms angular spread (left) and decay rate (right) from (3.24) and (3.27). Reported values in the literature [48, 2, 82, 145] are drawn as vertical lines and values of α_R from [57, 21] as horizontal lines. Note, in several scenarios from [145], the angular spread exceeds $\pi/8$, and thus, they are excluded from Fig. 3.8. We admit, that in [57, 21], α_R was fitted using a slightly different model but as shown in [T1] these differences are negligible.

The reported rms angular spread values range from 0.1 rad [82] up to $> \pi/8$ rad [145] which can be explained by varying antenna characteristics, carrier frequencies as well as geometric setups. However, as pointed out in the introduction, in this thesis, a simple description of DM is demanded. The outcome of the proposed scattering model is in the range of reported values from measurement campaigns.

3.3 Concluding remarks

Geometrical optics enable the description of position-related information in multipath propagation with only a few parameters. Knowledge of the geometric environment and the node positions enables to calculate the expected angles and delays of multipath components as shown in Section 3.1. Less attention is paid on the multipath amplitude: the amplitude is affected due to path loss as

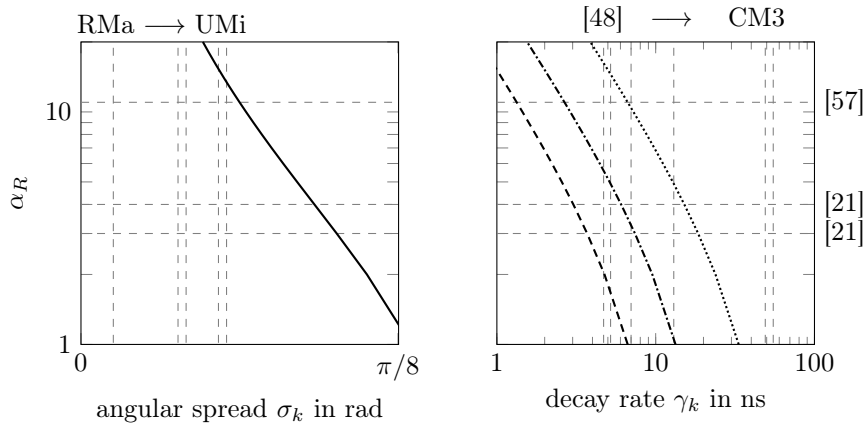


Figure 3.8: Relation of α_R to angular spread (left) and decay rate (right). The decay rate is drawn for various path lengths $c\tau_k$ of 10 ----, 20 -.-.-, 50 m Vertical lines denote reported values in the literature from (in ascending order) RMa, Indoor Office, UMa, CM5, UMi of σ_k ; and [48], CM1, CM5, CM7, CM9, CM3 of γ_k .

well as due to attenuation at the reflection. While path loss can be described using the calculated distance and some assumptions on propagation losses due to atmospheric influences, the attenuation loss originating at the reflection point requires knowledge of the material properties, e.g. its dielectric constant or surface structure. Clearly, this requirement limits the versatile employment of a localization system.

The calculation of the propagation parameters is illustrated for single-bounce reflections but can be extended easily to the multiple-bounce case [70]. However, one may identify two reasons for the limitation of single-bounce reflections only. First, evaluations using ray-tracing demonstrate sparse channels at increasing carrier frequencies, e.g. at mm-waves [82, 86], which may be explained by the increased path loss. As argued in [86], the majority of power is captured in the direct path and single-bounce reflections. Second, the extension to multiple-bounce reflections comes with a strong increase of complexity. In geometrical optics, the visibility of the deterministic paths needs to be evaluated. The complexity of this problem scales quadratically with the number of reflective surfaces [88].

Additive DM deteriorates the vital position-related information. To model this influence we have investigated the stochastic part of the spreading function, as shown in Section 3.2. Its description using first and second moments is motivated by results obtained from extensive channel measurement campaigns [82, 145, 2]. The moments can be parameterized based on site-specific theoretic modeling (Section 3.2.2) as well as empirical characterizations (Section 3.2.1). However, theoretic modeling requires knowledge of the reflecting material's parameters while empirical characterizations may be inappropriate to describe the site-specific DM power.

Hence, we may conclude by stating that the proposed spreading function is able to characterize position-related information. The employment of its param-

eters beyond deterministic descriptions in angular and delay domain, especially specular and dense multipath amplitudes, needs to be verified.

Chapter 4

Localization using a single base station

Conventional localization systems exploit time-of-arrival [37] and direction-of-arrival [99] information from several anchor nodes (or base stations) [1]. Several recent attempts are proposed to reduce the number of anchors to a single one by exploiting angle-delay information contained in the direct path [46] as well as in multipath propagation [92, 113, 3]. Therein, the angular information is often obtained from measurements using multiple antennas, radiating in an isotropic manner. Then, angular information is covered in the carrier signal's phase whose estimation requires phase-coherent measurements [31, 78]. To establish these measurements the oscillators at each antenna are locked such that the phase difference of the carrier signal gets accessible.

To circumvent synchronization and calibration issues of phase-coherent measurements [144], one may exploit multiple directive antennas. The directive antennas attenuates MPC amplitudes as function of the corresponding MPC angle of departure or arrival. Sequential switching of the antennas enables to infer MPC angle information from the difference in MPC amplitudes. It is interesting to note that the description of switchable, directive antennas is similar to a description using electronically-steerable analog beamformers of phased-arrays [14]. Each directive antenna corresponds to one state of the steerable beamformer, as employed by commercial off-the-shelf routers [14]. However, fusion of consecutive measurements is challenging due to random phase-offsets originating from the non-phase-coherent measurements.

This chapter aims at circumventing the requirement of phase-coherent measurements of multiple, isotopic radiation antennas or of consecutive measurements using analog beamforming or directive antennas. The measurement model is introduced in Section 4.1 and analyzed in Section 4.2 with respect to the position error bound. An algorithm is presented in Section 4.3 exploiting MPC angle information from non-phase-coherent measurements. The conclusive discussion in Section 4.4 reveals that each multipath carries additional spatial information in angle and delay domain. The comparison to a single antenna demonstrates that the additional angle domain counteracts negative effects from path overlap.

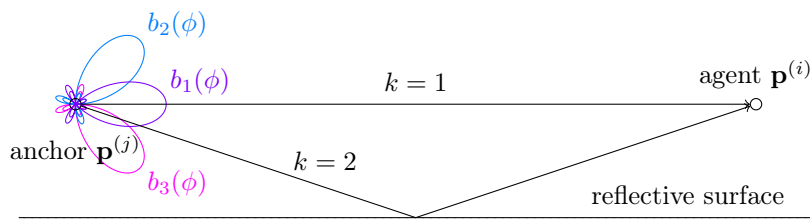


Figure 4.1: The anchor is equipped with $M = 3$ directive antennas, providing angle information contained in multipath $k = 1$ and $k = 2$.

4.1 Measurement model in angle-delay domain

A single anchor is present at known position $\mathbf{p}^{(j)} \in \mathbb{R}^2$. The anchor is equipped with M directive antennas (equivalent to the outcome of an analog beamformer with M switching states) with known complex-valued beampattern $b_m(\phi)$ of the m th antenna, as illustrated in Figure 4.1. As the position of the anchor node is known beforehand also the orientation of the directive antennas is assumed to be known beforehand. The agent node with unknown position $\mathbf{p}^{(i)} \in \mathbb{R}^2$ has access to a single antenna radiating in an isotropic manner. Due to the use of a single agent node, the index i is dropped throughout this section by stating $\mathbf{p} \equiv \mathbf{p}^{(i)}$. The isotropic radiation antenna at the agent alleviates the requirement of estimating the agent's orientation which is in general unknown (as the agent moves).

In accordance to (3.1), the MPC parameters $\boldsymbol{\theta}_k = [\phi_k^{\text{a},(j)}, \tau_k] \equiv [\phi_k^{(j)}, \tau_k]$ are reduced to the anchor-side azimuth angle $\phi_k^{(j)} \equiv \phi_k^{\text{a},(j)}$ and delay τ_k . Driving M antennas, the observed signal $\mathbf{r}_m \in \mathbb{C}^N$ from directive antenna m can be written as

$$\mathbf{r}_m = \sum_{k=1}^K b_m(\phi_k^{(j)}) \alpha_k \mathbf{s}(\tau_k) + \mathbf{w}_m \quad (4.1)$$

where α_k , $\phi_k^{(j)}$ and τ_k define the amplitude, angle of arrival (at the anchor) and delay of the k th specular reflection (or LOS if it is not blocked), which can be expressed as function of \mathbf{p} (as shown in Sec. 3.1). Term $\mathbf{s}(\tau) = [s(0 \cdot T_s - \tau), s(1 \cdot T_s - \tau), \dots, s((N-1)T_s - \tau)]^T$ denotes the transmitted signal $s(t)$, shifted by delay τ and sampled with period T_s . Finally, $\mathbf{w}_m \in \mathbb{C}^N$ describes circularly symmetric, additive, white Gaussian noise with variance $\sigma^2 = N_0/T_s$ where $N_0/2$ is the two-sided power spectral density. This 2-dimensional channel model deduces from the 3-dimensional model (3.1) by setting $b^{(i)}(\mathbf{u}^{(i)}) = \frac{1}{\sqrt{2\pi}}$ (agent radiates in an isotropic manner), $b^{(j)}(\mathbf{u}^{(j)}) = b(\phi^{(j)})$ (anchor employs directive antennas where we drop index m) and $\nu_k(\mathbf{u}^{(i)}, \mathbf{u}^{(j)}, \tau) = 0$ (neglecting diffuse multipath).

4.2 Information contained in measurements

In this section we analyze the contained information of (4.1) regarding the agent position. This analysis gains insights in the mutual dependence between the parameters which turns out to be substantial in the parameter estimation.

Let $\hat{\mathbf{p}}$ be the estimate of \mathbf{p} given the measurements $\{\mathbf{r}_m\}$. We aim at describing the expected covariance $\mathbb{E}\{(\hat{\mathbf{p}} - \mathbf{p})(\hat{\mathbf{p}} - \mathbf{p})^T\}$ of the estimation error using the metric *squared position error bound* (SPEB) $\mathcal{P}(\mathbf{p})$ [114, 59, 79], defined as

$$\mathcal{P}(\mathbf{p}) = \text{trace}\{\mathbf{J}^{-1}(\boldsymbol{\theta})\}_{2 \times 2}. \quad (4.2)$$

where $\mathbf{J}(\boldsymbol{\theta})$ denotes the Fisher information matrix (FIM) for parameter vector

$$\boldsymbol{\theta} = \underbrace{[\mathbf{p}^T]}_{\substack{\text{agent} \\ \text{position}}}, \underbrace{[\Re\alpha_1 \dots \Re\alpha_k, \Im\alpha_1 \dots \Im\alpha_k]}_{\text{amplitudes}}]^T. \quad (4.3)$$

Parameter vector $\boldsymbol{\theta}$ covers the unknown variables in (4.1), namely the position \mathbf{p} and the complex-valued amplitudes, split into its real and imaginary parts using the operators \Re and \Im . The position is related to the MPC parameters ϕ_k and τ_k (see Sec. 3.1). The amplitudes are treated as nuisance parameters since we refrain from modeling them as function of \mathbf{p} as discussed in Sec. 2.1.1.

4.2.1 Position error bound considering path overlap

As shown in (4.2), $\mathcal{P}(\mathbf{p})$ is obtained by evaluating the trace of the top-left 2×2 submatrix of $\mathbf{J}^{-1}(\boldsymbol{\theta})$. To this end, we introduce an *equivalent* FIM (EFIM) $\mathbf{J}_e(\mathbf{p})$ [114, 126] such that $\mathbf{J}_e^{-1}(\mathbf{p}) = [\mathbf{J}^{-1}(\boldsymbol{\theta})]_{2 \times 2}$, resulting in

$$\mathcal{P}(\mathbf{p}) = \text{trace}\{\mathbf{J}_e^{-1}(\mathbf{p})\}. \quad (4.4)$$

The EFIM $\mathbf{J}_e(\mathbf{p})$ incorporates cross-dependencies of information between positions and amplitudes. As shown in the Appendix (Eq. (B.13), page 65) these cross-dependencies lower the contained position information if MPCs arrive simultaneously or closely to each other, in other words, if path overlap occurs. Path overlap prevents expressing $\mathbf{J}_e(\mathbf{p})$ as a sum of the individual MPC contributions [114]. However, having large bandwidths or highly directive antennas or both, path overlap is reduced [88] which motivates to introduce an EFIM $\tilde{\mathbf{J}}_e(\mathbf{p})$ valid in regions without path overlap.

4.2.2 Position error bound neglecting path overlap

We introduce an EFIM $\tilde{\mathbf{J}}_e(\mathbf{p})$ which is valid if no path overlap occurs. The corresponding SPEB $\tilde{\mathcal{P}}(\mathbf{p})$ results as

$$\tilde{\mathcal{P}}(\mathbf{p}) = \text{trace}\{\tilde{\mathbf{J}}_e^{-1}(\mathbf{p})\} \quad (4.5)$$

where $\tilde{\mathbf{J}}_e(\mathbf{p})$ is derived in Appendix B, yielding

$$\tilde{\mathbf{J}}_e(\mathbf{p}) = \underbrace{\sum_k \lambda_k^{(\tau)} \mathbf{D}(\phi_k^{(i)})}_{\text{delay information}} + \underbrace{\sum_k \lambda_k^{(\phi)} \mathbf{D}(\phi_k^{(i)} - \frac{\pi}{2})}_{\text{angle information}} \quad (4.6)$$

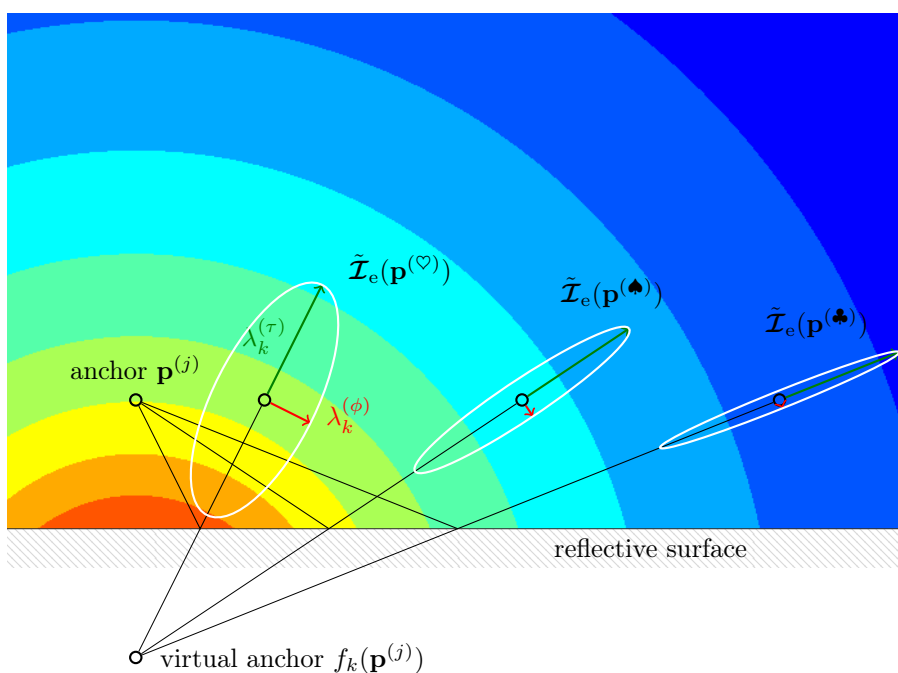


Figure 4.2: Illustration of the obtained equivalent Fisher Information Matrix $\tilde{\mathbf{J}}_e(\mathbf{p})$ valid if no path overlap occurs, drawn for three different agent positions $\mathbf{p}^{(\heartsuit)}$, $\mathbf{p}^{(\spadesuit)}$ and $\mathbf{p}^{(\clubsuit)}$ using a single reflection. The reflection's delay adds information along the propagation direction, scaled by constant $\lambda_k^{(\tau)}$. The angle adds orthogonal information whose information intensity $\lambda_k^{(\phi)}$ scales with the inverse of the squared path length $(c\tau)^2$ and thus, increasing path lengths (e.g. at $\mathbf{p}^{(\clubsuit)}$) contribute less information. The background image depicts $\text{trace}\{\tilde{\mathbf{J}}_e(\mathbf{p})\} = \lambda_k^{(\tau)} + \lambda_k^{(\phi)}$ where colors correspond to 2dB differences showing that the information decreases from its center point at $f_k(\mathbf{p}^{(j)})$.

separated into the impact from delay as well as angle information. The EFIM $\tilde{\mathbf{J}}_e(\mathbf{p})$ can be described as sum of $\lambda_k \mathbf{D}(\phi_k^{(i)})$ terms where λ_k denotes the information intensity along the direction $\mathbf{e}(\phi_k^{(i)}) \in \mathbb{R}^2$, contained in the 2×2 direction matrix $\mathbf{D}(\phi_k^{(i)}) = \mathbf{e}(\phi_k^{(i)})\mathbf{e}^H(\phi_k^{(i)})$ [114]. The information intensities $\lambda_k^{(\tau)}$ and $\lambda_k^{(\phi)}$ are written as

$$\lambda_k^{(\tau)} = \frac{8\pi^2 \beta^2 \text{SNR}}{c^2} \sum_m |b_m(\phi_k^{(j)})|^2 \quad (4.7)$$

$$\lambda_k^{(\phi)} = \frac{2\text{SNR}}{(c\tau_k)^2} \sum_m \left| \frac{db_m(\phi_k^{(j)})}{d\phi_k^{(j)}} \right|^2 \quad (4.8)$$

with $\beta^2 = \int_{-\infty}^{\infty} f^2 |S(f)|^2 df / \int_{-\infty}^{\infty} |S(f)|^2 df$ and $\text{SNR} = |\alpha_k|^2 \int_{-\infty}^{\infty} |S(f)|^2 df / N_0$ where $S(f) = \int_{-\infty}^{\infty} s(t) \exp\{-j2\pi ft\} dt$ and $\|\mathbf{s}\|^2 T_s = \int_{-\infty}^{\infty} |s(t)|^2 dt$.

Vector $\mathbf{e}(\phi_k^{(i)}) = [\cos \phi_k^{(i)}, \sin \phi_k^{(i)}]^T$ is parameterized by multipath azimuth angle $\phi_k^{(i)}$ of MPC k at agent i (not to be confused with angle $\phi_k^{(j)}$ at anchor j) and can be calculated using the relation from (3.5) resulting in

$$\text{direction } \mathbf{e}(\phi_k^{(i)}) = \frac{\mathbf{p} - f_k(\mathbf{p}^{(j)})}{\|\mathbf{p} - f_k(\mathbf{p}^{(j)})\|} \quad (4.9)$$

where function $f_k(\mathbf{p}^{(j)})$ describes the geometric environment. Note that, the spatial information obtained from angles is perpendicular to information from delays. This is seen by the constant of $\pi/2$ appearing in the argument of the direction matrix in (4.6).

The derived $\tilde{\mathbf{J}}_e(\mathbf{p})$ exemplifies that each reflection adds position information. The level of information is determined by $\lambda_k^{(\tau)}$ and $\lambda_k^{(\phi)}$ demonstrating a fundamental difference between delays and angles. While the impact of delays remains constant irrespective of the actual delay τ_k the impact of angles scales with the inverse of the path delay τ_k and therefore with increasing delay the contained information regarding angles has less importance [49]. Figure 4.2 exemplifies the EFIM of a single reflection for various points.

Interestingly, $\lambda_k^{(\tau)}$ increases with the beampattern's absolute value while $\lambda_k^{(\phi)}$ depends on the beampattern's first derivative demonstrating that large variations of the beampattern are beneficial for the angular intensity. Moreover, the bandwidth of the baseband signal, captured in β , affects information in delays only. Note, in (4.1) the signal's carrier phase is not included (due to non-phase-coherent measurements) and thus, angular information gets inaccessible once we employ antennas radiating in an isotropic manner ($b_m(\phi) = \text{const}$, $db_m(\phi)/d\phi = 0$).

4.2.3 Numeric evaluation

Finally, a numerical comparison between the SPEB $\mathcal{P}(\mathbf{p})$ (considers path overlap), and the SPEB $\tilde{\mathcal{P}}(\mathbf{p})$ (neglects path overlap), is provided. The 2-dimensional setup consists of a rectangular room with dimensions 6×8 m where the anchor node $\mathbf{p}^{(j)}$ is placed at coordinates $\mathbf{p}^{(j)} = [1, 1]^T$. The agent node $\mathbf{p}^{(i)}$ is placed in line-of-sight (LOS) conditions resulting in a LOS plus 4 first-order reflections.

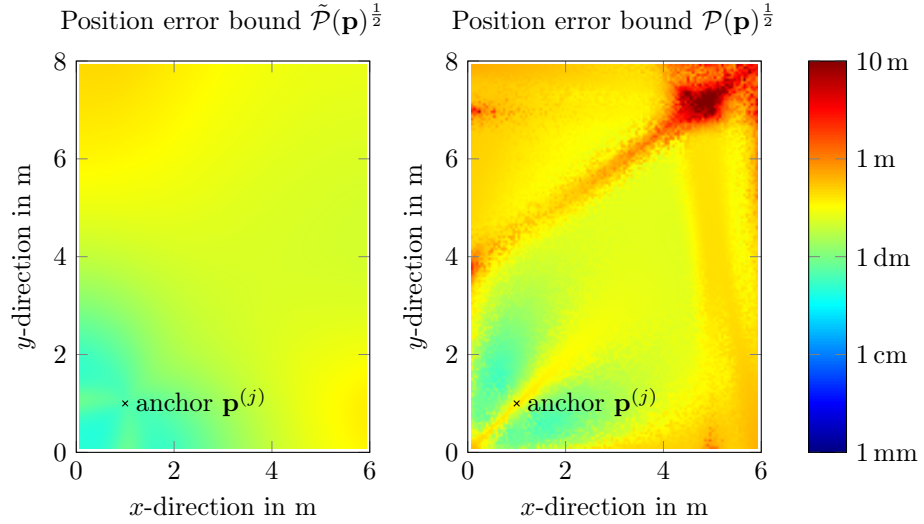


Figure 4.3: Illustration of position error bounds $\tilde{\mathcal{P}}(\mathbf{p})$ (no consideration of overlapping multipath) (left) and $\mathcal{P}(\mathbf{p})$ (explicit consideration of overlapping multipath) (right) for isotropic antennas. Red indicates less accuracy.

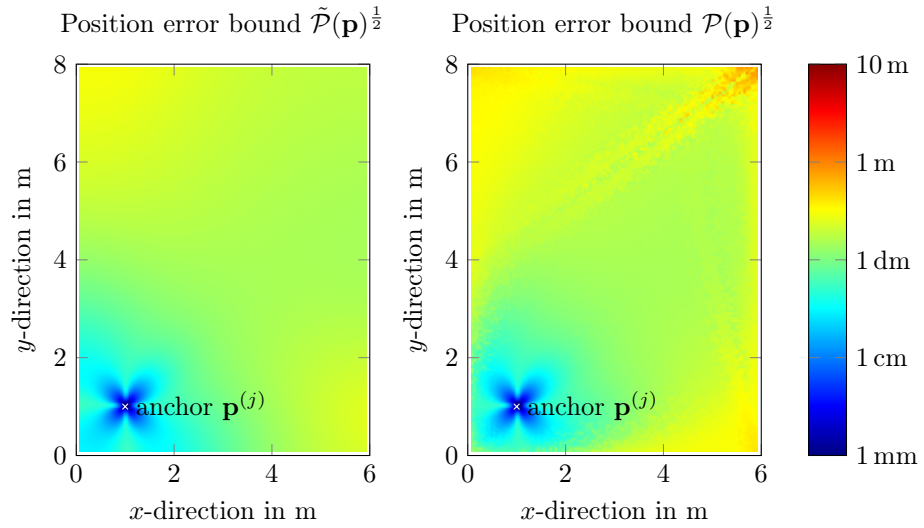


Figure 4.4: Equivalent to Fig. 4.3 incorporating angular resolution using $M = 4$ directive antennas.

The computer-generated data assume an attenuation of -3 dB at each reflection and furthermore an attenuation due to the free-space propagation, in total $\alpha_k = \frac{1}{c\tau_k}$ for the LOS and $\alpha_k = \frac{1}{\sqrt{2}c\tau_k}$ for reflections. The variance σ^2 of the Gaussian noise was set to an SNR of 25 dB at path distance of 1 m.

The outcome is strongly dependent on the design parameters transmitted signal $s(t)$ and beampattern $b_m(\phi)$. To ensure realistic conditions the transmitted signal is chosen as raised-cosine with pulse duration 2.4 ns and roll-off factor of 0.9. This signal corresponds to the identified transmitted signal of the DecaWave DW1000 UWB radio fulfilling the requirements of Channel 2 in the UWB standard IEEE 802.15.4 (2011), e.g. [T2]. The evaluation is conducted for two types of anchor antenna setups, a single, isotropic radiating antenna in comparison to four directive antennas, as described in the following.

Single antenna radiating in an isotropic manner

In the first experiment a single antenna radiating in an isotropic manner is used at both agent node i and anchor node j , i.e. $M = 1$ and $b_1(\phi) = \frac{1}{\sqrt{2\pi}}$. Subsequently angular information is not accessible (since the derivative of $b_1(\phi)$ is zero).

Figure 4.3 presents a comparison between $\mathcal{P}(\mathbf{p})$ (considering path overlap) and $\tilde{\mathcal{P}}(\mathbf{p})$ (neglecting path overlap). The comparison reveals that both SPEB achieve similar values except in regions with path overlap. Path overlap occurs at (x, y) coordinates from $(0, 7)$ to $(6, 7)$ where the reflection originating at the top and at the bottom coincide and at $(0, 4)$ to $(6, 8)$ where the reflections from top and right overlap.

Directive antennas

In the second experiment, angular resolution is provided by equipping the anchor with $M = 4$ directional antennas assembled circularly in $360^\circ/M = 90^\circ$ steps. The antennas have a half-power beamwidth of approximately 90° (see Appendix C). For a fair comparison to the experiment using a single antenna, we normalize the beampattern's energy to $\int_{-\pi}^{\pi} |b_m(\phi)|^2 d\phi = 1$, for all m which is required as the SPEB scales with the beampattern's absolute value.

Figure 4.4 presents the results for $\mathcal{P}(\mathbf{p})$ (considering path overlap) and $\tilde{\mathcal{P}}(\mathbf{p})$ (neglecting path overlap). We may identify three important improvements. First, driving 4 antennas results in 4 independent measurements which increases the accuracy (enlightened by the sum over M antennas in (4.7) and (4.8)). Second, the additional angular resolution lowers the SPEB. This reduction is higher in regions closer to the anchor (see (4.8)). Third, in comparison to the single antenna experiment, the negative effects originating from path overlap are strongly reduced. This can be justified since it is less likely that two MPCs arrive simultaneously in angle *and* delay domain which reduces the risk of path overlap.

4.3 Algorithms for non-phase-coherent measurements

The derived SPEB based on the measurement model from (4.1) illustrates the benefits of using directive antennas. In this section we aim at extending the measurement model to incorporate non-phase-coherent (NPC) measurements. Two algorithms are presented, tackling the information loss due to NPC measurements. Finally, a real-time positioning system is introduced, based on the presented algorithms.

4.3.1 Measurement model for non-phase-coherent measurements

As stated in the beginning of this chapter, directive antennas provide MPC angle information without the need of phase-coherent measurements. In absence of phase-coherency (the radio frequency clocks of both transceivers are not synchronized between two consecutive measurements) we can identify a random phase offset $e^{j\varphi_m}$ at each measurement (or antenna m), where φ_m is uniformly distributed within $[0, 2\pi)$. Based on (4.1), this can be mathematically formulated by introducing a NPC measurement model $\mathbf{r}_m^{\text{npc}} = e^{j\varphi_m} \mathbf{r}_m$ as

$$\mathbf{r}_m^{\text{npc}} = \sum_{k=1}^K b_m(\phi_k) \alpha_{k,m} \mathbf{s}(\tau_k) + e^{j\varphi_m} \mathbf{w}_m \quad (4.10)$$

with

$$\alpha_{k,m} = e^{j\varphi_m} \alpha_k. \quad (4.11)$$

In comparison to (4.1), the complex-valued MPC amplitudes $\alpha_{k,m}$ in (4.10) are different at each m , determined by the phase offset according to

$$\alpha_{k,m} = |\alpha_k| e^{j\angle\alpha_{k,m}} = |\alpha_k| e^{j\varphi_m + j\angle\alpha_k}. \quad (4.12)$$

4.3.2 Discussion and comparison of algorithms

The random phase offset prevents the estimation of α_k in 4.1 which implicitly defines the intensity information in angle and delay domain (see (4.7) and (4.8)). The presented measurement model in (4.10) is employed in [108, Alg. II],[T3]. In [108, Alg. II], the position estimate is based on a maximum likelihood (ML) criterion where it is assumed that MPC amplitudes from different antennas are not related to each other, in other words, the relation provided in (4.12) is not considered. It is shown that the position accuracy using four directive antennas at the anchor node gets improved in comparison to an antenna radiating in an isotropic manner. Still, there remains a large gap to the achievable accuracy given phase-coherent measurements ($e^{j\varphi_m}$ is known) [108, Alg. I]. The remaining gap can be reasoned by the fact that the position estimator based on NPC measurements [108, Alg. II] has no access to the antenna beam pattern, as theoretically derived in [T3]. The performance gain (in comparison to a single antenna) is obtained since the directive antennas point in different directions which decreases the risk of path overlap (see Fig. C.4 in Appendix C).

In [T3], we propose an algorithm capable of exploiting NPC measurements. Identifying the importance of an accurate MPC amplitude estimate, we approximate the non-linear and multi-parameter optimization problem by estimating the magnitude $|\alpha_k|$ in (4.12) as weighted average of $|\alpha_{k,m}|$ incorporating the antennas' beampattern as weights. The corresponding phase values are obtained from the *noisy* observation $\angle\alpha_{k,m}$ without any further processing [96]. We demonstrate in [T3] that for decreasing noise levels this approximation converges to the true complex-valued α_k .

In the following a comparison is provided in terms of the likelihood function of the phase-coherent and non-phase-coherent algorithms. The setup is equivalent to the one in the SPEB analysis, using four directive antennas and the IEEE 802.15.4 Channel 2 with a bandwidth of approximately 500 MHz. The real measured data is obtained from [108] using the laboratory room shown in Figs. 2.1 and 2.2. Figure 4.5 illustrates the likelihood function evaluated for points within the communication range of the anchor located at $\mathbf{p}^{(j)} = [-0.7, 1] \text{ m}$, for a non-phase-coherent processing using [108, Alg. II] (a) and [T3] (b) in comparison to a phase-coherent processing using [108, Alg. I] (c). Each colored point shows one likelihood value where dark red means very likely.

Starting with the phase-coherent processing, Fig. 4.5c demonstrates a strong global maximum at the true agent position \mathbf{p} . This is reasoned by the accurate amplitude estimation. If non-phase-coherent measurements are available only, [108, Alg. II] (Fig. 4.5a) suffers due to the independent amplitude estimates which are not related across antennas. The arising undesired, local maxima in the log likelihood function lead to strong outliers in the maximum likelihood estimation procedure. The approximate amplitude estimation in [T3] (Fig. 4.5b) mitigates the drawbacks from non-phase-coherent processing to a large extent, as shown in Fig. 4.5b.

4.3.3 Towards a real-time positioning system

The real-time indoor positioning system [43, 44, 45] exploits our proposed algorithm for NPC measurements [T3]. Measurements are conducted by an off-the-shelf UWB transceiver [T2]. The non-phase-coherent measurements are obtained by correlating the UWB preamble. Synchronization is performed using a two-way ranging protocol. As shown in [T2], the synchronization error's standard deviation is below 5 cm and thus, negligible. The angular resolution is achieved by switching four directive antennas (see Appendix C) at the UWB anchor node. The obtained NPC measurements are fed to the algorithm as presented in [T3].

Motivated from [T2] the computational complexity of the ML criteria is reduced by limiting the evaluated agent positions to those which are located on a circle between agent and anchor node where the radius of the circle results from two-way ranging. This limitation enables to reduce the number of evaluated points to 100. In [T3], 90 % of the position errors were below 40 cm which is comparable to the reported values in [43].

While the derived likelihood function from [T3] enables localization using a single measurement with each antenna [43] its accuracy and resistance to outlier may be further improved by incorporating prior information. The arising tracking filter infers the provided measurement given a prior distribution of the agent position. Presence of less prior information, e.g. the prior distribution

Figure 4.5a: Non-phase coherent processing. Amplitudes are obtained using [108, Alg. II].

Many undesired local maxima due to independent amplitude estimation.

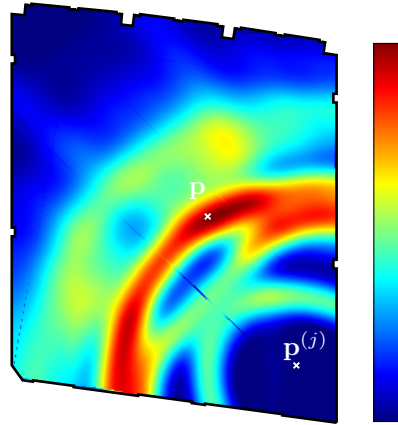


Figure 4.5b: Non-phase coherent processing. Amplitudes are obtained using [T3].

Strong suppression of local maxima due to improved processing of amplitude information.

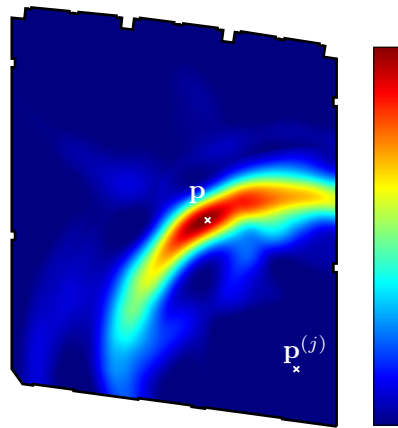
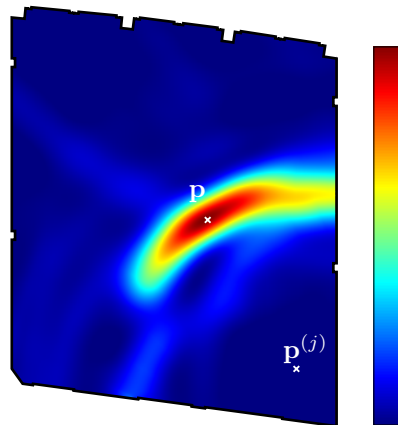


Figure 4.5c: Phase coherent processing.

Best performance justified by phase coherent amplitude estimation.



-6 -4 -2 0
 x -direction in m

Figure 4.5: Evaluation of log likelihood functions for a single measurement taken from [108]. The anchor at $\mathbf{p}^{(j)}$ is equipped with $M = 4$ antennas. Each pixel represents the likelihood value evaluated for the corresponding position.

consists of many local maxima, the usage of a particle filter may be beneficial. Once a clear strong global maximum is established (like in Fig. 4.5c), an approximation of the prior distribution to a Gaussian distribution and subsequently the employment of an extended Kalman filter may reduce the complexity even more.

4.4 Concluding remarks and outlook

This chapter has focused on assembling a localization system that employs directional antennas. Directional antennas provide multipath angle information without the need for phase-coherent multi-antenna radio front ends. An algorithm is derived which can avoid the loss of information due to non-phase-coherent measurements. Based on a theoretic analysis, condensed elements for designing a low-cost, real-time positioning system can be identified, as follows

- **Ensure measurement capabilities in angle-delay domain**, either at the anchor or at the agent or at both sides. Delay information appears perpendicular to the angle information which alleviates the MPC amplitude estimation, especially if path overlap occurs (compare the SPEB $\tilde{\mathcal{P}}(\mathbf{p})$ and $\mathcal{P}(\mathbf{p})$ in Fig. 4.4).
- **Put importance on the delay domain.** The information intensity associated to angles scales with the inverse of the distance while the information in delays remains constant. This is depicted in Fig. 4.2.

The derived PEB's explanatory power is limited since we excluded the effect from unknown phase-offsets. Describing the phase-offsets as random variable next to the additive Gaussian noise, may change the explanatory power of the PEB a lot. This highly relevant research question is left for future research. Moreover, the approximation in [T3] aims at estimating the absolute value of the MPC amplitudes but circumvents the estimation of phase-offsets. A joint or iterative estimation may be beneficial, especially at regions with considerable amount of path overlap.

Chapter 5

Avoiding base stations through cooperation

Imposing cooperation between agents has the potential to address several challenges in localization simultaneously. Rather than relying on information obtained from a number of static anchor nodes (or base stations) with known positions, in cooperative localization the agent nodes perform additional measurements to their neighboring nodes which is beneficial for improving coverage [103, 136], accuracy [143] or leveraging diversity [24].

Fundamental analysis demonstrates an improvement in achievable position accuracy for line-of-sight delay measurements [117] as well as for multipath delay information [79]. Based on the gained insights a number of cooperative localization algorithms have been derived. Treating the agent positions as unknown deterministic parameters, methods have been proposed based on optimization [10, 98, 38] or based on a likelihood function [18, 103]. Modeling the agent positions as a random variable, additional prior location information can be exploited [132, 111, 33] which is often formulated in a framework of tracking filters [33, 132].

As shown in [33], additional multipath information enables to reduce the required number of anchors. However, if information from anchors is non-available the cooperative network misses its coordinate system, and as a consequence, only *relative* positions are attainable. This is different once we consider that multipath components contain position information of the surrounding environment. This position information resettles the missing coordinate system such that the cooperative network can localize itself with respect to the environment. However, refraining from reliable information from anchors accompanies with reduced accuracy and robustness which is in a trade-off with reduced deployment costs of the localization system.

In the following a brief review is provided for localization where location information from anchors is replaced with estimated location information covered in propagation parameters. Figure 5.1 illustrates a setup of two cooperating agents employing multipath propagation. Based on this setup, in [T4] a low complexity algorithm is derived, based on [33]. In [T5], the algorithm is applied to real measurement data where we identified a strong dependency on the accuracy of the provided surrounding environment (the surface positions \mathbf{p}_2 and

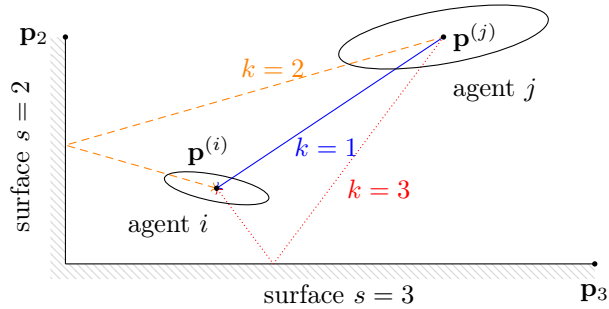


Figure 5.1: Two cooperating agents facilitate MPCs $k \in \{1, 2, 3\}$ for localization. The agent's prior uncertainty is represented by the ellipses. The higher uncertainty in the direction of MPC $k = 2$ compared to $k = 3$ needs to be accounted by the algorithm.

\mathbf{p}_3 in Fig. 5.1). In [T6] we propose to estimate both agents and surrounding environment simultaneously. Section 5.1 provides a brief review to Bayesian position estimation, relevant for [T4-T6]. Subsequently, Section 5.2 displays the impact of multipath information to agent positions as well as surrounding environment, elaborated in [T6]. Finally, Section 5.3 provides a conclusion and further remarks.

5.1 Introduction to Bayesian position estimation

Consider some prior knowledge is available, e.g. a rough guess of the agent positions. Furthermore, let us assume that the agent positions evolve over time. A natural description for this evolution is provided by a state-space model structure composed of motion model and measurement model

$$\text{motion model:} \quad \mathbf{x}_n = f_{\text{motion}}(\mathbf{x}_{n-1}) + \mathbf{w}_n \quad (5.1)$$

$$\text{measurement model:} \quad \mathbf{z}_n = f_{\text{meas}}(\mathbf{x}_n) + \mathbf{n}_n \quad (5.2)$$

where the state vector \mathbf{x}_n consists of the parameters of interest (usually the unknown agent positions and possibly some additional parameters like agent velocities) and the measurement vector \mathbf{z}_n captures the measurements (either at signal (Sec. 2.1) or multipath parameter level (Sec. 2.2)) at time n . The state-space relies on two assumptions. First, the position of agents at n depends on the previous position at $n - 1$ only, reflected by a motion model (or mobility model) as Markov process of first order. The motion model describes a deterministic transition from \mathbf{x}_{n-1} to \mathbf{x}_n in presence of unpredictable errors captured in the additive noise term \mathbf{w}_n . A prominent example is a constant-velocity motion model [129] assuming the agents continue their previous motion $(\mathbf{x}_n - \mathbf{x}_{n-1}) = (\mathbf{x}_{n-1} - \mathbf{x}_{n-2})$ [33][T4-T6]. Second, measurement \mathbf{z}_n at n is a function of the current state vector \mathbf{x}_n and conditionally independent from previous or future states. The measurement model relates the measurements \mathbf{z}_n to the agent positions (contained in \mathbf{x}_n), as described in Chapter 3.

The state-space model displays the state transition from $n - 1$ to n . Having measurements $\mathbf{z}_n, \mathbf{z}_{n-1}, \dots$ at hand plus some prior information of the initial

vector \mathbf{x}_0 , the state-space model can be exploited as inverse problem in order to estimate the current state vector \mathbf{x}_n [119].

5.1.1 Estimation in a Bayesian framework

A natural choice to estimate \mathbf{x}_n is provided by a Bayesian framework which allows to formulate a posterior probability distribution $p(\mathbf{x}_n|\mathbf{z}_{1:n})$. The posterior distribution describes the probability of state vector \mathbf{x}_n , given the current and previous measurements $\mathbf{z}_{1:n} = [\mathbf{z}_1^T, \dots, \mathbf{z}_n^T]^T$ and can be factorized as recursive relation [32]

$$\underbrace{p(\mathbf{x}_n|\mathbf{z}_{1:n})}_{\text{posterior at time step } n} \propto \underbrace{p(\mathbf{z}_n|\mathbf{x}_n)}_{\text{likelihood at time step } n} \int \underbrace{p(\mathbf{x}_n|\mathbf{x}_{n-1})}_{\text{transition probability at time } n} \underbrace{p(\mathbf{x}_{n-1}|\mathbf{z}_{1:n-1})}_{\text{posterior at time step } n-1} d\mathbf{x}_{n-1} \quad (5.3)$$

demonstrating that the posterior at n essentially depends on the previous posterior at $n-1$. Using Bayes theorem and neglecting the evidence term, the current posterior is proportional to the product of likelihood function $p(\mathbf{z}_n|\mathbf{x}_n)$ and prior distribution $p(\mathbf{x}_n|\mathbf{z}_{1:n-1})$ [7], where the prior distribution results as outcome of the integral operator in (5.3). The likelihood function $p(\mathbf{z}_n|\mathbf{x}_n)$ stems from the measurement model and the transition probability $p(\mathbf{x}_n|\mathbf{x}_{n-1})$ from the motion model.

5.1.2 Approximations

The recursive estimation of the posterior distribution of \mathbf{x}_n using the state-space provided in (5.1) and (5.2) discloses some challenges, arising from the non-linear measurement model. Remember that the recursive relation in (5.3) processes the arbitrary distribution of \mathbf{x}_n and not a single value, e.g. its mean. Having the state vector's posterior distribution from $n-1$, the distribution is affected by both motion and measurement model. While affine functions (like a linear motion model) preserve the shape of the distribution up to translation and orientation, a non-linear function (like the measurement model) may lead to distortions [129].

The arbitrary distributions of the state vector and non-linearities of the measurement model f_{meas} affects the implementation of (5.3). Approximations of (5.3) are required. In the following two *filters* are reviewed briefly asserting to estimate the state vector's posterior distribution.

Particle Filter

This implementation has received lot of attention as it retains non-linearities and arbitrary state vector distributions. The distributions are represented as set of realizations of the state vector. Evaluation of the likelihood function $p(\mathbf{z}_n|\mathbf{x}_n)$ for each realization maintains non-linearities and can be efficiently parallelized. Methods [132, 33][T4] demonstrate superior results by implementing (5.3) using a message passing scheme [143, 104].

Extended Kalman filter

As an alternative, in [T4-T6] the non-linear measurement model $f_{\text{meas}}(\mathbf{x}_n) \approx f_{\text{meas}}(\mathbf{x}_n^-) + \mathbf{H}_n(\mathbf{x}_n - \mathbf{x}_n^-)$ is linearized at the predicted mean \mathbf{x}_n^- using the

motion model, where \mathbf{H}_n denotes the Jacobian of f_{meas} . The arbitrary state vector distribution is described by its first and second moments equivalent to its representation as a Gaussian distribution parameterized by a mean vector and covariance matrix. Often denoted as extended Kalman filter, the linearization enables an analytic calculation how the measurement model affects the mean and covariance which results in a strong reduction of computational complexity [129].

Discussion

Conclusive statements on the performance of both approaches are challenging, due to the dependencies on the available information. In general, if less information is available, e.g. a small network topology consisting of two agents measuring only a few reflections, then the particle filter shows its strength as it tracks the complete posterior including multimodalities. Once a tight topology is established and many delay measurements arrive from various directions, the posterior distribution may be represented as a single Gaussian distribution, which may be handled sufficiently by an extended Kalman filter. The comparison in [T4] considers three agents in line-of-sight conditions demonstrating equivalent performance of the extended Kalman filter and a particle filter using 200 particles (realizations of the agent position) per agent.

5.2 Assembling the posterior distribution

This section aims at illustrating the inference of position information using multipath propagation. Of particular interest is the estimation of the state vector's posterior distribution which is calculated as inverse probability from the likelihood function and some prior distribution. The prior distribution is established from the prediction step using motion model f_{motion} and appears in (5.3) as outcome from the integral operator. The likelihood function $p(\mathbf{z}_n|\mathbf{x}_n)$ introduces fresh information obtained from multipath propagation measurements. In the following we highlight the interaction between prior information and the likelihood function and provide a few examples how multipath information is shared among the cooperative network.

Two agents i and j located at $\mathbf{p}_n^{(i)}$ and $\mathbf{p}_n^{(j)}$ aim at employing the measurement model at multipath parameter level in order to update their prior distribution. Additionally, to maintain uncertainties in the provided (but inaccurate) surrounding environment, the reflective surface's position \mathbf{p}_k is tracked as well. Thus, the state vector \mathbf{x}_n is described as

$$\mathbf{x}_n = \begin{bmatrix} \mathbf{p}_n^{(i)} \\ \mathbf{p}_n^{(j)} \\ \mathbf{p}_{k,n} \end{bmatrix}, \quad \mathbf{C}_n = \begin{bmatrix} \mathbf{C}_n^{(i)} & \mathbf{C}_n^{(i,j)} & \mathbf{C}_{k,n}^{(i)} \\ \mathbf{C}_n^{(i,j)} & \mathbf{C}_n^{(j)} & \mathbf{C}_{k,n}^{(j)} \\ \mathbf{C}_{k,n}^{(i)} & \mathbf{C}_{k,n}^{(j)} & \mathbf{C}_{k,n} \end{bmatrix} \quad (5.4)$$

where the corresponding covariance matrix \mathbf{C}_n captures on its diagonal the covariance $\mathbf{C}_n^{(i)}$ of agent i , covariance $\mathbf{C}_n^{(j)}$ of agent j and the covariance $\mathbf{C}_{k,n}$ of the reflective surface. The off-diagonal matrices describe their correlations where we assume for a moment that these correlations are initially zero. Moreover, in the remaining section, time index n is dropped unless explicitly required.

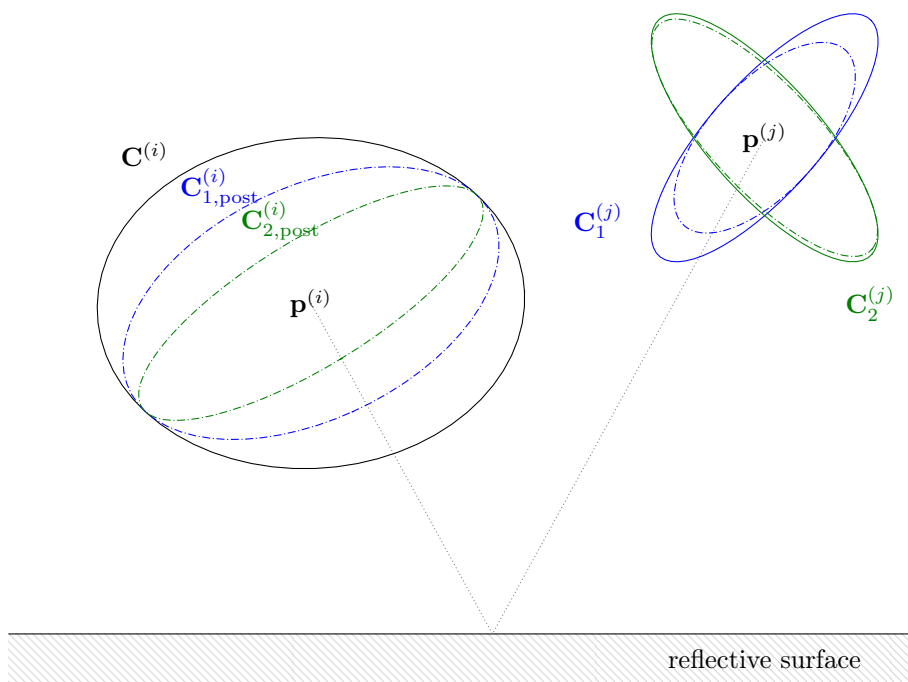


Figure 5.2: Two agents i and j share position information using a specular reflection \cdots for two cases of prior position uncertainty. Ellipses present the prior (solid) and the posterior covariance (dash-dotted) of the agent positions.

The agents are able to measure a single multipath delay $\mathbf{z}^{(i,j)} = \tau_k$ which is related to their positions using the measurement equation

$$\mathbf{z}^{(i,j)} = f_{\text{meas}}(\mathbf{p}^{(j)}, \mathbf{p}^{(i)}) = \frac{1}{c} \|\mathbf{p}^{(i)} - f_k(\mathbf{p}^{(j)})\| \quad (5.5)$$

from (2.8). Of particular interest is the Jacobian \mathbf{H} of the measurement function f_{meas} as it demonstrates how variations in the state vector correspond to variations in the multipath parameters. It is defined as

$$\mathbf{H} = \frac{\partial f_{\text{meas}}}{\partial \mathbf{x}} \quad (5.6)$$

$$= \left[\left(\frac{\partial \tau_k}{\partial \mathbf{p}^{(i)}} \right)^T, \left(\frac{\partial \tau_k}{\partial \mathbf{p}^{(j)}} \right)^T, \left(\frac{\partial \tau_k}{\partial \mathbf{p}_k} \right)^T \right]. \quad (5.7)$$

We assume that the agents have succeeded to calculate their prior distribution $p(\mathbf{x}_n | \mathbf{z}_{n-1}, \dots)$ using the motion model, defined by the Gaussian mean and variance from (5.4). The measurement function f_{meas} connects the variables in the state vector. As each variable is associated with a prior uncertainty in \mathbf{C} this uncertainty spreads to the residual variables, determined by the Jacobian \mathbf{H} . In the following, this exchange of uncertainty is illustrated where we decompose the relations to three parts, first, uncertainty of the cooperating agent, second, uncertainty in the delay measurement and third, uncertainty in the location of the reflective surface.

5.2.1 Impact of agent uncertainty

Large position uncertainty of a cooperating agent reduces the position information contained in the reflection. Figure 5.2 illustrates two agents i and j connected by a single specular component ----- . Ellipses describe the uncertainty before (solid) and after (dash-dotted) the exploitation of the delay of the specular reflection. Two cases of prior position uncertainty of agent j are illustrated: first, j is uncertain in the direction of the specular reflection, denoted by $\mathbf{C}_1^{(j)}$ --- ; second, it is certain along the specular reflection, denoted as $\mathbf{C}_2^{(j)}$ --- . In both cases agent i faces a constant prior uncertainty of $\mathbf{C}^{(i)}$.

As derived in [T6], delay information contributes to agent position information in the direction of the specular path. To calculate the posterior, the agents weigh between their own prior uncertainty, the measurement uncertainty as well as the prior uncertainty of the cooperating agent. This effect is envisioned at agent i whose uncertainty of the posterior reduces stronger if j is more certain along the direction of the specular component (compare $\mathbf{C}_{2,\text{post}}^{(j)}$ --- to $\mathbf{C}_{1,\text{post}}^{(j)}$ ---).

5.2.2 Impact of measurement noise

Increasing delay uncertainty reduces the contained information. Uncertainty in the delay measurements (e.g. due to large levels of overlapping multipath) are considered using the measure σ_k^2 from (2.10). Figure 5.3 depicts the posterior distributions $\mathbf{C}^{(i)}$ and $\mathbf{C}^{(j)}$ of cooperating agents i and j for infinite --- , modest --- and zero delay uncertainty --- . If the delay measurement is not reliable ($\sigma_k^2 \rightarrow \infty$) the posterior distribution remains unchanged with respect to the

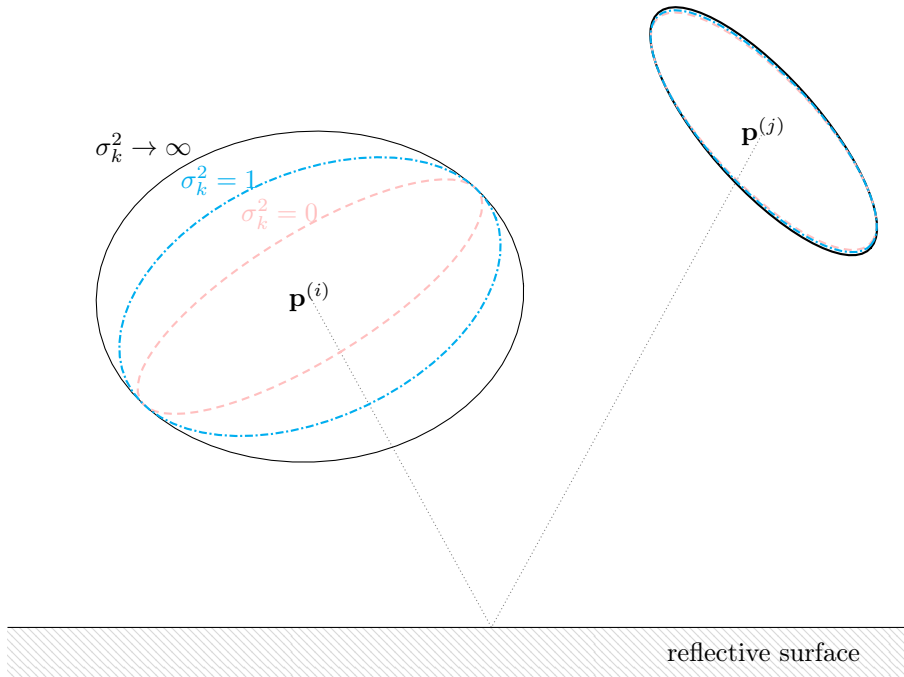


Figure 5.3: Equivalent to Fig. 5.2 for various levels of measurement noise σ_k^2 .

prior distribution. On the contrary, if the delay measurement is highly reliable ($\sigma_k^2 = 0$) the agent's information gain from the reflection is limited by the cooperating agent's uncertainty.

In Fig. 5.3, agent j is more certain regarding its position in the direction of the specular reflection while agent i is initially more uncertain. Thus, both agents gain differently from the same reflection determined by their prior position information.

5.2.3 Impact from uncertainty in the surrounding environment

We have analyzed the importance of prior information of the agents as well as the importance of measurement noise. Finally, we address uncertainties in the description of the geometric environment, denoted as floorplan, and its implications to the posterior distribution. Obviously, the geometric setup of the environment determines multipath parameters but in the literature its impact is neglected notoriously. Fixing the floorplan has advantages in reducing the complexity but limitations if the provided floorplan is not sufficiently accurate or if the electromagnetic waves do not follow geometrical optics. In [T6] the floorplan of the reflective surfaces has been included in the state-space model, demonstrating (i) increased accuracy and (ii) the potential to update and remedy errors and inaccuracies in the floorplan.

Figure 5.4 depicts a single reflection between agents where in Fig. 5.4 (top) both agents stick together such that the angle of incidence of the reflection is steep and in Fig. 5.4 (bottom) they are well separated resulting in a flat angle of

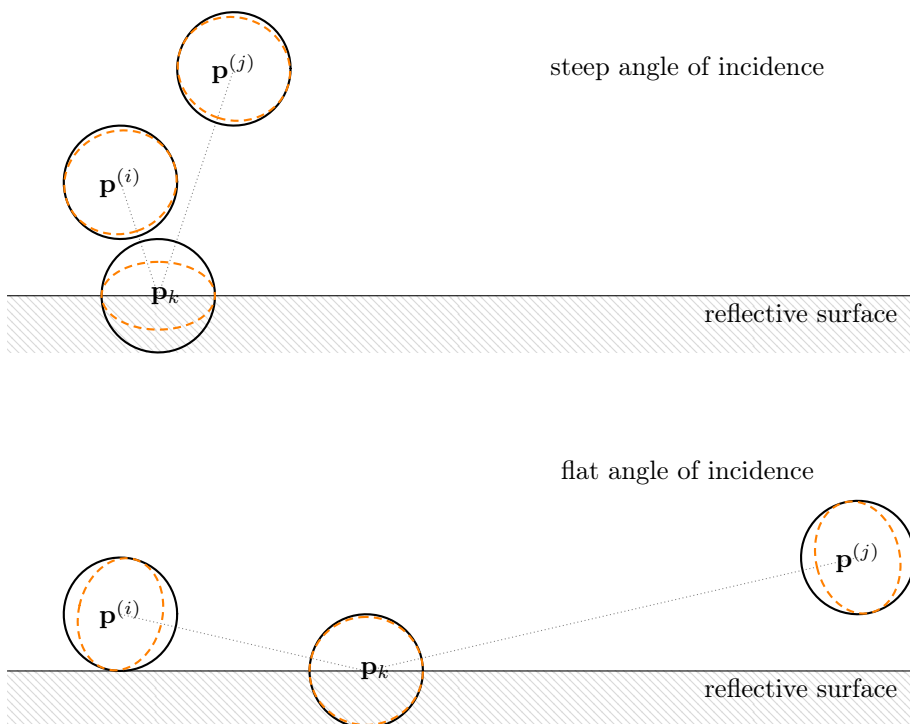


Figure 5.4: Illustration steep (top) and flat angle of incidence (bottom) with prior — and posterior uncertainty ----. Steep angles of incidence help the reflective surface to improve its accuracy while flat angles do a favor for agents.

incidence. For comparison, both agents and the reflective surface are equipped with equal prior distributions.

As studied in [T6] agent positions contribute differently to multipath components than reflective surfaces. While the contained delay information with respect to agents has a constant magnitude of 1, the information with respect to the reflective surface depends on the incident reflection angle and gets values in the range of 0 – 2.

Starting with the steep angle of incidence, an evaluation of the Jacobian \mathbf{H} shows that the delay measurement is approximately twice as sensitive to the position of the reflective surface than to the agent positions [77]. Thus, a provided measurement contributes to the posterior of the reflective surface twice as much. This is unveiled in Fig. 5.4 (top) where the reflective surface at \mathbf{p}_k reduces its posterior covariance ---- in the direction perpendicular to the surface while the agent posteriors remains approximately constant. Interestingly, as the Jacobian \mathbf{H} spreads the prior uncertainty, both agents are confronted with twice the prior uncertainty of the reflective surface, which limits their accessible information.

This is different at flat angles of incidence as shown in Fig. 5.4 (bottom). At flat angles the multipath delay is not sensitive to the position of the reflective surface and as a consequence, the reflective surface cannot gain information from the specular reflection delay. However, in comparison to the steep angle of incidence, both agents are able to use the delay information to narrow their

posterior distributions.

5.2.4 Mutual dependencies

The illustrations of the posterior distributions are valid for the agents and reflective surfaces but veil their mutual dependencies captured in the off-diagonal matrices in \mathbf{C} , see (5.4). These matrices maintain correlations which occur if the measurement equation provides information stemming from similar directions. E.g. in the chosen setup of Fig. 5.4 (top), position information is delivered mostly in the y direction accounted by correlations in the y direction as well.

As shown in [T6], these correlations are of particular importance once the floorplan is included in the state vector. The recursive estimation of the reflective surfaces aligns their position in accordance to the measurements but also considers their correlations which turns out to be a large benefit for updating the floorplan. Assuming a multipath component bounces a single reflective surface, this surface is able to update its position but simultaneously spreads this information to its correlated neighboring surfaces. Thus, all correlated surfaces contained in the floorplan benefit from each single reflection which strongly accelerates the floorplan convergence [T6].

5.3 Concluding remarks and outlook

The contributions [T4-T6] in cooperative localization have demonstrated that position information from anchors can be replaced by floorplan information obtained from multipath propagation. Relying on a floorplan places focus on the accuracy of this floorplan. In [T5] strong sensitivity to an inaccurate floorplan was demonstrated which can be circumvented by updating the floorplan simultaneously with the agent positions [T6].

The discussed methods in the literature avoid incorporating information regarding the state transition and instead, rely on constant-velocity motion models. Additional information of the movement, e.g. obtained from an inertial measurement unit [4, 65] has the potential to increase the accuracy of the prior distribution and thus, the posterior becomes less dependent on (potentially erroneous) estimated multipath parameters.

The proposed methods in [T4-T6] treat centralized, cooperative algorithms where all gathered measurements are collected at a central unit. This is different for the particle filter based methods [132, 33][T4]. Their message passing approach appears as distributed implementation where the agents share their beliefs among their neighbors. The increased accuracy has its price; despite the demanding computational complexity the required channel utilization (or network traffic) may be identified [35] as most important one. Channel utilization stems from message passing between nodes (in [132] 15000 particles per agent represent one message). To limit the channel utilization, several methods are possible. Research in [81, 27, 19] focuses on parametric descriptions of the messages while [T4] incorporate a well behaved likelihood function (single, unbiased peak and less multimodalities) simplifying the state vector's representation with less particles.

Chapter 6

Conclusion

Conventional localization services rely on line-of-sight measurements to numerous base stations. The aim of this thesis has been to reduce these demands for infrastructure by exploiting the radio signal propagation characteristics. Three research topics have been tackled: modeling of a site-specific radio channel, utilization of the angle-delay domain of radio signals and imposing cooperation among the users.

A site-specific channel model was presented in Chapter 3, able to characterize specular reflections as well as dense multipath. Therein, we describe specular reflections in a deterministic manner using geometrical optics and dense multipath as random variable using its statistical moments. The calculated power spectrum of dense multipath shows a good fit to reported distributions in the literature [T1]. We may conclude that the proposed model qualifies to create realistic, site-specific radio channels where specular reflections carry position information and dense multipath appears as self-interference. However, in this thesis, we treated dense multipath as undesired interference and did not acknowledge its position information covered in its statistical moments. The answer to the question, whether or not dense multipath is predominantly an enemy (self-interfering) or an undiscovered friend (position-related statistical moments), is left for future research. Moreover, our analysis demonstrated that dense multipath is non-uniformly distributed in the angle domain. This violates the assumption of uniform scattering in the angle domain [16], often used in multi-antenna systems [128]. It is of highest interest at what extent this violation affects established algorithms [92, 113, 3] as well as the proposed one in [T3].

In Chapter 4 we treated localization using a single base station. The presented low-cost approach avoids phase-coherent multi-antenna front ends by using directive antennas or electronically-steerable analog beamformers. We derived a fundamental bound on the localization performance demonstrating its robustness to path overlap of specular reflections. The proposed algorithm circumvents the arising non-linear, multi-parameter optimization problem by approximating the multipath amplitude estimation. We experienced only a minor performance loss in comparison to an algorithm with access to phase-coherent measurements [T3]. We may conclude that directive antennas provide angle information which suffices for positioning using a single base station. However, in this thesis, the analysis was constraint to a direct positioning scheme which

circumvents estimation of multipath components and their association to reflective surfaces. Deriving an algorithm capable to estimate multipath components is left for future research: exploring the angle-delay domain is a notoriously tough challenge, especially in presence of dense multipath [26, 29, 118] but may reduce the computational complexity of a direct positioning scheme [90],[T4].

In Chapter 5, a method was presented for localization where the frame-of-reference is provided from reflective surfaces. As a consequence, the cooperative users can estimate their global position coordinates without the need of base stations. We identified two challenges: the rising complexity due to cooperative localization [T4] and the sensitivity to an accurate description of the surface positions [T5]. To tackle both challenges, we proposed to simultaneously track the cooperating users and to refine the positions of the reflective surfaces using a Gaussian uncertainty description. Based on real measurement data, we showed in [T5,T6] the potential to track two cooperating users without any help from base stations or inertial measurement units. However, in this thesis, we refine the reflective surface positions using a strong prior information in the form of an initial floor plan. As future work, this refinement should be extended to detection of additional reflective surfaces. Often denoted as feature-based *simultaneous localization and mapping* [32, 129], feature detection rises entirely new challenges. Recent works, based on a single base station and exploiting the angle-delay domain, have shown a remarkable performance gain [36, 92, 113, 3, 13], worth to be adopted for avoiding base stations.

Appendices

Appendix A

Derivation of angular and delay power spectrum in far-field, related to Chapter 3.2

To calculate the ADPS $p_{\text{DM},k}(\boldsymbol{\theta})$ from (3.12) we substitute dA by multipath parameters $d\boldsymbol{\theta} = d\mathbf{u}^{(i)}d\mathbf{u}^{(j)}d\tau$, which can be factorized as

$$dA = \frac{(d^{(i)})^2}{\cos \theta^{(i)}} d\Omega(\mathbf{u}^{(i)}) \times \delta(\mathbf{u}^{(i)} - f_{\mathbf{u}^{(i)}}(\mathbf{u}^{(j)})) d\mathbf{u}^{(j)} \times \delta(\tau - f_\tau(\mathbf{u}^{(i)}, \mathbf{u}^{(j)})) d\tau. \quad (\text{A.1})$$

Let $\mathbf{u}^{(i)}$ point on reflection point \mathbf{q} associated with area dA , then the first factor explains dA as function of $d\Omega(\mathbf{u}^{(i)}) = \sin \phi^{e,(i)} d\phi^{a,(i)} d\phi^{e,(i)}$. The second factor ensures that both $\mathbf{u}^{(i)}$ and $\mathbf{u}^{(j)}$ point to \mathbf{q} using the function $f_{\mathbf{u}^{(i)}}$. The third factor establishes the relation between the delays and directions using f_τ . Both $f_{\mathbf{u}^{(i)}}$ and f_τ can be calculated using geometrical optics, equivalent to (3.5)-(3.7).

Plugging (A.1) in (3.12), we may identify the ADPS $p_{\text{DM},k}(\boldsymbol{\theta})$ as

$$p_{\text{DM},k}(\boldsymbol{\theta}) = \frac{S^2 \cos \theta^{(j)} \sin \phi^{e,(i)}}{k_{\alpha_R}^2 (d^{(j)})^2} \left(\frac{1 + \cos \psi}{2} \right)^{\alpha_R} \times \delta(\mathbf{u}^{(i)} - f_{\mathbf{u}^{(i)}}(\mathbf{u}^{(j)})) \delta(\tau - f_\tau(\mathbf{u}^{(i)}, \mathbf{u}^{(j)})). \quad (\text{A.2})$$

A.1 Angular delay power spectrum in far-field conditions

To calculate the angular power spectrum and the delay power spectrum in far-field conditions, we make the following approximations. In far-field conditions, the distance between reflective surface and both transceivers is large which allows to approximate $f_{\mathbf{u}^{(i)}}(\mathbf{u}^{(j)}) \approx \mathbf{u}^{(j)}$. Moreover, the reflective surface has infinite dimensions and is assumed to be located in the yz -plane such that $\mathbf{e}_k = \mathbf{u}_k^{(i)}$. Then, $f_\tau(\mathbf{u}^{(i)}, \mathbf{u}^{(j)}) \approx \frac{\tau_k}{\cos(\phi^{a,(j)}) \sin(\phi^{e,(j)})}$ as well as $d^{(j)} = \frac{c\tau_k}{2 \cos(\phi^{a,(j)}) \sin(\phi^{e,(j)})}$,

$\cos \psi \approx 2 \cos^2 \phi^{a,(j)} \sin^2 \phi^{e,(j)} - 1$ and $\cos \theta^{(j)} = \cos \phi^{a,(j)} \sin \phi^{e,(j)}$. Therefore, (A.2) can be written as

$$p_{\text{DM},k}^{\text{ff}}(\boldsymbol{\theta}) = \frac{S^2 \cos^{2\alpha_R+3}(\phi^{a,(j)}) \sin^{2\alpha_R+4}(\phi^{e,(j)})}{k_{\alpha_R} (c\tau_k)^2} \times \delta(\mathbf{u}^{(i)} - \mathbf{u}^{(j)}) \delta\left(\tau - \frac{\tau_k}{\cos(\phi^{a,(j)}) \sin(\phi^{e,(j)})}\right) \quad (\text{A.3})$$

Assuming j radiates in an isotropic manner, the received ADPS $p_{\text{DM},k}^{\text{ff}}(\mathbf{u}^{(i)}, \tau)$ at i results as

$$p_{\text{DM},k}^{\text{ff}}(\mathbf{u}^{(i)}, \tau) = \int_{\mathbb{S}^2} p_{\text{DM},k}^{\text{ff}}(\boldsymbol{\theta}) d\mathbf{u}^{(j)} \quad (\text{A.4})$$

Symmetry in $p_{\text{DM},k}^{\text{ff}}(\boldsymbol{\theta})$ between $\mathbf{u}^{(i)}$ and $\mathbf{u}^{(j)}$ yields the property of $p_{\text{DM},k}^{\text{ff}}(\mathbf{u}^{(i)}, \tau) = p_{\text{DM},k}^{\text{ff}}(\mathbf{u}^{(j)}, \tau)$ which enables to calculate the received ADPS $p_{\text{DM},k}^{\text{ff}}(\phi^a, \phi^e, \tau)$, valid for both i and j , as

$$p_{\text{DM},k}^{\text{ff}}(\phi^a, \phi^e, \tau) = \frac{S^2 \cos^{2\alpha_R+3}(\phi^a) \sin^{2\alpha_R+4}(\phi^e)}{k_{\alpha_R} (c\tau_k)^2} \delta\left(\tau - \frac{\tau_k}{\cos(\phi^a) \sin(\phi^e)}\right). \quad (\text{A.5})$$

A.2 Angular power spectrum

The azimuth power spectrum (APS) $p_{\text{DM},k}^{\text{ff}}(\phi^a)$ in far-field conditions follows by integration along elevation and delay of (A.5) according to

$$p_{\text{DM},k}^{\text{ff}}(\phi^a) = \int_{\tau_k}^{\infty} \int_{-\frac{\pi}{2}}^{\frac{\pi}{2}} p_{\text{DM},k}^{\text{ff}}(\phi^a, \phi^e, \tau) d\phi^e d\tau \quad (\text{A.6})$$

$$= \frac{4S^2 \cos^{2\alpha_R+3}(\phi^a)}{(c\tau_k)^2 k_{\alpha_R}} \int_{-\frac{\pi}{2}}^{\frac{\pi}{2}} \sin^{2\alpha_R+4}(\phi^e) d\phi^e \quad (\text{A.7})$$

$$= \frac{4S^2 \cos^{2\alpha_R+3}(\phi^a)}{(c\tau_k)^2 k_{\alpha_R}} 2^{2\alpha_R+4} B\left(\alpha_R + \frac{5}{2}, \alpha_R + \frac{5}{2}\right) \quad (\text{A.8})$$

$$= \frac{4S^2 \cos^{2\alpha_R+3}(\phi^a)}{(c\tau_k)^2 k_{\alpha_R}} 2^{2\alpha_R+4} \frac{\Gamma(\alpha_R + \frac{5}{2}) \Gamma(\alpha_R + \frac{5}{2})}{\Gamma(2\alpha_R + 5)} \quad (\text{A.9})$$

$$= \frac{4S^2 \sqrt{\pi} \cos^{2\alpha_R+3}(\phi^a)}{(c\tau_k)^2 k_{\alpha_R}} \frac{\Gamma(\alpha_R + \frac{5}{2})}{\Gamma(\alpha_R + 3)} \quad (\text{A.10})$$

where the limits of integration result from the infinite surface dimension ($\phi^e \in [-\frac{\pi}{2}, \frac{\pi}{2}]$) and the fact, that the shortest distance is defined by the specular component's delay τ_k . $B(\cdot, \cdot)$ and $\Gamma(\cdot)$ define the Beta [40, 3.621] and Gamma function [40, 8.384]. The elevation power spectrum follows equivalently.

A.3 Delay power spectrum

Calculation of the delay power spectrum (DPS) $p_{\text{DM},k}^{\text{ff}}(\tau)$ requires integration along the azimuth and elevation angle which is not straight forward. In the following, we substitute the angles by an area element on the surface and

subsequently express the area by polar coordinates defined on the surface. First, we substitute $d\phi^a d\phi^e = dA \cos \phi^a / d^2$ using the far-field property $\cos \theta = \cos \phi^a \sin \phi^e$, then, (A.5) can be rewritten as

$$\begin{aligned} p_{\text{DM},k}^{\text{ff}}(\tau) &= \int \frac{p_{\text{DM},k}^{\text{ff}}(\phi^a, \phi^e, \tau) \cos \phi^a}{d^2} dA \\ &= \int \frac{16S^2 \cos^{2\alpha_R+6}(\phi^a) \sin^{2\alpha_R+6}(\phi^e)}{(c\tau_k)^4 k_{\alpha_R}} \delta\left(\tau - \frac{\tau_k}{\cos \phi^a \sin \phi^e}\right) dA. \end{aligned} \quad (\text{A.11})$$

It is interesting to note that the power spectra in (A.11) results by integration along a closed curve on the surface. In far-field conditions, this curve degenerates to a circle. The radius of the circle, denoted as ξ , is defined by the Dirac-delta's argument in (A.11). To find an analytic solution we substitute dA by polar coordinates $dA = \xi d\xi d\varphi$ with radius ξ and angle φ . Radius ξ can be defined as $\xi = \frac{c}{2} \sqrt{\tau_o^2 - \tau_k^2}$ where τ_o denotes the delay between both transceivers via reflection points lying on the circle

$$\tau_o = \frac{\tau_k}{\cos \phi^a \sin \phi^e} \quad (\text{A.12})$$

and the shortest delay via the reflective surface (the circle's center point) is approximately τ_k . Calculation of $d\xi/d\tau_o$ results in $\xi d\xi = \frac{c^2}{4} \tau_o d\tau_o$ and finally, we can substitute surface area dA by delay τ_o according to

$$dA = \frac{c^2}{4} \tau_o d\varphi d\tau_o. \quad (\text{A.13})$$

The DPS $p_k^{\text{ff}}(\tau)$ can be rewritten by plugging (A.12) and (A.13) in (A.11) and integration along the circle results in

$$p_{\text{DM},k}^{\text{ff}}(\tau) = \int_{\tau_k}^{\infty} \int_0^{2\pi} \frac{4S^2 \tau_k^{2\alpha_R+2}}{c^2 \tau_o^{2\alpha_R+5} k_{\alpha_R}} \delta(\tau - \tau_o) d\varphi d\tau_o \quad (\text{A.14})$$

$$= \frac{S^2 8\pi \tau_k^{2\alpha_R+2}}{c^2 \tau^{2\alpha_R+5} k_{\alpha_R}} u(\tau - \tau_k) \quad (\text{A.15})$$

with unit-step (Heaviside) function $u(\tau)$.

Appendix B

Derivation of the position error bound, related to Chapter 4

Using matrix-vector notation, we can stack the M measurements, resulting in

$$\mathbf{r} = \mathbf{X}(\mathbf{p})\boldsymbol{\alpha} + \mathbf{w} \quad (\text{B.1})$$

with

$$\mathbf{r} = \begin{bmatrix} \mathbf{r}_1 \\ \vdots \\ \mathbf{r}_m \\ \vdots \\ \mathbf{r}_M \end{bmatrix}, \quad \mathbf{X}(\mathbf{p}) = \begin{bmatrix} \mathbf{X}_1(\mathbf{p}) \\ \vdots \\ \mathbf{X}_m(\mathbf{p}) \\ \vdots \\ \mathbf{X}_M(\mathbf{p}) \end{bmatrix}, \quad \boldsymbol{\alpha} = \begin{bmatrix} \alpha_1 \\ \vdots \\ \alpha_k \\ \vdots \\ \alpha_K \end{bmatrix}, \quad \mathbf{w} = \begin{bmatrix} \mathbf{w}_1 \\ \vdots \\ \mathbf{w}_m \\ \vdots \\ \mathbf{w}_M \end{bmatrix}$$

where vectors $\mathbf{r}_m \in \mathbb{C}^N$, $\mathbf{X}_m(\mathbf{p}) \in \mathbb{C}^{N \times K}$ and $\mathbf{w}_m \in \mathbb{C}^N$ define the sampled signals at m th antenna, and

$$\mathbf{X}_m(\mathbf{p}) = [b_m(\phi_1)\mathbf{s}(\tau_1) \quad b_m(\phi_2)\mathbf{s}(\tau_2) \quad \dots \quad b_m(\phi_K)\mathbf{s}(\tau_K)].$$

In (B.1) the geometric relations between signal parameters and position parameters are defined solely by the dependency of $\mathbf{X}_m(\mathbf{p})$ on \mathbf{p} . Since the remaining parameters in $\mathbf{X}_m(\mathbf{p})$ are known beforehand, the matrix can be assembled for any position hypothesis \mathbf{p} .

In the following we derive the SPEB valid for (B.1). Based on the log likelihood function $l(\mathbf{r}; \boldsymbol{\xi})$ parameterized on the MPC parameters $\boldsymbol{\xi}$ the Fisher information $\mathbf{J}(\boldsymbol{\xi})$ for $\boldsymbol{\xi}$ is calculated. Using the appropriate multipath model from Section 3.1 the Fisher information of MPCs can be related to Fisher information $\mathbf{J}(\boldsymbol{\theta})$ of agent position which subsequently yields the SPEB, summarized as

likelihood for MPC param.	Fisher information MPC parameters	Fisher information agent position	Position error bound
$l(\mathbf{r}; \boldsymbol{\xi})$	$\mathbf{J}(\boldsymbol{\xi})$	$\mathbf{J}(\boldsymbol{\theta})$	$\mathcal{P}(\mathbf{p})$
\longrightarrow	\longrightarrow	\longrightarrow	\longrightarrow

Careful distinction between parameter vector $\boldsymbol{\theta}$ and $\boldsymbol{\xi}$ is required. The agent position appears in $\boldsymbol{\theta}$, defined as

$$\boldsymbol{\theta} = \left[\underbrace{\mathbf{p}^T}_{\substack{\text{agent} \\ \text{position}}}, \underbrace{\Re\alpha_1 \dots \Re\alpha_k, \Im\alpha_1 \dots \Im\alpha_k}_{\text{amplitudes}} \right]^T \quad (\text{B.2})$$

where the remaining parameters cover the complex-valued amplitudes split into its real and imaginary parts, using the operators \Re and \Im , respectively.

The MPC parameters angles and delays appear in $\boldsymbol{\xi}$, defined as

$$\boldsymbol{\xi} = \left[\underbrace{\tau_1 \dots \tau_K}_{\text{delays}}, \underbrace{\phi_1 \dots \phi_K}_{\text{angles}}, \underbrace{\Re\alpha_1 \dots \Re\alpha_k, \Im\alpha_1 \dots \Im\alpha_k}_{\text{amplitudes}} \right]^T \quad (\text{B.3})$$

To relate the propagation parameters $\boldsymbol{\xi}$ to the position parameters in $\boldsymbol{\theta}$ proper relations are required. We employ the relations based on geometrical optics to model \mathbf{p} as function of ϕ_k and τ_k . This is different for modeling amplitudes which requires an accurate characterization of the surrounding environment (see Chapter 2). Thus, the MPC amplitudes are estimated from the measurement equivalent of treating amplitudes as nuisance parameter or auxiliary variables. Their appearance in $\boldsymbol{\theta}$ acknowledges the uncertainty in amplitudes and its impact on uncertainty in positions.

B.1 Likelihood function for MPC parameters

The channel model is Gaussian distributed $\mathcal{N}(\boldsymbol{\mu}(\boldsymbol{\xi}), \sigma^2 \mathbf{I})$ with mean $\boldsymbol{\mu}(\boldsymbol{\xi}) = \mathbf{X}(\mathbf{p})\boldsymbol{\alpha}$ and variance $\sigma^2 \mathbf{I}$. Hence, the log likelihood function $l(\mathbf{r}; \boldsymbol{\xi})$ of the channel response \mathbf{r} parameterized by the MPC parameters $\boldsymbol{\xi}$ can be defined by taking the logarithm of the Gaussian probability density function. Neglecting the constants it can be formulated as

$$l(\mathbf{r}; \boldsymbol{\xi}) \propto -\frac{1}{\sigma^2} \|\mathbf{r} - \boldsymbol{\mu}(\boldsymbol{\xi})\|^2. \quad (\text{B.4})$$

In the following we calculate the Fisher information of the MPC parameters using the presented likelihood function.

B.2 Fisher information for MPC parameters

The Fisher information matrix (FIM) $\mathbf{J}(\boldsymbol{\xi}) \in \mathbb{R}^{4K \times 4K}$ describes the amount of information contained in the measurements \mathbf{r} regarding the parameters $\boldsymbol{\xi}$. Based on the employed model of \mathbf{r} it enlightens the sensitivity of \mathbf{r} to variations in $\boldsymbol{\xi}$.

The Fisher information of the ℓ th row and ℓ' th column is defined as [62, Appendix 15C]

$$[\mathbf{J}(\boldsymbol{\xi})]_{\ell, \ell'} = 2\Re \left\{ \frac{1}{\sigma^2} \left(\frac{\partial \boldsymbol{\mu}(\boldsymbol{\xi})}{\partial \xi_\ell} \right)^H \frac{\partial \boldsymbol{\mu}(\boldsymbol{\xi})}{\partial \xi_{\ell'}} \right\}. \quad (\text{B.5})$$

Substituting $\boldsymbol{\mu}(\boldsymbol{\xi}) = \mathbf{X}(\mathbf{p})\boldsymbol{\alpha}$ and using (B.1) allows to rewrite $\mathbf{J}(\boldsymbol{\xi})$ using the symmetric submatrices $\boldsymbol{\Lambda}_\vartheta$ (with placeholder ϑ) as

$$\mathbf{J}(\boldsymbol{\xi}) = \begin{bmatrix} \boldsymbol{\Lambda}_\tau & \boldsymbol{\Lambda}_{\tau\phi} & \boldsymbol{\Lambda}_{\tau\alpha} \\ \boldsymbol{\Lambda}_{\phi\tau} & \boldsymbol{\Lambda}_\phi & \boldsymbol{\Lambda}_{\phi\alpha} \\ \boldsymbol{\Lambda}_{\alpha\tau} & \boldsymbol{\Lambda}_{\alpha\phi} & \boldsymbol{\Lambda}_\alpha \end{bmatrix} \begin{array}{l} \text{delays} \\ \text{angles} \\ \text{amplitudes real and imaginary-valued} \end{array} \quad (\text{B.6})$$

In general, a diagonal structure of $\mathbf{J}(\boldsymbol{\xi})$ is desired. Then, each parameter delivers unique information to the model and hence, the information regarding a specific parameter can be estimated from \mathbf{r} independent on the neighboring parameters.

B.3 Fisher information for agent position

Relation between the FIM $\mathbf{J}(\boldsymbol{\xi})$ containing MPC parameters to the FIM $\mathbf{J}(\boldsymbol{\theta})$ containing the agent position is performed using

$$\mathbf{J}(\boldsymbol{\theta}) = \mathbf{H}\mathbf{J}(\boldsymbol{\xi})\mathbf{H}^T \quad (\text{B.7})$$

where the Jacobian matrix $\mathbf{H} \in \mathbb{R}^{2 \times 4K}$ relates the variations in the parameters of $\boldsymbol{\xi}$ to $\boldsymbol{\theta}$, and results as

$$\mathbf{H} = \begin{bmatrix} \mathbf{H}_\tau & \mathbf{H}_\phi & \mathbf{0} \\ \mathbf{0} & \mathbf{0} & \mathbf{I} \end{bmatrix} \begin{array}{l} \text{agent position} \\ \text{amplitudes} \end{array}$$

delays
angles
amplitudes

(B.8)

with

$$\text{relation to delays } \mathbf{H}_\tau = \begin{bmatrix} \frac{\partial \tau_1}{\partial \mathbf{p}}, \dots, \frac{\partial \tau_K}{\partial \mathbf{p}} \end{bmatrix} \quad (\text{B.9})$$

$$\text{relation to angles } \mathbf{H}_\phi = \begin{bmatrix} \frac{\partial \phi_1}{\partial \mathbf{p}}, \dots, \frac{\partial \phi_K}{\partial \mathbf{p}} \end{bmatrix}. \quad (\text{B.10})$$

We restrain from modeling the positions as functions of the amplitude, mathematically depicted by the identity matrix \mathbf{I} in the lower-right of \mathbf{H} . Plugging (B.6) in (B.7) the FIM $\mathbf{J}(\boldsymbol{\theta})$ results in

$$\mathbf{J}(\boldsymbol{\theta}) = \begin{bmatrix} \mathbf{H}_\tau \boldsymbol{\Lambda}_\tau \mathbf{H}_\tau^T + 2\mathbf{H}_\tau \boldsymbol{\Lambda}_{\tau,\phi} \mathbf{H}_\phi^T + \mathbf{H}_\phi \boldsymbol{\Lambda}_\phi \mathbf{H}_\phi^T & \mathbf{H}_\tau \boldsymbol{\Lambda}_{\tau,\alpha} + \mathbf{H}_\phi \boldsymbol{\Lambda}_{\phi\alpha} \\ \boldsymbol{\Lambda}_{\alpha\tau} \mathbf{H}_\tau^T + \boldsymbol{\Lambda}_{\alpha\phi} \mathbf{H}_\phi^T & \boldsymbol{\Lambda}_\alpha \end{bmatrix} \quad (\text{B.11})$$

where the submatrix in the top-left illustrates the information regarding the agent position and the submatrices top-right and bottom-left depict the mutual dependencies between agent position and multipath amplitudes.

B.4 Position error bound considering path overlap

Finally the SPEB of the measurement model results by inversion of $\mathbf{J}(\boldsymbol{\theta})$ and evaluation of the trace of the top-left 2×2 submatrix. To reduce the complexity we introduce an *equivalent Fisher information matrix* (EFIM) [115] $\mathbf{J}_e(\mathbf{p}) \in \mathbb{R}^{2 \times 2}$ which has the property $\mathbf{J}_e^{-1}(\mathbf{p}) = [\mathbf{J}^{-1}(\boldsymbol{\theta})]_{2 \times 2}$ and thus, is related to the SPEB by

$$\mathcal{P}(\mathbf{p}) = \text{trace}\{\mathbf{J}_e^{-1}(\mathbf{p})\}. \quad (\text{B.12})$$

Using $\mathbf{J}(\boldsymbol{\theta})$ from (B.11) the EFIM results as

$$\begin{aligned} \mathbf{J}_e(\mathbf{p}) &= \mathbf{H}_\tau \boldsymbol{\Lambda}_\tau \mathbf{H}_\tau^T + 2\mathbf{H}_\tau \boldsymbol{\Lambda}_{\tau,\phi} \mathbf{H}_\phi^T + \mathbf{H}_\phi \boldsymbol{\Lambda}_\phi \mathbf{H}_\phi^T \\ &\quad - (\mathbf{H}_\tau \boldsymbol{\Lambda}_{\tau,\alpha} + \mathbf{H}_\phi \boldsymbol{\Lambda}_{\phi\alpha}) \boldsymbol{\Lambda}_\alpha^{-1} (\mathbf{H}_\tau \boldsymbol{\Lambda}_{\tau,\alpha} + \mathbf{H}_\phi \boldsymbol{\Lambda}_{\phi\alpha})^T \end{aligned} \quad (\text{B.13})$$

The EFIM gives important insights. It is directly related to the information on \mathbf{p} contained in $\boldsymbol{\xi}$. It is interesting to note that these terms in (B.13) which are solely related to angles and delays (the first line in (B.13)) add useful contributions to the agent position information. This is different for terms tied to amplitudes (appearing in the second line of (B.13)). The uncertainty in the amplitude estimate limits the accessible information of the positions.

At this point, complicated matrix expressions in (B.13) prohibit a further analysis. Insights may be extracted by assuming that the arrival of multipath is separated in angle or delay domain, as discussed in the following.

B.5 Position error bound neglecting path overlap

The SPEB in (B.12) is able to describe effects stemming from overlapping (superimposed) multipath. Overlapping multipath denote paths which arrive simultaneously in angle and delay domain and as a consequence, their parameters cannot be estimated independently which lowers the achievable SPEB. In this section we are interested in the SPEB if separated multipath (the opposite of overlapping multipath) are present only. We define a new SPEB

$$\tilde{\mathcal{P}}(\mathbf{p}) = \text{trace}\{\tilde{\mathbf{J}}_e^{-1}(\mathbf{p})\} \quad (\text{B.14})$$

valid for separated multipath (radio channels consisting of a few, separated multipath are often denoted as *sparse channel*). The explanatory power of this SPEB is valid at highly directive antennas and large bandwidths such that the beamwidth of $b_m(\phi)$ and pulse width of $s(t)$ get very short which results in negligible path overlap.

To calculate $\tilde{\mathcal{P}}(\mathbf{p})$ the structure of the submatrices $\boldsymbol{\Lambda}_\cdot$ needs to be revisited. First, in absence of path overlap the submatrices get diagonal. Moreover, assuming even (or odd) functions of $b_m(\phi)$ and $s(t)$ their derivatives are odd (or even) functions resulting in the inner products $\sum_m b_m(\phi) db_m(\phi)/d\phi = 0$ and $\mathbf{s}^H(\tau) d\mathbf{s}(\tau)/d\tau = 0$. Then off-diagonal submatrices in (B.6) result in $\mathbf{0}$; and the EFIM $\tilde{\mathbf{J}}_e(\mathbf{p})$ results from (B.13) as

$$\tilde{\mathbf{J}}_e(\mathbf{p}) = \mathbf{H}_\tau \boldsymbol{\Lambda}_\tau \mathbf{H}_\tau^T + \mathbf{H}_\phi \boldsymbol{\Lambda}_\phi \mathbf{H}_\phi^T \quad (\text{B.15})$$

$$= \underbrace{\sum_k \lambda_k^{(\tau)} \mathbf{D}(\phi_k^{(i)})}_{\text{delay information}} + \underbrace{\sum_k \lambda_k^{(\phi)} \mathbf{D}(\phi_k^{(i)} - \frac{\pi}{2})}_{\text{angle information}}. \quad (\text{B.16})$$

separated into the impact from delay as well as angle information. The EFIM $\tilde{\mathbf{J}}_e(\mathbf{p})$ can be described as sum of $\lambda_k \mathbf{D}(\phi_k)$ terms where λ_k denotes the information intensity along the direction $\mathbf{e}(\phi_k^{(i)}) \in \mathbb{R}^2$, contained in the 2×2 direction matrix $\mathbf{D}(\phi_k^{(i)}) = \mathbf{e}(\phi_k^{(i)}) \mathbf{e}^H(\phi_k^{(i)})$ [114]. Both $\lambda_k^{(\tau)}$ and $\lambda_k^{(\phi)}$ stem from the diag-

onals of Λ_τ and Λ_ϕ according to

$$\lambda_k^{(\tau)} = \frac{8\pi^2\beta^2\text{SNR}}{c^2} \sum_m |b_m(\phi_k)|^2 \quad (\text{B.17})$$

$$\lambda_k^{(\phi)} = \frac{2\text{SNR}}{(c\tau_k)^2} \sum_m \left| \frac{db_m(\phi_k)}{d\phi_k} \right|^2 \quad (\text{B.18})$$

with

$$\beta^2 = \frac{\int_{-\infty}^{\infty} f^2 |S(f)|^2 df}{\int_{-\infty}^{\infty} |S(f)|^2 df} \quad \text{and} \quad \text{SNR} = \frac{|\alpha_k|^2 \int_{-\infty}^{\infty} |S(f)|^2 df}{N_0} \quad (\text{B.19})$$

using $\sigma^2 = N_0/T_s$ and

$$S(f) = \int_{-\infty}^{\infty} s(t) \exp\{-j2\pi ft\} dt \quad (\text{B.20})$$

$$T_s \|\mathbf{s}\|^2 = \sum_n T_s |s(nT_s)|^2 = \int_{-\infty}^{\infty} |s(t)|^2 dt = \int_{-\infty}^{\infty} |S(f)|^2 df. \quad (\text{B.21})$$

The direction vector $\mathbf{e}(\phi_k^{(i)}) = [\cos \phi_k^{(i)}, \sin \phi_k^{(i)}]^T$ depends on the multipath angle $\phi_k^{(i)}$ of agent i (not to be confused with angle $\phi_k \equiv \phi_k^{(j)}$ at anchor j) and can be calculated using the relation (3.5) resulting in

$$\text{direction} \quad \mathbf{e}(\phi_k^{(i)}) = \frac{\mathbf{p} - f_k(\mathbf{p}^{(j)})}{\|\mathbf{p} - f_k(\mathbf{p}^{(j)})\|} \quad (\text{B.22})$$

where function $f_k(\mathbf{p}^{(j)})$ describes the geometric environment (see Section 2.1.1).

Appendix C

Characterization of wideband, directional antenna, related to Chapter 4

In this appendix, the directional antenna, used in Chapter 4, is analyzed with respect to its time and frequency response. Three experiments were conducted demonstrating that the antenna's half-power mainlobe-width is approximately 90° (Experiment 1). Within this mainlobe-width, the antenna has a constant frequency response, resulting in negligible distortions to the arriving signal (Experiment 2). The antenna suffices to separate arriving multipath components in angle domain (Experiment 3).

C.1 Measurement setup

The measurements were performed using an Imsens Correlative Channel Sounder with a bandwidth of 3.5-10.5 GHz. As transmitting antenna we used a vertical polarized, dipole-type antenna [66] which radiates in an isotropic manner. As receiving antenna we employed the directional antenna of interest. The measurement output of the Channel Sounder was convolved with a raised-cosine signal with pulse duration $T_p = 2.4$ ns, a roll-off factor of 0.8 at the resonant frequency of 5.5 GHz.

C.2 Experiment 1: Beampattern

Figure C.1 illustrates the beampattern of the directional antenna demonstrating a half-power mainlobe-width of approximately 90° for signal parameters defined in Sec. C.1.

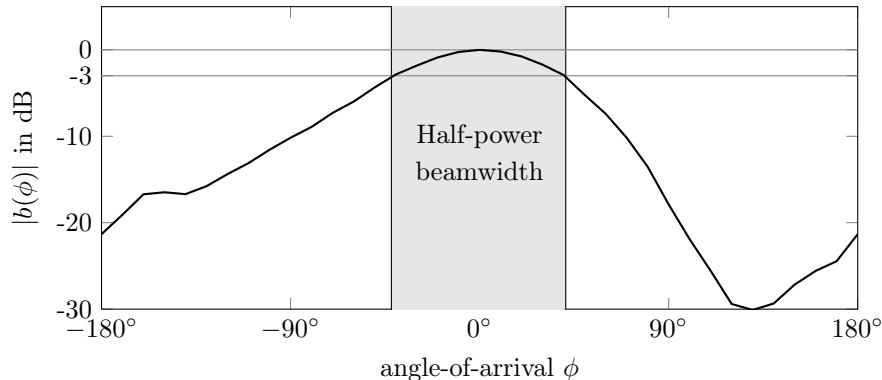


Figure C.1: Beampattern of the directional antenna as function of AOA.

C.3 Experiment 2: Distortions in time and frequency domain

In (4.1) the impact of the directive antenna is modeled as multiplicative factor. This assumption is valid if the antenna has a constant gain and phase for all frequencies within the passband, or in other words, there are no distortions of the arriving signals. In this experiment we illustrate distortions of the antenna for various angle-of-arrival (AOA) of $\{-180^\circ, -90^\circ, 0^\circ, 90^\circ\}$ (by rotating the directional antenna by these values). The distance between the transmitting and receiving antenna was 1.3 m. Figure C.2 exemplifies the received, baseband-equivalent signal and Figure C.3 illustrates the corresponding spectrum using the Fourier transform. We compare the received signal to the reference (raised-cosine signal) —. The comparison between the received signal and the reference shows only minor distortions for an AOA of 0° which is within the antenna's half-power mainlobe-width (see Fig. C.1). Once the signal arrives outside the antenna's mainlobe, distortions can be observed, especially at an AOA of -180° . However, the distortions for signals arriving within the mainlobe are negligible which motivates to describe the antenna's impact using a single scalar only.

C.4 Experiment 3: Diversity in delay and angle domains

In this section we investigate the potential of resolving multipath components in the delay and angle domains. We performed measurements using the directional antenna as receiver and the isotropic radiating antenna as transmitter, both located in the indoor scenario illustrated in Figures 2.1 and 2.2 at page 12. The transmitter moved at a 10×10 grid with spacing of 5 cm and center point $\mathbf{p}^{(i)}$ (see Figure 2.2), resulting in 100 measurements. The receiver remained at $\mathbf{p}^{(j)}$. For a comparison we repeated the experiment with isotropic radiating antennas at both transmitter and receiver.

We are particularly interested in the antenna's handling of the multipath

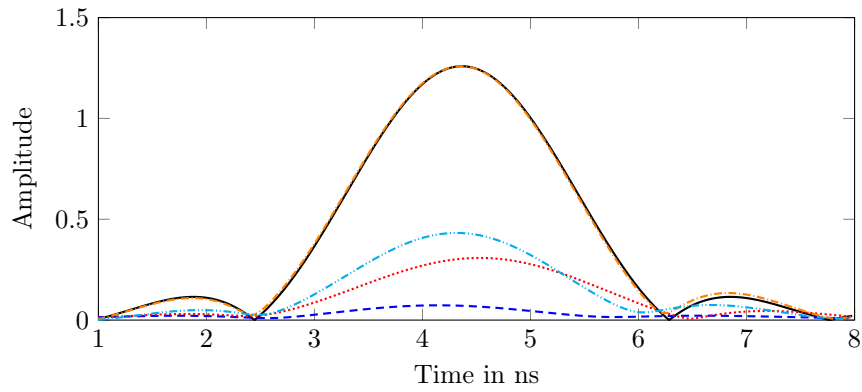


Figure C.2: Measured impulse response using various AOA of -180° $-$ -90° \cdots , 0° $-$ 90° $-$ in comparison to transmitted signal $-$.

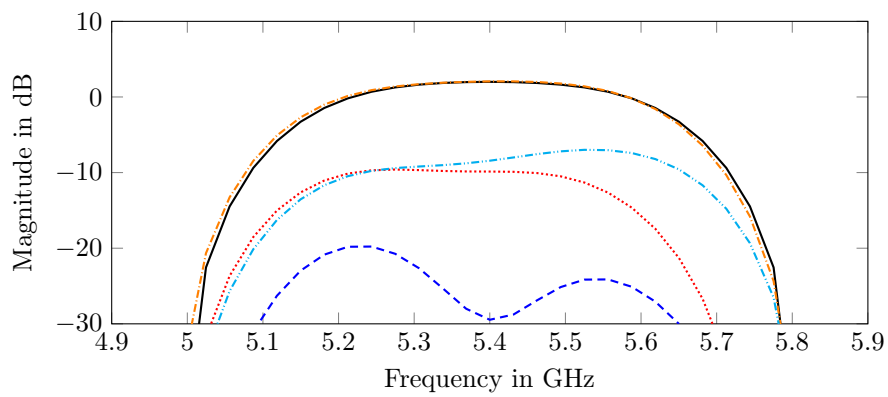


Figure C.3: Measured frequency response using various AOA of -180° $-$ -90° \cdots , 0° $-$ 90° $-$ in comparison to transmitted signal $-$.

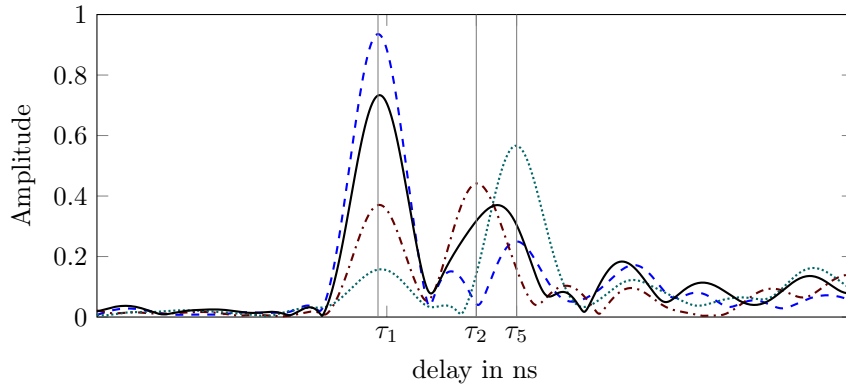


Figure C.4: Received signal \mathbf{r}_1 ---, \mathbf{r}_2 -.-.- and \mathbf{r}_5 for pointing the directional antenna to the LOS, 'plaster board east' and 'white board' in comparison to $\mathbf{r}_{\text{isotropic}}$ — obtained from an isotropic radiating antenna.

components. Considering flat walls as reflective material then the received signal at the proposed antenna can be decomposed into an LOS ($k = 1$) followed by two reflections, denoted as 'plaster board east' ($k = 2$) and 'white board' ($k = 5$). The expected delay of the LOS is $\tau_1 = 11.1$ ns and the delay of both reflections follow as $\tau_2 = 15.0$ ns and $\tau_5 = 16.6$ ns. The delays were obtained using a measuring tape where we neglected influences like diffraction or penetration. The arrival of both delays is below the pulse duration, i.e. $|\tau_5 - \tau_2| < T_p$, which will result in a path overlap.

To get insight in the ability of angular separation of the MPCs we steered the antenna in the direction of the arriving MPCs such that 0° in Fig. C.1 points along the MPC of interest resulting in the measurements \mathbf{r}_1 , \mathbf{r}_2 and \mathbf{r}_5 for the LOS ($k = 1$), 'plaster board east' ($k = 2$) and 'white board' ($k = 5$). The MPC AOA is fairly separated in the spatial domain ($\phi_2 = -94^\circ$ and $\phi_5 = 109^\circ$ for $\phi_1 = 0^\circ$). The measurement with isotropic radiating antennas is denoted as $\mathbf{r}_{\text{isotropic}}$.

Figure C.4 illustrates measurements at one transmitter position (in the grid). To start with the case if both antennas radiate in an isotropic manner —, we can observe that the LOS is well separated in the delay domain. Both reflections coincide and form a rise at approximately 15 ns. The shape of this superposition depends on the individual amplitudes and phases of both MPCs. Without additional information these parameters cannot be extracted for $k = 2$ and $k = 5$. This is different to the directional antenna which is able to decompose both MPCs. Steering the mainlobe to a specific MPC enables the suppression of the interfering MPCs which arrives at the same delay, especially at $k = 2$ and $k = 5$.

We complement the qualitative evaluation using the signal-to-interference-and-noise ratio (SINR) [141, 79]. The SINR is a solid metric to assess the reliability of specific MPCs. It quantifies the energy ratio of a useful specular MPC to interfering diffuse multipath. The interfering multipath causes small-scale fading of the amplitude of a specular MPC. A high SINR refers to little fading and hence the corresponding MPC will provide reliable position infor-

Table C.1: SINR in dB of MPC LOS, 'plaster board east' and 'white board' for steering the directional antenna's mainlobe along $k = 1, 2$ and 5.

arrival at	directional antenna steers to MPC			isotropic antenna [66]
	$k = 1$	$k = 2$	$k = 5$	
τ_1	24.6	20.2	13.2	26.4
τ_2	-3.8	12.7	10.1	2.8
τ_5	2.1	-0.8	16.7	6.1

mation [141, 90]. Table C.1 exemplifies the achieved SINR values for different steering of the antenna's mainlobe (first column) for the MPCs LOS ($k = 1$), 'plaster board east' ($k = 2$) and 'white board' ($k = 5$), each estimated from 100 measurements at different transmitter positions on the grid. The results for the antenna, radiating in an isotropic manner, are shown for comparison.

The SINR of the LOS attains the highest values justified by its isolation along the delay domain. The SINRs of 'plaster board east' and 'white board' are strongly dependent on the steering of the directional antenna demonstrating the ability to isolate a desired MPC in angular domain. This is in contrast to the antenna, radiating in an isotropic manner. The SINRs are reduced due to massive path overlap which cannot be resolved by the antenna.

Chapter 7

Bibliography

- [1] IsoLynx athlete tracking system. <http://www.finishlynx.com/isolynx/>. Accessed: 2018-08-01.
- [2] 3GPP. Study on channel model for frequencies from 0.5 to 100 GHz. Standard, 3GPP TR 38.901 version 14.1.1, August 2017.
- [3] Z. Abu-Shaban, X. Zhou, T. Abhayapala, G. Seco-Granados, and H. Wymeersch. Error bounds for uplink and downlink 3D localization in 5G millimeter wave systems. *IEEE Transactions on Wireless Communications*, 17(8):4939–4954, Aug 2018.
- [4] A. Alarifi, A. Al-Salman, M. Alsaleh, A. Alnafessah, S. Al-Hadhrani, M. A. Al-Ammar, and H. S. Al-Khalifa. Ultra wideband indoor positioning technologies: Analysis and recent advances. *Sensors*, 16(5):707, 2016.
- [5] J. B. Allen and D. A. Berkley. Image method for efficiently simulating small-room acoustics. *The Journal of the Acoustical Society of America*, 65(4):943–950, 1979.
- [6] P. Almers, E. Bonek, A. Burr, N. Czink, M. Debbah, V. Degli-Esposti, H. Hofstetter, P. Kyösti, D. Laurenson, G. Matz, et al. Survey of channel and radio propagation models for wireless MIMO systems. *EURASIP Journal on Wireless Communications and Networking*, 2007(1):019070, 2007.
- [7] M. S. Arulampalam, S. Maskell, N. Gordon, and T. Clapp. A tutorial on particle filters for online nonlinear/non-gaussian bayesian tracking. *IEEE Transactions on signal processing*, 50(2):174–188, 2002.
- [8] P. Bello. Characterization of randomly time-variant linear channels. *IEEE transactions on Communications Systems*, 11(4):360–393, 1963.
- [9] M. Bengtsson and B. Volcker. On the estimation of azimuth distributions and azimuth spectra. In *Vehicular Technology Conference, 2001. VTC 2001 Fall. IEEE VTS 54th*, volume 3, pages 1612–1615. IEEE, 2001.
- [10] P. Biswas and Y. Ye. Semidefinite programming for ad hoc wireless sensor network localization. In *Proceedings of the 3rd international symposium on Information processing in sensor networks*, pages 46–54. ACM, 2004.

- [11] J. Borenstein, H. R. Everett, L. Feng, and D. Wehe. Mobile robot positioning: Sensors and techniques. *Journal of robotic systems*, 14(4):231–249, 1997.
- [12] J. Borish. Extension of the image model to arbitrary polyhedra. *The Journal of the Acoustical Society of America*, 75(6), 1984.
- [13] R. M. Buehrer, H. Wymeersch, and R. M. Vaghefi. Collaborative sensor network localization: Algorithms and practical issues. *Proceedings of the IEEE*, 106(6):1089–1114, 2018.
- [14] J. Chen, D. Steinmetzer, J. Classen, E. Knightly, and M. Hollick. Pseudo lateration: Millimeter-wave localization using a single rf chain. In *2017 IEEE Wireless Communications and Networking Conference (WCNC)*, pages 1–6, March 2017.
- [15] C.-C. Chong and S. K. Yong. A generic statistical-based UWB channel model for high-rise apartments. *IEEE Transactions on Antennas and Propagation*, 53(8):2389–2399, 2005.
- [16] R. K. Cook, R. Waterhouse, R. Berendt, S. Edelman, and M. Thompson Jr. Measurement of correlation coefficients in reverberant sound fields. *The Journal of the Acoustical Society of America*, 27(6):1072–1077, 1955.
- [17] R.-M. Cramer, M. Z. Win, and R. A. Scholtz. Evaluation of the multipath characteristics of the impulse radio channel. In *Personal, Indoor and Mobile Radio Communications, 1998. The Ninth IEEE International Symposium on*, volume 2, pages 864–868. IEEE, 1998.
- [18] S. V. de Velde and H. Steendam. CUPID algorithm for cooperative indoor multipath-aided localization. In *2012 International Conference on Indoor Positioning and Indoor Navigation (IPIN)*, Nov 2012.
- [19] S. V. de Velde, H. Wymeersch, and H. Steendam. Comparison of message passing algorithms for cooperative localization under nlos conditions. In *2012 9th Workshop on Positioning, Navigation and Communication*, pages 1–6, March 2012.
- [20] V. Degli-Esposti and H. L. Bertoni. Evaluation of the role of diffuse scattering in urban microcellular propagation. In *Vehicular Technology Conference, 1999. VTC 1999-Fall. IEEE VTS 50th*, volume 3, pages 1392–1396. IEEE, 1999.
- [21] V. Degli-Esposti, F. Fuschini, E. M. Vitucci, and G. Falciasecca. Measurement and modelling of scattering from buildings. *IEEE Transactions on Antennas and Propagation*, 55(1):143–153, 2007.
- [22] V. Degli-Esposti, D. Guiducci, A. de’Marsi, P. Azzi, and F. Fuschini. An advanced field prediction model including diffuse scattering. *IEEE Transactions on Antennas and Propagation*, 52(7):1717–1728, 2004.
- [23] J. A. del Peral-Rosado, J. A. López-Salcedo, F. Zanier, and M. Crisci. Achievable localization accuracy of the positioning reference signal of 3gpp lte. In *Localization and GNSS (ICL-GNSS), 2012 International Conference on*, pages 1–6. IEEE, 2012.

- [24] Z. Ding, W. H. Chin, and K. K. Leung. Distributed beamforming and power allocation for cooperative networks. *IEEE Transactions on Wireless Communications*, 7(5):1817–1822, May 2008.
- [25] I. Dokmanic, R. Parhizkar, A. Walther, Y. M. Lu, and M. Vetterli. Acoustic echoes reveal room shape. *Proceedings of the National Academy of Sciences*, 2013.
- [26] J. Ehrenberg, T. Ewart, and R. Morris. Signal-processing techniques for resolving individual pulses in a multipath signal. *The Journal of the Acoustical Society of America*, 63(6):1861–1865, 1978.
- [27] B. Etzlinger, F. Meyer, F. Hlawatsch, A. Springer, and H. Wymeersch. Cooperative simultaneous localization and synchronization in mobile agent networks. *IEEE Trans. Signal Processing*, 65(14):3587–3602, 2017.
- [28] C. Falsi, D. Dardari, L. Mucchi, and M. Z. Win. Time of arrival estimation for UWB localizers in realistic environments. *EURASIP Journal on Advances in Signal Processing*, 2006(1), 2006.
- [29] M. Feder and E. Weinstein. Parameter estimation of superimposed signals using the EM algorithm. *IEEE Transactions on acoustics, speech, and signal processing*, 36(4):477–489, 1988.
- [30] B. H. Fleury. First-and second-order characterization of direction dispersion and space selectivity in the radio channel. *IEEE Transactions on Information Theory*, 46(6):2027–2044, 2000.
- [31] B. H. Fleury, M. Tschudin, R. Heddergott, D. Dahlhaus, and K. I. Pedersen. Channel parameter estimation in mobile radio environments using the sage algorithm. *IEEE Journal on Selected Areas in Communications*, 17(3):434–450, March 1999.
- [32] D. Fox, W. Burgard, H. Kruppa, and S. Thrun. A probabilistic approach to collaborative multi-robot localization. *Autonomous robots*, 8(3):325–344, 2000.
- [33] M. Froehle, E. Leitinger, P. Meissner, and K. Witrisal. Cooperative multipath-Assisted Indoor Navigation and Tracking (Co-MINT) Using UWB Signals. In *IEEE ICC Workshop on Advances in Network Localization and Navigation*, 2013.
- [34] F. Fuschini, S. Häfner, M. Zoli, R. Müller, E. M. Vitucci, D. Dupleich, M. Barbiroli, J. Luo, E. Schulz, V. Degli-Esposti, et al. Item level characterization of mm-wave indoor propagation. *EURASIP Journal on Wireless Communications and Networking*, 2016(1):4, 2016.
- [35] G. E. Garcia, L. S. Muppisetty, E. M. Schiller, and H. Wymeersch. On the trade-off between accuracy and delay in cooperative UWB localization: Performance bounds and scaling laws. *IEEE Transactions on Wireless Communications*, 13(8):4574–4585, Aug 2014.
- [36] C. Gentner, T. Jost, W. Wang, S. Zhang, A. Dammann, and U. C. Fiebig. Multipath assisted positioning with simultaneous localization and mapping. *IEEE Transactions on Wireless Communications*, (99), 2016.

- [37] S. Gezici, Z. Tian, G. B. Giannakis, H. Kobayashi, A. F. Molisch, H. V. Poor, and Z. Sahinoglu. Localization via ultra-wideband radios: a look at positioning aspects for future sensor networks. *IEEE signal processing magazine*, 22(4):70–84, 2005.
- [38] M. R. Gholami, H. Wymeersch, E. G. Ström, and M. Rydström. Wireless network positioning as a convex feasibility problem. *EURASIP Journal on Wireless Communications and Networking*, 2011(1):161, 2011.
- [39] A. S. Glassner. *An introduction to ray tracing*. Elsevier, 1989.
- [40] I. S. Gradshteyn and I. M. Ryzhik. *Table of integrals, series, and products*. Academic press, 1980.
- [41] S. Grebien, J. Kulmer, F. Galler, M. Goller, E. Leitinger, H. Arthaber, and K. Witrissal. Range Estimation and Performance Limits for UHF-RFID Backscatter Channels. *IEEE Journal of Radio Frequency Identification*, 1(1):39–50, March 2017.
- [42] B. Großwindhager, M. Rath, J. Kulmer, M. S. Bakr, C. A. Boano, K. Witrissal, and K. Römer. Dataset: single-anchor indoor localization with Decawave DW1000 and directional antennas. In *Proceedings of the First Workshop on Data Acquisition To Analysis*, pages 21–22. ACM, 2018.
- [43] B. Großwindhager, M. Rath, J. Kulmer, M. S. Bakr, C. A. Boano, K. Witrissal, and K. Römer. SALMA: UWB-based Single-Anchor Localization System using Multipath Assistance. In *Proceedings of the 16th ACM Conference on Embedded Networked Sensor Systems*, pages 132–144. ACM, 2018.
- [44] B. Großwindhager, M. Rath, J. Kulmer, S. J. Grebien, M. S. A. Bakr, C. A. Boano, K. Witrissal, and K. U. Römer. Demo Abstract: UWB-based Single-anchor Low-cost Indoor Localization System. In *15th ACM International Conference on Embedded Networked Sensor Systems (SensSys)*, 2017.
- [45] B. Großwindhager, M. Rath, J. Kulmer, S. Hinteregger, M. Bakr, C. A. Boano, K. Witrissal, and K. Römer. UWB-based single-anchor low-cost indoor localization system. In *Proceedings of the 15th ACM Conference on Embedded Network Sensor Systems*, page 34. ACM, 2017.
- [46] A. Guerra, F. Guidi, and D. Dardari. Single-anchor localization and orientation performance limits using massive arrays: Mimovs.beamforming. *IEEE Transactions on Wireless Communications*, 17(8):5241–5255, Aug 2018.
- [47] C. Gustafson. *60 GHz Wireless Propagation Channels: Characterization, Modeling and Evaluation*. PhD thesis, Lund University, 2014.
- [48] C. Gustafson, K. Haneda, S. Wyne, and F. Tufvesson. On mm-wave multipath clustering and channel modeling. *IEEE Transactions on Antennas and Propagation*, 62(3):1445–1455, 2014.

- [49] Y. Han, Y. Shen, X. Zhang, M. Z. Win, and H. Meng. Performance limits and geometric properties of array localization. *IEEE Transactions on Information Theory*, 62(2):1054–1075, Feb 2016.
- [50] K. Haneda. Channel models and beamforming at millimeter-wave frequency bands. *IEICE Transactions*, 98-B:755–772, 2015.
- [51] K. Haneda, J. Järveläinen, A. Karttunen, M. Kyrö, and J. Putkonen. A statistical spatio-temporal radio channel model for large indoor environments at 60 and 70 GHz. *IEEE Transactions on Antennas and Propagation*, 63(6):2694–2704, 2015.
- [52] S. Hinteregger, J. Kulmer, M. Goller, F. Galler, H. Arthaber, and K. Witrissal. UHF-RFID backscatter channel analysis for accurate wide-band ranging. In *2017 IEEE International Conference on RFID (RFID)*, pages 117–123, May 2017.
- [53] S. Hinteregger, E. Leitinger, P. Meissner, J. Kulmer, and K. Witrissal. Bandwidth dependence of the ranging error variance in dense multipath. In *2016 24th European Signal Processing Conference (EUSIPCO)*, pages 733–737, Aug 2016.
- [54] A. N. Hong, M. Rath, J. Kulmer, S. Grebien, K. N. Van, and K. Witrissal. Gaussian Process Modeling of UWB Multipath Components. In *2018 IEEE Seventh International Conference on Communications and Electronics (ICCE)*, pages 291–296, July 2018.
- [55] J. F. Hughes, A. Van Dam, J. D. Foley, M. McGuire, S. K. Feiner, D. F. Sklar, and K. Akeley. *Computer graphics: principles and practice*. Pearson Education, 2014.
- [56] S. Hur, S. Baek, B. Kim, Y. Chang, A. F. Molisch, T. S. Rappaport, K. Haneda, and J. Park. Proposal on millimeter-wave channel modeling for 5G cellular system. *IEEE Journal of Selected Topics in Signal Processing*, 10(3):454–469, 2016.
- [57] J. Järveläinen and K. Haneda. Sixty gigahertz indoor radio wave propagation prediction method based on full scattering model. *Radio Science*, 49(4):293–305, 2014.
- [58] M. A. Jensen and J. W. Wallace. A review of antennas and propagation for MIMO wireless communications. *IEEE Transactions on Antennas and Propagation*, 52(11):2810–2824, 2004.
- [59] D. B. Jourdan, D. Dardari, and M. Z. Win. Position error bound for UWB localization in dense cluttered environments. *IEEE Transactions on Aerospace and Electronic Systems*, 44(2):613–628, April 2008.
- [60] J. Järveläinen, K. Haneda, M. Kyrö, V.-M. Kolmonen, J.-i. Takada, and H. Hagiwara. 60 GHz radio wave propagation prediction in a hospital environment using an accurate room structural model. In *Antennas and Propagation Conference (LAPC), 2012 Loughborough*, pages 1–4. IEEE, 2012.

- [61] J. Karedal, S. Wyne, P. Almers, F. Tufvesson, and A. Molisch. A Measurement-Based Statistical Model for Industrial Ultra-Wideband Channels. *IEEE Transactions on Wireless Communications*, 2007.
- [62] S. Kay. *Fundamentals of Statistical Signal Processing: Estimation Theory*. Prentice Hall Signal Processing Series, 1993.
- [63] R. A. Kennedy and P. Sadeghi. *Hilbert Space Methods in Signal Processing*. Cambridge University Press, 2013.
- [64] J. Ko, Y.-J. Cho, S. Hur, T. Kim, J. Park, A. F. Molisch, K. Haneda, M. Peter, D.-J. Park, and D.-H. Cho. Millimeter-wave channel measurements and analysis for statistical spatial channel model in in-building and urban environments at 28 GHz. *IEEE Transactions on Wireless Communications*, 16(9):5853–5868, 2017.
- [65] M. Kok, J. D. Hol, and T. B. Schön. Indoor positioning using ultra-wideband and inertial measurements. *IEEE Transactions on Vehicular Technology*, 64(4):1293–1303, 2015.
- [66] C. Krall. *Signal processing for ultra wideband transceivers*. PhD thesis, Graz University of Technology, Austria, 2008.
- [67] J. Kulmer, S. Grebien, E. Leitinger, and K. Witrissal. Delay Estimation in Presence of Dense Multipath. *IEEE Wireless Communications Letters (in review)*, 2019.
- [68] J. Kulmer, S. Grebien, M. Rath, and K. Witrissal. On the unimportance of phase-coherent measurements for beampattern-assisted positioning. In *2018 IEEE Wireless Communications and Networking Conference (WCNC)*, pages 1–6, April 2018.
- [69] J. Kulmer, S. Hinteregger, B. Großwindhager, M. Rath, M. Bakr, E. Leitinger, and K. Witrissal. Using DecaWave UWB Transceivers for High-accuracy Multipath-assisted Indoor Positioning. In *IEEE ICC 2017 Workshop on Advances in Network Localization and Navigation (ANLN)*, 2017.
- [70] J. Kulmer, E. Leitinger, S. Grebien, and K. Witrissal. Anchorless cooperative tracking using multipath channel information. *IEEE Transactions on Wireless Communications*, 17(4):2262–2275, April 2018.
- [71] J. Kulmer, E. Leitinger, P. Meissner, S. Hinteregger, and K. Witrissal. Cooperative localization and tracking using multipath channel information. In *2016 International Conference on Localization and GNSS (ICL-GNSS)*, June 2016.
- [72] J. Kulmer, E. Leitinger, P. Meissner, and K. Witrissal. Cooperative Multipath-assisted Navigation and Tracking: A Low-Complexity Approach. In *1st EAI International Conference on Future access enablers of ubiquitous and intelligent infrastructures, 2015*. EAI, 2015.
- [73] J. Kulmer and P. Mowlae. Harmonic phase estimation in single-channel speech enhancement using von Mises distribution and prior SNR. In *2015 IEEE International Conference on Acoustics, Speech and Signal Processing (ICASSP)*, pages 5063–5067, April 2015.

- [74] J. Kulmer and P. Mowlae. Phase Estimation in Single Channel Speech Enhancement Using Phase Decomposition. *IEEE Signal Processing Letters*, 22(5):598–602, May 2015.
- [75] J. Kulmer, P. Mowlae, and M. K. Watanabe. A probabilistic approach for phase estimation in single-channel speech enhancement using von Mises phase priors. In *2014 IEEE International Workshop on Machine Learning for Signal Processing (MLSP)*, pages 1–6, Sep. 2014.
- [76] J. Kulmer, F. Wen, N. Garcia, H. Wymeersch, and K. Witrisal. Impact of rough surface scattering on stochastic multipath component models. In *Personal, Indoor, and Mobile Radio Communication (PIMRC), 2018 IEEE 29th Annual International Symposium on*. IEEE, 2018.
- [77] J. Kulmer and K. Witrisal. Revisiting the image source model: Towards geometry-based modeling of agent-to-agent channels. In *Workshop on Dependable Wireless Communications and Localization for the IoT*, September 2017.
- [78] M. Landmann. *Limitations of experimental channel characterisation*. PhD thesis, Technische Universität Ilmenau, 2008.
- [79] E. Leitinger, P. Meissner, C. Ruedisser, G. Dumphart, and K. Witrisal. Evaluation of position-related information in multipath components for indoor positioning. *IEEE Journal on Selected Areas in Communications*, 2015.
- [80] J. Levinson, J. Askeland, J. Becker, J. Dolson, D. Held, S. Kammell, J. Z. Kolter, D. Langer, O. Pink, V. Pratt, et al. Towards fully autonomous driving: Systems and algorithms. In *Intelligent Vehicles Symposium (IV), 2011 IEEE*, pages 163–168. IEEE, 2011.
- [81] J. Lien, U. J. Ferner, W. Srichavengsup, H. Wymeersch, and M. Z. Win. A comparison of parametric and sample-based message representation in cooperative localization. *International Journal of Navigation and Observation*, 2012, 2012.
- [82] A. Maltsev. Channel models for 60 GHz WLAN systems. Standard, IEEE Technical Report 802.11-09/0334r8, May 2008.
- [83] A. Maltsev, R. Maslennikov, A. Lomayev, A. Sevastyanov, and A. KHO-RYAEV. Statistical channel model for 60 GHz WLAN systems in conference room environment. *RADIOENGINEERING*, 20(2):409–422, June 2011.
- [84] F. Mani, F. Quitin, and C. Oestges. Accuracy of depolarization and delay spread predictions using advanced ray-based modeling in indoor scenarios. *EURASIP Journal on wireless communications and networking*, 2011(1):11, 2011.
- [85] F. Mani, F. Quitin, and C. Oestges. Directional spreads of dense multipath components in indoor environments: Experimental validation of a ray-tracing approach. *IEEE transactions on antennas and propagation*, 60(7):3389–3396, 2012.

- [86] M. Martinez-Ingles, D. P. Gaillot, J. Pascual-Garcia, J. Molina-Garcia-Pardo, M. Lienard, and J. Rodríguez. Deterministic and experimental indoor mmw channel modeling. *IEEE Antennas and Wireless Propagation Letters*, 13:1047–1050, 2014.
- [87] J. C. Maxwell. VIII. a dynamical theory of the electromagnetic field. *Philosophical transactions of the Royal Society of London*, 155:459–512, 1865.
- [88] P. Meissner. *Multipath-Assisted Indoor Positioning*. PhD thesis, Graz University of Technology, 2014.
- [89] P. Meissner, D. Arnitz, T. Gigl, and K. Witrisal. Analysis of an indoor UWB channel for multipath-aided localization. In *2011 IEEE International Conference on Ultra-Wideband (ICUWB)*, pages 565–569, Sept 2011.
- [90] P. Meissner, E. Leitinger, and K. Witrisal. UWB for robust indoor tracking: weighting of multipath components for efficient estimation. *IEEE Wireless Communications Letters*, 3(5):501–504, Oct. 2014.
- [91] P. Meissner and K. Witrisal. Analysis of Position-Related Information in Measured UWB Indoor Channels. In *6th European Conference on Antennas and Propagation (EuCAP)*, 2012.
- [92] R. Mendrzik, H. Wymeersch, G. Bauch, and Z. Abu-Shaban. Harnessing NLOS components for position and orientation estimation in 5G millimeter wave MIMO. *IEEE Transactions on Wireless Communications*, accepted for publication:1–1, 2018.
- [93] A. Molisch. *Wireless Communications*. Wiley, 2007.
- [94] P. Mowlae and J. Kulmer. Harmonic Phase Estimation in Single-Channel Speech Enhancement Using Phase Decomposition and SNR Information. *IEEE/ACM Transactions on Audio, Speech, and Language Processing*, 23(9):1521–1532, Sep. 2015.
- [95] P. Mowlae and J. Kulmer. Phase Estimation in Single-Channel Speech Enhancement: Limits-Potential. *IEEE/ACM Transactions on Audio, Speech, and Language Processing*, 23(8):1283–1294, Aug 2015.
- [96] P. Mowlae, J. Kulmer, J. Stahl, and F. Mayer. *Single Channel Phase-Aware Signal Processing in Speech Communication: Theory and Practice*. John Wiley & Sons, 2016.
- [97] P. Mowlae, J. Stahl, and J. Kulmer. Iterative joint MAP single-channel speech enhancement given non-uniform phase prior. *Speech Communication*, 86:85 – 96, 2017.
- [98] H. Naseri, M. Costa, and V. Koivunen. Multipath-aided cooperative network localization using convex optimization. In *2014 48th Asilomar Conference on Signals, Systems and Computers*, Nov 2014.

- [99] A. Nasipuri and K. Li. A directionality based location discovery scheme for wireless sensor networks. In *Proceedings of the 1st ACM international workshop on Wireless sensor networks and applications*, pages 105–111. ACM, 2002.
- [100] J. D. Parsons. *The mobile radio propagation channel*. Wiley, 2000.
- [101] J. Pascual-García, M. T. Martínez-Ingles, J. M. Molina-García-Pardo, J. V. Rodríguez, and V. Degli-Esposti. Experimental parameterization of a diffuse scattering model at 60 GHz. In *2015 IEEE-APS Topical Conference on Antennas and Propagation in Wireless Communications (APWC)*, pages 734–737, Sept 2015.
- [102] J. Pascual-García, J. M. Molina-García-Pardo, M. T. Martínez-Ingles, J. V. Rodríguez, and N. Saurín-Serrano. On the importance of diffuse scattering model parameterization in indoor wireless channels at mm-wave frequencies. *IEEE Access*, 4:688–701, 2016.
- [103] N. Patwari, J. N. Ash, S. Kyperountas, A. O. Hero, R. L. Moses, and N. S. Correal. Locating the nodes: cooperative localization in wireless sensor networks. *IEEE Signal Processing Magazine*, 22(4):54–69, July 2005.
- [104] J. Pearl. Fusion, propagation, and structuring in belief networks. *Artificial intelligence*, 29(3):241–288, 1986.
- [105] J. Poutanen, K. Haneda, J. Salmi, V.-M. Kolmonen, F. Tufvesson, and P. Vainikainen. Analysis of radio wave scattering processes for indoor MIMO channel models. In *Personal, Indoor and Mobile Radio Communications, 2009 IEEE 20th International Symposium on*, pages 102–106. IEEE, 2009.
- [106] G. G. Raleigh and J. M. Cioffi. Spatio-temporal coding for wireless communication. *IEEE Transactions on Communications*, 46(3):357–366, March 1998.
- [107] M. Rath, J. Kulmer, M. Bakr, G. B., and K. Witrissal. Indoor Localization and Communication Enhanced by Directional UWB Antennas. In *Workshop on Dependable Wireless Communications and Localization for the IoT*, September 2017.
- [108] M. Rath, J. Kulmer, M. S. Bakr, B. Großwindhager, and K. Witrissal. Multipath-assisted indoor positioning enabled by directional UWB sector antennas. In *18th IEEE International Workshop on Signal Processing Advances in Wireless Communications, SPAWC 2017, Sapporo, Japan, July 3-6, 2017*, pages 1–5, 2017.
- [109] K. Saito, J. ichi Takada, and M. Kim. Frequency characteristics of diffuse scattering in SHF band in indoor environments. *IEEE Transactions on Antennas and Propagation*, 65:4780–4789, 2017.
- [110] A. A. M. Saleh and R. Valenzuela. A statistical model for indoor multipath propagation. *IEEE Journal on Selected Areas in Communications*, 5(2):128–137, February 1987.

- [111] A. Savvides, H. Park, and M. B. Srivastava. The bits and flops of the n-hop multilateration primitive for node localization problems. In *Proceedings of the 1st ACM international workshop on Wireless sensor networks and applications*, pages 112–121. ACM, 2002.
- [112] T. Seidel, S.Y.; Rappaport. Site-specific propagation prediction for wireless in-building personal communication system design. *IEEE Transactions on Vehicular Technology*, 43, 1994.
- [113] A. Shahmansoori, G. E. Garcia, G. Destino, G. Seco-Granados, and H. Wymeersch. Position and orientation estimation through millimeter-wave MIMO in 5G systems. *IEEE Transactions on Wireless Communications*, 17(3):1822–1835, March 2018.
- [114] Y. Shen and M. Win. Fundamental limits of wideband localization; part I: a general framework. *IEEE Transactions on Information Theory*, 2010.
- [115] Y. Shen and M. Z. Win. Fundamental limits of wideband localization accuracy via fisher information. In *2007 IEEE Wireless Communications and Networking Conference*, pages 3046–3051, March 2007.
- [116] Y. Shen and M. Z. Win. On the use of multipath geometry for wideband cooperative localization. In *GLOBECOM 2009 - 2009 IEEE Global Telecommunications Conference*, pages 1–6, Nov 2009.
- [117] Y. Shen, H. Wymeersch, and M. Win. Fundamental limits of wideband localization - part II: cooperative networks. *IEEE Transactions on Information Theory*, 2010.
- [118] D. Shutin and B. H. Fleury. Sparse variational bayesian sage algorithm with application to the estimation of multipath wireless channels. *IEEE Transactions on Signal Processing*, 59(8):3609–3623, 2011.
- [119] D. Simon. *Optimal state estimation: Kalman, H infinity, and nonlinear approaches*. John Wiley & Sons, 2006.
- [120] P. F. M. Smulders. *Broadband wireless LANs: a feasibility study*. PhD thesis, Eindhoven University of Technology, 1995.
- [121] P. F. M. Smulders. Statistical characterization of 60-GHz indoor radio channels. *IEEE Transactions on Antennas and Propagation*, 57(10):2820–2829, Oct 2009.
- [122] Q. H. Spencer, B. D. Jeffs, M. A. Jensen, and A. L. Swindlehurst. Modeling the statistical time and angle of arrival characteristics of an indoor multipath channel. *IEEE Journal on Selected Areas in Communications*, 18(3):347–360, March 2000.
- [123] J. J. SPILKER. GPS signal structure and performance characteristics. *Navigation*, 25(2):121–146, 1978.
- [124] J. Stahl, P. Mowlae, and J. Kulmer. Phase-processing for voice activity detection: A statistical approach. In *2016 24th European Signal Processing Conference (EUSIPCO)*, pages 1202–1206, Aug 2016.

- [125] M. Steinbauer, A. F. Molisch, and E. Bonek. The double-directional radio channel. *IEEE Antennas and Propagation Magazine*, 43(4):51–63, Aug 2001.
- [126] P. Stoica, E. G. Larsson, and A. B. Gershman. The stochastic crb for array processing: A textbook derivation. *IEEE Signal Processing Letters*, 8(5):148–150, 2001.
- [127] S. Sukkariéh, E. M. Nebot, and H. F. Durrant-Whyte. A high integrity IMU/GPS navigation loop for autonomous land vehicle applications. *IEEE Transactions on Robotics and Automation*, 15(3):572–578, 1999.
- [128] P. D. Teal, T. D. Abhayapala, and R. A. Kennedy. Spatial correlation for general distributions of scatterers. *IEEE signal processing letters*, 9(10):305–308, 2002.
- [129] S. Thrun, W. Burgard, and D. Fox. *Probabilistic Robotics*. MIT, 2005.
- [130] L. Tian, V. Degli-Esposti, E. M. Vitucci, and X. Yin. Semi-deterministic radio channel modeling based on graph theory and ray-tracing. *IEEE Transactions on Antennas and Propagation*, 64(6):2475–2486, 2016.
- [131] L. Tian, V. Degli-Esposti, E. M. Vitucci, X. Yin, F. Mani, and S. X. Lu. Semi-deterministic modeling of diffuse scattering component based on propagation graph theory. In *Personal, Indoor, and Mobile Radio Communication (PIMRC), 2014 IEEE 25th Annual International Symposium on*, pages 155–160. IEEE, 2014.
- [132] S. Van de Velde, H. Wymeersch, P. Meissner, K. Witrisal, and H. Steendam. Cooperative multipath-aided indoor localization. In *2012 IEEE Wireless Communications and Networking Conference (WCNC)*. IEEE, 2012.
- [133] U. T. Virk, J.-F. Wagen, and K. Haneda. Simulating specular reflections for point cloud geometrical database of the environment. In *Antennas & Propagation Conference (LAPC), 2015 Loughborough*, pages 1–5. IEEE, 2015.
- [134] J.-F. Wagen, U. T. Virk, and K. Haneda. Measurements based specular reflection formulation for point cloud modelling. In *Antennas and Propagation (EuCAP), 2016 10th European Conference on*, pages 1–5. IEEE, 2016.
- [135] F. Wen, N. Garcia, J. Kulmer, K. Witrisal, and H. Wymersch. Tensor Decomposition Based BeamSpace ESPRIT for Millimeter Wave MIMO Channel Estimation. In *IEEE Global Telecommunications Conference (GLOBECOM)*, 2018.
- [136] M. Z. Win, A. Conti, S. Mazuelas, Y. Shen, W. M. Gifford, D. Dardari, and M. Chiani. Network localization and navigation via cooperation. *IEEE Communications Magazine*, 49(5), 2011.

- [137] M. Z. Win and R. A. Scholtz. Characterization of ultra-wide bandwidth wireless indoor channels: a communication-theoretic view. *IEEE Journal on Selected Areas in Communications*, 20(9):1613–1627, Dec 2002.
- [138] M. Z. Win, R. A. Scholtz, and M. A. Barnes. Ultra-wide bandwidth signal propagation for indoor wireless communications. In *Communications, 1997. ICC'97 Montreal, Towards the Knowledge Millennium. 1997 IEEE International Conference on*, volume 1, pages 56–60. IEEE, 1997.
- [139] K. Witrisal, S. Hinteregger, J. Kulmer, E. Leitinger, and P. Meissner. High-accuracy positioning for indoor applications: RFID, UWB, 5G, and beyond. In *2016 IEEE International Conference on RFID (RFID)*, pages 1–7, May 2016.
- [140] K. Witrisal and P. Meissner. Performance bounds for multipath-assisted indoor navigation and tracking (MINT). In *IEEE International Conference on Communications (ICC)*, 2012.
- [141] K. Witrisal, P. Meissner, E. Leitinger, Y. Shen, C. Gustafson, F. Tufveson, K. Haneda, D. Dardari, A. F. Molisch, A. Conti, and M. Z. Win. High-accuracy localization for assisted living. *IEEE Signal Processing Magazine*, 2016.
- [142] R. W. Wood. *Physical optics*. The Macmillan Company, 1905.
- [143] H. Wymeersch, J. Lien, and M. Z. Win. Cooperative localization in wireless networks. *Proceedings of the IEEE*, 2009.
- [144] J. Xiong and K. Jamieson. Arraytrack: a fine-grained indoor location system. Usenix, 2013.
- [145] S.-K. Yong. IEEE P802.15, TG3c channel modeling sub-committee final report. Standard, IEEE Technical Report 15-07-0584-01-003c, March 2007.

Part II

Included Papers

Impact of Rough Surface Scattering on Stochastic Multipath Component Models

Josef Kulmer, Fuxi Wen, Nil Garcia, Henk Wymeersch,
Klaus Witrisal

presented at Personal, Indoor, and Mobile Radio Communication (PIMRC), 2018
IEEE 29th Annual International Symposium on

Abstract

Multipath-assisted positioning makes use of specular multipath components (MPCs), whose parameters are geometrically related to the positions of the transceiver nodes. Diffuse scattering from rough surfaces affects the observed specular reflections in the angular and delay domains. Based on the effective roughness approach, the angular delay power spectrum can be calculated as a function of location parameters, which—in a next step—could be useful to accurately characterize the position-related information of MPCs. The calculated power spectra follow reported characteristics of stochastic multipath models, i.e. Gaussian shape in the angular domain and an exponential shape in the delay domain. The resulting angular and delay spreads are in an equivalent range to values reported in literature.

1 Introduction

Recent work in radio-based positioning exploits position-related information of multipath propagation [1, 2]. For this purpose, the multipath propagation is described using geometry-based stochastic channel models. These channel models characterize position-related information using geometrical relations between transmitter and receiver as well as the surrounding reflective objects. Geometrical optics then allows a proper modeling of specular multipath components (MPCs).

The stochastic channel component describes dense multipath, stemming from interaction with rough surfaces or small objects. In the context of localization, attempts are taken for a stochastic description of dense multipath, i.e. its characterization as zero-mean additive white Gaussian noise [2], or by placing additional scatter points [3] in the geometric setup. However, the characterization of the stochastic channel component will affect the potential outcome of localization algorithms. Proper stochastic models of dense multipath are required.

In literature, (geometry-based) stochastic channel models are parameterized by the standards IEEE 802.15.3c [4], IEEE 802.11ad [5] or 3GPP TR38.901 [6]. The purely stochastic channel models IEEE 802.15.3c [4] and 3GPP TR38.901 [6] rely on the Saleh Valenzuela propagation model which assumes that radio frequency power arrives in clusters [7]. The MPCs within a cluster are described statistically using *empirical* distributions. The parameters of the empirical distributions are fitted independently in the angular and delay domains. Both IEEE 802.15.3c and 3GPP TR38.901 have in common that the cluster parameters are not identified as function of a geometry based setup of transmitter / receiver.

The geometry-based stochastic channel model IEEE 802.11ad [5] aims at relating cluster parameters to a location specific setup. A main component within each cluster is identified, based on ray tracing, which can be classified as a specular component originating from a reflective surface, as illustrated in Figure 1. The main component is accompanied by dense multipath components stemming from a rough surface or small objects in its vicinity. These dense MPCs are unpredictable by ray tracing and parameterized in a stochastic manner using empirical distributions [5, 8], similarly to [4, 6].

The stochastic descriptions of dense multipath cover general scenarios, characterizing the average scattering behavior of reflective materials. Material specific scattering can be elaborated using additional information, i.e. the material's geometric dimension and dielectric parameters or both. In [9, 10] knowledge of material properties enable the prediction of the electromagnetic field. A stochastic description of rough surfaces is employed in [11–13] where the height of the rough surface is assumed to follow a zero-mean Gaussian density. Motivated by radiation theory, the authors in [14, 15] assume a certain scattering lobe for an incident ray, denoted as *effective roughness* approach. This approach is successfully employed in ray tracing [16–18], point cloud scattering [19–23] or propagation graph theory [24, 25]. It has been parameterized for several materials [23, 26]. Although effective roughness has shown to produce proper scattering models, its consequences for the channel's angular delay power spectrum (ADPS) are not discussed adequately.

In this paper we discuss the stochastic nature of dense multipath stemming

from rough surfaces, e.g. rough cast as well as balconies. Based on the effective roughness approach, we propose a scattering function which is symmetric with respect to transmitter and receiver positions. The scattering function enables the calculation of a joint angular delay power spectrum. The power spectrum describes dense multipath in a stochastic manner as a function of the geometric setup and the parameters of the rough surface. We analyze the power spectrum in the angular and delay domains and compare our results with measurements reported in literature.

The importance of this work for multipath-assisted positioning is as follows: Results in [27, 28] demonstrate that the range-information contributed by each MPC is related to the power ratio of the specular component and the dense multipath interfering with it, the so-called signal-to-interference-plus-noise ratio (SINR). The ADPS is needed to compute the SINR for some given probing signal with a defined bandwidth and directivity of the transceiver antennas. The SINR also agrees with the Ricean K-factor characterizing the amplitude fading of the MPC. The coherence distance of this fading is known to be related to the angular power spectrum. We therefore expect the results of this paper to be useful for the derivation of position error bounds and position estimation algorithms under realistic channel conditions.

2 Scattering function and implications on the angular delay power spectrum

We aim at relating the observed angular delay power spectrum to parameters based on the geometric setup using scattering models, which are originally introduced in [14, 15]. The scattering model treats a single planar, reflective surface which is illuminated by a transmitter. The impinging power at the reflective surface is attenuated and subsequently scattered in various directions. Parts of the reflected power arrive at the receiver with a certain ADPS. Figure 1 illustrates the setup for the azimuth domain.

2.1 Scattering model

Based on the Radar equation [29], the Lambertian [14] and directional scattering [15], we model the differential received power dP_r observed from differential surface element dA according to

$$dP_r = \frac{P_t \cos \theta_i}{d_i^2} \times \frac{dA \cos \theta_s}{d_s^2} \times \frac{(1 + \cos \psi)^{\alpha_R}}{k_{\alpha_R} 2^{\alpha_R}} \quad (1)$$

where we set both effective aperture area of the receiving antenna and the antenna gain of the transmitting antenna to 1. The first factor on the right-hand-side defines the intensity at surface area element dA with distance d_i (see Fig. 1) and transmitted power P_t . The angle θ_i between impinging ray and surface normal attenuates the intensity at dA according to the cosine law. Multiplication with area dA yields the reflected power which is scattered towards various directions. The second factor defines the recognized intensity by the receiver, scaled by the squared distance d_s^2 , where the cosine law is addressed by the angle θ_s between the scattered path and the surface normal.

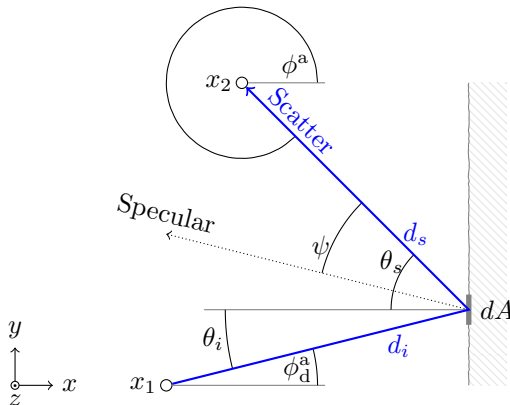


Figure 1: Illustration of a reflective surface, located along the yz plane, and the path from transceiver 1, located at x_1 , to transceiver 2 at x_2 via surface area element dA .

The third factor determines the impact from directive scattering, motivated by [15], where we assume that the majority of the impinging power is scattered along the direction of the specular one. Deviating scatter angles, denoted by angle ψ , lower the received power. The parameter α_R controls the level of surface roughness. At walls with only small levels of roughness (in comparison to the wavelength of mmWaves, e.g. window glass) the scattering lobe is narrow, controlled by high levels of α_R . Increasing levels of roughness yield spreading in various directions, described by small levels of α_R . The remaining k_{α_R} is a scaling factor such that the scattered power is independent on α_R and results by integration of factor 3 over ψ . The scattering attenuation factor, modeled in [14, 15], is neglected in (1) as it has no impact on the evaluated angular and delay spreads.

The presented scattering model is strongly related to the Lambertian [14] and the single-lobe directional scattering model [15]. It enables a smooth transition from Lambertian scattering (setting $\alpha_R = 0$) to directional scattering ($\alpha_R \rightarrow \infty$). Note that the single-lobe scattering model [15] treats the impinging wave using the cosine law, and the scattered wave by a directional scattering lobe. Hence, in a non-symmetric setup of transmitter / receiver position, the outcome will differ if the transceivers change their roles. The scattering model presented in (1) preserves symmetry where we assume that both impinging and scattered waves are attenuated by the cosine law plus an additional scattering lobe.

Figure 2 illustrates the scattering power for various directions θ_s of the Lambertian — [14], directional - - - [15, single-lobe directional model] and the proposed scattering model — for an impinging angle $\theta_i = 30^\circ$ with $\alpha_R = 2$. We can observe that at Lambertian scattering the impinging power is scattered according to the cosine law. The directional as well as the proposed scattering model radiate its power along the specular component.

The scattering functions describe the received differential power from a specific differential area element dA . In the following we rephrase (1) in order to calculate the resulting ADPS as *observed by the receiver*.

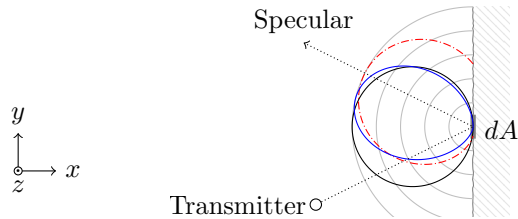


Figure 2: Polar plot of scattered power at dA for an impinging MPC with $\theta_i = 30^\circ$ illustrating the Lambertian —, directional - - - and proposed model —. The dotted arrow is the specular component.

2.2 Derivation of angular delay power spectrum

Having the differential scattering power dP_r from differential area dA we aim at calculating the joint ADPS. The power spectrum describes the spreading of the received power along the angular and delay domains. Integration of the ADPS over τ results in the angular power spectrum (APS). Equivalently, the delay power spectrum (DPS) is established by integration of the ADPS over both azimuth and elevation angles. Note, (1) is symmetric with respect to the position of transmitter and receiver and thus, the observed DPS remains equal if the transceivers exchange their role of transmitting and receiving. Still, in general the APS is different, i.e. the APS at position x_2 for a transmitting node at position x_1 is different to the APS at x_1 for a transmitting node at x_2 .

2.2.1 Joint angular delay power spectrum

The scattering model in (1) describes the received power from a desired area. In order to calculate the joint ADPS, we express the desired area as a function of azimuth ϕ^a , elevation ϕ^e and delay τ . Assuming the reflective surface is aligned with the yz -plane, we can substitute the differential area $dA = d\Omega d_s^2 / (\cos \phi^a \cos \phi^e)$ by a solid angle $d\Omega$ [30] which can be subsequently described as $d\Omega = \cos \phi^e d\phi^a d\phi^e$ of azimuth ϕ^a and elevation angle ϕ^e , resulting in $dA = d_s^2 / (\cos \phi^a) d\phi^a d\phi^e$. Substituting dA in (1) enables to calculate the total received power $P_r = \int dP_r$ and the ratio P_r/P_t ,

$$\frac{P_r}{P_t} = \iiint p(\phi^a, \phi^e, \tau) d\phi^a d\phi^e d\tau$$

where $p(\phi^a, \phi^e, \tau)$ denotes the spreading of the received power in the angular and delay domains, defined as joint ADPS

$$p(\phi^a, \phi^e, \tau) \triangleq \frac{\cos \theta_i \cos \theta_s (1 + \cos \psi)^{\alpha_R}}{k_{\alpha_R} d_i^2 \cos \phi^a} \delta(\tau - f_\tau(\phi^a, \phi^e)). \quad (2)$$

The Dirac delta $\delta(\cdot)$ relates a pair of angles (ϕ^a, ϕ^e) to its corresponding delay τ where the function $\tau = f_\tau(\phi^a, \phi^e)$ is calculated using trigonometric identities. The location dependent parameters $\{\theta_i, \theta_s, d_i, \psi\}$ in (2) are also derived from (ϕ^a, ϕ^e) .

2.2.2 Angular power spectrum

The azimuth APS $p(\phi^a)$ is calculated by integration of (2) along is elevation and delay domains, according to

$$p(\phi^a) = \iint p(\phi^a, \phi^e, \tau) d\phi^e d\tau. \quad (3)$$

Analytic solutions to (3) are challenging due to nonlinear relations between angles and geometric setup between both transceivers. We propose a numeric approximation by discretizing the angles. Therefore, we generate N_ϕ uniformly distributed angle pairs $\{(\phi_i^a, \phi_i^e)\}_{i=1}^{N_\phi}$ where each pair (ϕ_i^a, ϕ_i^e) has a constant solid angle $\Delta\Omega = 4\pi/N_\phi$. Then, (3) can be written as

$$p(\phi^a) \approx \sum_{\phi^e \in \mathcal{P}_{\phi^a}} p(\phi^a, \phi^e, \tau) \frac{\Delta\Omega}{\Delta\phi^a} \quad (4)$$

where $\mathcal{P}_{\phi^a} = \{\phi_i^e : 0 \leq |\bar{\phi}^a - \phi_i^a| < \Delta\phi^a/2\}$ contains the elevation angles $\{\phi_i^e\}$ associated to the azimuth angle of interest $\bar{\phi}^a$, with desired resolution $\Delta\phi^a$. The summation along the elevation angles for a desired azimuth angle accounts for both integrals in (3) where we apply the Dirac delta's sifting property.

The elevation APS follows equivalently to (3) by integration along the azimuth domain.

2.2.3 Delay power spectrum

Finally we calculate the DPS by integration of the joint ADPS (2) along both angles, according to

$$p(\tau) = \iint p(\phi^a, \phi^e, \tau) d\phi^a d\phi^e. \quad (5)$$

Here, the DPS for a desired delay $\bar{\tau}$ results by integration along angles (ϕ^a, ϕ^e) which fulfill $\bar{\tau} = f_\tau(\phi^a, \phi^e)$. Thus, we can approximate (5) as sum along angle pairs $(\phi^a, \phi^e) \in \mathcal{T}_{\bar{\tau}}$ with $\mathcal{T}_{\bar{\tau}} = \{(\phi_i^a, \phi_i^e) : 0 \leq |\bar{\tau} - f_\tau(\phi_i^a, \phi_i^e)| < \Delta\tau/2\}$, whose corresponding delay τ is equal to the desired delay $\bar{\tau}$, up to numeric resolution $\Delta\tau$, according to

$$p(\tau) = \sum_{(\phi^a, \phi^e) \in \mathcal{T}_{\bar{\tau}}} p(\phi^a, \phi^e) \frac{\Delta\Omega}{\Delta\tau}. \quad (6)$$

In the following we compare the proposed scattering model and the presented ones in [14, 15] in terms of resulting APS and DPS.

2.3 Analysis and comparison of APS

Application of the scattering models enables the calculation of a theoretic APS to be expected at the transceiver positions. In this section we aim at comparing the proposed scattering model with [14] (denoted as Lambertian) and [15] (denoted as directional scattering). We evaluate the azimuth's APS for two transceivers and three different levels of roughness, determined by $\alpha_R \in \{0, 2, 10\}$. We consider two scenarios of positions of transceivers. Scenario (a) examines a symmetric setup where the surface is located along the yz plane at

$x = 0$, transceiver x_1 at (x, y, z) coordinates of $x_1 = (-10, -5, 0)$ and transceiver x_2 at $x_2 = (-10, 5, 0)$, as illustrated in Fig. 3. Scenario (b) shows a non-symmetric setup where transceiver x_2 moves to position $x_2 = (-5, 5, 0)$ and the transceiver x_1 persists at $x_1 = (-10, -5, 0)$ (Fig. 4). In the numerical approximations we set $N_\phi = 10^6$, $\Delta\phi^a = \pi/100$ rad and $\Delta\tau = 1$ ns.

2.3.1 Symmetric scenario

Starting with the symmetric scenario (a), Figure 3 illustrates the APS of the proposed scattering model for various values of $\alpha_R = 0$ —, $\alpha_R = 2$ — and $\alpha_R = 10$ —. We compare the outcome to the Lambertian — (mathematically identical to the proposed one with $\alpha_R = 0$), and to the directional model using $\alpha_R = 2$ - - - and $\alpha_R = 10$ - - -. The calculation shows the azimuth plane where we set the elevation to $\phi^e = 0$. The direction of the specular component between both transceivers is shown as dotted, gray line. The APS of x_1 (x_2) are calculated assuming x_2 (x_1) radiates in an isotropic manner.

We can observe that the patterns are symmetric whether x_1 transmits to x_2 or opposite. A comparison between directional and proposed scattering model shows strong similarities. Note that, the directional model spreads its peak power along the specular component (as illustrated in Figure 2) but the peak power at the receiving node (x_1 or x_2) is not received from the direction of the specular component. This is a crucial finding and can be explained by the fact that the level of received scattering power from area dA depends on the illuminated intensity at dA . The intensity is largest in the vicinity of the transmitter with the consequence of increased scatter power from surface areas, close to the transmitter. At $\alpha_R = 0$ the peak power is received from a scattering point with shortest distance between transmitter and reflective surface. An increasing level of α_R narrows the angular spread. The angle's peak power moves towards the angle of the specular component.

2.3.2 Non-symmetric scenario

We proceed by evaluating the APS for the non-symmetric scenario (b) where x_2 is aligned closer to the reflective surface than x_1 yielding non-symmetric APS as well. This can be argued since x_2 is aligned close to the reflective surface while the distance between x_1 and surface area elements in the vicinity of x_1 is large. Thus, these surface area elements are illuminated by a similar power which is scattered to x_2 . The receiver observes arriving power from a wide range of directions which results in an increased angular spread.

Equivalent to the observations made at the symmetric scenario, the angular spread of the Lambertian scattering is largest. The angle's peak power moves towards the specular component's angle for rising α_R . Furthermore, the angular spread is reduced for increased α_R .

2.4 Analysis and comparison of the DPS

Finally, in Figure 5 we illustrate the delay power spectra for the symmetric and non-symmetric scenarios. In general, the magnitude scaling changes drastically showing a strong sensitivity to the delay domain. We can observe that the peak

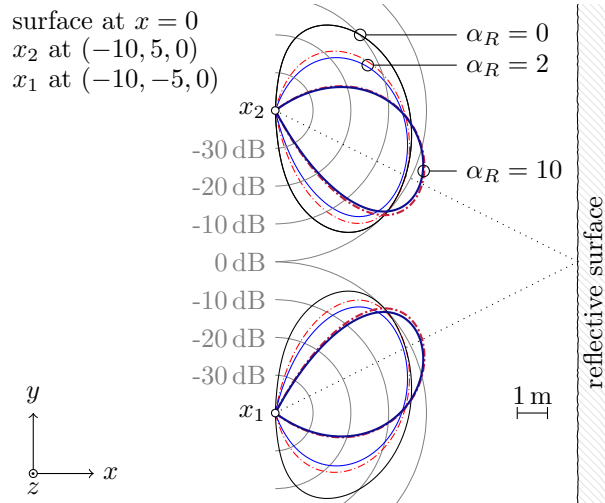


Figure 3: Polar plot of APS of the symmetric scenario using the proposed scattering model with $\alpha_R = 0$ —, $\alpha_R = 2$ — and $\alpha_R = 10$ — in comparison to Lambertian — (equivalent to the proposed one with $\alpha_R = 0$) and directional one, using $\alpha_R = 2$ - - - and $\alpha_R = 10$ - - -.

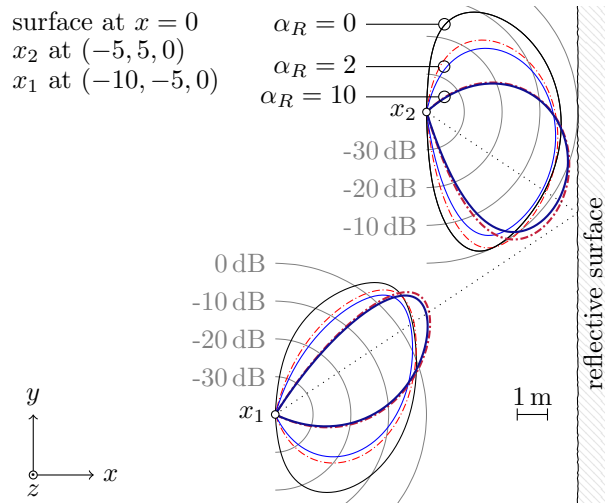


Figure 4: Equivalent to Figure 3 with x_2 at $(-5, 5, 0)$.

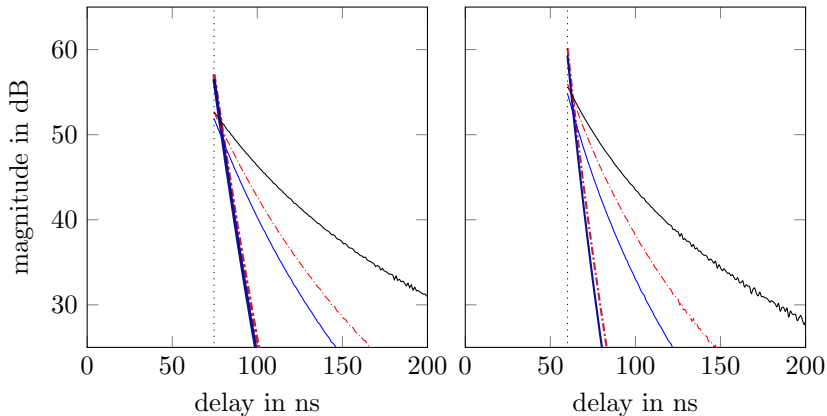


Figure 5: Delay power spectrum of scenario (a) (left) and (b) (right) using $\alpha_R = 0$ —, $\alpha_R = 2$ — and $\alpha_R = 10$ — in comparison to Lambertian —, and the directional model using $\alpha_R = 2$ - - - and $\alpha_R = 10$ - - -. The specular component's delay is shown as dotted, vertical line.

power arrives simultaneously with the specular component's delay (black dotted). At increasing delays the power is attenuated. The lowest power decay rate is achieved by the Lambertian scattering. Rising α_R (equivalent to reduced roughness) increases the power decay rate. This can be argued since the directional models reward dense multipaths stemming from the direction of the specular components.

We can conclude that the proposed scattering function is identical to the Lambertian model by setting $\alpha_R = 0$. At increased α_R it converges to the outcome of the directional scattering model, with the advantage of preserving a symmetric channel between both transceivers. Hence, in the following we proceed with the proposed scattering function and compare its shape with empirical distributions from literature.

3 Relation of scattering model to empirical distributions

The analysis and comparison of the proposed scattering model showed its potential to model both Lambertian and directional scattering. In this section we aim at relating the scattering model to empirical distributions, identified in literature and compare the calculated angular and delay spread to reported ones.

3.1 Empirical distribution of MPCs in literature

Empirical distributions of MPCs are provided by standardized channel models IEEE 802.15.3c [4], IEEE 802.11.ad [5] or 3GPP TR38.901 [6]. In these channel models, estimated MPCs are associated to clusters in angular delay domain using visual inspection or machine supported clustering [31]. Considering a single cluster, in angular domain, a (wrapped) Gaussian distribution [4, 6] or

Table 1: Identified ranges of parameters for the reported scenarios of IEEE 802.15.3c, IEEE 802.11ad, 3GPP TR38.901 and [32] where (L), (G), (WG) denote Laplacian, Gaussian and wrapped Gaussian distribution.

	IEEE 802.15.3c	IEEE 802.11ad	3GPP TR38.901	[32]
σ_{ϕ^a} in $^\circ$	10	5-10 (G)	2-22 (WG)	17-40 (L)
σ_{ϕ^e} in $^\circ$	-	5-10 (G)	3-9 (L)	11-17 (L)
γ in ns	7	4.5-8.7	5-11	4.6-4.8

Laplacian [4,32] with standard deviation σ_{ϕ^a} was identified for the azimuth, and a Laplacian with standard deviation σ_{ϕ^e} for the elevation angle. The mean value is calculated as average angle of the MPCs within a cluster. In delay domain, the MPCs follow an exponential decay [4,6] with rate γ , related to the cluster's first path. It is interesting to note that [5] differs to [4,6] by concatenating a rising and falling (pre and post cursor) exponential decay. Furthermore, in [5] a cluster-specific K-factor is defined as power ratio between a main component and the residual cluster paths. Hence, a comparison between the standardized channel models is not straight forward due to different angular distributions ((wrapped) Gaussian or Laplacian) and delay distributions (single decay and double decay).

Table 1 presents the identified parameters from [4], [5, post cursor decay rate], [6,32]. We can observe a wide range of the azimuth standard deviation σ_{ϕ^a} but narrow elevation σ_{ϕ^e} . The decay rates are in a similar range in low ns ranges of 4 to 11 ns.

3.2 Evaluation in angular domain

In angular domain, (wrapped) Gaussian or Laplacian or both distributions have been proposed to model the APS. Both Gaussian and Laplacian distribution are parameterized by a mean angle $\bar{\phi}$ and standard deviation σ_ϕ . In literature, $\bar{\phi}$ and σ_ϕ are calculated as first and central second moments (equivalent to the definitions of the mean and rms angular spreads). Figure 6 illustrates the APS at x_1 along the azimuth angle for scenario (b) for two levels of $\alpha_R = 0$ — and $\alpha_R = 10$ —. The Gaussian distribution (dashed) is shown for comparison. We can observe that at $\alpha_R = 0$ the Gaussian approximation is not able to follow the derived APS. At increasing $\alpha_R = 10$ the power is centralized along its mean value, thus, a Gaussian approximation is more appropriate.

We have repeated the calculation of APS for both scenarios. Table 2 reports the identified rms angular spreads as well as the gap $\epsilon_{\bar{\phi}}$ between the angles of the specular component and the mean angle from the APS. In case of the symmetric scenario (a) the APS as seen from transceiver x_1 is identical to the APS as seen from x_2 . At the non-symmetric scenario (b) x_2 is located closer to the reflective surface, yielding increased angular spread in comparison to x_1 . Decreasing levels of roughness (equivalent to narrowing the scattering lobe) from $\alpha_R = 0$ to $\alpha_R = 10$ lower the angular spread from approximately 31° to 12° in average. The angle gap $\epsilon_{\bar{\phi}}$ is largest at high levels of roughness and gets reduced with increasing α_R . Moreover, in non-symmetric setup (b) $\epsilon_{\bar{\phi}}$ is increased if the transceiver is located close to the reflective surface.

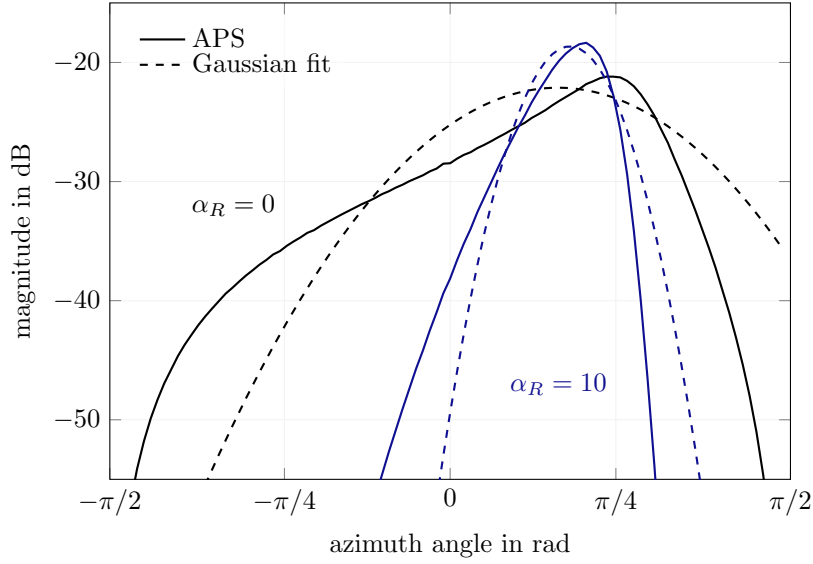


Figure 6: Illustration of APS at x_1 using scenario (b) with high levels $\alpha_R = 0$ (black) and low levels of roughness $\alpha_R = 10$ (blue).

Table 2: Identified azimuth angular spread for various levels of roughness α_R for both scenarios (a) and (b).

	α_R	0	2	4	6	8	10
(a)	$\sigma_{\phi^a}, \sigma_{\phi_d^a}$ in $^\circ$	32.2	21.6	17.2	14.7	13.1	11.9
	$\epsilon_{\bar{\phi}}$ in $^\circ$	9.4	4.7	3.0	2.1	1.5	1.2
(b)	$\sigma_{\phi_d^a}$ in $^\circ$ at x_1	23.8	15.7	12.4	10.5	9.3	8.4
	$\epsilon_{\bar{\phi}}$ in $^\circ$ at x_1	5.2	3.5	2.9	2.5	2.2	2.0
(b)	σ_{ϕ^a} in $^\circ$ at x_2	36.8	26.3	21.5	18.6	16.7	15.3
	$\epsilon_{\bar{\phi}}$ in $^\circ$ at x_2	10.4	4.9	2.9	1.8	1.2	0.8

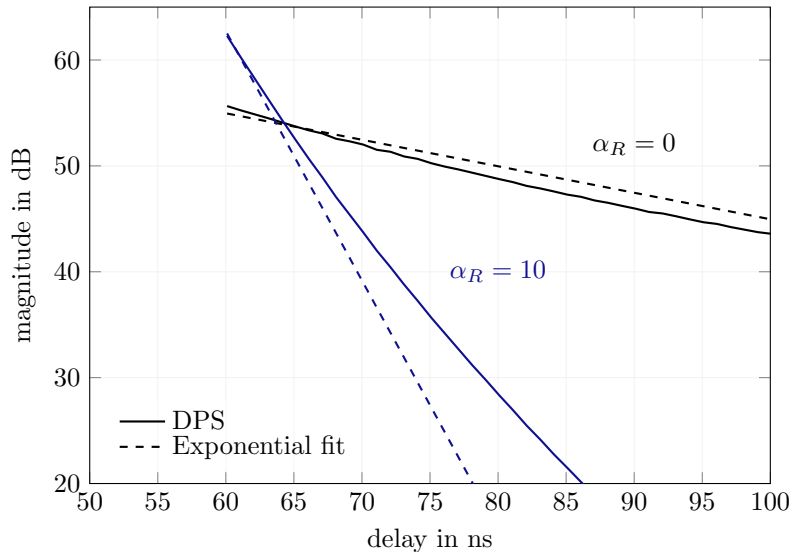


Figure 7: Illustration of DPS using scenario (b) with high levels $\alpha_R = 0$ (black) and low levels of roughness $\alpha_R = 10$ (blue).

Table 3: Identified decay rates of the DPS for various levels of roughness α_R for both scenarios (a) and (b).

	α_R	0	2	4	6	8	10
Scen. (a)	γ in ns	14.3	6.1	3.9	2.9	2.3	1.9
Scen. (b)	γ in ns	17.8	7.6	4.8	3.5	2.8	2.3

3.3 Evaluation in delay domain

In delay domain, IEEE 802.15.3c and 3GPP TR38.901 have identified an exponential decay, parameterized by decay rate γ . We calculate the decay rate as first moment of the DPS with respect to the excess array. Figure 7 illustrates the DPS of the non-symmetric scenario using the proposed scattering model. The fitted exponential decay function (dashed) is shown in comparison. We have evaluated γ for both scenarios as function of α_R , as shown in Table 3. At high levels of roughness ($\alpha_R = 0$) the arriving power is spread in the delay domain, resulting in an average decay rate of $\gamma \approx 16$ ns (across both scenarios). Rising levels of α_R yield decreasing $\gamma \approx 2.2$ ns.

3.4 Discussion

The calculated angular power spectrum show a bias between the specular component's angle and the mean value of the dense multipath power. Furthermore, the APS are not symmetric along their mean value. These findings encourage the consideration of dense multipath statistics for an unbiased estimation of the specular component's angle.

A comparison between the reported parameters from Table 1 and the calculated ones in Table 2 and 3 show strong accordance and both angular and delay parameters are in a similar range. Still, the parameters are calculated for an

infinite dimension of a planar surface. Limiting dimensions yield narrower APS as well as decreased decay rates. On the other hand, strong surface variations (like balconies or other heavily structured surfaces) may increase the decay rates which limits the explanatory power of this comparison. Furthermore, the results differ as function of the considered scenario, showing a strong dependency on the location setup. However, based on our findings, we support the average value of $\alpha_R = 4$, as proposed in [15].

The calculated shape of the DPS fits well to the reported exponential decay from IEEE 802.15.3c and 3GPP TR38.901. The double exponential decay, identified in IEEE 802.11ad, cannot be verified. This may be explained since the scattering model does not explicitly incorporate variations in the surface's heights or objects in the vicinity of the surface. Furthermore, the cluster's main component, identified by IEEE 802.11ad, is not predicted by the scattering model. It is worth noting that ray tracing applications consider an additional specular component [16] which may act as cluster's main MPC.

Our calculations consider isotropic radiating antennas while at mmWaves, reported cluster parameters are often based on measurements with highly directive horn antennas. A narrow antenna's radiation pattern will affect the angular cluster spread which lowers the explanatory power from the comparison with isotropic antennas. However, our literature study did not show a clear relation between radiation pattern and angular spread, i.e. narrower radiation pattern does not necessarily result in narrower angular spreads [33]. These findings are supported by preliminary evaluations of (2) where we considered the antenna's directivity in the angular domain. The resulting angular spread value can get raised or reduced, depending on the combination of geometric setup and antenna directivity.

4 Conclusion

We have proposed a symmetric scattering function, capable of modeling both Lambertian and directional scattering. The scattering function enables to derive the APS and DPS as functions of the geometric setup. The APS shows that the majority of arriving dense multipath power deviates from the direction of the specular component. Both APS and DPS are in accordance to reported empirical distributions and fitted parameters. In context of localization, dense multipath from rough surfaces adds non-zero-mean noise to specular components resulting in biased angular and delay estimates if not corrected for.

5 Acknowledgment

We are grateful to Dr. V. Degli-Esposti for the constructive discussions throughout this research.

References

- [1] K. Witrissal, P. Meissner, E. Leitinger, Y. Shen, C. Gustafson, F. Tufvesson, K. Haneda, D. Dardari, A. F. Molisch, A. Conti, and M. Z. Win, "High-accuracy localization for assisted living," *IEEE Signal Process. Mag.*, 2016.

- [2] A. Shahmansoori, G. E. Garcia, G. Destino, G. Seco-Granados, and H. Wymeersch, "Position and orientation estimation through millimeter-wave MIMO in 5G systems," *IEEE Trans. Wireless Commun.*, vol. 17, no. 3, pp. 1822–1835, 2018.
- [3] L. Liu, C. Oestges, J. Poutanen, K. Haneda, P. Vainikainen, F. Quitin, F. Tufvesson, and P. D. Doncker, "The COST 2100 MIMO channel model," *IEEE Wireless Commun.*, vol. 19, no. 6, pp. 92–99, December 2012.
- [4] S.-K. Yong, IEEE Technical Report 15-07-0584-01-003c Std., March 2007.
- [5] A. Maltsev, *Channel Models for 60 GHz WLAN Systems*, IEEE Technical Report 802.11-09/0334r8 Std., May 2008.
- [6] *Study on channel model for frequencies from 0.5 to 100 GHz*, 3GPP TR 38.901 version 14.1.1 Std., August 2017.
- [7] A. M. Saleh and R. A. Valenzuela, "A statistical model for indoor multipath propagation," *IEEE J. Sel. Areas Commun.*, vol. 5, no. 2, pp. 128–137, Feb. 1987.
- [8] A. Maltsev, R. Maslennikov, A. Lomayev, A. Sevastyanov, and A. Khoryaev, "Statistical channel model for 60 GHz WLAN systems in conference room environment," *RADIOENGINEERING*, vol. 20, no. 2, pp. 409–422, June 2011.
- [9] P. Beckmann and A. Spizzichino, "The scattering of electromagnetic waves from rough surfaces," *Norwood, MA, Artech House, Inc., 1987, 511 p.*, 1987.
- [10] K. F. Warnick and W. C. Chew, "Numerical simulation methods for rough surface scattering," *Waves in random media*, vol. 11, no. 1, pp. R1–R30, 2001.
- [11] W. S. Ament, "Toward a theory of reflection by a rough surface," *Proceedings of the IRE*, vol. 41, no. 1, pp. 142–146, Jan 1953.
- [12] O. Landron, M. J. Feuerstein, and T. S. Rappaport, "A comparison of theoretical and empirical reflection coefficients for typical exterior wall surfaces in a mobile radio environment," *IEEE Trans. Antennas Propag.*, vol. 44, no. 3, pp. 341–351, Mar 1996.
- [13] H. Budiarto, K. Horihata, K. Haneda, and J. Takada, "Superresolution measurement of non-specular wave scattering from building surface roughness," in *IEEE 58th Vehicular Technology Conference*. IEEE, 2003, pp. 11–15.
- [14] V. Degli-Esposti and H. L. Bertoni, "Evaluation of the role of diffuse scattering in urban microcellular propagation," in *IEEE 50th Vehicular Technology Conference*, vol. 3. IEEE, 1999, pp. 1392–1396.
- [15] V. Degli-Esposti, F. Fuschini, E. M. Vitucci, and G. Falciasecca, "Measurement and modelling of scattering from buildings," *IEEE Trans. Antennas Propag.*, vol. 55, no. 1, pp. 143–153, 2007.

- [16] V. Degli-Esposti, D. Guiducci, A. de'Marsi, P. Azzi, and F. Fuschini, "An advanced field prediction model including diffuse scattering," *IEEE Trans. Antennas Propag.*, vol. 52, no. 7, pp. 1717–1728, 2004.
- [17] F. Mani, F. Quitin, and C. Oestges, "Accuracy of depolarization and delay spread predictions using advanced ray-based modeling in indoor scenarios," *EURASIP Journal on wireless communications and networking*, vol. 2011, no. 1, p. 11, 2011.
- [18] —, "Directional spreads of dense multipath components in indoor environments: Experimental validation of a ray-tracing approach," *IEEE Trans. Antennas Propag.*, vol. 60, no. 7, pp. 3389–3396, 2012.
- [19] J. Järveläinen, K. Haneda, M. Kyro, V.-M. Kolmonen, J.-i. Takada, and H. Hagiwara, "60 GHz radio wave propagation prediction in a hospital environment using an accurate room structural model," in *Antennas and Propagation Conference (LAPC), 2012 Loughborough*. IEEE, 2012, pp. 1–4.
- [20] J. Järveläinen and K. Haneda, "Sixty gigahertz indoor radio wave propagation prediction method based on full scattering model," *Radio Science*, vol. 49, no. 4, pp. 293–305, 2014.
- [21] U. T. Virk, J.-F. Wagen, and K. Haneda, "Simulating specular reflections for point cloud geometrical database of the environment," in *Antennas & Propagation Conference (LAPC), 2015 Loughborough*. IEEE, 2015, pp. 1–5.
- [22] J.-F. Wagen, U. T. Virk, and K. Haneda, "Measurements based specular reflection formulation for point cloud modelling," in *Antennas and Propagation (EuCAP), 2016 10th European Conference on*. IEEE, 2016, pp. 1–5.
- [23] J. Pascual-García, J. M. Molina-García-Pardo, M. T. Martínez-Inglés, J. V. Rodríguez, and N. Saurín-Serrano, "On the importance of diffuse scattering model parameterization in indoor wireless channels at mm-wave frequencies," *IEEE Access*, vol. 4, pp. 688–701, 2016.
- [24] L. Tian, V. Degli-Esposti, E. M. Vitucci, X. Yin, F. Mani, and S. X. Lu, "Semi-deterministic modeling of diffuse scattering component based on propagation graph theory," in *IEEE 25th Annual International Symposium on Personal, Indoor, and Mobile Radio Communication*. IEEE, 2014.
- [25] L. Tian, V. Degli-Esposti, E. M. Vitucci, and X. Yin, "Semi-deterministic radio channel modeling based on graph theory and ray-tracing," *IEEE Trans. Antennas Propag.*, vol. 64, no. 6, pp. 2475–2486, 2016.
- [26] F. Fuschini, S. Häfner, M. Zoli, R. Müller, E. M. Vitucci, D. Dupleich, M. Barbiroli, J. Luo, E. Schulz, V. Degli-Esposti *et al.*, "Item level characterization of mm-wave indoor propagation," *EURASIP Journal on Wireless Communications and Networking*, vol. 2016, no. 1, p. 4, 2016.

- [27] E. Leitinger, P. Meissner, C. Ruedisser, G. Dumphart, and K. Witrisal, “Evaluation of position-related information in multipath components for indoor positioning,” *IEEE J. Sel. Areas Commun.*, 2015.
- [28] K. Witrisal, E. Leitinger, S. Hinteregger, and P. Meissner, “Bandwidth scaling and diversity gain for ranging and positioning in dense multipath channels,” *IEEE Wireless Commun. Lett.*, vol. 5, no. 4, pp. 396 – 399, Aug. 2016.
- [29] I. S. Merrill, “Radar handbook,” *John Wiley*,, 1990.
- [30] J. H. Lienhard, *A heat transfer textbook*. Phlogiston Press, Cambridge, Massachusetts, 2003.
- [31] C. Gustafson, *60 GHz Wireless Propagation Channels: Characterization, Modeling and Evaluation*, 2014, vol. 69.
- [32] C. Gustafson, K. Haneda, S. Wyne, and F. Tufvesson, “On mm-wave multipath clustering and channel modeling,” *IEEE Trans. Antennas Propag.*, vol. 62, no. 3, pp. 1445–1455, 2014.
- [33] P. F. M. Smulders, “Statistical characterization of 60-GHz indoor radio channels,” *IEEE Trans. Antennas Propag.*, vol. 57, no. 10, pp. 2820–2829, Oct 2009.

Using DecaWave UWB Transceivers for High-accuracy Multipath-assisted Indoor Positioning

Josef Kulmer, Stefan Hinteregger, Bernhard Großwindhager,
Michael Rath, Mustafa S. Bakr, Erik Leitinger, Klaus Witrissal
Graz University of Technology, Austria

presented at IEEE ICC 2017 Workshop on Advances in Network Localization and Navigation (ANLN)

Abstract

Robust indoor positioning and location awareness at a sub-meter accuracy typically require highly accurate radio channel measurements to extract precise time-of-flight measurements. Emerging UWB transponders like the DecaWave DW1000 chip offer to estimate channel impulse responses with reasonably high bandwidth and excellent clock stability, yielding a ranging precision below 10 cm. The competitive pricing of these chips allows scientists and engineers for the first time to exploit the benefits of UWB for indoor positioning without the need for a massive investment into experimental equipment.

This work investigates the performance of the DW1000 chip concerning position related information that can be extracted from its channel impulse response measurements. We evaluate the signal-to-interference-plus-noise ratio of the line-of-sight and reflected multipath components which is a key parameter determining the Cramér-Rao lower bound on the ranging error variance. We propose a novel and highly efficient positioning algorithm, which requires information from a single anchor only. Results demonstrate reliable and robust positioning at an accuracy below 0.5 m.

1 Introduction

Location awareness is a key feature for many upcoming application scenarios, e.g. asset tracking, autonomous navigation or ambient assisted living [1]. This location awareness can be achieved outdoors via global navigation satellite systems (GNSS), e.g. GPS, Galileo, Beidou. For indoor environments, where GNSS fail due to low signal-to-noise-ratios (SNR) and multipath propagation, a reliable and robust, yet cost-effective alternative is still pursued.

Indoors, the radio-channel is heavily influenced by multipath propagation leading to severe fading and pulse dispersion. To reduce these effects, ultra-wideband (UWB) signals have been proposed due to their superior time-resolution [2–5]. This advantageous property of UWB transceivers comes at the expense of higher hardware costs compared to off-the-shelf radio transponders used in today’s wireless sensor networks (e.g. Zigbee and Bluetooth Low Energy). However, with the emergence of UWB-chips like the DecaWave DW1000 [6] and the upcoming fifth generation (5G) of wireless networks, the cost for hardware components capable of providing high bandwidth signals is expected to fall over the next decade.

To further reduce hardware costs we propose to use single-anchor positioning techniques [1, 7, 8] which exploits signal reflections by incorporating floorplan knowledge. These specular reflections at flat surfaces are modeled as deterministic multipath components (MPCs) which can be estimated from accurate channel measurements. Algorithms exploiting deterministic MPCs have been developed and evaluated using channel measurements performed with high-end equipment, e.g. vector network analyzers or correlative channel sounders. To avoid any synchronization errors, the transmitter and receiver antennas are both wired to the same measurement equipment. This allows to perform channel measurements even in challenging scenarios. Non-wired devices need to establish a connection and synchronize first. Once a connection is established, the clock accuracy has to be better than 1 ns to guarantee the required localization at sub-meter accuracy. These requirements are usually reflected in cost-intensive hardware.

The previously mentioned DecaWave DW1000 chip is an IEEE 802.15.4 (2011) compliant UWB transceiver which operates on 6 frequency bands with center frequencies between 3.5 to 6.5 GHz and a bandwidth of 500 or 900 MHz. It provides the possibility of range measurements and retrieving the measured channel impulse response (CIR) which is necessary to exploit deterministic MPCs. While the ranging capabilities of the DW1000 have been evaluated in [9, 10], the acquired CIR and the possible exploitation of MPCs have not been analyzed yet. We use the competitively priced Pozyx platform [11] which incorporates the DW1000 chip and a suitable UWB antenna.

The main contributions of this paper are:

- We analyze the range and CIR measurements of the Pozyx platform (see Section 3),
- we evaluate the reliability of deterministic MPCs for ranging and positioning (Sec. 3.5),
- and we derive a single-anchor approximate maximum likelihood position estimator (Sec. 4).

An implementation of the proposed positioning algorithm and the used data set are available to the research community at <http://www2.spsc.tugraz.at/people/s0773094/dw>

2 Problem Formulation

We are interested in individual channel measurements between two nodes, both located in an indoor environment. The anchor node is placed at known position $\mathbf{a} \in \mathbb{R}^2$ and the agent node at unknown position $\mathbf{p}_n \in \mathbb{R}^2$ with n as measurement index. The agent aims at localizing its position using radio signals deteriorated by multipath propagation. The multipath propagation results from reflections of the radio signals with its surrounding environment. Knowledge of the environment enables to exploit rather than mitigate multipath propagation and allows to derive algorithms with improved accuracy and robustness.

2.1 Channel model

The channel impulse response of the propagation channel $h(t)$ is composed of deterministic and diffuse MPCs [4]

$$h(t) = \sum_{k \in \mathcal{K}} \alpha_k \delta(t - \tau_k) + \nu(t). \quad (1)$$

The first term on the right-hand-side models the deterministic MPCs $k \in \mathcal{K}$, each characterized by its complex-valued amplitude α_k and delay τ_k with $\delta(t)$ as Dirac delta function. These MPCs can be described using an environmental model, as further discussed in Section 2.2. The second term of (1) is denoted as diffuse multipath (DM) $\nu(t)$. It models scattering, originating at small objects and rough surfaces. These scatters are not explained by the environmental model and therefore, they are treated as additive noise. We define the DM as zero-mean Gaussian random process with an auto-correlation function $\mathbb{E}_\nu\{\nu(\tau)[\nu(u)]^*\} = S_\nu(\tau)\delta(\tau - u)$, introducing the uncorrelated scattering assumption [12]. Note, that the power delay profile $S_\nu(\tau)$ depends on both transmitter and receiver positions as well as the surrounding environment [13]. It is assumed to be stationary within a small region in the spatial domain (< 1 m) as discussed in 3.5.

2.2 Relation to geometry

Deterministic MPCs describe specular reflections originating at flat surfaces, e.g. walls and windows. Assuming information of the surrounding environment to be available (e.g. a floorplan is provided), these reflections can be modeled using an *image-source model* [14, 15] as illustrated in Figure 1. The anchor's position \mathbf{a} is mirrored at each reflective surface to obtain *virtual anchors* (VA) \mathbf{a}_k , where each \mathbf{a}_k is assigned to a MPC k .

Then, the delay τ_k is the geometric distance between \mathbf{p}_n and \mathbf{a}_k , scaled by the propagation velocity c

$$\tau_k = \frac{1}{c} \|\mathbf{p}_n - \mathbf{a}_k\| \quad \text{for all } k \in \mathcal{K} \quad (2)$$

with $\|\cdot\|$ representing the Euclidean norm. Defining the physical anchor position by $\mathbf{a}_1 \triangleq \mathbf{a}$ and virtual anchors by $k > 1$, then the delays τ_k of the deterministic MPCs' can be calculated using Eq. (2).

The set of MPCs \mathcal{K} depends on the location of both communicating nodes. We verify the existence of potential MPCs using a ray-tracer [16, p. 34] where we do not consider effects like diffraction or diffuse scattering.

In general, deterministic MPCs are vital for the positioning algorithm as they provide position-related information. An open question is the model order of (1), in other words, which MPCs shall we include in \mathcal{K} . The obvious rule *the more the better* may easily result in a model bias. Considering MPCs which are not contained in the impulse response (e.g. they are shadowed by other objects or strongly overlapped by DM) yield ambiguous results in the positioning algorithm. Therefore, we consider single-bounce reflections only as their *visibility* is more likely compared to MPCs which bounce several times before arrival. The importance of the MPC selection is further investigated in Sec. 4.2 and 4.3.

2.3 Reliability of MPCs

We employ the signal-to-interference-plus-noise-ratio (SINR) [1] to describe the reliability of a specific MPC k . It relates the path energy $|\alpha_k|^2$ to the interfering DM, evaluated at the MPC delay τ_k and scaled by the pulse duration T_p , and the measurement noise N_0 , according to

$$\text{SINR}_k = \frac{|\alpha_k|^2}{N_0 + T_p S_\nu(\tau_k)}. \quad (3)$$

The SINR has been demonstrated as reliability measure of MPCs suitable for the task of indoor positioning [4, 18]. In [1, 4] it was shown that the SINR endows a lower bound¹ on the squared error of the MPC delay estimation

$$\text{var}(\hat{\tau}_k) \geq (8\pi^2 \beta^2 \text{SINR}_k)^{-1} \quad (4)$$

with β as effective (root-mean-square) bandwidth.

3 Analysis of the received signal

This section presents an analysis of the capabilities of the low-cost experimental equipment and its potential to resolve and utilize multipath propagation. Subsection 3.1 introduces the hardware setup followed by presenting the reference system for comparison (3.2). In 3.3 and 3.4 device-specific parameters are discussed and in 3.5 results of the comparison between the low-cost equipment and the reference system are presented.

3.1 Measurement setup

Our work is based on the Pozyx platform which embeds the IEEE 802.15.4 (2011) compliant DecaWave DW1000 coherent UWB transceiver. Its dielectric

¹Assuming the pulse shape $s(t)$ (introduced in Sec. 3.4.1) is known with a constant PSD and deterministic MPCs are assumed to be orthogonal $\int s(t - \tau_i)s(t - \tau_j)dt = 0$, for all $(\tau_i, \tau_j) \in \mathcal{K}, \tau_i \neq \tau_j$

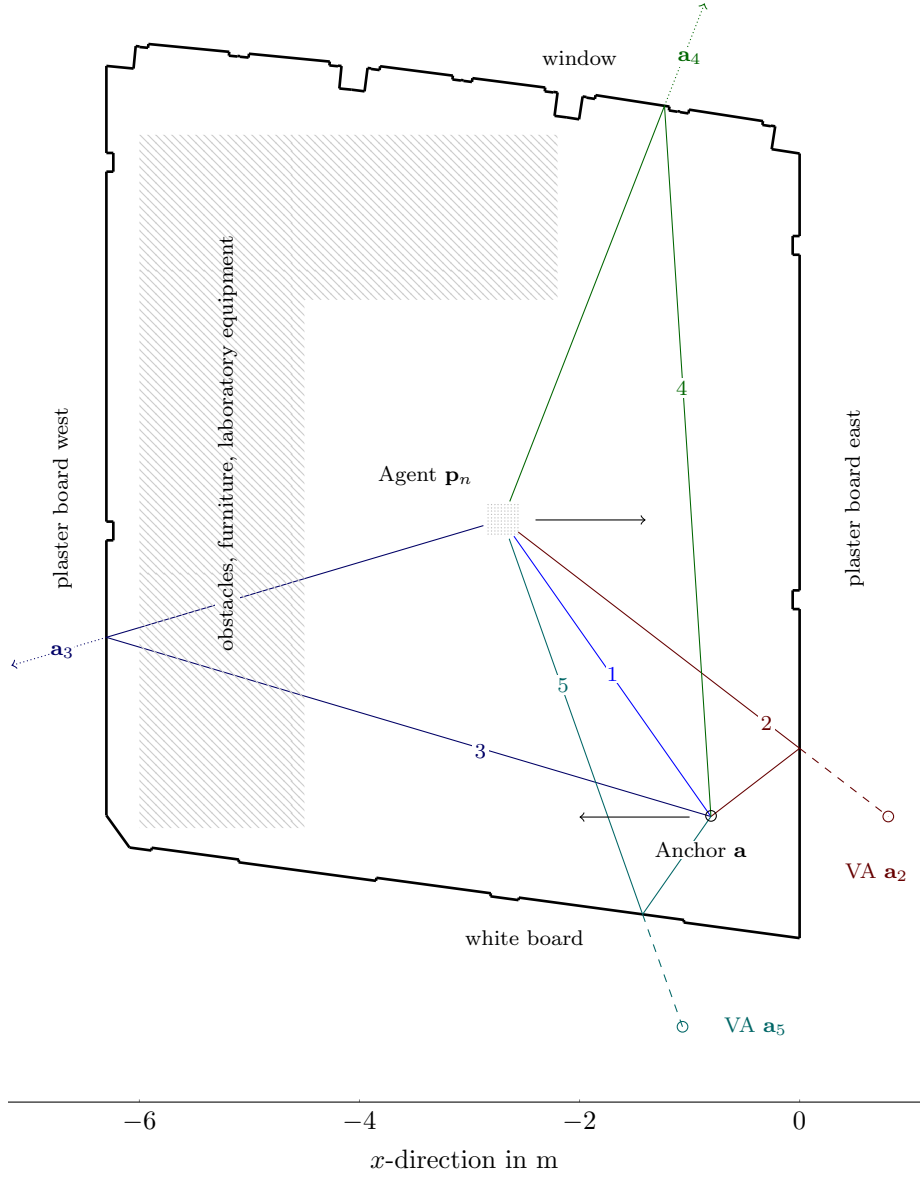


Figure 1: Illustration of the floorplan and deterministic MPCs between an agent located at \mathbf{p}_n and anchor at \mathbf{a} . The line-of-sight ($k = 1$) and multipath propagation originating at plaster board east ($k = 2$) and west (3), window (4) and white board (5) as well as their corresponding VA positions $\{\mathbf{a}_k\}_{k \in \mathcal{K}}$ are shown. The MPC at plaster board west is obstructed by furniture and laboratory equipment. The arrows next to agent and anchor indicate the orientation of the Pozyx platform according to the coordinate system defined in [17, p. 15].

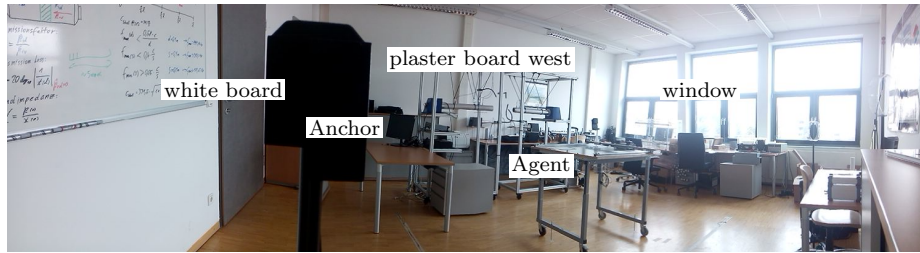


Figure 2: Picture of the measured room. The anchor and agent positions as well as the surfaces generating the analyzed MPCs are labeled (cf. Fig. 1).

chip antenna has an approximately uniform radiation pattern along its azimuth plane [17, p. 15].

The measurements were performed using two Pozyx nodes at positions \mathbf{a} and \mathbf{p}_n placed indoors under line-of-sight (LOS) conditions, 1.3 m off the floor, as illustrated in Figure 1. To take usage of the geometry model (Sec. 2.2) we calculated the positions of the VAs by using a building floorplan where we considered flat surfaces with a minimum length of 25 cm. To ensure realistic conditions the room was furnished and equipped with several laboratory devices (see Figure 2). The furniture and equipment was not considered in the floorplan. We constrain the geometry model to two dimensions. The inevitable reflections at floor, ceiling, and furniture subsequently contribute to undesired, diffuse MPCs.

The DecaWave DW1000 is able to perform range measurements with an accuracy within ± 10 cm [6, p. 7]). Further, it allows to return the estimated CIR, sampled at $T_s = 1.0016$ ns with a length of 1016 samples (using a pulse repetition frequency of 64 MHz). It supports the UWB Channel numbers 2 – 5, standardized by IEEE 802.15.4 (2011). The Channels 2, 3 and 5 have a bandwidth of 0.499 GHz and Channel 4 1.331 GHz which is of particular interest due to its superior bandwidth.

To get insight into the impact of bandwidth on the estimated CIR, in the following, we analyze the Channels $C \in \{2, 4\}$, both located at center frequency $f_c = 3.994$ GHz. The measurements were performed with a pulse-repetition frequency of 64 MHz and 128 preamble symbol repetitions.

3.2 Reference system

As a reference we use CIR measurements obtained by an Imsens Correlative Channel Sounder (ICCS). It allows to measure the impulse response between two antennas, both wired to the ICCS. Calibration of the ICCS yields a negligible synchronization error. We used self-made Euro-cent coin antennas [19, p. 86] on both agent and anchor with approximately uniform radiation patterns in azimuth domain.

Due to measurement constraints of the ICCS, the carrier frequency was set to 4.34 GHz (which is slightly above DecaWave’s $f_c = 3.994$ GHz, using Channels 2 and 4).

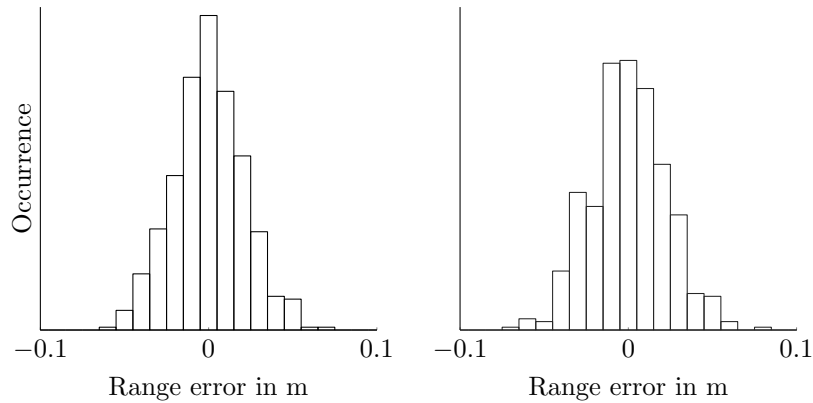


Figure 3: Histogram of (calibrated) range error of Channel 2 (left) and Channel 4 (right).

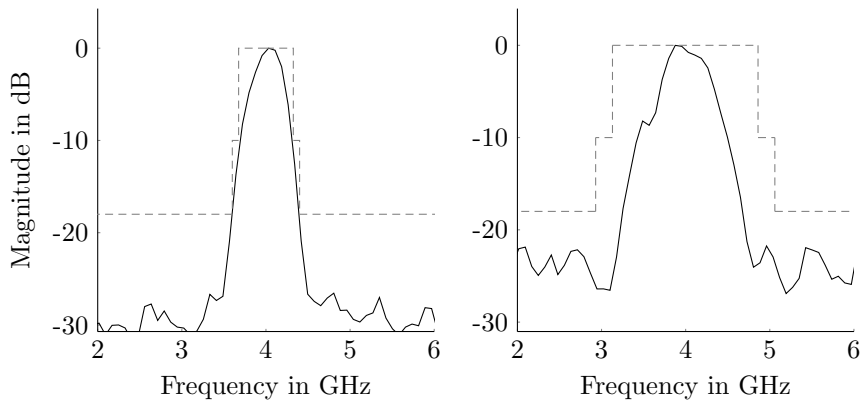


Figure 4: Utilized radio-frequency band of DW1000 (black, solid) of Channel 2 (left) and Channel 4 (right) and the standardized transmit PSD mask (gray, dashed).

3.3 Range estimate

At each measurement Pozyx returns one measured range and the associated CIR. The measured range, denoted as d'_{DW} , is available in a resolution of 4.69 mm (which corresponds to one period of the 63.9 GHz ranging sampling clock [6, p. 8]). To calibrate the range estimates, we performed 1000 measurements of each channel and calculated the mean μ and standard deviation σ of the difference between the *true* distance of both Pozyx devices $\|\mathbf{p}_n - \mathbf{a}\|$ (measured with a tape) and the estimated ranges d'_{DW} . The resulting calibrated range estimates for each channel follow as $d_{\text{DW}} = d'_{\text{DW}} - \mu$. Figure 3 illustrates the histograms of the (calibrated) range errors of both channels. The observed standard deviations of Channel 2 (denoted as $\sigma_2 = 0.054$ m) and Channel 4 ($\sigma_4 = 0.053$ m) are comparable to the reported ones in [9, 10, 20].

We calculated the theoretical lower bound on the ranging precision (Eq. (4)) using the estimated SINR values in Table 1. The lower bound of the LOS $\text{var}(\hat{\tau}_1)$

is 0.029^2m^2 and 0.018^2m^2 for Channels 2 and 4, respectively. These values are below the ranging accuracy of the DW1000, which is presumably explained by the fact that Pozyx performs several measurements for the two-way ranging and for estimating the clock offset between the transceivers.

3.4 Channel impulse response

The measurement of a CIR is limited to physical constraints, e.g. limited bandwidth and clock errors. This section treats the DW1000 specifications in more detail and modifies the channel model in (1) accordingly.

To analyze the utilized spectral band, we used a real-time scope connected to a dipole-style UWB antenna [19, p. 86] via a high-performance low noise amplifier to assess the signal spectrum of the transmitted UWB signals. Time gating was used to isolate the LOS pulse. Figure 4 shows the power spectral density (PSD) (black, solid) in comparison with the transmit power spectral density mask (gray, dashed), specified in IEEE 802.15.4 (2011). Both channels comply with the standard. The under-utilization of Channel 4 is justified by DecaWave's limitation of Channel 4 to 900 MHz [6, p. 204]. The effective (root-mean square) bandwidth β of Channels 2 and 4 are $\beta_2 \approx 0.14$ GHz and $\beta_4 \approx 0.24$ GHz.

Figure 5 exemplifies the estimated CIRs (black, solid) of Channel 4 (top) and Channel 2 (bottom) obtained from the DW1000. Both CIRs are composed of a separated LOS and several overlapping multipath components. The superior bandwidth of Channel 4 results in a higher time resolution, compared to Channel 2. Note, that the pulse shape is different at both channels, further, the CIR alignment along time domain includes an offset.

To address the impact of the observed pulse shape and CIR offset to the channel model, we describe the received signal by the DW1000 $r_{\text{DW}}(t)$ as a function of $h(t)$ according to

$$r_{\text{DW}}(t) = s(t) * h(t - t_0) + w(t) \quad (5)$$

where $*$, $s(t)$ and t_0 denote the convolution operator, the (energy normalized) pulse shape and CIR offset, respectively, and $w(t)$ is additive white Gaussian noise.

3.4.1 Pulse shape $s(t)$

To get insight on the pulse shape, in the following, we disassemble the CIR to a convolution of transmitted signal $p_{\text{PHY}}(t)$, the channel impulse response $h(t)$ and a *UWB reference pulse*² $r_{\text{PHY}}(-t)$ and the pulse shape in (5) follows as $s(t) \triangleq p_{\text{PHY}}(t) * r_{\text{PHY}}(-t)$.

IEEE 802.15.4 (2011) standardizes $r_{\text{PHY}}(t)$ and a few requirements on the magnitude of $|p_{\text{PHY}}(t) * r_{\text{PHY}}(-t)|$. The transmitted signal $p_{\text{PHY}}(t)$ is not defined and depends on the actual implementation in the radio-frequency transmitter. Since the implementation is not published by DecaWave but required to estimate the path amplitudes using the proposed channel model in (5) we approximate $s(t)$ as a raised cosine pulse. The pulse parameters for Channel 2 (denoted as

² $p_{\text{PHY}}(t)$ and $r_{\text{PHY}}(t)$ are defined by the physical layer (PHY); IEEE 802.15.4 (2011) recommends a cross-correlation with $r_{\text{PHY}}(t)$ which is equivalent to a convolution with $r_{\text{PHY}}(-t)$

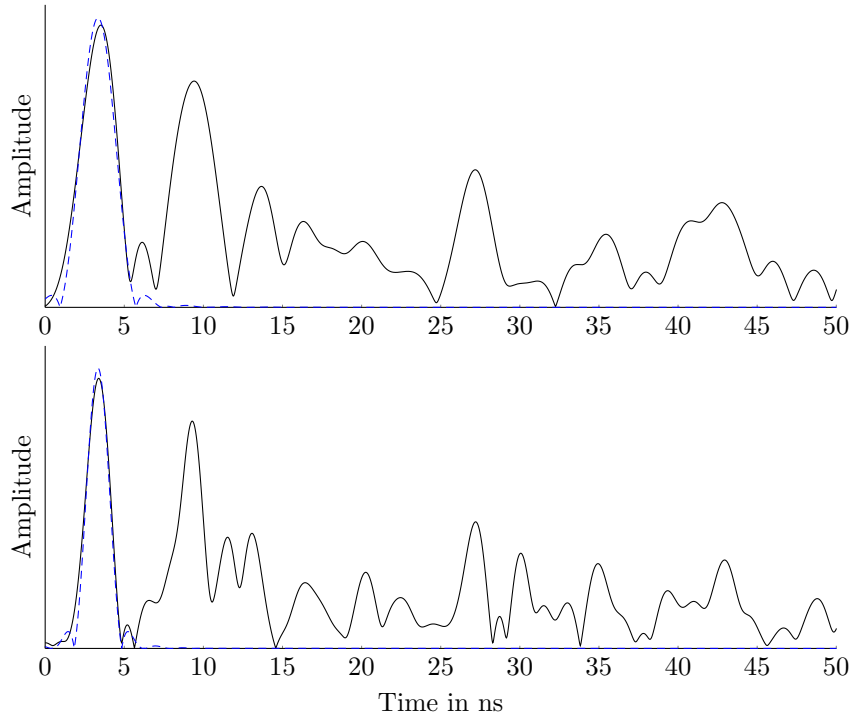


Figure 5: Estimated channel impulse response (black, solid) of Channel 2 (top) and Channel 4 (bottom) and the approximated raised-cosine pulse (blue, dashed) shifted to the delay of the first path. For improved illustration the CIRs are interpolated by a sinc function.

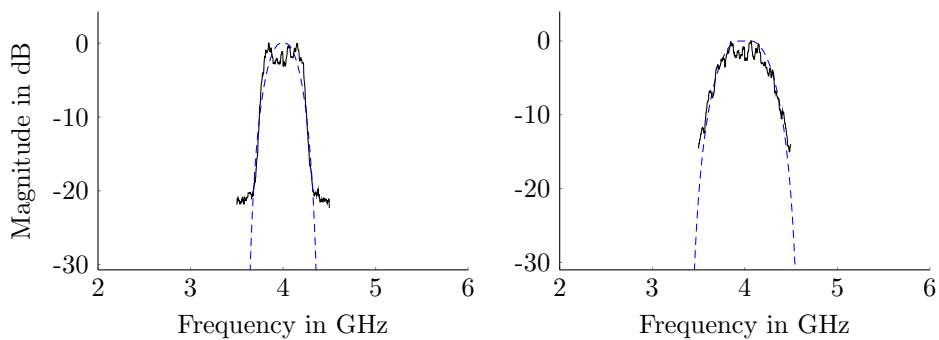


Figure 6: PSD (black, solid) of Channel 2 (left) and Channel 4 (right) of DW1000's CIR. The PSD of the approximated pulse shapes (blue, dashed) is shown for comparison.

Table 1: SINR in dB of deterministic MPCs for Channels 2 and 4 as well as both scenarios of CIR alignment with estimated (Scenario a) and expected ranges (Scenario b). The mean of the MPC's energy compared to the sum of all components, and SINR values obtained from Imsens Correlative Channel Sounder are shown for comparison. Low SINRs are subject to estimation errors [18, 21], indicated by *nan*.

MPC	Channel 2		Channel 4		Channel Sounder		Avg. distance	Energy
	a)	b)	a)	b)	$T_p = 2.4$ ns	$T_p = 1.5$ ns		
LOS	19.6	19.9	21.5	22.4	21.9	23.3	3.3 m	42%
plaster board east	3.2	3.7	-2.7	-2.2	-0.2	4.6	4.4 m	7%
plaster board west	-4.1	-2.3	<i>nan</i>	<i>nan</i>	-0.7	-2.7	9.5 m	2%
white board	8.6	8.6	11.5	11.8	9.9	13.2	4.9 m	39%
window	7.0	8.3	5.8	6.7	1.8	3.3	10.5 m	10%

$s_2(t)$) are a pulse duration of $T_p = 2.4$ ns and roll-off factor of $R = 0.9$ and for Channel 4 ($s_4(t)$) we use $T_p = 1.5$ ns and $R = 0.8$. Figure 5 illustrates the approximated pulse shapes (blue, dashed), shifted to the location of the first path and Fig. 6 illustrates the PSD of DW1000's CIR (black, solid) in comparison with the pulse shape (blue, dashed).

3.4.2 CIR offset t_0

The Pozyx platforms do not share any absolute timing information of the stored CIR which results in an unknown t_0 in (5). We propose to employ the DW1000 range measurement d_{DW} to adjust the CIR offset. The range measurement is associated to the *leading edge* of the first path [6, p. 116]. Identification of the first path followed by shifting of the CIR enables the correct alignment.

To obtain the first path delay, we estimated the $N = 10$ strongest MPCs contained in each CIR using *search and subtract* [18, 22] and define the MPC with the lowest delay as first path. Subsequently, the CIR is shifted along time until the first path delay t_{first} matches with the ranging information d_{DW}/c , and the aligned CIR $r(t)$ follows accordingly from

$$r(t) = r_{DW}(t - t_{\text{first}} + d_{DW}/c). \quad (6)$$

It is important to note, that the ranging information obtained from the Pozyx platform may be erroneous which may result in a wrongly aligned CIR. The correct alignment is important to guarantee an accurate MPC parameter estimation and will be discussed in the following section.

3.5 Analysis of MPCs for Ranging and Positioning

The previous sections offered potentials to embrace the DW1000's CIR. Finally, we will analyze the undertaken amendments in terms of SINR of selected MPCs. For this experiment, we placed one Pozyx at position \mathbf{a} where it remained for all measurements. The second Pozyx at \mathbf{p}_n moved on a 27×27 cm measurement grid with a spacing of 3 cm between adjacent measurement points, resulting in $n \in \{1, \dots, 100\}$ measurements, under LOS conditions (see Fig. 1).

We are interested in two scenarios: alignment of the CIR such that the first path delay t_{first} matches with

- a) the Pozyx range estimate d_{DW}/c , equivalent to Eq. (6)

$$r_{\text{est}}(t) = r(t) \quad (7)$$

- b) the expected first path delay, proportional to the actual distance between both platforms $\|\mathbf{p}_n - \mathbf{a}\|$

$$r_{\text{exp}}(t) = r_{DW}(t - t_{\text{first}} + \|\mathbf{p}_n - \mathbf{a}\|/c). \quad (8)$$

At both scenarios we employ the geometry model in (2) to predict the deterministic MPC delays $\{\tau_k\}_{k \in \mathcal{K}}$. We select those deterministic MPCs \mathcal{K} which exist at all measurement points, as illustrated in Figure 1. Then, for each MPC the amplitude results as projection of the received signal $r(t)$ onto the delayed pulse $s(t - \tau_k)$. Considering the Channels 2 and 4 the MPC amplitudes were estimated for all measurements n , using the appropriate signals $s_2(t)$ and $s_4(t)$, and both scenarios (Eq. (7) and (8)) of CIR alignment. Finally, the SINRs in

(3) follow by employing a moment-based estimator [18] applied on the estimated amplitudes.

Table 1 reports the SINRs for the evaluated measurements and scenarios. The obtained SINRs using the reference system ICCS are shown for comparison. The measured impulse responses of the ICCS were shaped with the approximated pulse shapes $s_2(t)$ and $s_4(t)$ of Channel 2 and 4, respectively.

In general, it can be observed that the estimated SINRs of the Pozyx device are in a comparable range to the ICCS using a uniform radiation pattern. The LOS reaches the highest SINR whereas the deterministic MPCs at the window and the white board still reach SINR values, adequate to be used for localization. Both MPCs at plaster board walls achieve rather poor SINR values. This can be argued by the material's weak reflection properties as well as the laboratory equipment which is placed along the path of the MPC of plaster board west.

The SINR of the aligned CIR using Pozyx's range measurement (Scenario a) is slightly decreased, compared to the aligned CIR using the expected delay (Scenario b). This minor degradation of 0 – 2 dB is caused by the uncertainty of the range measurement (see Fig. 3). The 3 dB main-lobe width of the auto-correlation function of $s_2(t)$ and $s_4(t)$ spans approximately (a time proportional distance of) 47 cm and 31 cm respectively. The range uncertainties σ_2 and σ_4 are much smaller than the 3 dB main-lobe width which explains the insensitivity of the SINR estimate with respect to the accuracy of the range estimate.

The estimated SINR levels are in a similar range to the ones reported in [18], which motivates exploitation of the MPCs for ranging and localization.

4 Localization using Pozyx

As shown in Table 1 the obtained CIR by DW1000 suffices to resolve and identify deterministic MPCs. In this section, we are interested if these MPCs can be further utilized. We focus on single-anchor localization [1, 7, 8] where an agent locates its position \mathbf{p}_n relying on time-of-arrival measurements to a single anchor at \mathbf{a} only. This application is of particular interest for low-cost solutions as the number of required anchor nodes can be reduced dramatically. We present an efficient algorithm for localization using the CIR and range measurements of the DW1000. Using the range estimate only with known \mathbf{a} , the position estimate of the agent $\hat{\mathbf{p}}_n$ is uniformly distributed on a circle around the anchor. The additional position-related information contained in the CIR [23] can be utilized to further identify the agent node's position.

4.1 Position estimation

In this section we derive an approximate maximum likelihood (ML) estimator for the agent position \mathbf{p} . Let \mathbf{r} denote the measured, complex-valued baseband CIR in vector notation, aligned according to (6) with a length of $T = 1016$. The pulse $s(t - \tau)$ shifted by delay τ , is denoted in vector notation as $\mathbf{s}(\tau) = [s(0 \cdot T_s - \tau), s(1 \cdot T_s - \tau), \dots, s((T - 1) \cdot T_s - \tau)]^\top$ and the measurement noise follows as $\mathbf{w} = [w(0 \cdot T_s), w(1 \cdot T_s), \dots, w((T - 1) \cdot T_s)]^\top$. Then, the signal model

can be rewritten as

$$\begin{aligned}\mathbf{r} &= \sum_{k \in \mathcal{K}} \alpha_k \mathbf{s}(\tau_k) + \mathbf{w} \\ &= \mathbf{S}(\boldsymbol{\tau}) \boldsymbol{\alpha} + \mathbf{w}\end{aligned}\quad (9)$$

with $\boldsymbol{\tau} = [\tau_1, \dots, \tau_{|\mathcal{K}|}]^\top$, $\mathbf{S}(\boldsymbol{\tau}) = [\mathbf{s}(\tau_1), \dots, \mathbf{s}(\tau_{|\mathcal{K}|})]$, $\boldsymbol{\alpha} = [\alpha_1, \dots, \alpha_{|\mathcal{K}|}]^\top$ and $|\mathcal{K}|$ as number of deterministic MPCs.

We simplify the channel model (1) by neglecting the DM and approximate the noise vector as a white, stationary Gaussian process³. The likelihood function of (9) with respect to the delays $\boldsymbol{\tau}$ and amplitudes $\boldsymbol{\alpha}$ then follows as

$$p(\mathbf{r}|\boldsymbol{\tau}, \boldsymbol{\alpha}) \propto \exp \{ - \|\mathbf{r} - \mathbf{S}(\boldsymbol{\tau}) \boldsymbol{\alpha}\|^2 \}.\quad (10)$$

To simplify (10) we use the observation [24] that for a given $\boldsymbol{\tau}$ the amplitudes are calculated as linear least squares solution according to

$$\hat{\boldsymbol{\alpha}} = (\mathbf{S}(\boldsymbol{\tau})^H \mathbf{S}(\boldsymbol{\tau}))^{-1} \mathbf{S}(\boldsymbol{\tau})^H \mathbf{r}$$

with the superscript $(\cdot)^H$ as Hermitian transpose. To maximize (10) with respect to the agent position \mathbf{p} , the deterministic MPC delays $\boldsymbol{\tau}$ are substituted with \mathbf{p} and $\{\mathbf{a}_k\}_{k \in \mathcal{K}}$ using (2). Then the ML can be reformulated and the ML solution of the agent position estimate $\hat{\mathbf{p}}$ follows as

$$\hat{\mathbf{p}} = \underset{\mathbf{p} \in \mathcal{P}}{\operatorname{argmax}} p(\mathbf{r}|\mathbf{p}, \{\mathbf{a}_k\}_{k \in \mathcal{K}}).\quad (11)$$

A numerical evaluation of (11) is exhaustive since the ML function is multimodal and the set of possible solutions \mathcal{P} contains all positions within the communication range to the anchor [23]. We approximate (11) by considering I sampling points $\mathcal{P} = \{\mathbf{p}^{(i)}\}_{i=1}^I$. The sampling points are uniformly distributed around \mathbf{a} with a radius that is Gaussian with mean d_{DW} , i.e.

$$\begin{aligned}d^{(i)} &\sim \mathcal{N}(d_{\text{DW}}, \sigma^2) \\ \phi^{(i)} &\sim \mathcal{U}(0, 2\pi) \\ \mathbf{p}^{(i)} &= [d^{(i)} \cos(\phi^{(i)}), d^{(i)} \sin(\phi^{(i)})]^\top + \mathbf{a}\end{aligned}$$

where $\mathcal{N}(\cdot, \cdot)$ and $\mathcal{U}(\cdot, \cdot)$ represent the Gaussian and Uniform distribution and σ^2 is the range variance from Sec. 3.3. Sampling points which lie outside the area of interest (i.e. outside the room) are rejected.

4.2 Evaluation using MPCs predicted by the environmental model

The following quantitative evaluation uses the environmental model to predict the set of deterministic MPCs \mathcal{K}_p , limited to first-order reflections (namely the MPCs in Table 1)⁴. The agent was placed at $n \in \{101, \dots, 200\}$ positions \mathbf{p}_n

³Note, that the discussed ML position estimator in [23] aims at finding an optimal solution (by employing SINR measurements) while in this work we introduce further approximations to obtain a *practical* solution

⁴The limitation to first-order reflections has been done for simplicity. Higher-order reflections have usually low SINRs (< 5 dB) at a bandwidth below 1 GHz [4]

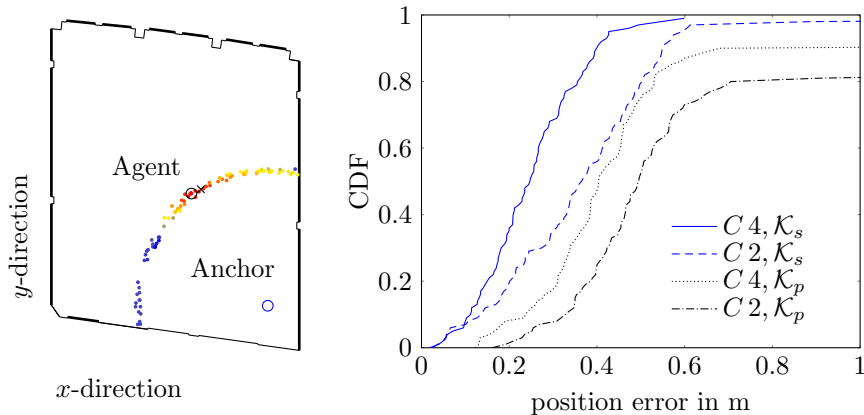


Figure 7: Illustration of ML localization (left) utilizing multipath propagation. The agent is placed indoors (black cross) employing information of a single anchor (blue circle) to estimate its position (black circle). The CDF of 100 different positions (right) illustrates the impact of using deterministic MPCs predicted by the environmental model \mathcal{K}_p , and selected with reasonable high SINRs \mathcal{K}_s for both channels $C = \{2, 4\}$.

on a 27×27 cm grid, different to the grid used in Sec. 3.1. The anchor remained at the same position \mathbf{a} as in Sec. 3.1.

The ML estimate in (11) (using \mathcal{K}_p) was applied to each n individually with $I = 100$ and the error between expected and estimated agent position follows as $\epsilon_n = \|\hat{\mathbf{p}}_n - \mathbf{p}_n\|$. Figure 7 exemplifies the floorplan (left) and the cumulative distribution function (CDF) of ϵ_n (right). The sampling points in \mathcal{P} are colored according to the likelihood (10). A brighter color indicates that the underlying multipath propagation model fits better to the CIR observation. The maximum is marked with a black circle. We performed the evaluation for both channels 2 and 4. The resulting CDF of ϵ_n (Fig. 7 right) stimulates two interpretations. First, the superior bandwidth of channel 4 yields increased accuracy due to the improved possibility of MPC separation along time domain. Second, both CDFs barely reach the 90% limit within 1 m. This can be reasonably argued as the algorithm expects deterministic MPCs at both plaster boards. Their rather low SINR values (see Table 1) indicate that both MPCs are inadequate to be used for positioning. This finding can be interpreted as a biased channel model which subsequently results in a performance loss.

The following section evaluates the potential gain by selecting those MPCs with reasonable high SINRs.

4.3 Evaluation using selected MPCs

As reported in Table 1, not all deterministic MPCs predicted by the environmental model are suitable to be exploited for localization. In this section we evaluate the derived ML estimator (11), limiting the deterministic MPCs to those with high SINRs, namely $\mathcal{K}_s = \{\text{LOS, window, white board}\}$. The agent and anchor positions as well as the parameters of the ML estimator were set similarly to Sec. 4.2. Figure 7 (right) compares the CDFs. We can observe that

the position error of both channels is decreased and the 90% limit is reached within approximately 0.5 m. The improvement may be counterintuitive since less deterministic MPCs are employed ($|\mathcal{K}_s| = 3$ compared to $|\mathcal{K}_p| = 5$). It is obtained because only those MPCs \mathcal{K}_s with high SINRs are used.

5 Conclusions

In this paper, we have evaluated the ranging and positioning capabilities of DecaWave's DW1000 incorporated into the Pozyx hardware platform. After analyzing the reliability of deterministic MPCs, we developed a positioning algorithm capable of using position related information contained in these MPCs using measurements to a single anchor only. The positioning error for a challenging indoor scenario is below 0.5 m for both analyzed IEEE 802.15.4 (2011) channels. We can conclude that the Pozyx devices suffice to provide a CIR suitable for single-anchor localization. Selecting those deterministic MPCs that have high SINRs increases the performance. Our future work will expand the usage of low-cost hardware including tracking filters for synchronization and positioning.

References

- [1] K. Witrissal, P. Meissner, E. Leitinger, Y. Shen, C. Gustafson, F. Tufvesson, K. Haneda, D. Dardari, A. F. Molisch, A. Conti, and M. Z. Win, "High-accuracy localization for assisted living," *IEEE Signal Processing Magazine*, 2016.
- [2] D. Dardari, A. Conti, U. Ferner, A. Giorgetti, and M. Z. Win, "Ranging With Ultrawide Bandwidth Signals in Multipath Environments," *Proc. IEEE*, vol. 97, no. 2, pp. 404–426, 2009.
- [3] Y. Shen and M. Win, "Fundamental limits of wideband localization; part I: a general framework," *IEEE Transactions on Information Theory*, 2010.
- [4] E. Leitinger, P. Meissner, C. Ruedisser, G. Dumphart, and K. Witrissal, "Evaluation of position-related information in multipath components for indoor positioning," *IEEE Journal on Selected Areas in Communications*, 2015.
- [5] T. Nguyen, Y. Jeong, H. Shin, and M. Win, "Machine Learning for Wideband Localization," *Selected Areas in Communications, IEEE Journal on*, vol. PP, no. 99, pp. 1–1, 2015.
- [6] DecaWave, "DW1000 User Manual," *Version 2.05*, 2015.
- [7] R. Parhizkar, I. Dokmanic, and M. Vetterli, "Single-channel indoor microphone localization," in *2014 IEEE International Conference on Acoustics, Speech and Signal Processing (ICASSP)*, May 2014, pp. 1434–1438.
- [8] S. V. de Velde and H. Steendam, "CUPID algorithm for cooperative indoor multipath-aided localization," in *2012 International Conference on Indoor Positioning and Indoor Navigation (IPIN)*, Nov 2012, pp. 1–6.

- [9] J. Wang, A. K. Raja, and Z. Pang, "Prototyping and Experimental Comparison of IR-UWB Based High Precision Localization Technologies," in *IEEE Smart World Congress*, Aug 2015, pp. 1187–1192.
- [10] F. Hammer, R. Yudanto, K. Neumann, M. Pichler, J. Cockx, C. Niestroj, and F. Petré, "Performance Evaluation of 3D-Position Estimation Systems," *IEEE Sensors Journal*, vol. 16, no. 16, pp. 6416–6424, Aug 2016.
- [11] Pozyx - Accurate Positioning. [Online]. Available: <http://www.pozyx.io>
- [12] P. Bello, "Characterization of Randomly Time-Variant Linear Channels," *IEEE Transactions on Commun. Sys.*, vol. 11, no. 4, pp. 360–393, Dec 1963.
- [13] A. Molisch, "Ultra-wide-band propagation channels," *Proceedings of the IEEE*, 2009.
- [14] J. Borish, "Extension of the image model to arbitrary polyhedra," *The Journal of the Acoustical Society of America*, vol. 75, no. 6, pp. 1827–1836, 1984.
- [15] J. Kulmer, E. Leitinger, P. Meissner, S. Hinteregger, and K. Witrisal, "Co-operative localization and tracking using multipath channel information," in *2016 International Conference on Localization and GNSS (ICL-GNSS)*, June 2016.
- [16] P. Meissner, "Multipath-Assisted Indoor Positioning," Ph.D. dissertation, Graz University of Technology, 2014.
- [17] DecaWave, "DWM1000 Datasheet," *Version 1.4*, 2016.
- [18] P. Meissner and K. Witrisal, "Analysis of Position-Related Information in Measured UWB Indoor Channels," in *6th European Conference on Antennas and Propagation (EuCAP)*, 2012.
- [19] C. Krall, "Signal processing for ultra wideband transceivers," Ph.D. dissertation, Graz University of Technology, Austria, 2008.
- [20] W. Chantaweesomboon, C. Suwatthikul, S. Manatrinon, K. Athikulwongse, K. Kaemarungsi, R. Ranron, and P. Suksompong, "On performance study of UWB real time locating system," in *2016 7th International Conference of Information and Communication Technology for Embedded Systems (ICTES)*, 2016, pp. 19–24.
- [21] L. J. Greenstein, D. G. Michelson, and V. Erceg, "Moment-method estimation of the Ricean K-factor," *IEEE Communications Letters*, vol. 3, no. 6, pp. 175–176, 1999.
- [22] C. Falsi, D. Dardari, L. Mucchi, and M. Z. Win, "Time of arrival estimation for UWB localizers in realistic environments," *EURASIP Journal on Advances in Signal Processing*, vol. 2006, no. 1, pp. 1–13, 2006.
- [23] E. Leitinger, M. Froehle, P. Meissner, and K. Witrisal, "Multipath-Assisted Maximum-Likelihood Indoor Positioning using UWB Signals," in *IEEE ICC 2014 Workshop on Advances in Network Localization and Navigation (ANLN)*, 2014.

- [24] G. H. Golub and V. Pereyra, “The differentiation of pseudo-inverses and nonlinear least squares problems whose variables separate,” *SIAM Journal on numerical analysis*, vol. 10, no. 2, pp. 413–432, 1973.

On the Unimportance of Phase-Coherent Measurements for Beampattern-Assisted Positioning

Josef Kulmer*, Stefan Grebien*, Michael Rath, Klaus Witrisal
Graz University of Technology, Austria

*Authors contributed equally to this work

2018 IEEE Wireless Communications and Networking Conference (WCNC)

Abstract

Accurate indoor radio positioning requires high-resolution measurements to either utilize or mitigate the impact of multipath propagation. This high resolution can be achieved using large signal-bandwidth, leading to superior time resolution and / or multiple antennas, leading to additional angle resolution. To facilitate multiple antennas, phase-coherent measurements are typically necessary. In this work we propose to employ non-phase-coherent measurements obtained from directional antennas for accurate single-anchor indoor positioning. The derived algorithm exploits beampatterns to jointly estimate multipath amplitudes to be used in maximum likelihood position estimation. Our evaluations based on measured and computer generated data demonstrate only a minor degradation in comparison to a phase-coherent processing scheme.

1 Introduction

Robust and accurate indoor radio positioning can be provided by (ultra-) wide-band (UWB) measurements, making use of the time-of-arrival of the line-of-sight (LOS) component [1, 2]. Depending on the bandwidth of the employed signal, multipath propagation distorts the received signal, leading to wrong time-of-arrival and subsequently position estimates [2]. By increasing the bandwidth, it is not only possible to increase the time-resolution, leading to a more separated LOS component, but also to estimate the time-of-arrival of specular multipath components (MPC), resulting from reflections at objects in the room, e.g. walls and windows [3]. These specular MPCs can be used for positioning if a geometric model of the environment is used as prior information. However, these specular components are influenced by path-overlap, i.e. different MPCs arriving at the same time, making the estimation process troublesome.

To overcome effects from path-overlap, antenna arrays [4] are beneficial due to their additional spatial information. Alternatively, the employment of directional antennas has shown increased positioning accuracy, using received signal strength [5] or UWB ranging [6]. Recently, it has been shown that utilizing an array of directional antennas at the base station can enhance multipath-resolved positioning as well [7]. The directionality of the antennas can be used to jointly estimate the amplitudes of the LOS and the specular MPCs. To employ the method derived in [7], phase-coherent measurements are necessary for the different antennas.

Low cost UWB transceivers like the BeSpoon UM100 [8] or the DecaWave DW1000 [9] enable the usage of high bandwidths for battery powered sensors enabling applications like ambient assisted living, autonomous navigation or asset tracking [10]. While laboratory-grade measurement equipment, e.g., vector network analyzers, provide phase-coherent processing, these low-cost UWB chipsets are not able to maintain a stable phase-lock for more than a single measurement. Thus, the previously developed methods which require phase-coherency cannot be employed directly.

The main contributions of this paper are:

- We formulate algorithms for directional antennas based on phase-coherent / non-phase-coherent processing.
- We derive a single-anchor positioning algorithm utilizing non-phase-coherent amplitude estimates.
- We evaluate the proposed, the phase-coherent, and the non-phase-coherent position estimator and compare the results to the Cramér Rao lower bound.
- We show the applicability to real measured data.

An implementation of the proposed positioning algorithm and the used data set are available to the research community at

<http://www2.spsc.tugraz.at/people/s0773094/WCNC2017/>

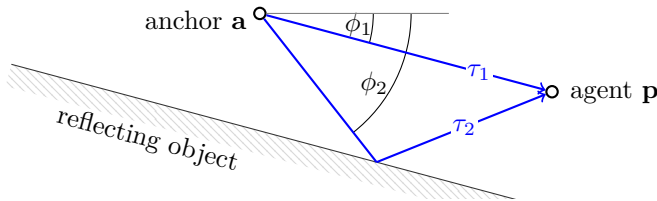


Figure 1: Illustration of geometry model for specular reflections between anchor position \mathbf{a} and agent position \mathbf{p} . The multipath components $k = 1, 2$ are characterized by delays τ_1, τ_2 and angles ϕ_1, ϕ_2 .

2 Signal model and position estimate

We consider the propagation channel between an anchor at position \mathbf{a} and an agent at position \mathbf{p} . The anchor is equipped with M antennas where $b_m(\phi)$ is the complex-valued beampattern of the m th antenna for direction ϕ . The agent employs a single-antenna with a uniform radiation pattern. We model the baseband equivalent propagation channel for the m th antenna as tapped delay line

$$h_m(t) = \sum_{k=1}^K b_m(\phi_k) \alpha_k \delta(t - \tau_k) \quad (1)$$

where K is the number of multipath components, α_k , τ_k and ϕ_k are the complex-valued amplitude, propagation delay and direction of the k th MPC, and $\delta(t)$ is the Dirac delta function with time t . Note, the MPC parameters are independent of the used antenna. The impact of the antenna is described by the beampattern $b_m(\phi_k)$ only.

Our objective is the estimation of the agent position \mathbf{p} using measured channel impulse responses. To ensure robust positioning we require an immediate connection between \mathbf{p} and channel measurements. We do not estimate the MPC parameters angle and delay from the channel measurements. In this paper we derive likelihood functions which compare channel measurements with parameters of channel models. The likelihoods are solely parameterized by hypothesized agent positions. Still, linking the channel model to hypothesized agent positions requires appropriate descriptions of the MPC parameters τ_k , ϕ_k and α_k .

Starting with delays τ_k and angles ϕ_k , we employ a geometry model as introduced in [11], [12] and [13]. The geometry model describes the wave propagation as rays, traveling from \mathbf{a} to \mathbf{p} as illustrated in Figure 1. Hereby, we consider specular reflections at objects and neglect propagation effects like diffraction or penetration. Each specular reflection conveys position-related information which can be recursively used to estimate the agent position [13, Appendix A]. The example in Figure 1 provides two MPCs, a line-of-sight ($k = 1$) and one specular reflection ($k = 2$) originating at the reflective surface. Knowledge of the location of the reflective surface enables to estimate the agent position \mathbf{p} using the MPC parameters of the line-of-sight τ_1, ϕ_1 and of the reflection τ_2, ϕ_2 .

Relating the remaining MPC parameter α_k to agent and anchor positions is not straightforward. Similar to [13] we refrain from modeling the MPC amplitudes (e.g. using path loss models). In contrast to τ_k and ϕ_k , the amplitudes

are the only MPC parameters which are estimated from channel measurements.

2.1 Signal model

Absence of a proper model for MPC amplitudes requires their accurate estimation. In [7] the authors have estimated the MPC amplitudes jointly, incorporating information from all M channels. The joint estimation requires phase-coherent processing, i.e. adjacent measurements are phase-coherent which requires the synchronization of the transmitting and receiving clocks. Although phase-coherent processing is nowadays provided by state-of-the-art measurement equipment, low-cost transceivers are not able to maintain a stable phase-lock for more than a single measurement. Adjacent measurements are characterized by a phase offset which affects the estimation of α_k . We emphasize explicitly the phase offset of the m th antenna as a constant $e^{j\varphi_m}$. Then, the received signal can be denoted as

$$r_m(t) = e^{j\varphi_m} \sum_{k=1}^K b_m(\phi_k) \alpha_k s(t - \tau_k) + w_m(t), \quad (2)$$

where $s(t)$ denotes the band-limited transmitted signal and $w_m(t)$ is additive, white Gaussian noise with a double-sided power spectral density of $N_0/2$. Sampling of (2) with sampling period T_s yields

$$r_m[n] = e^{j\varphi_m} \sum_{k=1}^K b_m(\phi_k) \alpha_k s_{\tau_k}[n] + w_m[n] \quad (3)$$

with sampled measurement $r_m[n] = r_m(nT_s)$, delayed transmitted signal $s_{\tau}[n] = s(nT_s - \tau)$ and measurement noise $w_m[n] = w_m(nT_s)$ with variance $\sigma^2 = N_0/T_s$.

In the following we formulate a position estimator based on the maximum likelihood (ML) criterion, using (3). We start by formulating a non-phase-coherent likelihood function for a single-antenna measurement (Section 2.2) and proceed with a phase-coherent likelihood function for multiple antennas (Sec. 2.3.1).

2.2 Non-phase-coherent ML estimate

2.2.1 Likelihood function for single-antenna

Having a single-antenna measurement available, we can rewrite (3) in matrix-vector notation as

$$\mathbf{r}_m = e^{j\varphi_m} \mathbf{X}_m \boldsymbol{\alpha} + \mathbf{w}_m \quad (4)$$

where

$$\begin{aligned} \mathbf{r}_m &= [r_m[0], r_m[1], \dots, r_m[N-1]]^T \in \mathbb{C}^{N \times 1} \\ \mathbf{s}_{\tau_k} &= [s_{\tau_k}[0], s_{\tau_k}[1], \dots, s_{\tau_k}[N-1]]^T \in \mathbb{C}^{N \times 1} \\ \mathbf{X}_m &= [b_m(\phi_1) \mathbf{s}_{\tau_1}, \dots, b_m(\phi_K) \mathbf{s}_{\tau_K}] \in \mathbb{C}^{N \times K} \\ \boldsymbol{\alpha} &= [\alpha_1, \dots, \alpha_K]^T \in \mathbb{C}^{K \times 1} \\ \mathbf{w}_m &= [w_m[0], w_m[1], \dots, w_m[N-1]]^T \in \mathbb{C}^{N \times 1} \end{aligned}$$

and

$$\boldsymbol{\tau} = [\tau_1, \dots, \tau_K]^T \in \mathbb{R}^{K \times 1}, \boldsymbol{\phi} = [\phi_1, \dots, \phi_K]^T \in \mathbb{R}^{K \times 1}$$

with measurement length N . Throughout this section we aim at estimating the MPC amplitudes from channel measurements. We admit that having only a single-antenna measurement at hand there are ambiguous solutions for phase-offset and MPC amplitudes. The phase-offset appears as constant phase error in the amplitude estimates and thus, only their product $e^{j\varphi_m} \boldsymbol{\alpha}$ can be estimated explicitly. Let

$$\boldsymbol{\alpha}_m = e^{j\varphi_m} \boldsymbol{\alpha} \quad (5)$$

with entries $\boldsymbol{\alpha}_m = [\alpha_{1,m}, \dots, \alpha_{K,m}]^T$ be the amplitudes $\alpha_{k,m} = e^{j\varphi_m} \alpha_k$ containing the phase-offset. Then the values in \mathbf{r}_m are distributed as complex Normal $\mathcal{N}(\mathbf{X}_m \boldsymbol{\alpha}_m, \sigma^2 \mathbf{I}_{N \times N})$ with $\mathbf{I}_{N \times N}$ denoting the N -dimensional identity matrix. The probability density function in log domain follows as

$$\begin{aligned} \log p(\mathbf{r}_m) &= -N \log(\pi \sigma^2) \\ &\quad - \frac{1}{\sigma^2} (\mathbf{r}_m - \mathbf{X}_m \boldsymbol{\alpha}_m)^H (\mathbf{r}_m - \mathbf{X}_m \boldsymbol{\alpha}_m). \end{aligned} \quad (6)$$

Neglecting the constants, a log likelihood function L^{sa} for single-antenna measurements would be

$$L^{\text{sa}}(\mathbf{r}_m; \boldsymbol{\alpha}_m, \boldsymbol{\tau}, \boldsymbol{\phi}) = -\frac{1}{\sigma^2} (\mathbf{r}_m - \mathbf{X}_m \boldsymbol{\alpha}_m)^H (\mathbf{r}_m - \mathbf{X}_m \boldsymbol{\alpha}_m) \quad (7)$$

where we identify the phase-offset and MPC parameters as the unknowns in the log likelihood function.

We propose to estimate $\hat{\boldsymbol{\alpha}}_m$ conditioned on $\boldsymbol{\tau}$ and $\boldsymbol{\phi}$ by maximization of the log likelihood function according to

$$\frac{\partial L^{\text{sa}}(\mathbf{r}_m; \boldsymbol{\alpha}_m, \boldsymbol{\tau}, \boldsymbol{\phi})}{\partial \boldsymbol{\alpha}_m} = \frac{-2}{\sigma^2} (\mathbf{X}_m^H \mathbf{r}_m - \mathbf{X}_m^H \mathbf{X}_m \boldsymbol{\alpha}_m). \quad (8)$$

Setting the derivative to zero, the ML solution $\hat{\boldsymbol{\alpha}}_m^{\text{sa}}$ results in

$$\hat{\boldsymbol{\alpha}}_m^{\text{sa}} = (\mathbf{X}_m^H \mathbf{X}_m)^{-1} \mathbf{X}_m^H \mathbf{r}_m. \quad (9)$$

In the special case of non-overlapping MPCs, i.e. $\mathbf{s}_{\tau_1}^H \mathbf{s}_{\tau_2} = 0$ for any $\tau_1 \neq \tau_2$, the amplitudes $\hat{\boldsymbol{\alpha}}_m^{\text{sa}} = [\hat{\alpha}_{1,m}^{\text{sa}}, \dots, \hat{\alpha}_{K,m}^{\text{sa}}]$ in (9) can be calculated independently according to

$$\hat{\alpha}_{k,m}^{\text{sa}} = \frac{b_m^*(\phi_k)}{|b_m(\phi_k)|^2} \frac{\mathbf{s}_{\tau_k}^H \mathbf{r}_m}{\|\mathbf{s}_{\tau_k}\|^2} \quad (10)$$

demonstrating the impact of the beampattern on the estimation of $\hat{\alpha}_{k,m}^{\text{sa}}$. Plugging (4) in (10) demonstrates that the amplitude estimate attains the true one according to

$$\hat{\alpha}_{k,m}^{\text{sa}} = \alpha_{k,m} + \frac{1}{b_m(\phi_k)} \frac{\mathbf{s}_{\tau_k}^H \mathbf{w}_m}{\|\mathbf{s}_{\tau_k}\|^2}. \quad (11)$$

Note, we can identify the second term on the right-hand-side of (11) as error term calculated as projection of the additive noise \mathbf{w}_m on the normalized transmitted signal $\mathbf{s}_{\tau_k} / \|\mathbf{s}_{\tau_k}\|^2$. Its scaling by the inverse of the beampattern can be

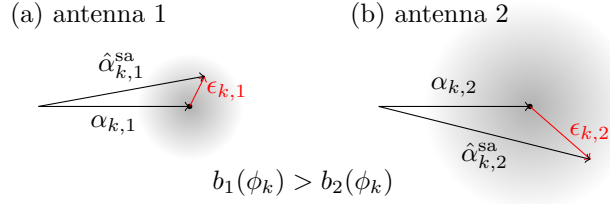


Figure 2: Illustration of single-antenna amplitude estimate comparing antennas $m = 1$ (a) and $m = 2$ (b) where $b_1(\phi_k) > b_2(\phi_k)$. As shown in (11) the amplitude estimates can be decomposed into a true α_k plus an additive noise term $\epsilon_{k,m} = \frac{1}{b_m(\phi_k)} \mathbf{s}_{\tau_k}^H \mathbf{w}_m / \|\mathbf{s}_{\tau_k}\|^2$ which is zero-mean complex Gaussian distributed (indicated by the black circles). The increased amplitude gain by the beampattern of (a) compared to (b) is reflected in a more robust amplitude estimation.

interpreted as an undesired noise gain. We can conclude that MPCs with arriving angles ϕ within the antenna's mainlobe ($|b(\phi)|$ is large) are subject to less interference by additive noise, as illustrated in Figure 2.

Using an appropriate geometry model, the MPC parameters τ_k and ϕ_k in (7) can be expressed as function of anchor \mathbf{a} and hypothesized agent position $\tilde{\mathbf{p}}$. Furthermore, we employ (9) for the amplitude in (7) which enables to define the likelihood function parametrized solely on the hypothesized agent position $\tilde{\mathbf{p}}$, such that

$$L^{\text{sa}}(\mathbf{r}_m; \tilde{\mathbf{p}}) \triangleq L^{\text{sa}}(\mathbf{r}_m; \hat{\boldsymbol{\alpha}}_m^{\text{sa}}, \boldsymbol{\tau}, \phi). \quad (12)$$

It is an interesting finding that antenna m 's beampattern affects the estimation of the amplitudes in (10) but its impact is canceled out once we plug the amplitude estimate in the likelihood function (12). Hence, the direction information provided by the beampatterns cannot be used when only a single-antenna measurement is considered.

2.2.2 Non-phase-coherent ML position estimate

We proposed to employ the ML criterion to estimate the agent position using the measured \mathbf{r}_m . Keeping in mind that at non-phase-coherent measurements the phase-offsets $e^{j\varphi_m}$ are inaccessible, the MPC amplitudes need to be estimated for each m independently. Therefore, we define the non-phase-coherent position estimate $\hat{\mathbf{p}}^{\text{ncoh}}$ which maximizes the sum of the single-antenna log likelihood functions according to

$$\hat{\mathbf{p}}^{\text{ncoh}} = \arg \max_{\tilde{\mathbf{p}}} \sum_{m=1}^M L^{\text{sa}}(\mathbf{r}_m; \tilde{\mathbf{p}}). \quad (13)$$

Since the non-phase-coherent likelihood function has no access to angle information, the main information source are the MPC delays which are used to find the agent position (see Figure 1). Maximization of $\sum_{m=1}^M L^{\text{sa}}(\mathbf{r}_m; \tilde{\mathbf{p}})$ requires the evaluation of $\tilde{\mathbf{p}}$ at feasible positions (e.g. any point in the communication

range to the anchor). Note that each $L^{\text{sa}}(\mathbf{r}_m; \tilde{\mathbf{p}})$ employs a local amplitude estimate α_m^{sa} which limits the potential performance gain of (13). In the following we derive a position estimate seeking for a global α .

2.3 Phase-coherent ML estimate

2.3.1 Likelihood function for multiple antennas

Deriving a likelihood function for multiple antennas is straightforward. Each antenna measurement provides additional information of the MPC amplitudes. Hence, we can model the channel measurements as

$$\mathbf{r} = \Phi \mathbf{X} \alpha + \mathbf{w} \quad (14)$$

with

$$\mathbf{r} = \begin{bmatrix} \mathbf{r}_1 \\ \vdots \\ \mathbf{r}_M \end{bmatrix}, \Phi = \begin{bmatrix} e^{j\varphi_1} \mathbf{I}_{N \times N} & & 0 \\ & \ddots & \\ 0 & & e^{j\varphi_M} \mathbf{I}_{N \times N} \end{bmatrix}$$

$$\mathbf{X} = \begin{bmatrix} \mathbf{X}_1 \\ \vdots \\ \mathbf{X}_M \end{bmatrix} = \begin{bmatrix} b_1(\phi_1) \mathbf{s}_{\tau_1} & \dots & b_1(\phi_K) \mathbf{s}_{\tau_K} \\ \vdots & & \vdots \\ b_M(\phi_1) \mathbf{s}_{\tau_1} & \dots & b_M(\phi_K) \mathbf{s}_{\tau_K} \end{bmatrix}, \mathbf{w} = \begin{bmatrix} \mathbf{w}_1 \\ \vdots \\ \mathbf{w}_M \end{bmatrix}$$

where $\Phi \in \mathbb{C}^{MN \times MN}$ accounts for the phase-offsets. From (14) the values in \mathbf{r} are distributed as complex Normal $\mathcal{N}(\Phi \mathbf{X} \alpha, \sigma^2 \mathbf{I}_{MN \times MN})$. The log likelihood function $L^{\text{ma}}(\mathbf{r}; \tilde{\mathbf{p}})$ for multiple antennas is derived equivalent to the single-antenna ones according to

$$L^{\text{ma}}(\mathbf{r}; \tilde{\mathbf{p}}) = -\frac{1}{\sigma^2} (\mathbf{r} - \Phi \mathbf{X} \hat{\alpha}^{\text{ma}})^H (\mathbf{r} - \Phi \mathbf{X} \hat{\alpha}^{\text{ma}}) \quad (15)$$

with amplitude estimate

$$\hat{\alpha}^{\text{ma}} = (\mathbf{X}^H \mathbf{X})^{-1} \mathbf{X}^H \Phi^H \mathbf{r}. \quad (16)$$

In contrast to (12), the multiple antenna likelihood takes advantage of the beam-pattern (contained in \mathbf{X}) but requires a known phase-offset Φ .

To get more insight in the derived likelihood function, we assume non-overlapping MPCs which enables to rewrite (16) as

$$\hat{\alpha}_k = c \sum_{m=1}^M e^{-j\varphi_m} b_m^*(\phi_k) \mathbf{s}_{\tau_k}^H \mathbf{r}_m. \quad (17)$$

with normalization factor

$$c = \frac{1}{\sum_{m=1}^M |b_m(\phi_k)|^2 \|\mathbf{s}_{\tau_k}\|^2} \quad (18)$$

The sum on the right-hand-side of (17) can be interpreted as weighted average of the projection of the measured signal \mathbf{r}_m onto the delayed, transmitted signal

\mathbf{s}_{τ_k} . The beampattern $b_m^*(\phi_k)$ accounts for the weighting and the phase-offset $e^{-j\varphi_m}$ is required for phase-coherent averaging.

To give an impression regarding the relation between single and multiple antenna amplitude estimates, we identify (10) in (17) yielding

$$\hat{\alpha}_k = c \sum_{m=1}^M e^{-j\varphi_m} \|\mathbf{s}_{\tau_k}\|^2 |b_m(\phi_k)|^2 \hat{\alpha}_{k,m}^{\text{sa}}. \quad (19)$$

Hence, $\hat{\alpha}_k$ can be interpreted as weighted average of the single-antenna amplitudes $\hat{\alpha}_{k,m}^{\text{sa}}$. The weighting by the beampattern counteracts the adverse effect of noise gain in (11).

2.3.2 Phase-coherent position estimate

Having phase-coherent measurements at hand, i.e. φ_m are known, we can obtain $L^{\text{ma}}(\mathbf{r}; \tilde{\mathbf{p}})$, and the estimated agent position $\hat{\mathbf{p}}^{\text{coh}}$ follows accordingly

$$\hat{\mathbf{p}}^{\text{coh}} = \arg \max_{\tilde{\mathbf{p}}} L^{\text{ma}}(\mathbf{r}; \tilde{\mathbf{p}}). \quad (20)$$

We can conclude that the amplitudes in $L^{\text{ma}}(\mathbf{r}; \tilde{\mathbf{p}})$ are estimated in a phase-coherent fashion. Thus, the vital beampattern information became accessible but its deployment is limited to known phase-offsets.

3 Beampattern assisted non-phase-coherent position estimate

In this work we make use of the antenna beampattern and simultaneously consider the phase-offset as nuisance. We propose to use (13) but exchange the amplitude estimation (9) by considering a weighted average of amplitudes, similar to (17). Rather than processing the complex-valued beampattern information, we propose to average only the absolute values and keep the noisy phase of the individual measurements [14].

We define an optimization problem, motivated by (13), according to

$$\hat{\mathbf{p}}^{\text{pro}} = \arg \max_{\tilde{\mathbf{p}}} \sum_{m=1}^M \ell^{\text{pro}}(\mathbf{r}_m; \tilde{\mathbf{p}}) \quad (21)$$

where ℓ^{pro} follows similar to (7) as

$$\ell^{\text{pro}}(\mathbf{r}_m; \tilde{\mathbf{p}}) = -\frac{1}{\sigma^2} (\mathbf{r}_m - \mathbf{X}_m \boldsymbol{\alpha}_m^{\text{avg}})^H (\mathbf{r}_m - \mathbf{X}_m \boldsymbol{\alpha}_m^{\text{avg}}). \quad (22)$$

The required amplitudes $\boldsymbol{\alpha}_m^{\text{avg}}$ are estimated as follows.

3.1 Estimation of amplitudes

We aim at calculating MPC amplitudes $\boldsymbol{\alpha}_m^{\text{avg}}$ for each m which preserve the phase-offset of m while considering their beampattern. Let $\boldsymbol{\alpha}_m^{\text{avg}} = [\alpha_{1,m}^{\text{avg}}, \dots, \alpha_{K,m}^{\text{avg}}]^T$ then the amplitude of the k th MPC and m th antenna follows as

$$\alpha_{k,m}^{\text{avg}} = |\alpha_k^{\text{avg}}| e^{j\angle \alpha_{k,m}^{\text{sa}}}. \quad (23)$$

We propose to estimate the amplitude's absolute value $|\alpha_k^{\text{avg}}|$ and corresponding phase $e^{j\angle\alpha_k^{\text{sa}}}$ independently¹. Starting with $|\alpha_k^{\text{avg}}|$ we seek for a weighted average using the provided beampattern information. Motivated by the phase-coherent amplitude estimate in (19) we exchange the complex-valued average by an absolute-valued average, by defining

$$\begin{aligned} |\alpha_k^{\text{avg}}| &\triangleq c \sum_{m=1}^M \left| e^{-j\varphi_m} \|\mathbf{s}_{\tau_k}\|^2 |b_m(\phi_k)|^2 \hat{\alpha}_{k,m}^{\text{sa}} \right| \\ &= c \sum_{m=1}^M \|\mathbf{s}_{\tau_k}\|^2 |b_m(\phi_k)|^2 |\hat{\alpha}_{k,m}^{\text{sa}}|. \end{aligned} \quad (24)$$

Having a weighted average of amplitudes, the corresponding phase $e^{j\angle\alpha_k^{\text{sa}}}$ follows from the single-antenna estimates (9).

3.2 Insights

We are interested in the behavior of the amplitude approximation (23). Plugging (10) and (24) in (23) results in

$$\alpha_{k,m}^{\text{avg}} = ce^{j\angle b_m^*(\phi_k) \mathbf{s}_{\tau_k}^H \mathbf{r}_m} \sum_{m'=1}^M |b_{m'}^*(\phi_k) \mathbf{s}_{\tau_k}^H \mathbf{r}_{m'}| \quad (25)$$

and plugging (4) in (25) yields

$$\alpha_{k,m}^{\text{avg}} = \alpha_k e^{j\varphi_m} \chi_{k,m} \quad (26)$$

where the multiplicative term $\chi_{k,m}$ accounts for the induced error due to the approximation in (23). In case of non-overlapping MPCs, $\chi_{k,m}$ can be formulated as

$$\chi_{k,m} = \frac{\sum_{m'=1}^M |b_{m'}(\phi_k)|^2 \|\mathbf{s}_{\tau_k}\|^2 |1 + \xi_{k,m'}^{-1}|}{\sum_{m'=1}^M |b_{m'}(\phi_k)|^2 \|\mathbf{s}_{\tau_k}\|} e^{j\angle(1 + \xi_{k,m}^{-1})} \quad (27)$$

where $\xi_{k,m}$ can be interpreted similar to a signal to noise ratio as

$$\xi_{k,m} = \frac{e^{j\varphi_m} b_m(\phi_k) \alpha_k \|\mathbf{s}_{\tau_k}\|^2}{\mathbf{s}_{\tau_k}^H \mathbf{w}}. \quad (28)$$

It can be shown that for increasing $\xi_{k,m}$ the error term $\chi_{k,m}$ attains a value of one showing that $\alpha_{k,m}^{\text{avg}}$ asymptotically attains the true $e^{j\varphi_m} \alpha_k$

$$\alpha_{k,m}^{\text{avg}} \xrightarrow{\xi_{k,m} \rightarrow \infty} e^{j\varphi_m} \alpha_k \quad (29)$$

In case of overlapping MPCs $\xi_{k,m}$ contains additional cross terms stemming from $\mathbf{s}_{\tau_k}^H \mathbf{X}_m$ in (25). These cross terms can be interpreted as additional bias in $\xi_{k,m}$ which hinders to attain to the true amplitudes.

¹An iterative optimization scheme would be necessary to estimate a single φ_m per antenna and use (16) to estimate the complex amplitudes. Thus we opted for the simple closed-form expression presented above.

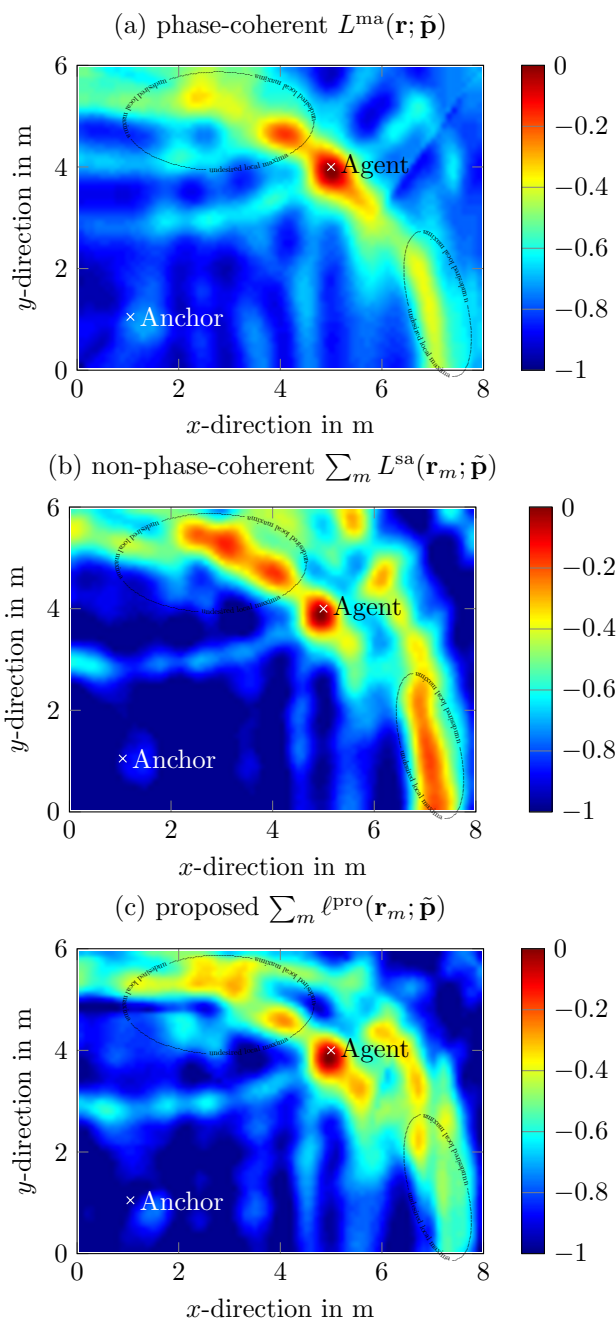


Figure 3: Evaluated log likelihood function $L^{\text{ma}}(\mathbf{r}; \tilde{\mathbf{p}})$, shown in (a), $\sum_m L^{\text{sa}}(\mathbf{r}_m; \tilde{\mathbf{p}})$ (b) and $\sum_m \ell^{\text{pro}}(\mathbf{r}_m; \tilde{\mathbf{p}})$ (c) for various positions $\tilde{\mathbf{p}}$. The coherent amplitude estimate in (16) (a) utilizes the antennas beampattern which results in a strong global maximum at the true agent position while suppressing neighboring local maxima. The independent estimation of the MPC amplitudes, shown in (b), ignores the vital information provided by the beampattern, resulting in several strong local maxima in the likelihood function. Averaging of absolute MPC amplitudes using (24) (c) reveals a performance gain compared to independent estimation (Fig. 3b). Local maxima are strongly reduced and the global maximum is clearly located at the agent's true location.

3.3 Implementation

The amplitudes used in (22) are calculated using (23) where the elements $\hat{\alpha}_{k,m}^{\text{sa}}$ in (23) and (24) are taken from the single-antenna measurements using (9). Note, overlapping multipath is reflected in non-orthogonal columns in \mathbf{X}_m troubling the matrix inversion in (9). Therefore, in case of path overlap we exchange (9) and estimate the amplitudes iteratively as explained in the following: Starting with the first MPC $k = 1$ we estimate only one amplitude $\hat{\alpha}_{1,m}$ using (10). We continue by subtracting the estimated MPC $\hat{\alpha}_{1,m}\mathbf{s}_{\tau_1}$ from the measurement \mathbf{r}_m . Then, the second MPC's amplitude $\hat{\alpha}_{2,m}$ is estimated from \mathbf{r}_m (where the first MPC is already subtracted). This procedure (estimation and subtraction) is continued until K is reached. In this way we can circumvent the issue of overlapping paths. We use the iterative amplitude estimation if there is at least one pair of MPC delays $\tau_k, \tau_{k'}$ with (heuristically chosen) distance below $|\tau_k - \tau_{k'}| < \frac{1}{4}T_p$ with pulse duration T_p .

A comparison in terms of computational costs reveals similar complexity of the proposed method and the non-phase-coherent method. Additional costs are justified by the MK multiplications in (23) and K times $M - 1$ multiply and add operations in (24).

4 Evaluation

Our evaluation is twofold. First, we provide a qualitative comparison of the derived likelihood functions and proceed with a quantitative evaluation of the achieved position accuracy. For the evaluation of the likelihood functions we generated an indoor scenario with an anchor located at $\mathbf{a} = [1, 1]^T$ m and an agent at $\mathbf{p} = [5, 4]^T$ m, both placed inside a rectangular room with dimensions 8×6 m. To ensure a realistic scenario we employ the directive antenna from [7] with known complex-valued beampattern $b_m(\phi)$ scaled to $\max_{\phi}|b_m(\phi)| = 1$. The antenna's half-power beamwidth is roughly 90° along the azimuth angle. We use $M = 4$ antennas, circularly assembled in $360^\circ/M = 90^\circ$ steps. The multipath parameters are obtained as follows: the MPC delay and angle are calculated using the geometry model in [13]. The MPC amplitude is attenuated by -3 dB at each reflection point. The path loss is considered using Friis' equation which scales the amplitude with the inverse of the path length. We model single reflections resulting in a line-of-sight (LOS) plus four reflections. As transmitted pulse we employ a raised cosine signal with $T_p = 2.4$ ns and roll-off factor $R = 0.9$, sampled at $T_s = 1.0016$ ns. Note, in [15] those parameters were identified to describe IEEE 802.15.4 (2011) Channel 2 of the DecaWave DW1000 UWB radio. The variance $\sigma^2 = N_0/T_s$ of the Gaussian noise $w_m[n]$ was set to a signal-to-noise-ratio $\frac{|\alpha|^2 \|\mathbf{s}_\tau\|^2}{N_0}$ equal to 30 dB for a path distance of 1 m.

The derived position estimates $\hat{\mathbf{p}}^{\text{coh}}$, $\hat{\mathbf{p}}^{\text{ncoh}}$ and $\hat{\mathbf{p}}^{\text{pro}}$ are based on the likelihoods in (15), (12) and (22), respectively, which justifies the importance of well-conditioned likelihood functions, i.e. single unique maxima while suppressing neighboring local maxima. In this qualitative comparison we illustrate the likelihood functions for the phase-coherent in (15) (Figure 3a) and non-phase-coherent case $\sum_m L^{\text{sa}}(\mathbf{r}_m; \hat{\mathbf{p}})$ (Figure 3b) in comparison with the proposed method $\sum_m \ell^{\text{pro}}(\mathbf{r}_m; \hat{\mathbf{p}})$ (Figure 3c).

The comparison between the phase-coherent and non-phase-coherent likelihood functions (Figures 3a and 3b) reveals the importance of the beampattern, used in $L^{\text{ma}}(\mathbf{r}; \tilde{\mathbf{p}})$. Its outcome is characterized by a strong global maxima at the true agent position. Local maxima in the vicinity of the true agent position are strongly suppressed. This enables a reliable position estimate using the ML scheme (15) applied to $L^{\text{ma}}(\mathbf{r}; \tilde{\mathbf{p}})$. In contrast, the likelihood $\sum_m L^{\text{sa}}(\mathbf{r}_m; \tilde{\mathbf{p}})$ for non-phase-coherent suffers due to the inaccessible beampattern information resulting in several local maxima in $\sum_m L^{\text{sa}}(\mathbf{r}_m; \tilde{\mathbf{p}})$. These local maxima deteriorate the position accuracy especially at low SNRs.

The proposed method $\sum_m \ell^{\text{pro}}(\mathbf{r}_m; \tilde{\mathbf{p}})$ employs the approximation in (23) to make use of the beampattern while preserving non-phase-coherent processing. The fair comparison between both non-phase-coherent methods in Figures 3b and 3c shows the potential performance gain. The global maximum is clearly visible at the true agent position and neighboring local maxima are suppressed. The remarkable likelihood outcome attains a similar performance as $L^{\text{ma}}(\mathbf{r}; \tilde{\mathbf{p}})$ (Fig. 3) without the need of phase-coherent processing.

We proceed with a quantitative evaluation of the proposed algorithm in comparison with phase-coherent position estimates. We randomly place the agent position \mathbf{p} inside the rectangular room from the previous evaluation and keep the anchor node fixed at $\mathbf{a} = [1, 1]^T$ m. We repeat the experiment 1000 times and calculate the ML solutions $\hat{\mathbf{p}}^{\text{coh}}$, $\hat{\mathbf{p}}^{\text{ncoh}}$ and $\hat{\mathbf{p}}^{\text{pro}}$. Furthermore, we compute a lower bound on the root mean square position error based on the Cramér-Rao inequality at each of the evaluated positions. We evaluated the functions for points $\tilde{\mathbf{p}}$ on a grid with 25×25 cm spacing, resulting in 9 sampling points/m². Figure 4 exemplifies the cumulative distribution function (CDF) of the position error. The phase-coherent position estimate $\hat{\mathbf{p}}^{\text{coh}}$ (dashed, black) achieves the smallest position errors due to its access to known phase- offsets. Both $\hat{\mathbf{p}}^{\text{ncoh}}$ (dash-dotted, green) and $\hat{\mathbf{p}}^{\text{pro}}$ (solid, blue) are based on non-coherent processing. This information loss leads to a performance degradation especially for $\hat{\mathbf{p}}^{\text{ncoh}}$. In contrast, the results of the proposed method outperform the competitive method $\hat{\mathbf{p}}^{\text{ncoh}}$, and is able to diminish the gap towards the results of $\hat{\mathbf{p}}^{\text{coh}}$ without the requirement of known phase-offsets.

Finally, we employ the algorithms on real measured data, taken from [7]. The measurements were performed in a laboratory room with dimensions of 6×8 m, as illustrated in [7, Figure 1]. For a fair comparison we choose same signal parameters $T_p = 2.4$ ns, $R = 0.9$ and carrier frequency $f_c = 5.4$ GHz as in [7]. The CDF of the position error is shown in Fig. 5. The proposed method (solid, blue) outperforms the non-phase-coherent position estimate (dash-dotted, green). Although no access to phase-offsets is provided, the proposed method is able to approach the phase-coherent position estimate (dotted, black) with only a minor performance loss. We can observe that 90 % of the errors are below 40 cm.

From our results based on real and computer generated data we can conclude that the additional costs for phase-coherent measurements need to be carefully reconsidered when facing the outperforming results of the proposed method.

5 Conclusion

In this work we have developed an algorithm capable of high-accuracy indoor positioning, demanding a single-anchor setup only. We elaborate the impact of

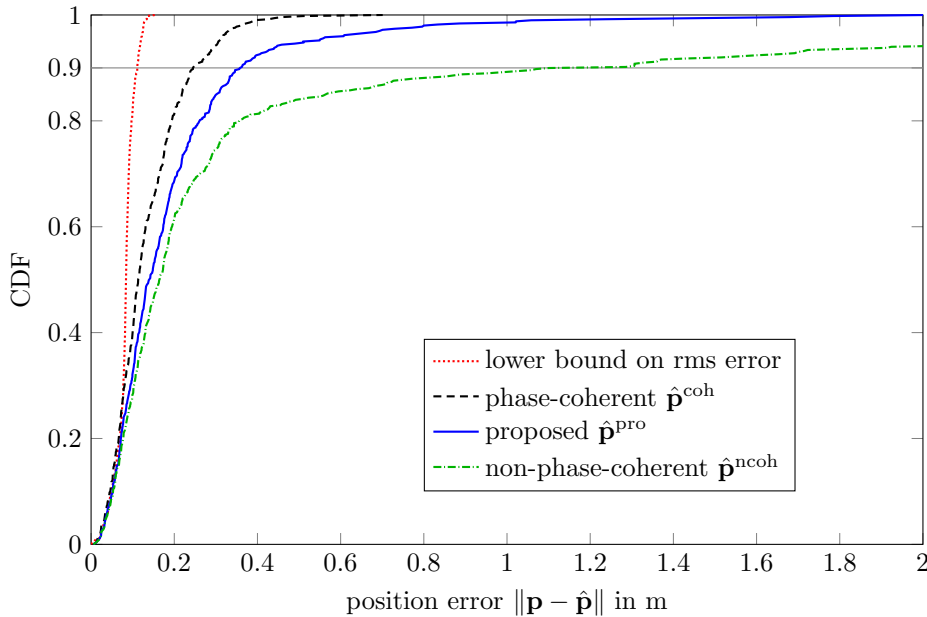


Figure 4: CDF of phase-coherent $\hat{\mathbf{p}}^{\text{coh}}$, non-phase-coherent $\hat{\mathbf{p}}^{\text{ncoh}}$ and of the proposed position estimate $\hat{\mathbf{p}}^{\text{pro}}$ using computer generated data.

phase-coherent measurements for joint MPC amplitude estimates. Our analysis unveiled the possibility to circumvent the necessity of phase-coherent measurements while minimizing the penalty on the position performance.

References

- [1] Y. Shen and M. Z. Win, “Fundamental limits of wideband localization—part I: A general framework,” vol. 56, no. 10, pp. 4956–4980, Oct. 2010.
- [2] E. Leitinger, P. Meissner, C. Rudisser, G. Dumphart, and K. Witrisal, “Evaluation of position-related information in multipath components for indoor positioning,” *IEEE JSAC*, vol. 33, no. 11, pp. 2313–2328, Nov. 2015.
- [3] P. Meissner, D. Arnitz, T. Gigl, and K. Witrisal, “Analysis of an indoor UWB channel for multipath-aided localization,” in *IEEE Intern. Conf. on Ultra-Wideband, ICUWB*, Bologna, Italy, Sep. 2011.
- [4] Y. Han, Y. Shen, X. P. Zhang, M. Z. Win, and H. Meng, “Performance limits and geometric properties of array localization,” vol. 62, no. 2, pp. 1054–1075, Feb. 2016.
- [5] G. Giorgetti, A. Cidronali, S. K. S. Gupta, and G. Manes, “Single-anchor indoor localization using a switched-beam antenna,” *IEEE Communications Letters*, vol. 13, no. 1, pp. 58–60, January 2009.
- [6] H. Zhang, X. Cui, B. An, and T. A. Gulliver, “A distance and angle estimated method based on single UWB station,” in *2013 IEEE Interna-*

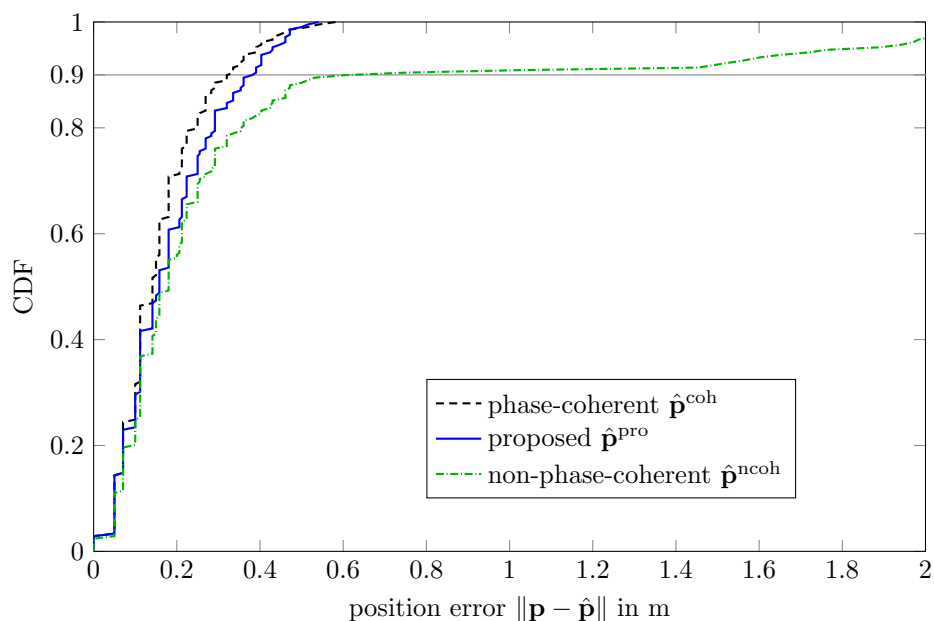


Figure 5: CDF of phase-coherent $\hat{\mathbf{p}}^{\text{coh}}$, non-phase-coherent $\hat{\mathbf{p}}^{\text{ncoh}}$ and of the proposed position estimate $\hat{\mathbf{p}}^{\text{pro}}$ using measured data from [7].

tional Conference on Signal Processing, Communication and Computing (ICSPCC 2013), Aug 2013, pp. 1–6.

- [7] M. Rath, J. Kulmer, M. S. Bakr, B. Großwindhager, and K. Witrals, “Multipath-assisted indoor positioning enabled by directional UWB sector antennas,” in *18th IEEE International Workshop on Signal Processing Advances in Wireless Communications, SPAWC*, 2017.
- [8] BeSpoon, *UM100 Evaluation Kit Quick Start Guide*, BeSpoon, 2015.
- [9] DecaWave, *DW1000 User Manual, Version 2.05*, DecaWave, 2015.
- [10] K. W. *et al.*, “High-accuracy localization for assisted living: 5g systems will turn multipath channels from foe to friend,” *IEEE MSP*, vol. 33, no. 2, pp. 59–70, March 2016.
- [11] J. B. Allen and D. A. Berkley, “Image method for efficiently simulating small-room acoustics,” *The Journal of the Acoustical Society of America*, vol. 65, no. 4, pp. 943–950, 1979.
- [12] J. Borish, “Extension of the image model to arbitrary polyhedra,” *The Journal of the Acoustical Society of America*, vol. 75, no. 6, 1984.
- [13] J. Kulmer, E. Leitinger, S. Grebien, and K. Witrals, “Anchorless cooperative tracking using multipath channel information,” *IEEE Transactions on Wireless Communications*, 2018.

- [14] P. Mowlaee, J. Kulmer, J. Stahl, and F. Mayer, *Single Channel Phase-Aware Signal Processing in Speech Communication: Theory and Practice*. Wiley, 2016.
- [15] J. Kulmer, S. Hinteregger, B. Grosswindhager, M. Rath, M. Bakr, E. Leitinger, and K. Witrissal, “Using DecaWave UWB transceivers for high-accuracy multipath-assisted indoor positioning,” in *ICC2017: WT03-5th IEEE ICC Workshop on Advances in Network Localization and Navigation (ANLN) (ICC2017-WT03)*, Paris, France, May 2017, pp. 219–225.

Cooperative Multipath-assisted Navigation and Tracking: A Low-Complexity Approach

Josef Kulmer, Erik Leitinger, Paul Meissner, Klaus Witrisal

presented at 1st EAI International Conference on Future access enablers of ubiquitous and intelligent infrastructures, 2015

Abstract

Wireless localization has become a key technology for cooperative agent networks. However, for many applications, it is still illusive to reach the desired level of *accuracy* and *robustness*, especially in indoor environments which are characterized by harsh multipath propagation. In this work we introduce a cooperative low-complexity algorithm that utilizes multipath components for localization instead of suffering from them. The algorithm uses two types of measurements: (i) *bistatic* measurements between agents and (ii) *monostatic* (bat-like) measurements by the individual agents. Simulations that use data generated from a realistic channel model, show the applicability of the methodology and the high level of accuracy that can be reached.

1 Introduction

Location awareness is a key component of many future wireless applications. However, achieving the needed level of accuracy is still elusive in many cases, especially in indoor environments which are characterized by harsh multipath conditions. Promising candidate systems thus either use sensing technologies that provide remedies against multipath or they fuse information from multiple information sources [10, 1].

In *Multipath-assisted indoor navigation and tracking (MINT)* [6, 4] multipath components (MPCs) can be associated to the local geometry using a known floor plan. In this way, MPCs can be seen as signals from additional (virtual) anchors (VAs). Ultra-wideband (UWB) signals are used because of their superior time resolution facilitating the separation of MPCs. Hence, additional position-related information is exploited that is contained in the radio signals. All other—not geometrically modelled—propagation effects included in the signals constitute interference to the useful position-related information and are called diffuse multipath (DM) [8]. Insight on the position-related information that is conveyed in the signals can be gained by an analysis of performance bounds, such as the Cramér-Rao lower bound (CRLB) [4]. In [4], the CRLB for cooperative MINT was derived using *bistatic* measurements between agents and *monostatic* measurements from an agent itself. The same measurement model will be used in this work. Cooperation between agents is another method to increase the amount of available information [11] and thus to reduce the localization outage. In this work, we present a low-complexity variant of [2] that is based on data-association (DA) and extended Kalman filtering (EKF) [7]. The method relies on the same factor graph as presented in [2], but in contrast it just uses the extracted MPC delays and complex path amplitudes¹ instead of the complete received signals. The key contributions of this paper are (i) incorporate VAs into a joint state space with the agents, and (ii) formulate the cooperative algorithm that uses DA of MPC delays with according VAs and an EKF for tracking the joint state of the agents and the according VAs.

2 Problem Formulation

We assume M agents at positions $\mathbf{p}_1^{(m)}$ with $m \in \mathcal{N}_m = \{1, 2, \dots, M\}$, which cooperate with one another. As outlined in the introduction, every agent conducts a monostatic measurement, meaning it emits a pulse and receives the multipath signal reflected by the environment, and conventional bistatic measurements with all other agents and the fixed anchors. All bistatic and monostatic measurements are distributed such that every agent is able to exploit information from any of its received and/or transmitted signals.

Fig. 1 illustrates the geometric model for multipath-assisted positioning. A signal exchanged between the agents m' and m at positions $\mathbf{p}_1^{(m')}$ and $\mathbf{p}_1^{(m)}$, respectively, contains specular reflections at the room walls, indicated by the black lines. These reflections can be modeled geometrically using VAs $\mathbf{p}_k^{(m')}$, mirror images of the anchor w.r.t. walls that can be computed from the floor

¹These are used to compute online, the reliability measure of the MPCs in form a signal-to-interference-plus-noise-ratio (SINR) that is used to compute the according MPC's delay uncertainty.

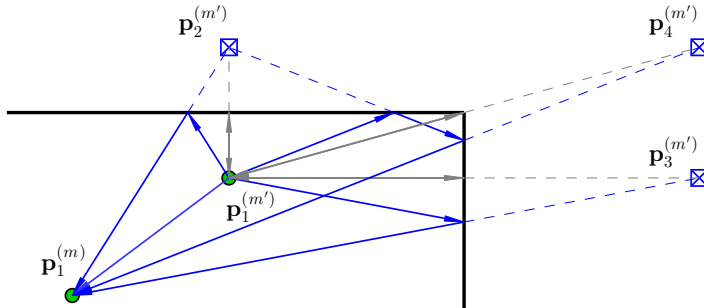


Figure 1: Illustration of multipath geometry using VAs for (i) bistatic transmissions (blue) between an agents and for (ii) a monostatic measurement (gray) by an agent.

plan [6]. We call this the bistatic setup. If the agents are equipped accordingly, they can use monostatic measurements, indicated by the gray lines. Here, the node at $\mathbf{p}_k^{(m')}$ acts as anchor for itself with its own set of VAs.

2.1 Signal Model

In this Section, we simplify the setup—for the ease of readability—to a single (fixed) anchor located at position $\mathbf{p}_1 \in \mathbb{R}^2$ and one agent at position $\mathbf{p} \in \mathbb{R}^2$. Note that two-dimensional position coordinates are used throughout the paper, for the sake of simplicity. A *baseband* UWB signal $s(t)$ is exchanged between the anchor and the agent. The corresponding received signal is modeled as [4]

$$r(t) = \sum_{k=1}^K \alpha_k s(t - \tau_k) + (s * \nu)(t) + w(t) \quad (1)$$

where $\{\alpha_k\}$ and $\{\tau_k\}$ are the complex amplitudes and delays of the deterministic MPCs, respectively. We model these delays by VAs at positions $\mathbf{p}_k \in \mathbb{R}^2$, yielding $\tau_k = \frac{1}{c} \|\mathbf{p} - \mathbf{p}_k\| = \frac{1}{c} d(\mathbf{p}_k, \mathbf{p})$, with $k = 1 \dots K$, where c is the speed of light and $d(\cdot)$ is the Euclidean distance. K is equivalent to the number of visible VAs at the agent position \mathbf{p} . We assume the energy of $s(t)$ is normalized to one.

The DM $(s * \nu)(t)$ is modeled as a zero-mean Gaussian random process which is non-stationary in the delay domain and colored due to the spectrum of $s(t)$. For DM we assume uncorrelated scattering along the delay axis τ , hence the auto-correlation function (ACF) of $\nu(t)$ is given by $K_\nu(\tau, u) = \mathbb{E}_\nu \{\nu(\tau)[\nu(u)]^*\} = S_\nu(\tau)\delta(\tau - u)$, where $S_\nu(\tau)$ is the PDP of DM at the agent position \mathbf{p} . The DM process is assumed to be quasi-stationary in the spatial domain, which means that $S_\nu(\tau)$ does not change in the vicinity of position \mathbf{p} [4]. Finally, $w(t)$ denotes an additive white Gaussian noise (AWGN) process with double-sided power spectral density (PSD) of $N_0/2$.

2.2 Channel Estimation

The arrival time estimation $\hat{\tau}_{k,n}^{(m,m')}$ at time step n between two agents at positions $\mathbf{p}_{1,n}^{(m)}$ and $\mathbf{p}_{1,n}^{(m')}$, where $m, m' \in \mathcal{N}_m$, is realized as an iterative least-squares approximation of the received signal [7]. The according path amplitudes $\hat{\alpha}_{k,n}^{(m,m')}$ are estimated using a projection of the received signal $r_n^{(m,m')}(t)$ onto a unit-energy pulse $s(t - \hat{\tau}_{k,n}^{(m,m')})$. The number of estimated MPCs $\hat{K}_n^{(m,m')}$ should be chosen according to the number of expected specular paths in an environment. The finite set of measured delays is written as $\mathcal{Z}_n^{(m)} = \bigcup_{m'} \mathcal{Z}_n^{(m,m')} = \bigcup_{m'} \{\hat{d}_{k,n}^{(m,m')}\}_{k=1}^{\hat{K}_n^{(m,m')}}$, where $\hat{d}_{k,n}^{(m,m')} = c\hat{\tau}_{k,n}^{(m,m')}$.

2.3 Data Association (DA)

The set of expected MPC delays $\mathcal{D}_n^{(m,m')} = \{d(\mathbf{p}_{n,k}^{(m')}, \mathbf{p}_{1,n}^{(m)}) : \mathbf{p}_{n,k}^{(m,m')} \in \mathcal{A}_n^{(m,m')}\}$ is computed from the distances of each VA in $\mathcal{A}_n^{(m,m')}$ to the predicted position $\mathbf{p}_{1,n}^{(m)}$ of agent m at time step n . As $\mathcal{D}_n^{(m,m')}$ and the set of measured delays $\mathcal{Z}_n^{(m,m')}$ are sets of usually different cardinalities, i.e. $|\mathcal{Z}_n^{(m,m')}| = \hat{K}_n^{(m,m')} \neq |\mathcal{D}_n^{(m,m')}| = K_n^{(m,m')}$, no conventional distance measure is defined and therefore there is no straightforward way of an association. We employ a well-known multi-target miss-distance, the *optimal sub-pattern assignment* (OSPA) metric [9]. As described in [7, 3], after the DA was applied for all agents, the following union sets are defined: (i) the set of associated discovered (and optionally a-priori known) VAs $\mathcal{A}_{n,\text{ass}}^{(m)} = \bigcup_{m'} \mathcal{A}_{n,\text{ass}}^{(m,m')}$, (ii) the corresponding set of associated measurements $\mathcal{Z}_{\text{timestepsym,ass}}^{(m)} = \bigcup_{m'} \mathcal{Z}_{n,\text{ass}}^{(m,m')}$.

3 State Space and Measurement Model

The state dynamics are characterized by a linear, constant-velocity motion model. Each agent $\mathbf{x}_n^{(m)}$ is described by its position $\mathbf{p}_{1,n}^{(m)}$ and velocity $\mathbf{v}_{1,n}^{(m)}$ according to $\mathbf{x}_n^{(m)} = [(\mathbf{p}_{1,n}^{(m)})^T, (\mathbf{v}_{1,n}^{(m)})^T]^T$. The position of the agent is mirrored at a each wall segment in order to obtain the positions of the corresponding VAs $\mathbf{p}_{k,n}^{(m)}$. The orientation of the wall segments determine the relation between the movement gradients of the agent and the corresponding VAs. We describe this relation by introducing a VA transition matrix $\mathbf{P}_k^{(m)}$ (cf. [4]). The state space model for agent m is thus characterized by

$$\tilde{\mathbf{x}}_n^{(m)} = \underbrace{\begin{bmatrix} \mathbf{F} & \mathbf{0}_{4 \times 2K_n} \\ \mathbf{0}_{2K_n \times 2} & \mathbf{P}^{(m)} \end{bmatrix}}_{\tilde{\mathbf{F}}^{(m)}} \tilde{\mathbf{x}}_{n-1}^{(m)} + \underbrace{\begin{bmatrix} \mathbf{G} \\ \mathbf{0}_{2K_n \times 2} \end{bmatrix}}_{\tilde{\mathbf{G}}^{(m)}} \mathbf{n}_{a,n}, \quad (2)$$

with

$$\mathbf{F} = \begin{bmatrix} 1 & 0 & \Delta T & 0 \\ 0 & 1 & 0 & \Delta T \\ 0 & 0 & 1 & 0 \\ 0 & 0 & 0 & 1 \end{bmatrix}, \quad \mathbf{G} = \begin{bmatrix} \frac{\Delta T^2}{2} & 0 \\ 0 & \frac{\Delta T^2}{2} \\ \Delta T & 0 \\ 0 & \Delta T \end{bmatrix},$$

$\tilde{\mathbf{x}}_n^{(m)} = [\mathbf{x}_n^{\text{T}(m)}, \mathbf{p}_{2,n}^{\text{T}(m)}, \dots, \mathbf{p}_{K,n}^{\text{T}(m)}]^{\text{T}}$ and $\mathbf{P}^{(m)} = [\mathbf{P}_2^{\text{T}(m)}, \dots, \mathbf{P}_{K_n}^{\text{T}(m)}]^{\text{T}}$ with dimensions $(2K_n \times 2)$. Under the assumption of independent movement of the agents, the motion model finally results in

$$\underbrace{\begin{bmatrix} \tilde{\mathbf{x}}_n^{(1)} \\ \vdots \\ \tilde{\mathbf{x}}_n^{(M)} \end{bmatrix}}_{\tilde{\mathbf{x}}_n} = \begin{bmatrix} \tilde{\mathbf{F}}^{(1)} & & \mathbf{0} \\ & \ddots & \\ \mathbf{0} & & \tilde{\mathbf{F}}^{(M)} \end{bmatrix} \underbrace{\begin{bmatrix} \tilde{\mathbf{x}}_{n-1}^{(1)} \\ \vdots \\ \tilde{\mathbf{x}}_{n-1}^{(M)} \end{bmatrix}}_{\tilde{\mathbf{x}}_{n-1}} + \begin{bmatrix} \tilde{\mathbf{G}}_n^{(1)} \\ \vdots \\ \tilde{\mathbf{G}}_n^{(M)} \end{bmatrix} \mathbf{n}_{a,n}. \quad (3)$$

The according linearized measurement model is defined as

$$\begin{bmatrix} \tilde{\mathbf{z}}_n^{(1)} \\ \vdots \\ \tilde{\mathbf{z}}_n^{(M)} \end{bmatrix} = \begin{bmatrix} \tilde{\mathbf{H}}_n^{(1)} & & \mathbf{0} \\ & \ddots & \\ \mathbf{0} & & \tilde{\mathbf{H}}_n^{(M)} \end{bmatrix} \begin{bmatrix} \tilde{\mathbf{x}}_n^{(1)} \\ \vdots \\ \tilde{\mathbf{x}}_n^{(M)} \end{bmatrix} + \tilde{\mathbf{n}}_{z,n}. \quad (4)$$

where $\tilde{\mathbf{z}}_n^{(m)}$ stacks the monostatic measurements from the m -th agent and the bistatic measurements to all other agents. The stack vector $\tilde{\mathbf{n}}_{z,n}$ contains the according measurement noise with covariance matrix \mathbf{R}_n described in [7]. The linearized column-wise stacked measurement matrices $\tilde{\mathbf{H}}_n^{(m)} = [(\tilde{\mathbf{H}}_n^{(\eta=1,m)})^{\text{T}}, \dots, (\tilde{\mathbf{H}}_n^{(\eta=M,m)})^{\text{T}}]^{\text{T}}$ are described in (5), with $m, \eta \in \mathcal{N}_m$ and $m \neq \eta$. The matrices $\mathbf{H}_{\xi,\mu,n}^{(\eta,\eta,m)} = [\frac{\partial d(\mathbf{p}_{\mu,n}^{(\eta)}, \mathbf{p}_{1,n}^{(m)})}{\partial x_{\xi,n}^{(\eta)}}, \frac{\partial d(\mathbf{p}_{\mu,n}^{(\eta)}, \mathbf{p}_{1,n}^{(m)})}{\partial y_{\xi,n}^{(\eta)}}]$ define the derivatives of the distance measurements w.r.t. the x - and y -position coordinates. The upper-left sub-block of (5) holds the derivatives of the monostatic measurements w.r.t. the m -th agent position. The upper diagonal sub-block holds the according derivatives w.r.t. to the monostatic VA positions of the m -th agent. The lower-left sub-block holds derivatives of the bistatic measurement equations to all other agent positions and according VA positions ($\eta = 1 \dots M$ and $m \neq \eta$) w.r.t. the m -th agent position. The lower-right diagonal sub-block holds the equivalent derivatives w.r.t. to the according bistatic VA positions.

$$\tilde{\mathbf{H}}_n^{(\eta,m)} = \begin{bmatrix} \mathbf{H}_{1,2,n}^{(m,m,m)} & \mathbf{0} & \mathbf{0} & \mathbf{H}_{2,2,n}^{(m,m,m)} & \dots & \mathbf{0} & \dots & \mathbf{0} \\ \vdots & \vdots \\ \mathbf{H}_{1,K_n,n}^{(m,m,m)} & \mathbf{0} & \mathbf{0} & \mathbf{0} & \dots & \mathbf{H}_{K_n,K_n,n}^{(m,m,m)} & \dots & \mathbf{0} \\ \mathbf{H}_{1,1,n}^{(\eta,m,m)} & \mathbf{0} & \dots & \mathbf{0} & \dots & \mathbf{0} & \dots & \vdots \\ \vdots & \vdots \\ \mathbf{H}_{1,K_n,n}^{(\eta,m,m)} & \mathbf{0} & \mathbf{0} & \mathbf{0} & \dots & \mathbf{0} & \dots & \mathbf{H}_{K_n,K_n,n}^{(\eta,m,m)} \end{bmatrix} \quad (5)$$

4 Results

We evaluate the performance of the proposed algorithm in terms of localization error and computational time using synthetic data in a two-dimensional space. The transmit signal consists of a raised-cosine pulse with a roll-off factor of $R = 0.6$, a pulse duration of $T_p = 0.5$ ns and unit energy. The received signals

of the monostatic and bistatic measurements are modeled according to (1). Each reflection attenuates the pulse by 3 dB. The free-space loss is modeled according to Friis' transmission equation. The parameters of the DM are set according to [4] and the power of the additive white noise is set to $N_0 = 2 \cdot 10^{-16}$ W/Hz. In order to achieve a fair comparison to the proposed method in [2] we choose the same parameter setup and simulation scenario as shown in Figure 2. Three agents m move independently along trajectories under partly non-line-of-sight conditions where we assume a given start position. Figure 2 shows an example of the estimated agent positions $\hat{\mathbf{p}}_{1,n}$, $\hat{\mathbf{p}}_{2,n}$ and $\hat{\mathbf{p}}_{3,n}$ using the proposed EKF-based algorithm are indicated for every 5-th position. At each time step n the agents run monostatic and bistatic measurements to the neighboring agents. The utilized likelihood function of [2, eq. (8)] simplifies the proposed system model (Sec. III in [2]). We accounted this by changing the likelihood function to eq. (7) of [2]. Further, [2] undermines the uncertainty of the neighboring beliefs by reducing the size of the neighboring particles to the mean value (see Sec. V-B of [2]). We omit this simplification.

The maximum number of extracted MPCs is limited to $K_n^{(\dots)} = 12, \forall n$ (see 2.2). The initial position of each VA $\mathbf{p}_{k,n}^{(m)}$ as well as the corresponding VA transition matrix $\mathbf{P}_k^{(m)}$ are calculated in advance. Figure 3 illustrates the cumulative distribution function (CDF) of the localization error of the proposed algorithm (CoMINT EKF) compared to [2] of ten trajectory realizations—each evaluated with 50 monte carlo runs. The comparison reveals the strong influence on performance of localization error and computational demand [2] regarding its implementation scheme of message passing (i.e. particle or parametric message representation and scheduling). Choosing a sample-based message representation the localization error reduces with increasing number of particles on the cost of computational complexity. Denoting N as the number of particles representing the message passing scheme [2], faces a complexity of $\mathcal{O}(MN^2)$ [5]. The proposed method has a complexity of $\mathcal{O}(M^2K_n^3)$ determined by the data association stage [9]. Since the number of particles N is much higher compared to the number of extracted MPC $K_n^{(\dots)}$ the proposed method outperforms [2] in terms of computational complexity. We proof this claim by comparison of the average computational time for localization scaled to the proposed method. Depending on the number of particles the average computational time of the proposed method speeds up by a factor of approximately 217, 756 and 2355 for 100, 250 and 500 particles, respectively.

The gain in terms of computational time is established by the assumption of Gaussian distance errors. Figure 3 indicates the influence of this assumption by comparison to [2] with different number of particles of 100, 250 and 500. The proposed method reaches a performance comparable to [2] with a number of particles from 100 – 250 where 90% of the errors are located within 2 cm.

5 Conclusions

We have presented a new low-complexity algorithm for cooperative localization of agents using multipath information. The simulation results show that bistatic as well as monostatic measurements contribute a significant amount of information for localizing the agents with a high level of accuracy. The

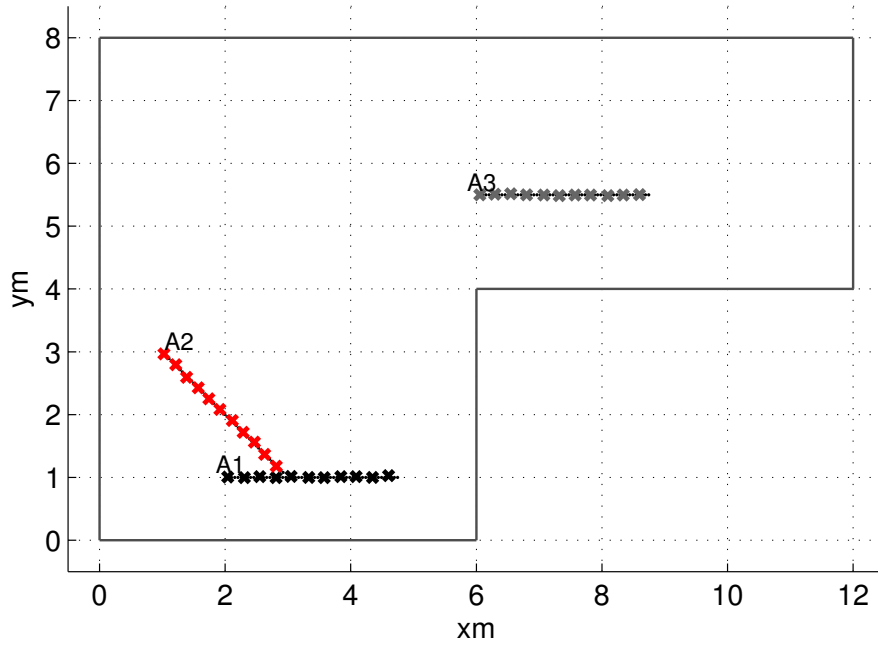


Figure 2: Simulation scenario as in [2] with three agents moving along different trajectories.

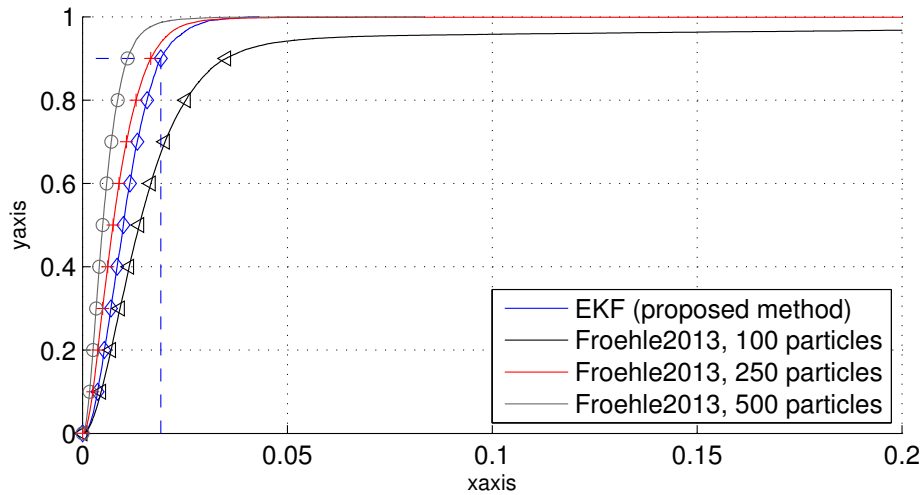


Figure 3: CDF of the localization error of the proposed algorithm (CoMINT EKF) (blue) compared to [2] with a different size of 500 (gray), 250 (red) and 100 (black) particles of each agent.

simulation results pinpoint also the robustness, i.e. low level of localization outages, of the cooperative algorithm when multipath information is used from both types of measurements. The most important attained fact is that the proposed low-complexity algorithm reaches almost the same performance than the particle-based method using several orders of magnitude less computational resources.

References

- [1] Conti, A., Dardari, D., Guerra, M., Mucchi, L., Win, M.: Experimental Characterization of Diversity Navigation. *IEEE Systems Journal* (2014)
- [2] Froehle, M., Leitinger, E., Meissner, P., Witrival, K.: Cooperative Multipath-Assisted Indoor Navigation and Tracking (Co-MINT) Using UWB Signals. In: *IEEE ICC Workshop on Advances in Network Localization and Navigation* (2013)
- [3] Leitinger, E., Meissner, P., Lafer, M., Witrival, K.: Simultaneous Localization and Mapping using Multipath Channel Information. In: *Communications Workshops (ICC), 2015 IEEE International Conference on* (2015)
- [4] Leitinger, E., Meissner, P., Ruedisser, C., Dumphart, G., Witrival, K.: Evaluation of Position-related Information in Multipath Components for Indoor Positioning. *Selected Areas in Communications, IEEE Journal on* (2015)
- [5] Lien, J., Ferner, U.J., Srichavengsup, W., Wymeersch, H., Win, M.Z.: A comparison of parametric and sample-based message representation in cooperative localization. *International Journal of Navigation and Observation* (2012)
- [6] Meissner, P.: Multipath-Assisted Indoor Positioning. Ph.D. thesis, Graz University of Technology (2014)
- [7] Meissner, P., Leitinger, E., Witrival, K.: UWB for Robust Indoor Tracking: Weighting of Multipath Components for Efficient Estimation. *IEEE Wireless Communications Letters* (2014)
- [8] Michelusi, N., Mitra, U., Molisch, A., Zorzi, M.: UWB Sparse/Diffuse Channels, Part I: Channel Models and Bayesian Estimators. *IEEE Transactions on Signal Processing* (2012)
- [9] Schuhmacher, D., Vo, B.T., Vo, B.N.: A Consistent Metric for Performance Evaluation of Multi-Object Filters. *IEEE Transactions on Signal Processing* (2008)
- [10] Shen, Y., Mazuelas, S., Win, M.: Network Navigation: Theory and Interpretation. *IEEE Journal on Selected Areas in Communications* (2012)
- [11] Wymeersch, H., Lien, J., Win, M.Z.: Cooperative Localization in Wireless Networks. *Proceedings of the IEEE* (2009)

Cooperative Localization and Tracking using Multipath Channel Information

Josef Kulmer, Erik Leitinger, Paul Meissner, Stefan Hinteregger,
and Klaus Witrisal

presented at 2016 International Conference on Localization and GNSS (ICL-GNSS)

Abstract

Indoor environments are characterized by harsh multipath conditions. Multipath - assisted indoor navigation and tracking (MINT) exploits position-related features of the propagation channel to improve its *accuracy* and *robustness*. In this work we introduce an anchor-free, cooperative MINT algorithm. The algorithm uses monostatic and bistatic (cooperative) measurements conducted by the agents. The estimated multipath components are associated to virtual anchors exploiting their position-related information. We present a proof-of-concept using data from an ultra-wideband measurement campaign, reaching a position accuracy better than 6 cm for 90 % of the measurement points.

1 Introduction

Radio-based position tracking with high levels of *accuracy* and *robustness* has received a lot of attention over the last decades. The achievable performance depends strongly on the environment determining the radio propagation. In indoor environments high levels of accuracy and robustness are hindered by harsh multipath propagation. The undesired multipath can be countered by data fusion of multiple information sources [1] or by providing remedies against the errors induced by the multipath propagation [2].

Another way of tackling this problem is to exploit useful position-related information contained in multipath components (MPCs) [3]. Association of the MPCs to the surrounding geometry enables improved localization performance, as shown in [3–7]. The received signal is modeled as a superposition of the line-of-sight component (LOS) and so-called *deterministic* MPCs originating from reflections at objects, e.g. wall segments. These reflections can be used to gain additional information for localization and tracking, which is especially needed in scenarios with a low number of anchor nodes. Localization methods relying on a single-anchor node were presented in [8–10].

A low number of anchor nodes reduces the position accuracy and robustness. This can be circumvented by cooperation among the agents as shown in [10–15]. In [12] several agents locate their positions using a single anchor by employing a sum-product based message passing algorithm. The method shown in [13] presents cooperative localization of two agents and three anchors using convex optimization. In [14] and [15] cooperative tracking is realized without using any infrastructure but exploiting multipath. The tracking algorithms are realized using the belief propagation scheme SPAWN [11] and an algorithm based on extended Kalman filters, respectively.

In this work we present an anchor-free, cooperative tracking algorithm exploiting multipath propagation as extension to [15] by considering uncertainty of virtual anchors (VAs). We use ultra-wideband (UWB) signals as their superior time resolution enables separation of MPCs. The MPCs can be modeled as signals emitted from virtual anchors. This yields a simple geometric model of the delays of the deterministic MPCs which allows exploiting their position related information as shown in Fig. 1. The agent and corresponding VA positions are tracked with an extended Kalman Filter (EKF) making use of *monostatic* and *bistatic* measurements. To obtain the monostatic measurements, each agent acts as receiver and transmitter whereas the bistatic measurements are performed in between neighboring (cooperating) agents (see Fig. 1). We show the performance of the proposed algorithm for synthetic and real measurement data in terms of accuracy and robustness with respect to imprecise floorplans.

The key contributions of this paper are:

- We formulate the relations between the agent and VA positions, velocities and covariances.
- We present an anchor-free, cooperative algorithm using data association of MPC delays with according VAs and assemble the EKF for tracking the joint state of the agents and the according VAs.
- We show the applicability of the presented algorithm on real data.

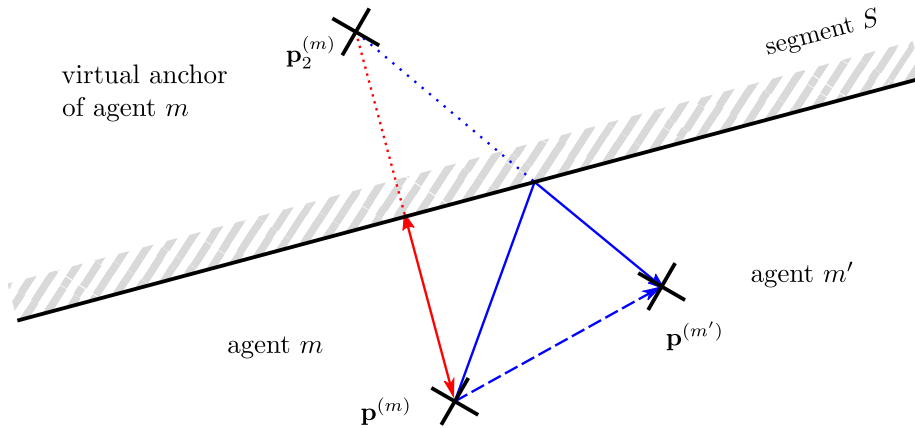


Figure 1: Multipath propagation of monostatic (red) and bistatic (blue) measurements. The emitted pulse of agent m is received by its neighbor m' (bistatic) and by itself (monostatic) and contains the line-of-sight and a multipath component due to the reflection at wall segment S . Mapping of the reflection to the virtual anchor at position $\mathbf{p}_2^{(m)}$ models the geometry of the multipath component.

The paper is organized as follows: Section 2 provides an overview about the subject and introduces the geometric-stochastic signal model and the VA motion model, respectively. Section 3 describes the implementation of the cooperative algorithm, while Sections 4 and 5 wrap up the paper with results, discussions, and conclusions.

2 Problem Formulation

Several clock-synchronized agents $m \in \mathcal{N}_m = \{1, \dots, M\}$ aim at localizing their positions $\mathbf{p}_n^{(m)}$ at time step n using monostatic and bistatic measurements. The measurements are performed by transmitting UWB signals $s(t)$ which interact with the environment resulting in multipath propagation. We apply a geometrical model for multipath propagation by employing VAs, as illustrated in Fig. 1. In the bistatic measurement setup, the emitted pulse of agent m is received at neighboring agent m' as a sum of an LOS component (dashed blue line) and a reflection (solid blue line) at the wall segment S (solid gray line). We model this reflection as a pulse emitted from VA $\mathbf{p}_2^{(m)}$, whose position is defined by the image-source-model [16]. In the monostatic measurement setup, the pulse is emitted and received by agent m . Again, the reflection at the wall segment (solid red line) is modeled as a pulse emitted from a VA at position $\mathbf{p}_2^{(m)}$. For a better readability, we drop the time step index n .

2.1 Signal Model

The received signal $r^{(m',m)}(t)$ of agent m' for the emitted pulse $s(t)$ of agent m is modeled according to [3, 17]

$$r^{(m',m)}(t) = \sum_{k=1}^{K^{(m',m)}} \alpha_k^{(m',m)} s(t - \tau_k^{(m',m)}) + (s * \nu^{(m',m)})(t) + w(t), \quad (1)$$

for both monostatic ($m = m'$) and bistatic ($m \neq m'$) measurements. The first term of (1) denotes the sum of deterministic MPCs with complex amplitudes $\alpha_k^{(m',m)}$ and delays $\tau_k^{(m',m)}$, originating from agent m with corresponding VAs at positions $\mathbf{p}_k^{(m)}$. The delays are calculated according to $\tau_k^{(m',m)} = \frac{1}{c} \|\mathbf{p}^{(m')} - \mathbf{p}_k^{(m)}\|$ with $k \in \{1, \dots, K^{(m',m)}\}$ and c denoting the speed of light. The number of VAs $K^{(m',m)}$ depends on the agent positions $\mathbf{p}^{(m)}$ and $\mathbf{p}^{(m')}$. The model does not distinguish between the LOS component and reflected MPCs by declaring $\mathbf{p}_1^{(m)} = \mathbf{p}^{(m)}$.

The second term in (1) denotes the convolution of the transmitted signal $s(t)$ and the diffuse multipath (DM) $\nu^{(m',m)}$. The DM is modeled as a realization of a non-stationary, zero-mean Gaussian random process. We assume uncorrelated scattering along τ , resulting in an auto-correlation function of $K_\nu^{(m',m)}(\tau, u) = \mathbb{E}_\nu \{ \nu^{(m',m)}(\tau) \nu^{(m',m)*}(u) \} = S_\nu^{(m',m)}(\tau) \delta(\tau - u)$ with $S_\nu^{(m',m)}(\tau)$ denoting the power delay profile (PDP) of the diffuse multipath. According to [18], the PDP depends on the position of transmitter and receiver and is quasi-stationary in the spatial domain. Note, that the DM comprises all other not modeled, dense MPCs and represents a interference to the useful deterministic MPCs.

The last term denotes additive white Gaussian noise with a double-sided power spectral density (PSD) of $N_0/2$.

2.2 Virtual Anchor Motion Model

In the proposed anchor-free MINT algorithm the moving agents share the hypothesis regarding their positions among the neighboring agents. The movement of the agents is reflected in moving virtual anchors. In this section we describe the relations between position, movement and covariance of the agents and the corresponding VAs. For a better readability, we consider first-order reflections only, restricted to a two-dimensional floorplan. The model can be extended to higher-order reflections (cf. [3]) and three dimensions.

We describe the position and orientation of the wall segment S by the vectors \mathbf{p}_S and $l_S \mathbf{e}_S$, respectively, with l_S as length and \mathbf{e}_S as unit vector indicating the direction of wall segment as shown in Fig. 2. The closest distance between S and agent m is calculated by the projection of $(\mathbf{p}_S - \mathbf{p}^{(m)})$ onto $\mathbf{R}_{\frac{\pi}{2}} \mathbf{e}_S$, where $\mathbf{R}_{\frac{\pi}{2}}$ denotes the rotation matrix by $\frac{\pi}{2}$, yielding

$$d_{m,S} = (\mathbf{p}_S - \mathbf{p}^{(m)})^T \mathbf{R}_{\frac{\pi}{2}} \mathbf{e}_S. \quad (2)$$

The VA position $\mathbf{p}_2^{(m)}$ is calculated according to

$$\mathbf{p}_2^{(m)} = \mathbf{p}^{(m)} + 2d_{m,S} \mathbf{R}_{\frac{\pi}{2}} \mathbf{e}_S. \quad (3)$$

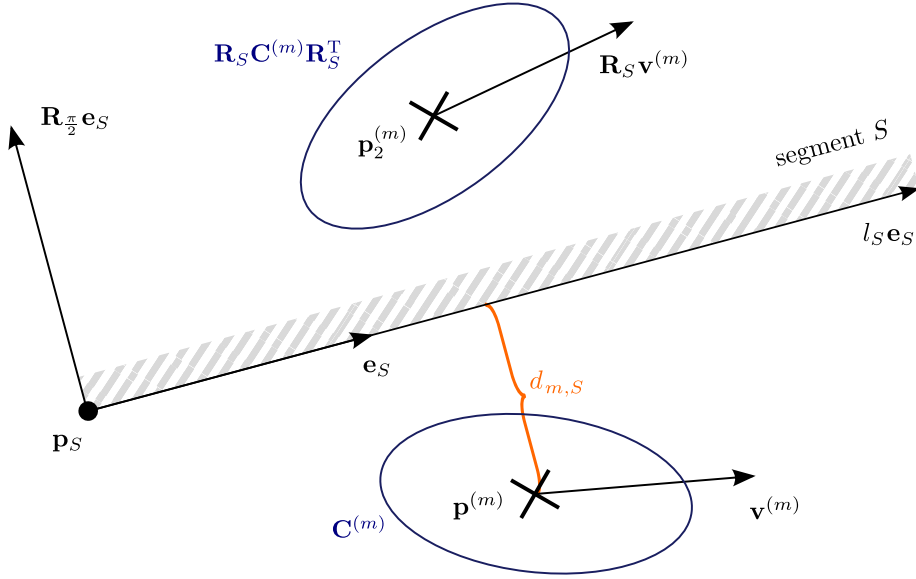


Figure 2: Illustration of agent position $\mathbf{p}^{(m)}$, velocity $\mathbf{v}^{(m)}$ and covariance $\mathbf{C}^{(m)}$. The wall segment's orientation, indicated by \mathbf{p}_S and \mathbf{e}_S , translates the velocity and covariance of agent m to its corresponding virtual anchors.

The motion of the agents shifts the position of the corresponding VAs, as shown in Figure 2. Agent m moves with velocity $\mathbf{v}^{(m)}$ resulting in a mirrored movement of $\mathbf{p}_2^{(m)}$ dependent on the orientation of the wall segment S . Projection of $\mathbf{v}^{(m)}$ to the orientation of S leads to the decomposition

$$\mathbf{v}^{(m)} = (\mathbf{e}_S^T \mathbf{v}^{(m)}) \mathbf{e}_S + (\mathbf{e}_S^T \mathbf{R}_{\frac{\pi}{2}}^T \mathbf{v}^{(m)}) \mathbf{R}_{\frac{\pi}{2}} \mathbf{e}_S, \quad (4)$$

where the first term on the right-hand-side represents the movement along the wall segment and the second-term the movement orthogonal to the wall segment. Mirroring of the orthogonal component and rearranging leads to the movement of the VA, given as

$$\mathbf{v}_{\mathbf{p}_2}^{(m)} = (\mathbf{e}_S \mathbf{e}_S^T - \mathbf{R}_{\frac{\pi}{2}} \mathbf{e}_S \mathbf{e}_S^T \mathbf{R}_{\frac{\pi}{2}}^T) \mathbf{v}^{(m)} = \mathbf{R}_S \mathbf{v}^{(m)}. \quad (5)$$

We denote \mathbf{R}_S as VA transition matrix. It translates the movement of the agent to the movement of the corresponding VA and depends on the orientation of the wall segment only. Further, we employ \mathbf{R}_S to relate the covariance of the VAs to the covariance of the corresponding agent $\mathbf{C}^{(m)}$, as illustrated in Figure 2. Employing eigenvalue decomposition, the covariance matrix $\mathbf{C}^{(m)}$ can be represented as $\mathbf{C}^{(m)} = \mathbf{Q} \mathbf{\Lambda} \mathbf{Q}^T$ where the columns of the rotation matrix \mathbf{Q} consist of the eigenvectors of $\mathbf{C}^{(m)}$ and $\mathbf{\Lambda}$ contains the eigenvalues. The covariance of the VA is expressed as follows

$$\mathbf{C}_{\mathbf{p}_2}^{(m)} = \mathbf{R}_S \mathbf{Q} \mathbf{\Lambda} \mathbf{Q}^T \mathbf{R}_S^T, \quad (6)$$

where \mathbf{R}_S mirrors the eigenvectors in \mathbf{Q} depending on the orientation of S .

3 Proposed Algorithm

The proposed algorithm employs at each time step n monostatic and bistatic measurements, conducted by the agents. The multipath components' delays and amplitudes of each measurement are estimated. The delays are assigned to virtual anchors to model the geometry of the MPCs. The corresponding amplitudes are used to model the uncertainty of the MPCs.

3.1 Channel Estimation

We use peak-picking for estimating the delays of the deterministic MPCs $\hat{\tau}_{k,n}^{(m',m)}$, implemented as an recursive least-squares approximation [8], written as

$$\hat{\tau}_{k,n}^{(m',m)} = \operatorname{argmin}_{\tau} \int_0^T |r_n^{(m',m)}(t) - \hat{r}_{k-1,n}^{(m',m)}(t) - \hat{\alpha}(\tau)s(t-\tau)|^2 dt, \quad (7)$$

with $\hat{r}_{k-1,n}^{(m',m)}(t)$ as template signal for the deterministic MPCs, estimated up to the $(k-1)$ -th iteration step, and

$$\hat{\alpha}_{k,n}^{(m',m)} = \hat{\alpha}(\hat{\tau}_{k,n}^{(m',m)}), \quad (8)$$

with

$$\hat{\alpha}(\tau) = \int_0^T s^*(t-\tau)(r_n^{(m',m)}(t) - \hat{r}_{k-1,n}^{(m',m)}(t)) dt, \quad (9)$$

and T as measurement duration. The template signal

$$\hat{r}_{k-1,n}^{(m',m)}(t) = \sum_{k'=1}^{k-1} \hat{\alpha}_{k',n}^{(m',m)} s(t - \hat{\tau}_{k',n}^{(m',m)})$$

is initialized with $\hat{r}_{0,n}^{(m',m)}(t) = 0$. Alternating between (7) and (8), the MPC parameters $\hat{\tau}_{k,n}^{(m',m)}$ and $\hat{\alpha}_{k,n}^{(m',m)}$ are recursively estimated until a predefined number $\hat{K}_n^{(m',m)}$ is reached. The channel estimation is done for each monostatic and bistatic measurement resulting in sets of estimated distances $\mathcal{Z}_n^{(m',m)} = \{\hat{d}_{k,n}^{(m',m)}\}_{k=1}^{\hat{K}_n^{(m',m)}}$ with $\hat{d}_{k,n}^{(m',m)} = c\hat{\tau}_{k,n}^{(m',m)}$.

3.2 Data Association (DA)

The estimated distances obtained from the channel estimation are now associated to expected distances calculated from VAs' positions. We calculate the set of expected distances as

$$\mathcal{D}_n^{(m',m)} = \{\|\hat{\mathbf{p}}_{1,n}^{(m')} - \hat{\mathbf{p}}_{k,n}^{(m)}\|\}_{k=1}^{K_n^{(m',m)}}, \quad (10)$$

where $\hat{\mathbf{p}}_{k,n}^{(m')}$ refers to the predicted position computed with an EKF at n . We reduce the set of expected distances to the visible ones by performing optical *ray-tracing* [19]. The number of expected distances depends on the number of segments and their visibility, and is in general different to the number of estimated MPC $|\mathcal{D}_n^{(m',m)}| = K_n^{(m',m)} \neq |\mathcal{Z}_n^{(m',m)}| = \hat{K}_n^{(m',m)}$. We use the *optimal*

sub-pattern assignment (OSPA) metric [20] to assign the expected distances to the estimated ones, where we allow a maximum discrepancy of d_c between expected and estimated distance for each MPC [8]. Finally, the assigned distances are stacked in the vector $\mathbf{z}_n^{(m',m)}$.

3.3 State Space and Measurement Model

We describe the state dynamics using a linear, constant-velocity motion model. In the following we describe the state vector of a single agent m . We drop the agent index m for a better readability. The joint state space of the agent and the corresponding VAs is given as

$$\tilde{\mathbf{x}}_n = [\mathbf{p}_{1,n}^T, \mathbf{v}_n^T, \mathbf{p}_{2,n}^T, \dots, \mathbf{p}_{\tilde{K}_n+1,n}^T]^T, \quad (11)$$

with \tilde{K}_n denoting the number of assigned VAs at n . The state space model for one agent follows as

$$\tilde{\mathbf{x}}_n = \underbrace{\begin{bmatrix} \mathbf{F} & \mathbf{0}_{4 \times 2\tilde{K}_n} \\ \mathbf{0}_{2\tilde{K}_n \times 2} & \tilde{\mathbf{R}}_{S,n} \end{bmatrix}}_{\tilde{\mathbf{F}}_n} \tilde{\mathbf{x}}_{n-1} + \underbrace{\begin{bmatrix} \mathbf{G} \\ \mathbf{0}_{2\tilde{K}_n \times 2} \end{bmatrix}}_{\tilde{\mathbf{G}}_n} \mathbf{n}_{a,n}, \quad (12)$$

$$\mathbf{F} = \begin{bmatrix} 1 & 0 & \Delta T & 0 \\ 0 & 1 & 0 & \Delta T \\ 0 & 0 & 1 & 0 \\ 0 & 0 & 0 & 1 \end{bmatrix} \quad \mathbf{G} = \begin{bmatrix} \frac{\Delta T^2}{2} & 0 \\ 0 & \frac{\Delta T^2}{2} \\ \Delta T & 0 \\ 0 & \Delta T \end{bmatrix},$$

and $\mathbf{n}_{a,n}$ as zero mean driving noise.

The stacked VA transition matrix $\tilde{\mathbf{R}}_{S,n} = [\mathbf{R}_{S_2}^T, \dots, \mathbf{R}_{S_{\tilde{K}_n+1}}^T]^T$ with dimension $(2\tilde{K}_n \times 2)$ translates the movement \mathbf{v}_n of the agent to the corresponding VAs. It is structured in the same manner as the stacked VAs' positions and each entry \mathbf{R}_{S_k} is calculated according to (5).

The covariance of the state vector of one agent is written as

$$\tilde{\mathbf{C}}_n = \begin{bmatrix} \mathbf{C}_{\mathbf{p},n} & \mathbf{C}_{\mathbf{pv},n} & \mathbf{0}_{4 \times 2\tilde{K}_n} \\ \mathbf{C}_{\mathbf{pv},n}^T & \mathbf{C}_{\mathbf{v},n} & \\ \mathbf{0}_{2\tilde{K}_n \times 4} & & \tilde{\mathbf{C}}_{S,n} \end{bmatrix}, \quad (13)$$

where $\mathbf{C}_{\mathbf{p},n}$, $\mathbf{C}_{\mathbf{v},n}$ and $\mathbf{C}_{\mathbf{pv},n}$ are the position and velocity covariance and cross-covariance matrices, respectively. The block-diagonal matrix $\tilde{\mathbf{C}}_{S,n} = \text{diag}\{[(\mathbf{R}_{S_2} \mathbf{C}_{\mathbf{p},n} \mathbf{R}_{S_2}^T)^T, \dots, (\mathbf{R}_{S_{\tilde{K}_n}} \mathbf{C}_{\mathbf{p},n} \mathbf{R}_{S_{\tilde{K}_n}}^T)^T]\}$ with dimension $(2\tilde{K}_n \times 2\tilde{K}_n)$ aligns the covariance of the position of the agent to the VA positions, as in (6).

The individual state spaces of the cooperating agents m are stacked into a joint state space as follows

$$\underbrace{\begin{bmatrix} \tilde{\mathbf{x}}_n^{(1)} \\ \vdots \\ \tilde{\mathbf{x}}_n^{(M)} \end{bmatrix}}_{\mathbf{x}_n} = \begin{bmatrix} \tilde{\mathbf{F}}_n^{(1)} & & \mathbf{0} \\ & \ddots & \\ \mathbf{0} & & \tilde{\mathbf{F}}_n^{(M)} \end{bmatrix} \underbrace{\begin{bmatrix} \tilde{\mathbf{x}}_{n-1}^{(1)} \\ \vdots \\ \tilde{\mathbf{x}}_{n-1}^{(M)} \end{bmatrix}}_{\mathbf{x}_{n-1}} + \begin{bmatrix} \tilde{\mathbf{G}}_n^{(1)} \\ \vdots \\ \tilde{\mathbf{G}}_n^{(M)} \end{bmatrix} \mathbf{n}_{a,n}, \quad (14)$$

and $\mathbf{C}_n = \text{diag} \{ [\tilde{\mathbf{C}}_n^{(1)}, \dots, \tilde{\mathbf{C}}_n^{(M)}] \}$, where we assume independent movement of the agents.

The measurement model translates the agent and VA positions to distances of the MPCs according to

$$\mathbf{z}_n = h_n(\mathbf{x}_n) + \mathbf{n}_n, \quad (15)$$

with \mathbf{n}_n as zero mean measurement noise. The measured distances of the associated MPCs (see 3.2) for the monostatic and bistatic measurements are stacked in

$$\mathbf{z}_n = [\mathbf{z}_n^{(1,1)}, \dots, \mathbf{z}_n^{(1,M)}, \mathbf{z}_n^{(2,1)}, \dots, \mathbf{z}_n^{(2,M)}, \dots, \mathbf{z}_n^{(M,M)}]^T$$

of length $\bar{K}_n = \sum_{m'} \sum_m \tilde{K}_n^{(m',m)}$. The EKF employs the Jacobian \mathbf{H}_n of the non-linear measurement function $h_n(\mathbf{x}_n)$ with respect to the agent and VA positions in \mathbf{x}_n . It is constructed as follows: the rows in \mathbf{H}_n transform the positions of one pair of a VA and an agent. For each measured distance $\bar{k} \in \{1, \bar{K}_n\}$, let m' denote the receiving agent and k the transmitting VA of agent m . Further, let μ and η be the indices locating $\mathbf{p}_{1,n}^{(m')}$ and $\mathbf{p}_{k,n}^{(m)}$ within the joint state vector. Then, the vector $\mathbf{h}_{\bar{k},n}^{(m',m)} = \left[\frac{\partial \|\mathbf{p}_{1,n}^{(m')} - \mathbf{p}_{k,n}^{(m)}\|}{\partial x_n^{(\mu)}}, \frac{\partial \|\mathbf{p}_{1,n}^{(m')} - \mathbf{p}_{k,n}^{(m)}\|}{\partial y_n^{(\eta)}} \right]$ determines the derivative of the Euclidean norm with respect to the x - and y -position coordinates of the agent and $-\mathbf{h}_{\bar{k},n}^{(m',m)}$ of the VA position where the negative sign accounts for the derivative with respect to the VA. We plug $\mathbf{h}_{\bar{k},n}^{(m',m)}$ and $-\mathbf{h}_{\bar{k},n}^{(m',m)}$ in \mathbf{H}_n at row \bar{k}_n and columns μ and η , respectively.

3.4 Range Uncertainty Estimation

The uncertainty of the measured distances $\text{var}\{\hat{d}_{k,n}^{(m',m)}\}$ is related to the SINR of the corresponding delay estimate, employing the information inequality according to [8, 21]

$$\text{var}\{\hat{d}_{k,n}^{(m',m)}\} \geq \left(\frac{8\pi^2\beta^2}{c^2} \text{SINR}_{k,n}^{(m',m)} \right)^{-1}, \quad (16)$$

where β is the effective (root mean square) bandwidth of $s(t)$. We estimate the SINR using a method of moments estimator [8] taking the corresponding amplitudes $\{\hat{\alpha}_{k,i}^{(m',m)}\}_{i=n-N}^n$ over a window of N past measurements into account and compute the distance variances of each MPC according to (16).

The measurement noise covariance matrix is assembled as follows

$$\mathbf{R}_n = \text{diag}\{\text{var}\{\hat{d}_{k,n}^{(m',m)}\}\} \quad \forall m, m', k. \quad (17)$$

4 Results

The performance of the proposed algorithm is evaluated in terms of localization error and robustness to uncertainties in the floorplan. We test the algorithm using scenarios with synthetic and measured data as explained in the following.

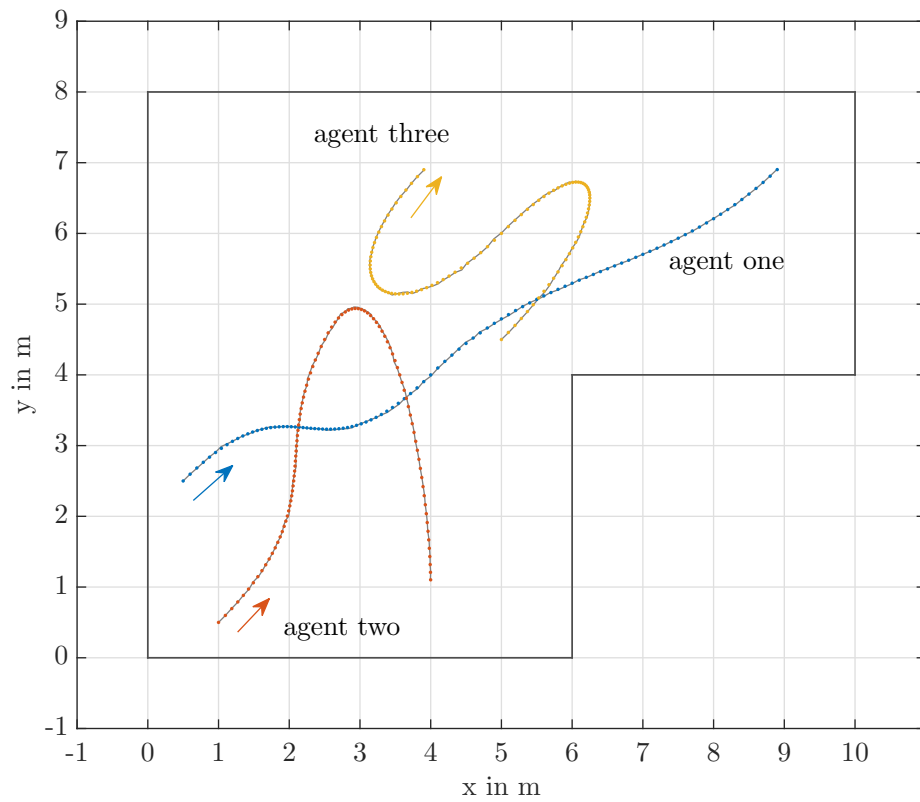


Figure 3: Simulation scenario with synthetically generated signals: three agents move independently along the trajectories (dotted) with varying velocity.

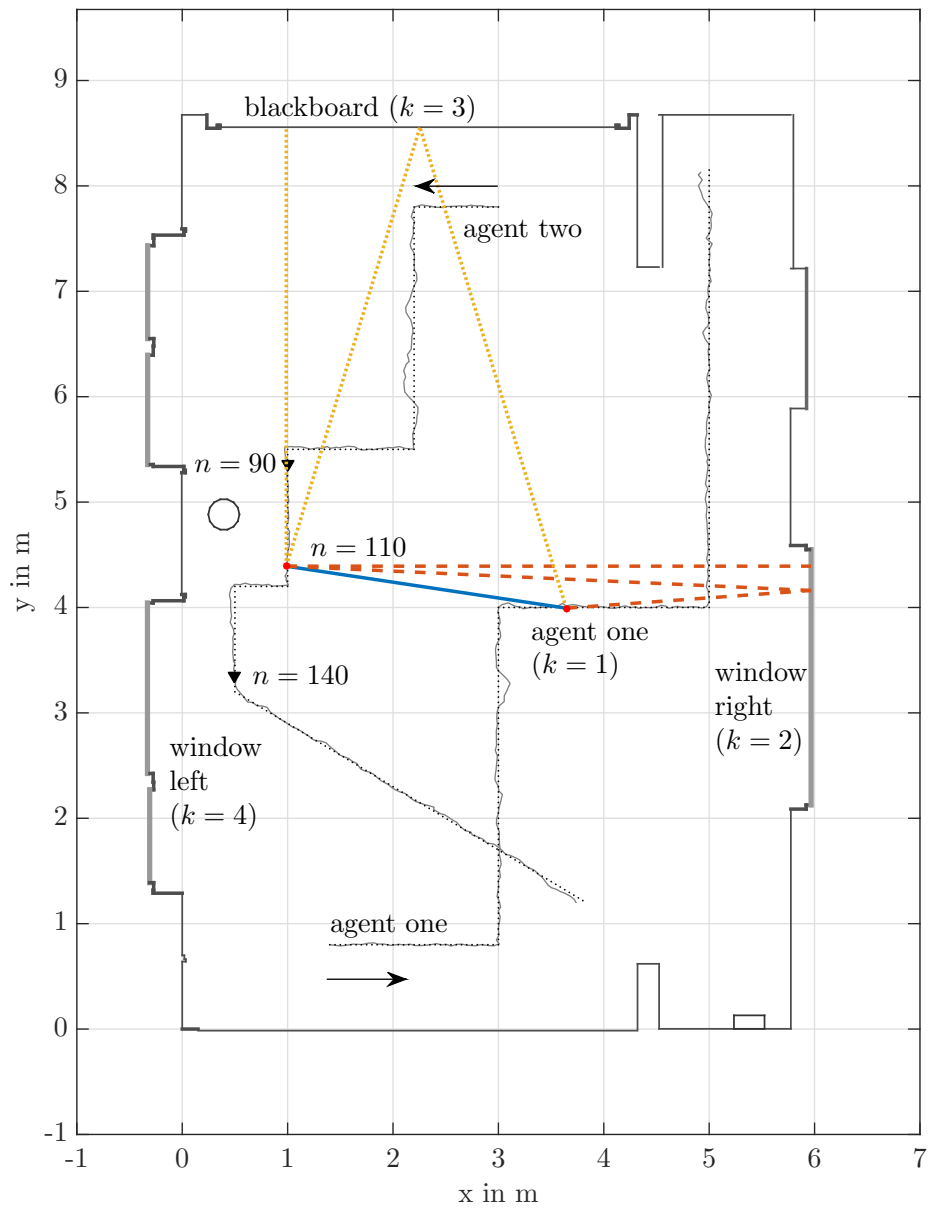


Figure 4: Scenario with measured data obtained in the Seminar room (floorplan uncertainty $r = 1$ mm): two agents locate their position employing MPCs along the trajectories. Multipath components are shown for time step $n = 110$.

4.1 Setup for synthetic data

The setup for the synthetic scenario is as follows: a unit-energy root-raised-cosine pulse with roll-off factor of $R = 0.6$ and a pulse duration of $T_p = 0.5$ ns acts as transmit signal $s(t)$. The received signal is modeled according to (1) considering first-order reflections only. We employ a free-space propagation model attenuating the received pulses according to Friis' transmission equation. Each reflection is accounted as an additional attenuation of 3 dB. We set the parameters of the DM according to [3], where also a validation of the model is presented. The SNR between LOS (at 1 m) and additive white noise is set to 26 dB. We use $M = 3$ agents moving along the trajectories with varying velocities, shown in Figure 3. The trajectories consist of 100 position points for each agent.

4.2 Setup for measured data

The measured data are obtained using a *Rohde and Schwarz ZVA-24* VNA within a frequency range from 3.1 to 10.6 GHz. We shape the data with a root-raised-cosine pulse with roll-off factor of $R = 0.6$ and a pulse duration of $T_p = 0.5$ ns at a carrier frequency of $f_c = 7$ GHz [22]. We use self-made Euro-cent coin antennas [23] with a uniform radiation pattern in azimuth domain. The antennas are connected to the VNA to omit the required synchronization accuracy among the agents in the order of 10^{-10} s. Figure 4 illustrates the scenario: two agents move along their trajectories consisting of 220 positions with a spacing of 5 cm. In both scenarios no anchors are used.

4.3 Implementation

We employ an EKF for tracking the agent states jointly with the VA states. Once a new agent joins the cooperative localization, the positions of the agents' VAs are initialized according to (3) followed by assembling the VA transitions (5). At each time step n the joint state is predicted by (14) followed by associating (see Sec. 3.2) the expected MPCs with the estimated ones (Sec. 3.1). Finally, the EKF update step is performed to obtain the estimated agent positions $\hat{\mathbf{p}}_n^{(m)}$.

The number of expected MPCs $K_n^{(m',m)}$ (3.2) depends on the agents' positions and the rooms' geometry. The floorplans of both scenarios are dominated by parallel walls which results in $K_n^{(m',m)} = 4$ expected MPCs in each received signal $r_n^{(m',m)}(t)$.

We set the cutoff-distance in (3.2) to $d_c = cT_p = 0.15$ m and the number of estimated MPCs $\hat{K}_n^{(m',m)}$ in (3.1) to $\hat{K}_n^{(m',m)} = 1.5K_n^{(m',m)}$. Expected distance pairs within a range below the cutoff-distance of d_c are not considered in (10) for reduction of wrong data associations.

The algorithm considers past measurements received within a distance of 0.2 m for MPCs' range uncertainty estimation (see Sec. 3.4). The range uncertainty is used as a measure of reliability and thus gives insights on the algorithm's behavior. Figure 5 exemplifies the correspondent SINRs of selected MPCs of the measured data of agent two's trajectory from time step $n = 90$ to $n = 140$, as shown in Fig. 4. To illustrate the impact of these reflections on the

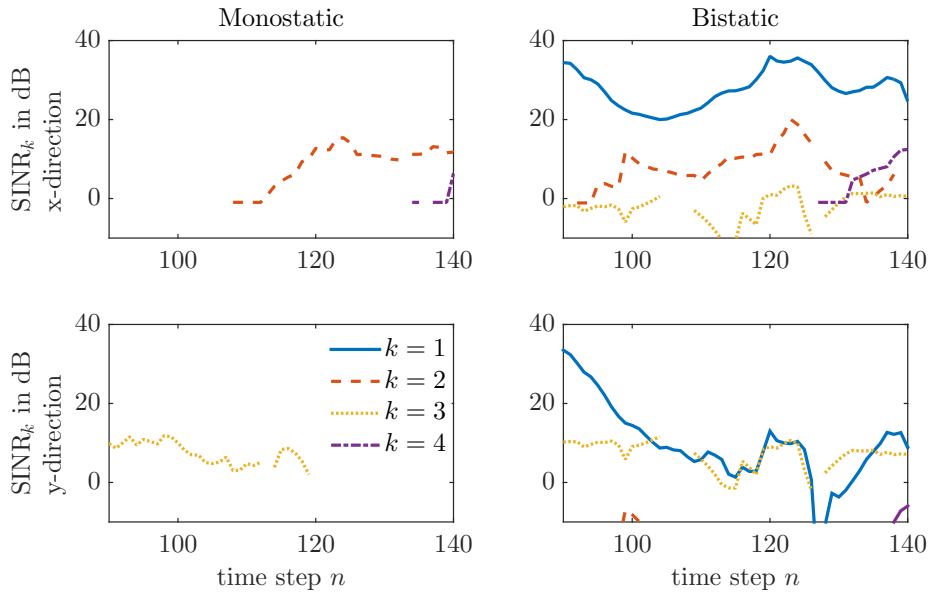


Figure 5: SINR of LOS and multipath components along x -direction (top) and y -direction (bottom) of monostatic (left) and bistatic (right) measurements of agent two from time step $n = 90$ to $n = 140$ (see Fig. 4) of LOS ($k = 1$), window right ($k = 2$), blackboard ($k = 3$) and window left ($k = 4$).

task of positioning we decompose the SINR values into x - and y -components. The high SINR of the LOS between both agents ($k = 1$) indicates a low range uncertainty resulting in a strong impact on the positioning algorithm. The reflections at the right window ($k = 2$) and left window ($k = 4$) add information especially in the x -direction and the reflection at the blackboard ($k = 3$) in the y -direction. At time step $n = 120$ agent two moves behind a concrete pillar which blocks the reflection to the blackboard in the monostatic measurement. In this case, information along the y -direction is only obtained from the bistatic measurement. In general, the MPCs with index $k = \{2, 3, 4\}$ have approximately same SINRs resulting in a similar importance weight in positioning as well.

4.4 Impact of floorplan

The performance of the proposed algorithm depends on the accuracy of the provided floorplan. An imprecise floorplan leads to wrong estimates of the positions of the VAs. We examine the robustness of the algorithm when uncertainties in the floorplan are present by adding uniformly distributed noise $\mathcal{U}(-r/2, r/2)$ within the range r to the positions of the wall segments according to

$$\mathbf{p}_{S_i} = \bar{\mathbf{p}}_{S_i} + \left[\mathcal{U}\left(-\frac{r}{2}, \frac{r}{2}\right), \mathcal{U}\left(-\frac{r}{2}, \frac{r}{2}\right) \right]^T, \forall i \quad (18)$$

with $\bar{\mathbf{p}}_{S_i}$ as true position of wall segment S_i .

We perform 1000 Monte-Carlo (MC) runs with different levels of uncertainty r . We define an MC run with a maximum position error below 1 m as

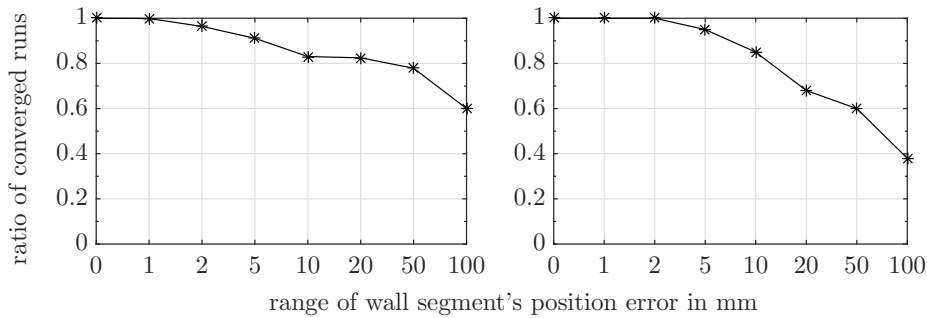


Figure 6: Illustration of the ratio of converged runs dependent on the range of the wall segment's position error r for scenarios with synthetic (left) and measured data (right).

converged. Figure 6 presents the impact of r on the ratio of converged runs. It can be seen that all MC runs converge at small wall segment position errors of $r \leq 1$ mm. Enlarging r increases the number of outliers. The 90 % level of converged runs lies at approximately $r = 5$ mm for both synthetic and measured data. Figures 7 and 8 show the cumulative distribution functions (CDF) of the localization error for converged runs for the scenarios with synthetic and real measurement data, respectively. In general, the scenario with synthetic data has a better performance as the synthetically generated MPCs are more stable and reliable throughout most of the scenario, compared to the real measured data. Further, the algorithm takes usage of more measurements (three monostatic and three bistatic measurements). This experiment results in an error below 25 mm in 90 % of the runs, given a highly accurate floorplan. Increasing the floorplan uncertainty up to $r = 100$ mm lowers the performance. The scenario with measured data achieves a position error of below 60 mm in 90 % of the converged runs for $r = 10$ mm. The impact of uncertainty in the floorplan is in general larger compared to the synthetic data as the reduced number of agents leads to less measurements (two monostatic and one bistatic measurement). Furthermore, the true positions of the segments $\bar{\mathbf{p}}_{S_i}$ may contain a bias due to measurement errors in the existing floorplan.

5 Conclusions

We have presented a cooperative tracking algorithm exploiting multipath propagation by using floorplan information but without fixed anchors at known locations. The performance evaluation with synthetic and measured data reveals the impact of deterministic multipath components to achieve high levels of accuracy. Given an accurate floorplan, the number of outages can be reduced to zero showing a high robustness. In future work we will further address the initialization of the joint state vector and model the floorplan's uncertainty.

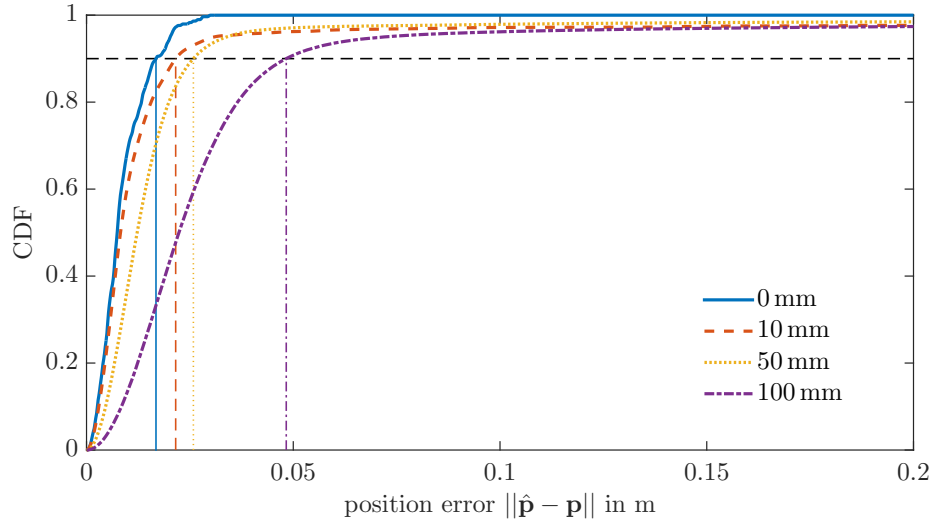


Figure 7: CDF of the localization error for synthetic data using different ranges of wall segment errors of $r = \{0, 10, 50, 100\}$ mm for $T_p = 0.5$ ns. Given a highly accurate floorplan ($r = 10$ mm) the error distance is below 25 mm in 90 % of the runs. Only converged runs are considered.

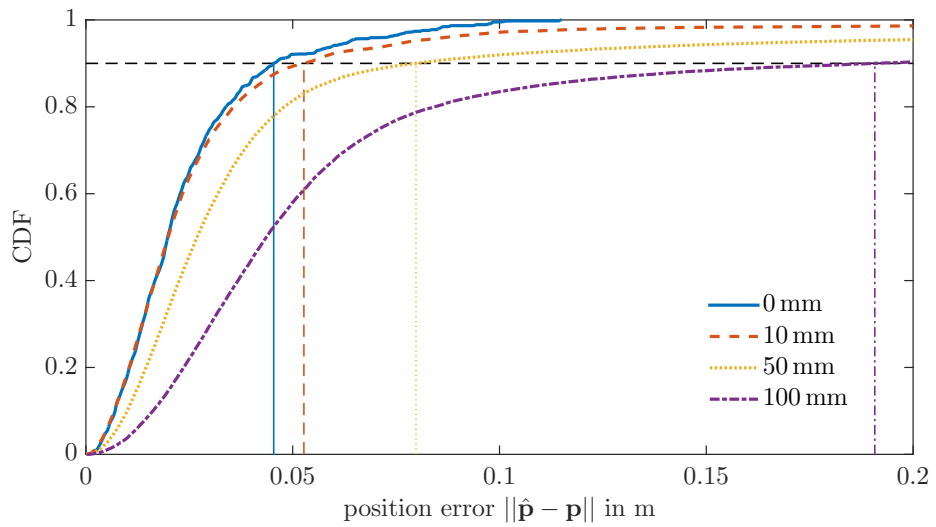


Figure 8: CDF of the localization error for measured data using different ranges of wall segment errors of $r = \{0, 10, 50, 100\}$ mm for $T_p = 0.5$ ns. Given a highly accurate floorplan ($r = 10$ mm) the error distance is below 60 mm in 90 % of the runs. Only converged runs are considered.

References

- [1] A. Conti, D. Dardari, M. Guerra, L. Mucchi, and M. Win, “Experimental Characterization of Diversity Navigation,” *IEEE Systems Journal*, 2014.
- [2] Y. Shen, S. Mazuelas, and M. Win, “Network Navigation: Theory and Interpretation,” *IEEE J. Sel. Areas Commun.*, 2012.
- [3] E. Leitinger, P. Meissner, C. Ruedisser, G. Dumphart, and K. Witrisal, “Evaluation of Position-related Information in Multipath Components for Indoor Positioning,” *IEEE J. Sel. Areas Commun.*, 2015.
- [4] K. Witrisal, P. Meissner, E. Leitinger, Y. Shen, C. Gustafson, F. Tufveson, K. Haneda, D. Dardari, A. F. Molisch, A. Conti, and M. Z. Win, “High-Accuracy Localization for Assisted Living,” *IEEE Signal Processing Magazine*, 2016, special Issue on Assisted Living.
- [5] P. Meissner, “Multipath-Assisted Indoor Positioning,” Ph.D. dissertation, Graz University of Technology, 2014.
- [6] R. Parhizkar, I. Dokmanic, and M. Vetterli, “Single-channel indoor microphone localization,” in *Acoustics, Speech and Signal Processing (ICASSP), 2014 IEEE International Conference on*, 2014.
- [7] W. Xu, F. Quitin, M. Leng, W. P. Tay, and S. G. Razul, “Distributed localization of a RF target in NLOS environments,” *IEEE J. Sel. Areas Commun.*, vol. 33, no. 7, pp. 1 – 14, Jul. 2015.
- [8] P. Meissner, E. Leitinger, and K. Witrisal, “UWB for Robust Indoor Tracking: Weighting of Multipath Components for Efficient Estimation,” *IEEE Wireless Communications Letters*, 2014.
- [9] E. Tsalolikhin, I. Bilik, and N. Blaunstein, “A single-base-station localization approach using a statistical model of the NLOS propagation conditions in urban terrain,” *Vehicular Technology, IEEE Transactions on*, vol. 60, no. 3, pp. 1124–1137, 2011.
- [10] S. Van de Velde and H. Steendam, “Cupid algorithm for cooperative indoor multipath-aided localization,” in *Indoor Positioning and Indoor Navigation (IPIN), IEEE International Conference on*, 2012.
- [11] H. Wymeersch, J. Lien, and M. Z. Win, “Cooperative Localization in Wireless Networks,” *Proceedings of the IEEE*, 2009.
- [12] S. Van de Velde, H. Wymeersch, P. Meissner, K. Witrisal, and H. Steendam, “Cooperative multipath-aided indoor localization,” in *IEEE Wireless Communications and Networking Conference (WCNC)*, 2012.
- [13] H. Naseri, M. Costa, and V. Koivunen, “Multipath-aided cooperative network localization using convex optimization,” in *Signals, Systems and Computers, 2014 48th Asilomar Conference on*, 2014.
- [14] M. Froehle, E. Leitinger, P. Meissner, and K. Witrisal, “Cooperative Multipath-Assisted Indoor Navigation and Tracking (Co-MINT) Using UWB Signals,” in *IEEE ICC 2013 Workshop on Advances in Network Localization and Navigation (ANLN)*, 2013.

- [15] J. Kulmer, E. Leitinger, P. Meissner, and K. Witrival, "Cooperative Multipath-assisted Navigation and Tracking: A Low-Complexity Approach," in *1st EAI International Conference on Future access enablers of ubiquitous and intelligent infrastructures, 2015*. EAI, 2015.
- [16] J. B. Allen and D. A. Berkley, "Image method for efficiently simulating small-room acoustics," *The Journal of the Acoustical Society of America*, vol. 65, no. 4, pp. 943–950, 1979.
- [17] K. Witrival and P. Meissner, "Performance bounds for multipath-assisted indoor navigation and tracking (MINT)," in *IEEE International Conference on Communications (ICC)*, 2012.
- [18] A. Molisch, "Ultra-Wide-Band Propagation Channels," *Proceedings of the IEEE*, 2009.
- [19] —, *Wireless communications*. John Wiley & Sons, 2007, page 132.
- [20] D. Schuhmacher, B.-T. Vo, and B.-N. Vo, "A Consistent Metric for Performance Evaluation of Multi-Object Filters," *IEEE Transactions on Signal Processing*, 2008.
- [21] E. Leitinger, P. Meissner, M. Lafer, and K. Witrival, "Simultaneous Localization and Mapping using Multipath Channel Information," in *IEEE International Conference on Communications (ICC)*, 2015.
- [22] P. Meissner, E. Leitinger, M. Lafer, and K. Witrival, "MeasureMINT UWB database," 2013, Publicly available database of UWB indoor channel measurements.
- [23] C. Krall, "Signal processing for ultra wideband transceivers," Ph.D. dissertation, Graz University of Technology, Austria, 2008.

Anchorless Cooperative Tracking Using Multipath Channel Information

Josef Kulmer, Erik Leitinger, Stefan Grebien, Klaus Witrissal

published at IEEE Transactions on Wireless Communications,
pp. 2262-2275, vol. 17, 2018

Abstract

Highly accurate location information is a key facilitator to stimulate future services for the commercial and public sectors. Positioning and tracking of absolute positions of wireless nodes usually requires information provided from technical infrastructure, e.g. satellites or fixed anchor nodes, whose maintenance is costly and whose limited operating coverage narrows the positioning service. In this paper we present an algorithm aiming at tracking of absolute positions without using information from fixed anchors, odometers or inertial measurement units. We perform radio channel measurements in order to exploit position-related information contained in multipath components (MPCs). Tracking of the absolute node positions is enabled by estimation of MPC parameters followed by association of these parameters to a floorplan. To account for uncertainties in the floorplan and for propagation effects like diffraction and penetration, we recursively update the provided floorplan using the measured MPC parameters. We demonstrate the ability to localize two agent nodes without the employment of further infrastructure, using data from ultra-wideband channel measurements. Further, we show the potential performance gain if also one fixed anchor is available and we validate the algorithm for a range of different signal bandwidths and number of nodes.

1 Introduction

Many applications in wireless radio networks demand knowledge of the nodes' absolute positions. Two types of nodes are considered, namely mobile agents and fixed anchors with unknown and known positions, respectively. The agents intend to track their positions using measurements of position-related signal parameters obtained from radio transmissions to the anchors [1]. To ensure an accurate positioning, highly effective measurements are necessary. In practice, the measurements are often disturbed, especially in harsh radio propagation environments e.g. in urban areas or indoors. Reliable measurements are hindered due to the limited coverage of global navigation satellite systems, radio-propagation effects e.g. multipath propagation and non-line-of-sight (NLOS) conditions, or interference by other agents. Several attempts to encounter adverse radio propagation effects have been proposed, e.g. identification and mitigation of NLOS conditions [2–4], data fusion of multiple information sources [5] or providing remedies against the errors induced by the multipath propagation [6].

A promising idea to deal with multipath propagation is utilization rather than mitigation. Multipath components (MPCs) originate at objects, e.g. planar surfaces and walls. Assuming the objects' locations are known a-priori or learned from previous measurements then the agents can take advantage of the position-related information contained in the MPCs [7–18].

The methods presented in [9–11] associate MPCs to the surrounding geometry yielding the possibility to track the agents' absolute positions with a single anchor only. To push the limits of accuracy and robustness, the methods in [12–16] introduce cooperation among the agents too. In [12] the performance gain was shown in terms of position error for a varying number of cooperating agents and a single anchor. In [13] the mathematical model is relaxed to a convex optimization problem. The gained performance is demonstrated for two agents and three anchors.

The availability of only a small number of anchors and cooperating agents results in a limited number of measurements which can be used for positioning. To encounter ambiguities and inaccuracies, the methods in [14–16] assume the employment of *self* measurements, where each agent is equipped with a transmitting and a receiving antenna located next to each other. Measuring the channel impulse response between these antennas enables the estimation of MPCs whose parameters depend only on one agent's position (and antenna properties) as well as the surrounding environment. These measurements therefore serve as an attractive additional information source for the task of positioning.

In this work we present an anchor-free, centralized, cooperative tracking algorithm. It takes advantage of position-related information contained in the measured channel impulse responses. We consider *relative* measurements between neighboring agents and *self* measurements where the agents act simultaneously as transmitters and receivers. Such a setup applies for example to applications in a Car-To-X scenario, emergency service personnel entering a building, and (automated) vehicles in a production facility. The proposed algorithm estimates parameters of deterministic MPCs and associates the estimated delays to expected ones. To calculate the expected delays, we consider planar surfaces (e.g. walls) in an indoor environment described by a provided floorplan. To account for inaccuracies in the floorplan, as well as for effects like penetra-

tion and diffraction of the electromagnetic waves, the associated MPC delays are used to simultaneously adapt the floorplan while tracking the agents' positions. The proposed method aims at refining the (possibly inaccurate) floorplan rather than discovering additional features (as proposed in SLAM [19]). We assume a static environment.

The key contributions of this paper are:

- We formulate the relationship between the agent positions, the environment model and the measured MPC delays. It is assumed that agents are synchronized with each other.
- We present an anchor-free, centralized, cooperative algorithm using data association of MPC delays and formulate an extended Kalman filter (EKF) for simultaneous tracking of the agents' positions and the floorplan.
- We demonstrate the ability of the algorithm to track agents without information obtained from fixed anchors or an inertial measurement unit.
- We recursively update the environment model to remedy uncertainties in the provided floorplan.
- We show the performance in adverse scenarios considering a varying number of agents and channel bandwidths.

The paper is organized as follows: Section 2 provides an overview of the problem and introduces the signal and geometry models. Section 3 describes the implementation of the cooperative algorithm. Section 4 presents an evaluation and discussion using a static environment and Sec. 5 wraps up the paper with a conclusion. We note that this work extends our conference publication [16], in what follows. We introduce a geometry model for relating MPC delays to agent positions as well as environment features. We verify the performance gain for a varying number of agents, consider the influence of the channel bandwidth and the impact of obtaining range information from a fixed anchor.

2 Problem Formulation

Consider a synchronized network of agents $m \in \mathcal{M} = \{1, \dots, M\}$ located in an indoor-environment as shown in Fig. 1. The agents aim at estimating their positions¹ $\{\mathbf{p}^{(m)}\}$ using radio signals affected by multipath propagation. The multipath propagation originates from the interaction of the transmitted unit-energy signal $s(t)$ with its surrounding environment, e.g. reflections at flat surfaces like wall segments. The time delays of the reflections convey information about the surrounding environment and can be exploited for localizing the agents.

We use UWB signals motivated by their superior time resolution which enables a temporal separation of the multipath components in indoor environments. We employ *self* and *relative* channel measurements conducted by the agents. The self measurement is individually performed by each agent m by

¹Similar to [7,13,17,20–22] we model the agent's positions and the surrounding environment in two dimensions. The restriction is reasonable since most positioning applications have knowledge about the agent's height and the extension to three dimensions is straight-forward.

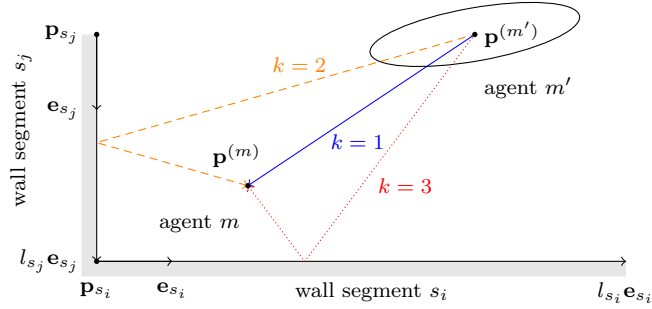


Figure 1: Illustration of cooperative localization utilizing multipath propagation. The receiving agent m facilitates the MPCs $k \in \mathcal{K}^{(m',m)} = \{1, 2, 3\}$ for localization. The transmitting agent m' is uncertain about its position, represented by the ellipse. The higher position uncertainty of m' in direction of MPC $k = 2$ compared to $k = 3$ needs to be accounted by agent m .

emitting the signal $s(t)$ and receiving the corresponding superposition of reflections originating at the surrounding environment. The relative measurements are performed by two cooperating agents m and m' , yielding a received signal composed of the sum of the line-of-sight (LOS) and multipath components. The delays of the components depend on both agents' positions, indicating that the position accuracy of cooperating agents is related as well [7, 23–25].

2.1 Signal Model

We model the baseband-equivalent received signal $r^{(m',m)}(t)$ of agent m for the emitted signal $s(t)$ of agent m' according to [7, 26]

$$r^{(m',m)}(t) = \sum_{k \in \mathcal{K}^{(m',m)}} \alpha_k^{(m',m)} s(t - \tau_k^{(m',m)}) + (s * \nu^{(m',m)})(t) + w(t). \quad (1)$$

The first term on the right-hand-side denotes the deterministic MPCs which can be related to an environment model. The set $\mathcal{K}^{(m',m)}$ contains the modeled MPCs at agents' positions $\mathbf{p}^{(m)}$ and $\mathbf{p}^{(m')}$. Each deterministic MPC $k \in \mathcal{K}^{(m',m)}$ is characterized by its amplitude $\alpha_k^{(m',m)}$ and delay $\tau_k^{(m',m)}$. The relation between MPC delays, agent positions and the surrounding environment will be further discussed in Sec. 2.2.

The second term of (1) covers all *residual* components which are not modeled by the environment model as well as scattering at small objects or rough surfaces. It is defined as the convolution of $s(t)$ with diffuse multipath (DM) $\nu^{(m',m)}(t)$. We model DM as a zero-mean Gaussian random process which is non-stationary in the delay domain τ , defined by the auto-correlation function $\mathbb{E}\{\nu \nu^{(m',m)*}(\tau) [\nu^{(m',m)}(u)]^*\} = S_\nu^{(m',m)}(\tau) \delta(\tau - u)$ where $S_\nu^{(m',m)}(\tau)$ denotes the power delay profile (PDP) of DM. The PDP is quasi-stationary in the spatial domain. At the large scale, it is a function of the positions of transmitter and receiver, determined by the surrounding environment [27].

The last term denotes additive white Gaussian noise with a double-sided power spectral density of $N_0/2$. The signal model in (1) is applied for the

relative measurements ($m \neq m'$) as well as for the self measurements by setting $m = m'$.

2.2 Geometry model

The agents are capable of estimating the MPC delays from the received signal. To link the estimated delays to the environment, we employ a geometry model as illustrated in Fig. 1. Agent m receives the emitted pulse of agent m' as a sum of the LOS component and reflections at wall segments s_i and s_j .

We consider reflections originating at planar surfaces, e.g. walls, doors, and windows, in the following denoted as *wall segments*. Each wall segment $s \in \mathcal{S} = \{1, \dots, S\}$ is described by its location $\mathbf{p}_s \in \mathbb{R}^2$ (an end point of the wall segment) and orientation $l_s \mathbf{e}_s$ with l_s as length and the unit-vector $\mathbf{e}_s \in \mathbb{R}^2$ as the direction of the wall segment as illustrated in Fig. 1.

The wall segments reflecting the deterministic MPC k are denoted by $\mathbf{s}_k^{(m',m)}$, consisting of the indices of the wall segments $\mathbf{s}_k^{(m',m)} = [s_1, \dots, s_I]$, with I as number of reflecting segments, in the following referenced as *reflection order*.

Given the geometry model, the delays of both the LOS and the reflections can be denoted as a function of the interacting agents $\mathbf{p}^{(m)}$ and $\mathbf{p}^{(m')}$, and the bounced wall segments, denoted as

$$\tau_k^{(m',m)} = \frac{1}{c} d(\mathbf{p}^{(m')}, \mathbf{p}^{(m)}, \mathbf{s}_k^{(m',m)}) \quad (2)$$

where c is the speed of light (see Appendix 7 for the derivation).

As we assume a reciprocal channel between m' and m , the MPC delays are equal whether m' acts as the receiver or transmitter, i.e. $\tau_k^{(m',m)} = \tau_k^{(m,m')}$ (see Appendix 8). We consider a two-dimensional environment model. Reflections which are not contained in the geometry model (e.g. reflections by floor or ceiling, or at furniture) are treated as DM in (1).

3 Proposed algorithm

The proposed algorithm tracks the agent's positions as well as the locations of the wall segments using an EKF [19]. We describe the state dynamics by the joint state vector \mathbf{x}_n with discrete time step n by employing a state-space and a measurement model

$$\text{state-space model: } \mathbf{x}_n = f(\mathbf{x}_{n-1}) + \mathbf{n}_{a,n} \quad (3)$$

$$\text{measurement model: } \mathbf{z}_n = h(\mathbf{x}_n) + \mathbf{n}_n \quad (4)$$

where $\mathbf{n}_{a,n}$ and \mathbf{n}_n are the process noise and measurement noise, respectively. The EKF² estimates the agents' positions $\{\mathbf{p}_n^{(m)} : m \in \mathcal{M}\}$ and the locations of the wall segments $\{\mathbf{p}_s : s \in \mathcal{S}\}$ using the estimated MPC delays $\{\hat{d}_{k,n}^{(m',m)} = c\hat{\tau}_{k,n}^{(m',m)} : m, m' \in \mathcal{M}\}$ (scaled by c), as measurement input of the filter. Note, the joint state vector \mathbf{x}_n is introduced in Sec. 3.4 and time step n has been added to position vectors and MPC delays.

²The choice of the EKF is reasoned due to the weak non-linearity of the measurement model in the vicinity of the linearization point.

The algorithm is formulated by a prediction and an update step. At the prediction step the movement of the agents is modeled by a constant-velocity motion model (Sec. 3.1) using (3). The update step predicts the multipath propagation employing the geometry model of Section 2.2 and updates the agent positions and the wall segment locations (Sec. 3.4) using (4).

3.1 State-space model of agents

We use a constant-velocity motion model to track the agents' positions. The state vector of a single agent m is characterized by its position $\mathbf{p}_n^{(m)}$ and velocity $\mathbf{v}_n^{(m)}$

$$\mathbf{x}_n^{(m)} = [(\mathbf{p}_n^{(m)})^\top, (\mathbf{v}_n^{(m)})^\top]^\top$$

and the movement of each agent follows as

$$\mathbf{x}_n^{(m)} = \mathbf{F}\mathbf{x}_{n-1}^{(m)} + \mathbf{G}\mathbf{n}_{a,n}^{(m)}$$

with

$$\mathbf{F} = \begin{bmatrix} 1 & 0 & \Delta T & 0 \\ 0 & 1 & 0 & \Delta T \\ 0 & 0 & 1 & 0 \\ 0 & 0 & 0 & 1 \end{bmatrix} \quad \mathbf{G} = \begin{bmatrix} \frac{\Delta T^2}{2} & 0 \\ 0 & \frac{\Delta T^2}{2} \\ \Delta T & 0 \\ 0 & \Delta T \end{bmatrix}$$

where we assume that the driving acceleration noise $\mathbf{n}_{a,n}^{(m)}$ follows a zero-mean, Gaussian distribution (assumed to be independent across m and n) with variance σ_a^2 and ΔT denotes the sample period of n . The individual state vectors of the cooperating agents $m \in \mathcal{M}$ are stacked into a state vector of all agents $\mathbf{x}_n^{\mathcal{M}} = [(\mathbf{x}_n^{(1)})^\top, \dots, (\mathbf{x}_n^{(M)})^\top]^\top$ and the motion model becomes

$$\underbrace{\begin{bmatrix} \mathbf{x}_n^{(1)} \\ \vdots \\ \mathbf{x}_n^{(M)} \end{bmatrix}}_{\mathbf{x}_n^{\mathcal{M}}} = \underbrace{\begin{bmatrix} \mathbf{F} & & \mathbf{0} \\ & \ddots & \\ \mathbf{0} & & \mathbf{F} \end{bmatrix}}_{\mathbf{F}^{\mathcal{M}}} \underbrace{\begin{bmatrix} \mathbf{x}_{n-1}^{(1)} \\ \vdots \\ \mathbf{x}_{n-1}^{(M)} \end{bmatrix}}_{\mathbf{x}_{n-1}^{\mathcal{M}}} + \underbrace{\begin{bmatrix} \mathbf{G} & & \mathbf{0} \\ & \ddots & \\ \mathbf{0} & & \mathbf{G} \end{bmatrix}}_{\mathbf{n}_{a,n}^{\mathcal{M}}} \underbrace{\begin{bmatrix} \mathbf{n}_{a,n}^{(1)} \\ \vdots \\ \mathbf{n}_{a,n}^{(M)} \end{bmatrix}}_{\mathbf{n}_{a,n}^{\mathcal{M}}}. \quad (5)$$

3.2 Measurement model

The measurement model relates the positions of the agents to delays of deterministic MPCs. Using the predicted agent positions from the motion model, the algorithm calculates a set of expected MPC delays. The expected delays are associated to estimated MPC delays obtained from the measured channel impulse responses. Finally, the employed EKF facilitates the measurement model for updating the agents' positions by consideration of the associated MPC delays.

3.2.1 Estimation of multipath components

To estimate the delays of the MPCs, each agent performs self and relative channel measurements. An iterative least-squares approximation [28, 29] is used to extract one MPC per iteration ℓ from each measurement $r_n^{(m,m)}(t)$.

Initializing the signal $r^{(\ell)}(t)$ with $r^{(0)}(t) = r_n^{(m',m)}(t)$ the delay $\hat{\tau}_{\ell,n}^{(m',m)}$ of the strongest MPC in $r^{(\ell)}(t)$ is estimated as

$$\hat{\tau}_{\ell,n}^{(m',m)} = \operatorname{argmin}_{\tau} \int_0^T |r^{(\ell)}(t) - a^{(\ell)}(\tau)s(t-\tau)|^2 dt$$

with

$$a^{(\ell)}(\tau) = \int_0^T [s(t-\tau)]^* r^{(\ell)}(t) dt \quad (6)$$

where T denotes the measurement duration. The corresponding amplitude follows as $\hat{\alpha}_{\ell,n}^{(m',m)} = a^{(\ell)}(\hat{\tau}_{\ell,n}^{(m',m)})$. Both $\hat{\tau}_{\ell,n}^{(m',m)}$ and $\hat{\alpha}_{\ell,n}^{(m',m)}$ are estimated from $r^{(\ell)}(t)$ at each iteration step ℓ , followed by updating $r^{(\ell+1)}(t)$ according to

$$r^{(\ell+1)}(t) = r^{(\ell)}(t) - \hat{\alpha}_{\ell,n}^{(m',m)} s(t - \hat{\tau}_{\ell,n}^{(m',m)})$$

until the $Z_n^{(m',m)}$ strongest MPCs are found.

The estimated MPC delays of each self and relative measurement are multiplied by c to obtain the MPC ranges $\hat{d}_{\ell,n}^{(m',m)} = c\hat{\tau}_{\ell,n}^{(m',m)}$, which are stored in the sets

$$\mathcal{Z}_n^{(m',m)} = \{\hat{d}_{\ell,n}^{(m',m)}\}_{\ell=1}^{Z_n^{(m',m)}}. \quad (7)$$

3.2.2 Prediction of deterministic MPCs

Employing the motion model (5) yields the predicted agent positions $\check{\mathbf{p}}_n^{(m)}$ contained in $\check{\mathbf{x}}_n^{\mathcal{M}} = \mathbf{F}^{\mathcal{M}} \mathbf{x}_{n-1}^{\mathcal{M}}$. The expected range of MPC k follows from the geometry model (see Sec. 2.2) as

$$\check{d}_{k,n}^{(m',m)} = d(\check{\mathbf{p}}_n^{(m')}, \check{\mathbf{p}}_n^{(m)}, \mathbf{s}_k^{(m',m)}), \quad \text{for all } k \in \mathcal{K}_n^{(m',m)}. \quad (8)$$

The set of expected MPCs $\mathcal{K}_n^{(m',m)}$ depends on the agents' positions and the environment. As the propagation of deterministic MPCs is potentially affected by obstacles and neighboring wall segments, we verify their existence using an optical ray-tracer³ [30, p. 132] to obtain the set of deterministic MPCs $\mathcal{K}_n^{(m',m)}$. Finally, we gather the expected ranges in the set

$$\mathcal{D}_n^{(m',m)} = \{\check{d}_{k,n}^{(m',m)} : k \in \mathcal{K}_n^{(m',m)}\}. \quad (9)$$

3.2.3 Association of expected to deterministic MPCs

To associate the estimated ranges $\mathcal{Z}_n^{(m',m)}$ to expected ranges $\mathcal{D}_n^{(m',m)}$ we use the Munkres algorithm [31] based on an *optimal sub-pattern assignment* metric [32]. The Munkres algorithm aims at associating each expected range $\check{d}_{k,n}^{(m',m)}$ to a measured one $\hat{d}_{\ell,n}^{(m',m)}$. The outcome $\mathcal{A}_n^{(m',m)}$ contains pairs of associated ranges $(\hat{d}_{\ell,n}^{(m',m)}, \check{d}_{k,n}^{(m',m)})$, labeled by MPC indices $k \in \mathcal{K}_n^{(m',m)}$. Note, that we apply a cut-off distance d_c [29] which limits the discrepancy between each associated

³Application of the ray-tracer to the examples shown in Fig. 9 and 10 yields six and seven deterministic MPCs for the self and relative measurement, respectively, considering first- and second-order reflections.

pair to a maximum distance, $|\hat{d}_{k,n}^{(m',m)} - \check{d}_{k,n}^{(m',m)}| \leq d_c$. Setting d_c to small values (in sub-meter range) limits the number of potential associations. A higher value enables more associations but also increases the risk of wrong associations (see Sec. 4.6).

After the association, the measured and the expected ranges of each associated pair $(\hat{d}_{k,n}^{(m',m)}, \check{d}_{k,n}^{(m',m)}) \in \mathcal{A}_n^{(m',m)}$ are stacked in the vectors

$$\mathbf{z}_n^{(m',m)} = [\dots, \hat{d}_{k,n}^{(m',m)}, \dots] \quad (10)$$

$$\mathbf{d}_n^{(m',m)} = [\dots, \check{d}_{k,n}^{(m',m)}, \dots]. \quad (11)$$

3.2.4 Update step

The associated ranges of the self and relative measurements are stacked in the observation vector \mathbf{z}_n according to

$$\mathbf{z}_n = [\mathbf{z}_n^{(1,1)}, \dots, \mathbf{z}_n^{(1,M)}, \mathbf{z}_n^{(2,1)}, \dots, \mathbf{z}_n^{(2,M)}, \dots, \mathbf{z}_n^{(M,M)}]^\top \quad (12)$$

and the expected ranges in

$$\mathbf{d}_n = [\mathbf{d}_n^{(1,1)}, \dots, \mathbf{d}_n^{(1,M)}, \mathbf{d}_n^{(2,1)}, \dots, \mathbf{d}_n^{(2,M)}, \dots, \mathbf{d}_n^{(M,M)}]^\top$$

both with length $K_n = \sum_{m',m} |\mathcal{A}_n^{(m',m)}|$. The EKF employs the Jacobian $\mathbf{H}_n^{\mathcal{M}}$ of the non-linear function (8) [19] to describe the gradient of the deterministic MPC ranges with respect to the agent positions, evaluated at the predicted agent positions

$$\mathbf{H}_n^{\mathcal{M}} = \left. \frac{\partial h(\mathbf{x}^{\mathcal{M}})}{\partial \mathbf{x}^{\mathcal{M}}} \right|_{\mathbf{x}^{\mathcal{M}} = \check{\mathbf{x}}_n^{\mathcal{M}}} = \begin{bmatrix} \mathbf{h}_{1,n}^{\mathcal{M}} \\ \vdots \\ \mathbf{h}_{\kappa,n}^{\mathcal{M}} \\ \vdots \\ \mathbf{h}_{K_n,n}^{\mathcal{M}} \end{bmatrix}. \quad (13)$$

Each row $\kappa \in [1, K_n]$ of $\mathbf{H}_n^{\mathcal{M}}$ considers one associated range.

Assuming the κ th row belongs to MPC k obtained at a self measurement of agent m then the range gradient of (8) (derived in Appendix 9.0.1) follows as

$$\dot{\mathbf{d}}_{k,n}^{(m)} = \left. \frac{\partial d(\mathbf{p}^{(m)}, \mathbf{p}^{(m)}, \mathbf{s}_k^{(m,m)})}{\partial \mathbf{p}^{(m)}} \right|_{\mathbf{p}^{(m)} = \check{\mathbf{p}}_n^{(m)}}$$

and the κ th row of $\mathbf{H}_n^{\mathcal{M}}$ is defined as

$$\mathbf{h}_{\kappa,n}^{\mathcal{M}} = [0, \dots, \underbrace{(\dot{\mathbf{d}}_{k,n}^{(m)})^\top}_{\text{index } \mu}, \dots, 0] \quad (14)$$

where μ is the index of the m th agent position $\mathbf{p}_n^{(m)}$ within the state vector $\mathbf{x}_n^{\mathcal{M}}$.

In case that κ belongs to MPC k estimated at a relative measurement between agents m and m' then the range gradients from Appendix 9.0.2 are em-

ployed,

$$\begin{aligned}\dot{\mathbf{d}}_{k,n}^{(m')} &= \left. \frac{\partial d(\mathbf{p}^{(m')}, \check{\mathbf{p}}_n^{(m)}, \mathbf{s}_k^{(m',m)})}{\partial \mathbf{p}^{(m')}} \right|_{\mathbf{p}^{(m')} = \check{\mathbf{p}}_n^{(m')}} \\ \dot{\mathbf{d}}_{k,n}^{(m)} &= \left. \frac{\partial d(\check{\mathbf{p}}_n^{(m')}, \mathbf{p}^{(m)}, \mathbf{s}_k^{(m',m)})}{\partial \mathbf{p}^{(m)}} \right|_{\mathbf{p}^{(m)} = \check{\mathbf{p}}_n^{(m')}}\end{aligned}$$

and the κ th row of $\mathbf{H}_n^{\mathcal{M}}$ follows as

$$\mathbf{h}_{\kappa,n}^{\mathcal{M}} = \left[0, \dots, \underbrace{(\dot{\mathbf{d}}_{k,n}^{(m')})^\top}_{\text{index } \mu}, \dots, \underbrace{(\dot{\mathbf{d}}_{k,n}^{(m)})^\top}_{\text{index } \nu}, \dots, 0 \right]$$

with μ and ν denoting the indices which locate the positions of agents m' and m within $\mathbf{x}_n^{\mathcal{M}}$, respectively.

3.3 Range uncertainty estimation

The proposed algorithm uses the MPC-range uncertainty $\text{var}\{\hat{d}_{k,n}^{(m',m)}\}$ to describe the measurement noise \mathbf{n}_n . To estimate the range uncertainties we employ the signal-to-interference-plus-noise ratio (SINR) of the corresponding MPCs which defines the Cramér-Rao lower bound [7, 29]

$$\text{var}\{\hat{d}_{k,n}^{(m',m)}\} \geq \left(\frac{8\pi^2 \beta^2}{c^2} \text{SINR}_{k,n}^{(m',m)} \right)^{-1}$$

with

$$\text{SINR}_{k,n}^{(m',m)} = \frac{|\tilde{\alpha}_{k,n}^{(m',m)}|^2}{N_0 + T_p S_\nu^{(m',m)}(\tilde{\tau}_{k,n}^{(m',m)})}$$

where β is the effective (root mean square) bandwidth and T_p the pulse duration of $s(t)$. The SINR is a function of the MPC amplitudes $\tilde{\alpha}_{k,n}^{(m',m)}$ and the PDP $S_\nu^{(m',m)}(\tau)$ evaluated at MPC delays $\tau = \tilde{\tau}_{k,n}^{(m',m)}$ [7].

As the parameter estimation of MPCs as well as their association to expected ones may be erroneous, especially if only one snapshot of the channel impulse response is available, we propose to employ the geometry model to calculate the MPC delays $\tilde{\tau}_{k,n}^{(m',m)}$ using (2), once the update step of the agents' positions is performed. The corresponding amplitudes $\tilde{\alpha}_{k,n}^{(m',m)}$ are estimated by projection of the received signal on the delayed pulse $s(t - \tilde{\tau}_{k,n}^{(m',m)})$ (equivalent to (6)). Finally, the SINR is estimated using a method-of-moments estimator [29] taking the amplitudes $\{\tilde{\alpha}_{k,i}^{(m',m)}\}_{i=n-N}^{n-1}$ over a window of N past measurements into account.

An alternative way of estimating the measurement noise considers the variance of the differences between the estimated $\hat{d}_{k,n}^{(m',m)}$ and the expected ranges $\check{d}_{k,n}^{(m',m)}$ over N past measurements. However, this method can be applied only for MPCs assigned to expected ones. Weak MPCs are unlikely to be discovered at each measurement which may result in a biased variance estimation due to less observation points.

Assuming independence among the measurements the range uncertainties of each self and relative measurement are stacked according to (12) and a diagonal measurement noise covariance matrix follows as

$$\mathbf{R}_n = \text{diag}([\dots, \text{var}\{\hat{d}_{k,n}^{(m',m)}\}, \dots]). \quad (15)$$

3.4 Incorporation of wall segment uncertainty

The proposed algorithm models the wave propagation employing a geometry model where the MPCs are assumed to be reflected at planar surfaces, e.g. wall segments, whose locations are known. In practice, several violations of the geometry model have to be considered. First, the locations of the wall segments, used for modeling the multipath propagation, are typically provided by building plans with limited accuracy, leading to biased expected MPC delays. Further, wall segments consist of multiple layers of materials, each with different reflection and transmission properties. The reduced propagation speed inside the materials adds a positive bias to the distance estimates.

To address the aforementioned sources of errors we propose to consider the geometry model within the state-space. Inclusion of the wall segments in the state-space allows to recursively update the segment locations using the estimated MPC ranges. Stacking the wall segment locations at time step n in the vector $\mathbf{p}_n^S = [\mathbf{p}_{1,n}^\top, \dots, \mathbf{p}_{S,n}^\top]^\top$ with dimension $(2S \times 1)$ yields the joint state vector consisting of agents and wall segments according to

$$\mathbf{x}_n = [(\mathbf{x}_n^M)^\top, (\mathbf{p}_n^S)^\top]^\top.$$

The covariance of the stacked segment locations is described by

$$\mathbf{P}_n^S = \begin{bmatrix} \mathbf{P}_{1,1,n} & & \mathbf{P}_{1,S,n} \\ & \ddots & \\ \mathbf{P}_{S,1,n} & & \mathbf{P}_{S,S,n} \end{bmatrix}$$

where $\mathbf{P}_{s,s,n}$ is the covariance of wall segment s and $\mathbf{P}_{s',s,n}$ is the cross-covariance between the segment s' and s . Then, the covariance of the state vector \mathbf{x}_n follows as

$$\mathbf{P}_n = \begin{bmatrix} \mathbf{P}_n^M & \mathbf{P}_n^{M,S} \\ (\mathbf{P}_n^{M,S})^\top & \mathbf{P}_n^S \end{bmatrix}$$

with \mathbf{P}_n^M and $\mathbf{P}_n^{M,S}$ being the covariance of the agent state vector \mathbf{x}_n^M and the cross-covariance of agent positions and segment locations, respectively.

The state-space and measurement models are adapted accordingly. Assuming the segments to be static, the state-space model in (5) is extended as follows

$$\begin{aligned} \mathbf{x}_n &= \begin{bmatrix} \mathbf{F}^M & \mathbf{0}_{(4M \times 2S)} \\ \mathbf{0}_{(2S \times 4M)} & \mathbf{0}_{(2S \times 2S)} \end{bmatrix} \mathbf{x}_{n-1} + \begin{bmatrix} \mathbf{n}_{a,n}^M \\ \mathbf{0}_{(2S \times 2)} \end{bmatrix} \\ &= \mathbf{F} \mathbf{x}_{n-1} + \mathbf{n}_{a,n}. \end{aligned} \quad (16)$$

with covariance \mathbf{Q}_n of the process noise $\mathbf{n}_{a,n}$. The measurement model considers the relation between deterministic MPC ranges and wall segment locations. Its Jacobian, evaluated for the predicted state $\check{\mathbf{x}}_n = \mathbf{F} \mathbf{x}_{n-1}$, is defined as (c.f. (13))

$$\mathbf{H}_n = \left. \frac{\partial h(\mathbf{x})}{\partial \mathbf{x}} \right|_{\mathbf{x}=\check{\mathbf{x}}_n} = \begin{bmatrix} \mathbf{h}_{1,n} \\ \vdots \\ \mathbf{h}_{K,n} \end{bmatrix}. \quad (17)$$

Assuming the κ th measurement in \mathbf{z}_n belongs to MPC k of the channel between agent m' and m , respectively, then the range gradients with respect to the locations of the segments⁴ $\{\check{\mathbf{p}}_{s,n}\}$ follow as

$$\dot{\mathbf{d}}_{k,s,n} = \left. \frac{\partial d(\check{\mathbf{p}}_n^{(m)}, \check{\mathbf{p}}_n^{(m')}, \mathbf{s}_k^{(m',m)})}{\partial \mathbf{p}_s} \right|_{\mathbf{p}_s = \check{\mathbf{p}}_{s,n}}$$

and row $\mathbf{h}_{\kappa,n}$ is written as

$$\mathbf{h}_{\kappa,n} = \left[\mathbf{h}_{\kappa,n}^{\mathcal{M}}, \dots, \underbrace{\dot{\mathbf{d}}_{k,1,n}^{\top}}_{\text{index } \eta_1}, \dots, \underbrace{\dot{\mathbf{d}}_{k,I,n}^{\top}}_{\text{index } \eta_I}, \dots \right]$$

where the indices η_1, \dots, η_I locate the segment indices in $\mathbf{s}_k^{(m',m)}$ within the state vector, and $\mathbf{h}_{\kappa,n}^{\mathcal{M}}$ is defined in (14).

The algorithm includes all wall segment locations $\{\mathbf{p}_{s,n} : s \in \mathcal{S}\}$ in the state vector \mathbf{x}_n in order to take advantage of the correlation with the agents $\mathbf{P}_n^{\mathcal{M},\mathcal{S}}$ as well as the correlation inbetween any two wall segments $\mathbf{P}_{s',s,n}$. These correlations spread the obtained information to the neighboring wall segments not assigned to an MPC at n , which is important as the number of associated MPCs K_n is in general small compared to the number of modeled wall segments S .

A summary of the algorithm, including the EKF equations [19], is presented in Algorithm 1.

4 Results

The proposed algorithm for anchor-less tracking of cooperating agents is based on several simplifications, e.g. the assumption of non-overlapping MPCs to ensure an accurate data association, and the necessity of a reliable building floorplan used for the geometry model. Further, the EKF facilitates a linearized measurement model to obtain the estimated agent positions using the measured distances. To validate these simplifications we performed an extensive measurement campaign using several agents in different setups. In Section 4.3 we demonstrate the possibility of tracking two agents without anchor information, taking into account wall segment uncertainties. In Section 4.4 we evaluate the potential performance gain when also a fixed anchor is available. Finally, in Section 4.5 we stress the robustness regarding uncertain floorplans and different signal bandwidths.

4.1 Setup for measured data

We obtained the measured data using a (maximum length sequence) channel sounder by *Ilmsens* [33] which spans a bandwidth of 3.5 – 10.5 GHz with an output power (at the antenna) of approx. –40 dBm/MHz. The received impulse response is shaped with a raised-cosine pulse with roll-off factor of $R = 0.6$ at a carrier frequency of $f_c = 7$ GHz [34]. Throughout the experiments in Sections 4.3 and 4.4 we keep the pulse duration T_p of the raised-cosine pulse

⁴Note, in (16) the segments are assumed to be static which results in $\check{\mathbf{p}}_{s,n} = \hat{\mathbf{p}}_{s,n-1}$ for all s .

Algorithm 1: Summary of the proposed algorithm.

assemble state vector \mathbf{x}_0 , covariance \mathbf{P}_0 , process noise \mathbf{Q}_0 and measurement noise \mathbf{R}_0 using the initialization values from Sec. 4.2

foreach $n > 0$ **do**

- predict state vector $\check{\mathbf{x}}_n = \mathbf{F}\mathbf{x}_{n-1}$
- covariance prediction $\check{\mathbf{P}}_n = \mathbf{F}\mathbf{P}_{n-1}\mathbf{F}^\top + \mathbf{Q}_n$
- foreach** *measurement between m and m'* **do**
 - estimate MPC delays $\mathcal{Z}_n^{(m',m)}$; c.f. (7)
 - predict deterministic MPC delays $\mathcal{D}_n^{(m',m)}$ at $\check{\mathbf{x}}_n$; c.f. (9)
 - associate estimated and predicted MPCs resulting in $\mathbf{z}_n^{(m',m)}$ and $\mathbf{d}_n^{(m',m)}$; c.f. (10) and (11)
- stack all measurements in \mathbf{z}_n and predictions in \mathbf{d}_n
- compute the Jacobian \mathbf{H}_n at $\check{\mathbf{x}}_n$; c.f. (17)
- estimate measurement noise \mathbf{R}_n ; c.f. (15)
- Kalman gain $\mathbf{K}_n = \check{\mathbf{P}}_n\mathbf{H}_n(\mathbf{H}_n\check{\mathbf{P}}_n\mathbf{H}_n^\top + \mathbf{R}_n)^{-1}$
- state estimate $\hat{\mathbf{x}}_n = \check{\mathbf{x}}_n + \mathbf{K}_n(\mathbf{z}_n - \mathbf{d}_n)$
- covariance estimate $\hat{\mathbf{P}}_n = (\mathbf{I} - \mathbf{K}_n\mathbf{H}_n)\check{\mathbf{P}}_n$
- foreach** *measurement between m and m'* **do**
 - foreach** *MPC $k \in \mathcal{K}_n^{(m',m)}$* **do**
 - calculate delay $\{\tilde{\tau}_{k,n}^{(m',m)}\}$ at $\hat{\mathbf{x}}_n$
 - estimate amplitude $\{\tilde{\alpha}_{k,n}^{(m',m)}\}$ and measurement noise; c.f. Sec. 3.3

fixed at $T_p = 0.5$ ns (corresponding to a 3 dB bandwidth of 2 GHz), while in Sec. 4.5 we evaluate the impact of T_p on the algorithm. We use self-made Eurocent coin antennas [35, p. 86] [36] with approximately uniform radiation patterns in azimuth domain and zeros in the directions of floor and ceiling. Thus, MPCs at floor and ceiling are attenuated by the beampattern. The agents were placed 1.2 m above the floor. To perform the self localization, each agent is equipped with two antennas, one acting as transmitter and the other one as receiver. We used RF switching matrices [37] to automate the measurements, facilitating up to 4 transmitter and 6 receiver antennas.

4.2 Implementation and initialization

The algorithm was implemented according to Algorithm 1. The agents' positions are initialized at $n = 0$ with their true⁵ positions. The agents' position covariance is initialized with $\mathbf{P}_0^{\mathcal{M}} = \text{diag}([\sigma_{\text{agent}}^2, \dots, \sigma_{\text{agent}}^2])$ with $\sigma_{\text{agent}}^2 = 0.03^2$ m², the wall segment uncertainties are initialized with $\{\mathbf{P}_{s,s,0} = \text{diag}([\sigma_{\text{seg}}^2, \sigma_{\text{seg}}^2]) : s \in \mathcal{S}\}$ and $\sigma_{\text{seg}}^2 = 0.003^2$ m², and the cross-correlations $\mathbf{P}_0^{\mathcal{M},\mathcal{S}}$ and $\mathbf{P}_{s',s,0}$ are initialized with zeros (for all $s', s \in \mathcal{S} : s' \neq s$). The driving noise σ_a^2 is set according to the maximum agent velocity of $\|\mathbf{v}_{\text{max}}\| = 0.025$ m/step such that $\sigma_a^2 = (\|\mathbf{v}_{\text{max}}\|/(3\Delta T))^2$ with $\Delta T = 1$ step. The measurement noise is initialized with $\mathbf{R}_0 = \text{diag}([0.07^2, \dots, 0.07^2])$ m².

The expected number of MPCs $|\mathcal{K}_n^{(m',m)}|$ depends on the agents' positions and the room geometry (see Sec. 3.2.2). The number of deterministic first-order reflections in the received signals is in the order of four to six whereas hundreds of higher-order reflections can be found. However, higher-order reflections are strongly affected by path overlap, resulting in challenging data association. Thus, the geometry model considers first- and second-order MPCs only.

We set the cut-off distance (c.f. Sec. 3.2.3) to $d_c = cT_p$ and the number of estimated MPCs $Z_n^{(m',m)}$ (Sec. 3.2.1) to $Z_n^{(m',m)} = 1.5|\mathcal{K}_n^{(m',m)}|$. MPC pairs whose expected ranges are equal within the cut-off distance d_c are not considered in (8) for avoiding wrong data associations. For the MPCs' range uncertainty estimation (see Sec. 3.3), the algorithm considers past measurements received within a distance (along the agent track) of 0.2 m.

4.3 Proof-of-concept experiment

We first present a proof-of-concept experiment. We are interested in how the algorithm gathers information necessary for tracking without the use of anchors. Further, we stress its robustness of dealing with a bias in the provided floorplan.

The agent network consists of two agents $m \in \{1, 2\}$ moving along trajectories of $n \in \{1, \dots, 200\}$ with velocity 2.5 cm/step, as shown in Fig. 2. The floorplan considers planar surfaces, e.g. concrete walls, doors, windows. To limit the number of deterministic MPCs, we consider wall segments of a length $l_s > 0.25$ m resulting in 71 modeled wall segments. At each n , two self-measurements and one relative measurement are performed. The estimated and associated MPCs are illustrated for $n = 90$.

⁵The *true* position was obtained using a measuring tape whose limited accuracy may introduce an error in the range of 1 cm.

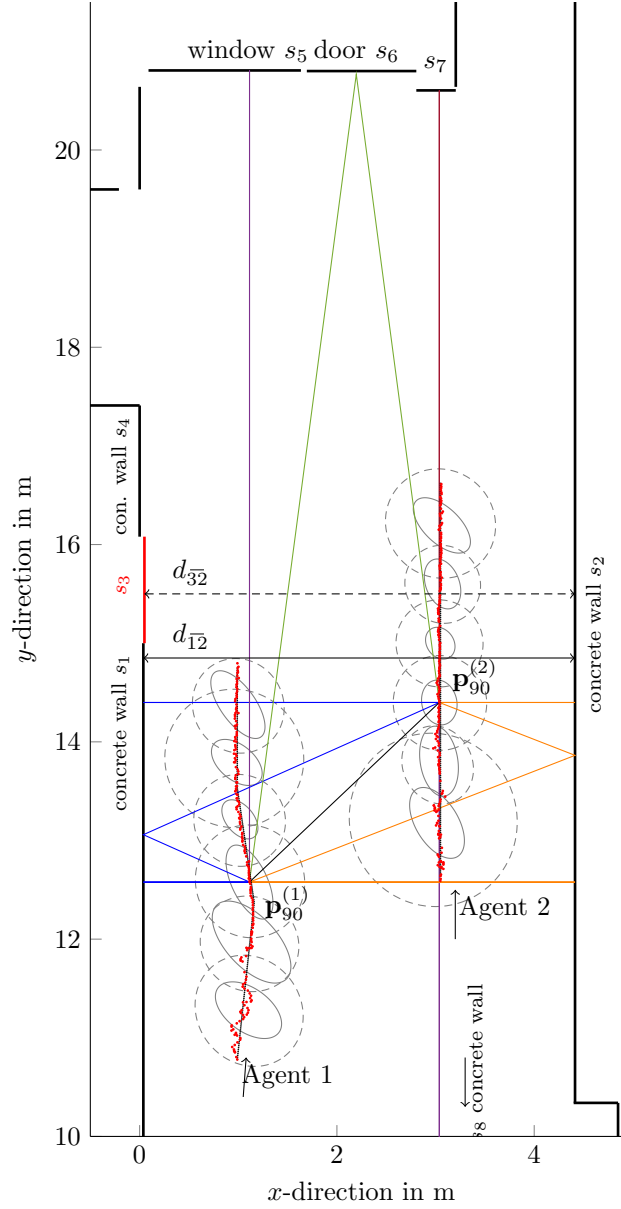


Figure 2: Proof of concept scenario: Two agents move independently along the trajectories (dotted, black) and estimate their positions (dotted, red). The proposed algorithm tracks the agents by exploiting MPC delays and corresponding SINRs (see Fig. 3). Measured and associated MPCs are illustrated for time step $n = 90$. The ellipses illustrate the standard deviation of the position estimates before (dashed, scaled by a factor of 10) and after the update step (solid, scaled by a factor of 40) at $n = \{30, 60, \dots, 180\}$.

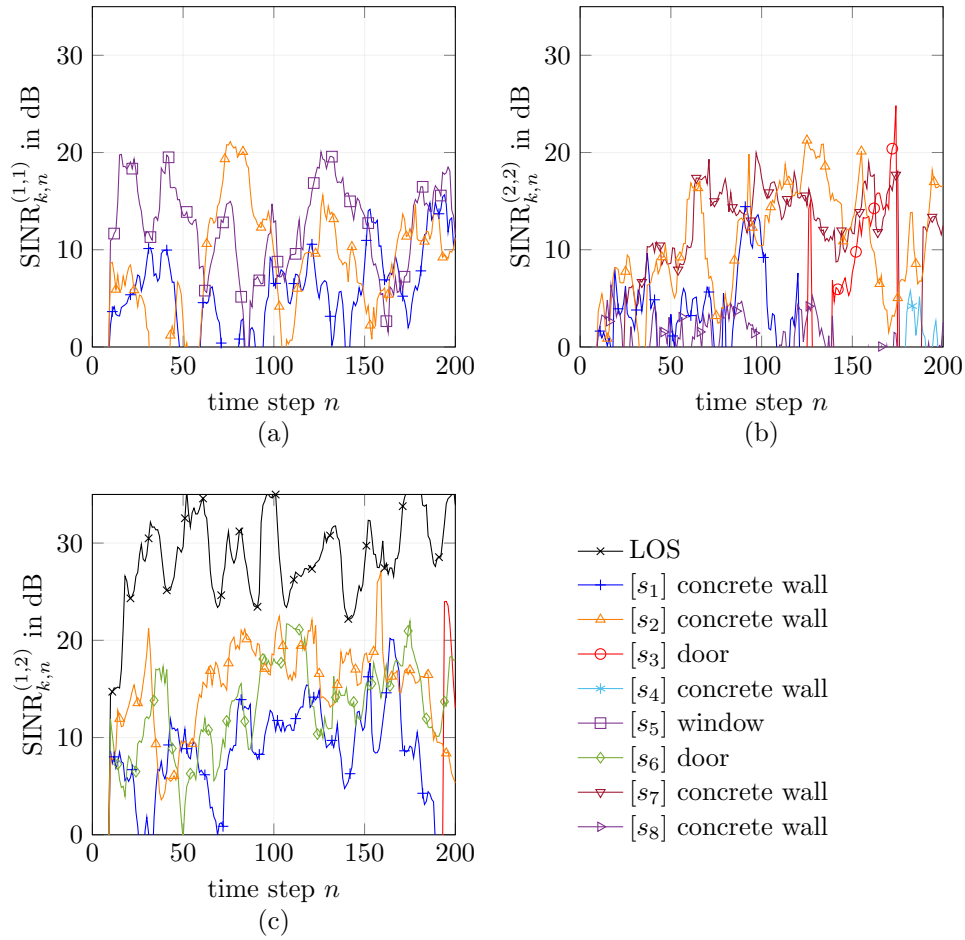


Figure 3: Estimated SINR-values obtained from agent one's (a) and agent two's (b) self measurements, respectively, and from relative measurements between both agents (c). The associated wall segments in $\mathbf{s}_k^{(m',m)}$ and corresponding multipath propagation paths are illustrated in Fig. 2. High SINR-values indicate a reliable MPC range measurement. The range of the LOS is most accurate, justified by its high SINR.

4.3.1 Reliability of MPCs

Fig. 3 illustrates the SINRs of the LOS and first-order MPCs bounced at wall segments $\{s_i : i = 1, \dots, 8\}$, respectively. The SINRs reveal information regarding the reliability of the MPCs used in the tracking filter (c.f. Sec. (3.3)). We can observe that the LOS serves as an important component justified by its high SINR. The reflections at concrete walls $\{s_1, s_2, s_4, s_7, s_8\}$, doors $\{s_3, s_6\}$ and the window $\{s_5\}$ are also promising candidates although their SINRs are lower compared to the LOS.

Both agents are closely surrounded by walls along the x -direction whereas the y -direction provides more space. In general, closely-located wall segments result in stronger MPCs which are valuable for positioning. This observation translates to a lower standard deviation of the position error along the x -direction, illustrated by the ellipses in Fig. 2.

4.3.2 Floorplan inaccuracies

As the proposed algorithm facilitates deterministic MPCs, its performance is strongly dependent on the accuracy of the provided floorplan. We can consider two challenges: (i) the electromagnetic waves experience a different floorplan due to effects like diffraction and penetration and (ii) the provided floorplan is inaccurate, e.g. pin boards mounted on the wall segments are not considered. The algorithm cannot distinguish between both cases. It employs the estimated MPC parameters to recursively update the floorplan. At each time step n the EKF weighs between the prior segment location and the measured MPC ranges using the prior covariance and the measurement noise. Each measured MPC provides location information to the floorplan. We are interested in the impact of prior location information on the convergence behavior of the floorplan. Figure 4 exemplifies the distance $d_{\bar{3}2}$ between wall segments s_3 and s_2 (see Fig. 2) in comparison with the distance $d_{\bar{1}2}$ between the wall segments s_1 and s_2 along n . According to the building floorplan, both s_1 and s_3 are in-line, resulting in $d_{\bar{3}2} \approx d_{\bar{1}2}$.

We initialized the location of s_3 with a bias of 0.1 m along its x -direction and analyze the rate of convergence using different initializations of the segment uncertainty σ_{seg} , namely $\sigma^* = 10$ mm, $\sigma^\diamond = 3$ mm, and $\sigma^\circ = 1$ mm, resulting in distances $d_{\bar{3}2}^*$, $d_{\bar{3}2}^\diamond$, and $d_{\bar{3}2}^\circ$, respectively. Wall segments s_1 and s_2 are associated to MPC measurements, starting with $n = 1$ and the distance between both segments attains $d_{\bar{1}2} \approx 4.38$ m. At time steps $n \in \{120, \dots, 175\}$, an MPC from segment s_3 is discovered in Agent 2's self measurement. Immediately the segment location is rearranged such that the expected MPC range matches with the measured one and $d_{\bar{3}2}$ converges to $d_{\bar{1}2}$. Figure 4 (b) exemplifies the standard deviation $([\mathbf{P}_{3,3,n}]_x)^{\frac{1}{2}}$ of wall segment s_3 along its x -direction. The more estimated MPCs are associated to s_3 , the lower gets its variance. We can observe that a high prior uncertainty of σ^* enables a fast adaption of the wall segment location and the initial bias is reduced. If the wall segment prior uncertainty is lowered (σ°) then the EKF relies more on the prior locations and the convergence rate is reduced.

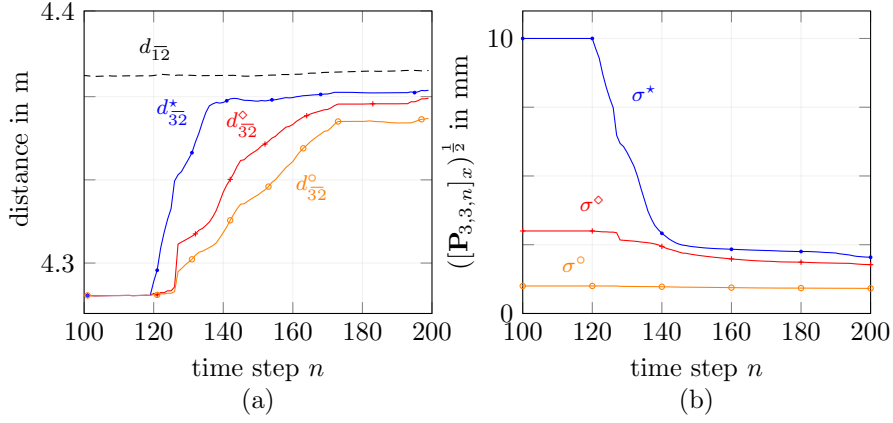


Figure 4: Adaption of floorplan dependent on the initialized wall segment uncertainty. The rate of convergence of the distance between s_2 and s_3 for different initializations of uncertainty $\sigma^* = 10$ mm, $\sigma^\circ = 3$ mm and $\sigma^\circ = 1$ mm results in convergence rates d_{32}^* , d_{32}° and d_{32}° . Higher uncertainties (b) lead to a faster floorplan adaption (a).

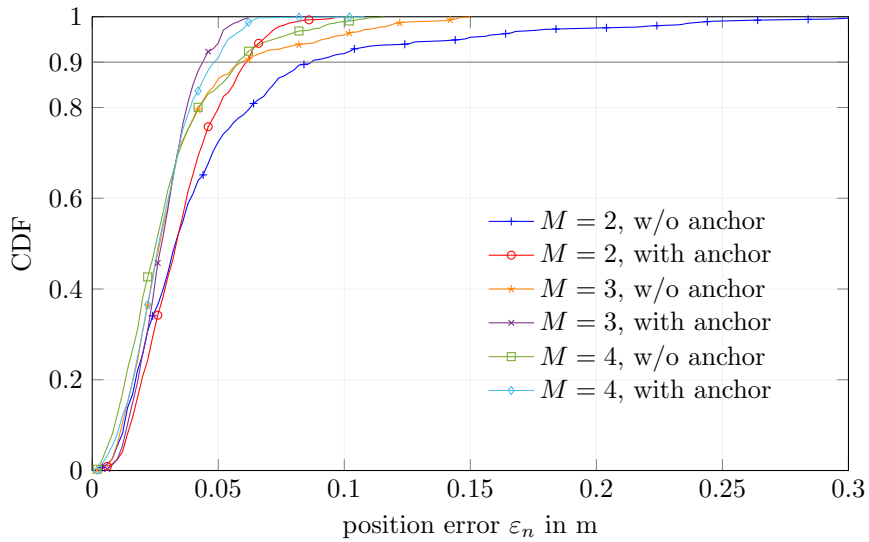


Figure 5: CDF of the agent's position error for different number $M \in \{2, 3, 4\}$ of cooperating agents with and without anchor for $T_p = 0.5$ ns.

4.4 Impact of anchor and number of agents

To evaluate the benefit of a fixed anchor we introduce M cooperating agents plus one anchor at position $\mathbf{p}^{(a)}$, as illustrated in Fig. 7. The agents move independently along their trajectories of $n \in \{1, \dots, 200\}$ with varying velocities of 1 – 2.5 cm/step and perform, in summary, M self and $M(M - 1)/2$ relative measurements at each n . Additionally, each agent runs one relative measurement to the fixed anchor. These measurements are treated in the same manner as the relative measurements between the agents. The transmitting agent in (2) is set to the anchor's position ($\mathbf{p}^{(m')} = \mathbf{p}^{(a)}$) and the additional measurement equations $\{\tau_{k,n}^{(a,m)}\}$, for all $k, m\}$ are added to (13).

We are interested in the performance in terms of position error for different sizes of the agent network, $M = \{2, 3, 4\}$, with and without the use of an additional fixed anchor. Figure 5 illustrates the cumulative distribution functions (CDFs) of the position error $\varepsilon_n = \sum_m \|\hat{\mathbf{p}}_n^{(m)} - \mathbf{p}_n^{(m)}\|$ with $\mathbf{p}_n^{(m)}$ as true position of agent m . It can be observed that the presence of a fixed anchor improves the position error, especially for a small agent network of $M = 2$ which is justified by the higher number of available channel measurements (for $M = 2$, five channel measurements are available with anchor information compared to three channel measurements without). An increasing network size decreases the position error. The performance for $M = 3$ and $M = 4$ is similar but with a slight decrease for $M = 4$ due to NLOS conditions of Agent 4 (see Fig. 7). We can conclude that the algorithm is capable of tracking the agents' positions with only a minor degradation of the position error if no fixed anchor is used.

4.5 Impact of floorplan accuracy and signal bandwidth

As the algorithm relies strongly on the provided floorplan, we investigate further the impact of an inaccurate floorplan. Therefore, we initialized the locations $\{\mathbf{p}_{s,n} : s \in \mathcal{S}\}$ at $n = 0$ by adding independent, uniformly distributed noise samples to the true locations \mathbf{p}_s

$$\mathbf{p}_{s,0} = \mathbf{p}_s + \mathbf{n}_s, \text{ for all } s \in \mathcal{S}.$$

The elements in \mathbf{n}_s have been sampled from $\mathcal{U}(-r/2, r/2)$ with range r . Further, we are interested in the impact of the pulse duration T_p of the transmitted signal on the position accuracy. The proposed algorithm utilizes MPC parameters whose estimation is biased in case of overlapping MPCs and affected by diffuse multipath propagation. To ensure resolvable MPCs in the time domain, short pulse duration (corresponding to high bandwidths) are beneficial.

In the following, we compare the proposed algorithm with and without consideration of the segment uncertainty using \mathbf{x}_n and \mathbf{x}_n^M , respectively. We propose to evaluate the agents' position error relative to the floorplan. We consider the loss of an absolute coordinate system if the segment locations are included in the state vector by introducing a center of gravity of the floorplan

$$\hat{\mathbf{p}}_n^g = \left(\sum_{s \in \mathcal{S}} \hat{\mathbf{P}}_{s,s,n}^{-1} \right)^{-1} \sum_{s \in \mathcal{S}} \hat{\mathbf{P}}_{s,s,n}^{-1} \hat{\mathbf{p}}_{s,n}.$$

The center of gravity $\hat{\mathbf{p}}_n^g$ can be interpreted as weighted average of the floorplan feature locations. Uncertain wall segments (indicated by a large covariance

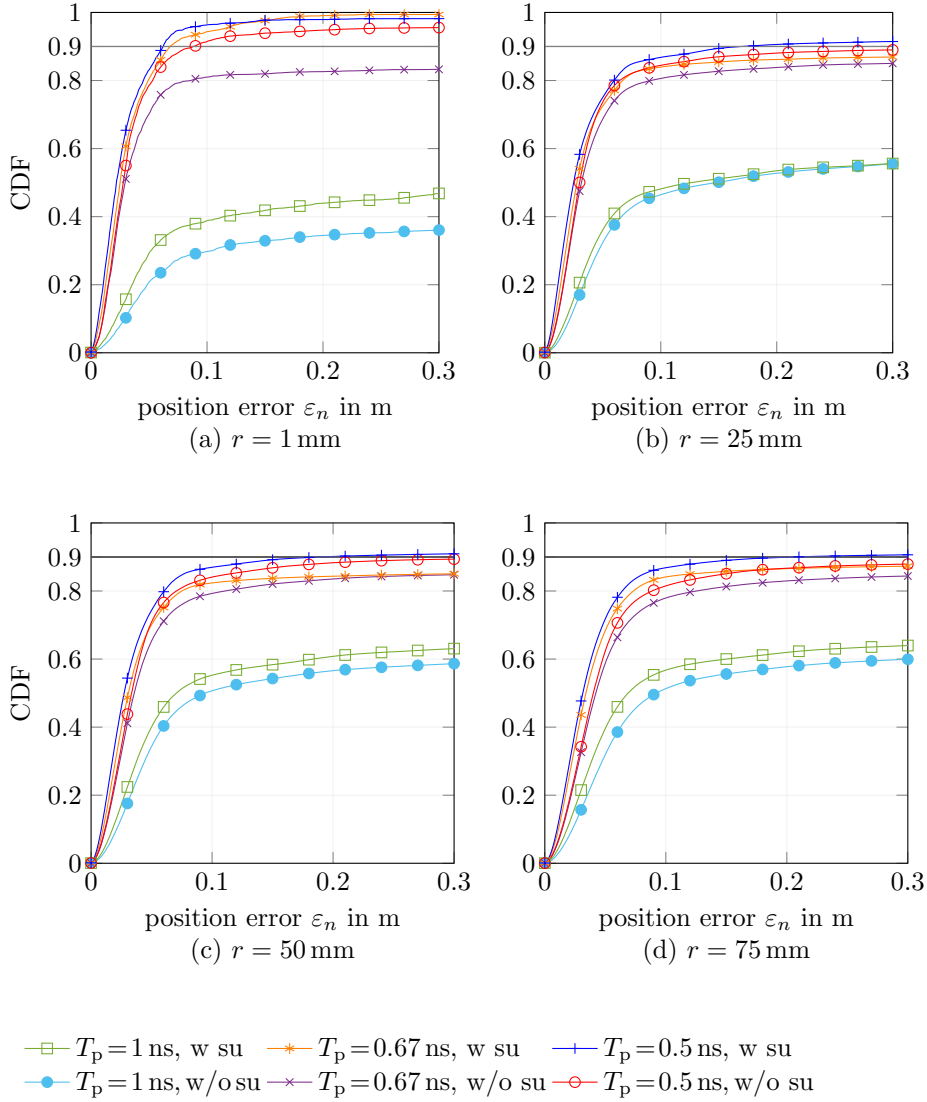


Figure 6: CDF of the position error using different ranges of floorplan errors of $r = 1$ mm (a), $r = 25$ mm (b), $r = 50$ mm (c) and $r = 75$ mm (d) against pulse duration $T_p \in \{1, 0.67, 0.5\}$ ns, with segment update (w su) and without segment update (w/o su).

$\{\hat{\mathbf{P}}_{s,s,n}\}$) will be less considered in $\hat{\mathbf{p}}_n^g$. The agents' position errors (relative to the floorplan) follow from

$$\varepsilon_n = \sum_m \|(\hat{\mathbf{p}}_n^{(m)} - \mathbf{p}_n^{(m)}) - (\hat{\mathbf{p}}_n^g - \mathbf{p}_0^g)\|$$

where the vector $(\hat{\mathbf{p}}_n^g - \mathbf{p}_0^g)$ accounts for the floorplan adaptation. To obtain the agent positions relative to the floorplan, the movement of $\hat{\mathbf{p}}_n^g$ is subtracted from the position error. We evaluate different levels of floorplan uncertainties $r \in \{1, 25, 50, 75\}$ mm and pulse duration $T_p \in \{0.5, 0.67, 1\}$ ns, each with 100 Monte Carlo runs. Figure 6 illustrates the CDFs of the position error, averaged for agent network sizes of $M = 2, 3$ and 4.

The position error depends strongly on the pulse duration seen by a poor performance at $T_p = 1$ ns. At smaller pulse duration, $T_p \in \{0.67, 0.5\}$ ns, the algorithm performs better because the MPCs tend to be more separated in the time domain yielding a more reliable MPC parameter estimation and association.

In general, we can observe that the position error degrades when a biased floorplan is initialized. This leads to a biased geometry model and subsequently to a challenging association of measured and predicted MPC delays. Including the floorplan in the state-space (using \mathbf{x}_n) enables to remedy the bias in order to get a more consistent floorplan.

4.6 Discussion and remarks

The algorithm requires to set the initial uncertainty of agents and wall segment locations at $n = 0$. At each time step the EKF updates the agent positions and segment locations by weighing between prior information (from the prediction step) and measured MPC delays associated to measurement noise. A wall segment which is uncertain about its location is more affected by the update step than a certain one (see Fig. 4). In [19, p. 317] the initialization of $\sigma_{\text{seg}}^2 \rightarrow \infty$ is proposed in order to enable a fast adaption. In this case the algorithm relies strongly on the MPC delay measurements and the quality of their data association. We prefer a low value of $\sigma_{\text{seg}}^2 = 0.003^2 \text{ m}^2$ since a slow adaption is more robust to noisy delay measurements and wrong data associations.

We do not add process noise to the segment locations. Each measured MPC thus reduces the segment location uncertainty (see Fig. 4). Low values of uncertainty prohibit a further adaption and thus a limitation of the lower variance may be useful to keep the adaptation active. However, in this work we are interested in how the adaptation of the floorplan can be beneficial and we did not implement such a limit.

The data association step is performed using the predicted agent positions. An increased accuracy of the predicted positions yields an increased quality in the data association as well. We recognized that a small cut-off distance between expected and estimated ranges of $d_c = 0.15$ m (at $T_p = 0.5$ ns) is vital when the agent network is off track. A mismatch between predicted and true agent positions yields wrong data associations. As shown in [38], the limitation of the maximum offset to d_c lowers wrong associations.

At the EKF prediction step the covariance of the agents is increased by the driving acceleration noise (with variance σ_a^2). In order to track trajectories with

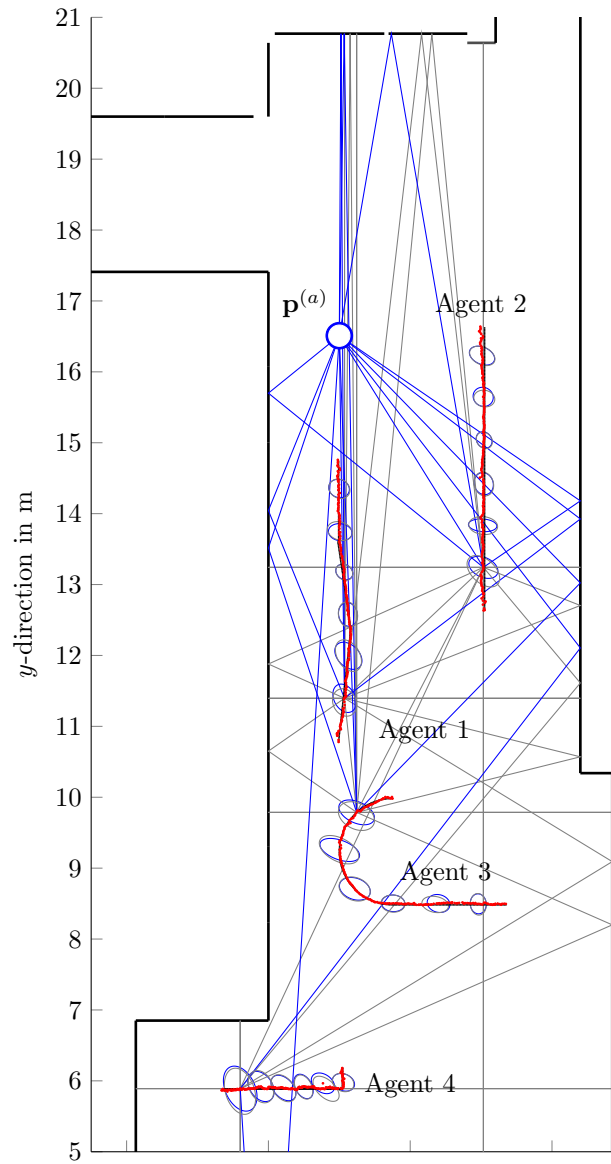


Figure 7: Illustration of floorplan and agent movement. The agents track their positions (dotted, red) using multipath propagation (gray). Obtaining additional information from a fixed anchor (blue) at $\mathbf{p}^{(a)}$ improves the accuracy, as shown in Fig. 5. The ellipses illustrate the standard deviation of the position estimate with (blue) and without anchor information (gray), scaled by a factor of 40 at $n = \{30, 60, \dots, 180\}$.

abrupt changes we set the $3\sigma_a$ point equal to the maximum velocity $\|\mathbf{v}_{\max}\| = 0.025$ m/step. We recognized that a smaller driving acceleration noise improves the accuracy but the algorithm was no longer able to follow abrupt turns in the trajectory as it puts too much importance on the motion model. We evaluated the algorithm in a static scenario where the only moving objects are the agents. In a non-static environment, additional (untracked) objects are present which deteriorate the multipath propagation. Subsequently, the SINRs of the MPCs are lowered, the algorithm relies less on MPC delays, and the position estimation uncertainty is increased. In this work, we did not evaluate the importance of static environments.

The complexity of the algorithm is mainly determined by the number of agents M . Considering all agents are located within their communication range then each additional agent requires M channel measurements (Sec. 3.2.1), range predictions (Sec. 3.2.2), data associations (Sec. 3.2.3), and range uncertainty estimations (Sec. 3.3). The EKF matrix inversion has a complexity of $\mathcal{O}((MK)^{2.4})$ [19, p. 43] with K as average number of associated MPCs (in practice approx. 4 – 6) and the complexity of the EKF matrix multiplication scales quadratically with the size of the state vector.

Ensuring high localization accuracy goes hand in hand with high synchronization accuracy. At self measurements the transmitter is co-located with the receiver which enables the usage of the same clock. At relative measurements transmitter and receiver are spatially separated and synchronization of the clocks is necessary. Any synchronization error will be reflected in a biased MPC parameter estimation. In literature, strategies to cope or neglect its impact have been proposed, e.g. joint positioning and synchronization [39], or a two-way exchange of pilot sequences like in IEEE 802.15.4a UWB radios [40] or using differential timing information inbetween MPCs [7]. In this work we omit the required synchronization by wiring the antennas to the channel sounder. State of the art UWB radios [40] induce a synchronization error with variance of 5^2 cm² which will affect the presented localization accuracy in a comparable range.

5 Conclusions

In this paper, we have presented a centralized, cooperative tracking algorithm for wireless networks without the need for further infrastructure, e.g. fixed anchors. We have developed an algorithm based on an extended Kalman filter which makes use of position-related information contained in measured channel impulse responses. To address uncertainties in the environment model we have included the floorplan in the state-space model. The performance evaluation with measured data has shown the feasibility of using deterministic MPCs to simultaneously track absolute agent positions and adapt the floorplan without employing information from an inertial measurement unit or from fixed anchors. The results demonstrate the necessity of high signal bandwidths exceeding 1 GHz to prevent overlapping of deterministic MPCs in an indoor environment. Our future work will address the reduction of the required bandwidth, the derivation of distributed tracking filters as well as the exploration of additional features in the geometry model.

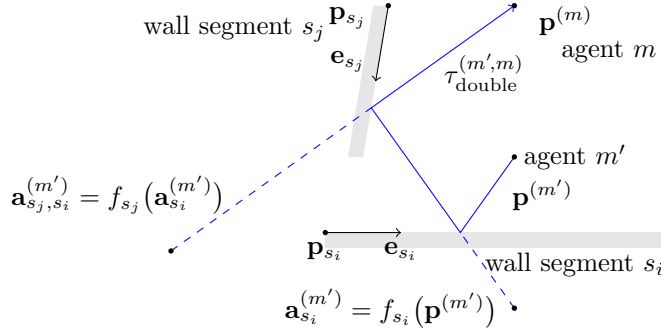


Figure 8: Illustration of multipath propagation using an image-source model. The position of the transmitting agent m' is mirrored at wall segments s_i and s_j , respectively, to obtain $\mathbf{a}_{s_j, s_i}^{(m')}$.

6 Appendix

7 Derivation of the geometry model

We describe the path of a deterministically modeled MPC k as a function of the positions of the transmitting agent m' , the receiving agent m , and the reflected surfaces. Each MPC is associated to a vector $\mathbf{s}_k^{(m', m)}$ consisting of the indices of the reflecting wall segments in chronological order $\mathbf{s}_k^{(m', m)} = [\dots, s_i, s_j, \dots, s_I]$ where I is the reflection order. Each wall segment $s \in \mathcal{S}$ is described by its location \mathbf{p}_s and alignment \mathbf{e}_s , as illustrated in Fig. 8. The transmitted signal from agent m' is reflected at the wall segments s_i and s_j and finally received by agent m . To calculate the delay of the MPC, an image-source model is used which mirrors the position of the transmitting agent at each reflecting wall segment to obtain mirrored images of the agent position.

Application of the image-source model for a first-order MPC is equivalent with mirroring the position $\mathbf{p}^{(m')}$ at segment $s \in \mathcal{S}$ [16, 41]

$$\begin{aligned} \mathbf{a}_s^{(m')} &= \mathbf{p}^{(m')} - 2\mathbf{T}_s(\mathbf{p}^{(m')} - \mathbf{p}_s) \\ &= (\mathbf{I} - 2\mathbf{T}_s)\mathbf{p}^{(m')} + 2\mathbf{T}_s\mathbf{p}_s \end{aligned} \quad (18)$$

with $\mathbf{T}_s = \mathbf{U}_{\frac{\pi}{2}}\mathbf{e}_s\mathbf{e}_s^\top\mathbf{U}_{\frac{\pi}{2}}^\top$ and $\mathbf{U}_{\frac{\pi}{2}}$ is a rotation matrix by $\pi/2$ (i.e. $\mathbf{U}_{\frac{\pi}{2}} = [[0, 1]^\top, [-1, 0]^\top]$). In (18) the matrix multiplication with \mathbf{T}_s extracts the component of $(\mathbf{p}^{(m')} - \mathbf{p}_s)$ which is orthogonal to \mathbf{e}_s . Under the assumption that the segment's location \mathbf{p}_s and alignment \mathbf{e}_s are fixed, the terms $(\mathbf{I} - 2\mathbf{T}_s)$ (denoted as *Householder matrix*) and $2\mathbf{T}_s\mathbf{p}_s$ can be calculated beforehand. Rewriting (18) as a function depending on the agent's position yields the affine transformation

$$\mathbf{a}_s^{(m')} = f_s(\mathbf{p}^{(m')}).$$

Higher-order reflections are modeled straight forwardly. Each reflecting segment is equipped with a virtual source, as shown in Fig. 8. The virtual source $\mathbf{a}_{s_i}^{(m')} = f_{s_i}(\mathbf{p}^{(m')})$, corresponding to segment s_i , is mirrored at segment s_j to

obtain $\mathbf{a}_{s_i, s_j}^{(m')} = f_{s_j}(\mathbf{a}_{s_i}^{(m')})$, which again can be expressed as a function of the agent's position according to

$$\mathbf{a}_{s_i, s_j}^{(m')} = f_{s_j}(f_{s_i}(\mathbf{p}^{(m')})) = f_{s_j} \circ f_{s_i}(\mathbf{p}^{(m')}).$$

The resulting MPC delay $\tau_{\text{double}}^{(m', m)}$ is calculated as norm of the geometric distance between $\mathbf{a}_{s_i, s_j}^{(m')}$ and the receiver position $\mathbf{p}^{(m)}$, scaled by the speed of light c

$$\tau_{\text{double}}^{(m', m)} = \frac{1}{c} \|\mathbf{p}^{(m)} - \mathbf{a}_{s_i, s_j}^{(m')}\|.$$

These steps can be generalized for an arbitrary deterministic MPC delay by considering the reflected segments $\mathbf{s}_k^{(m', m)} = [s_1, \dots, s_I]$ in the function composition of $\{f_s : s \in \mathbf{s}_k^{(m', m)}\}$ according to

$$\tau_k^{(m', m)} = \frac{1}{c} \|\mathbf{p}^{(m)} - (f_{s_I} \circ \dots \circ f_{s_1})(\mathbf{p}^{(m')})\| \quad (19)$$

denoted as measurement equation

$$\tau_k^{(m', m)} = \frac{1}{c} d(\mathbf{p}^{(m')}, \mathbf{p}^{(m)}, \mathbf{s}_k^{(m', m)}) \quad (20)$$

which relates the delay of MPC k to the agents' positions $\mathbf{p}^{(m)}$ and $\mathbf{p}^{(m')}$.

The advantage of using (20) is that the MPC delays are being decomposed into the positions of the agents m and m' and the geometry of the wall segments. It was constructed by mirroring agent position $\mathbf{p}^{(m')}$ at wall segments s_i followed by s_j . In the following (Appendix 8) we show for the general case that this procedure is equal to mirroring agent position $\mathbf{p}^{(m)}$ first by s_j followed by s_i and thus, (20) is capable of describing the delay gradients w.r.t both agent positions. In Appendix 9 we illustrate regularly occurring MPCs and their impact on the positioning algorithm.

8 Channel reciprocity

The proposed geometric model distinguishes between the transmitting and receiving agents located at $\mathbf{p}^{(m')}$ and $\mathbf{p}^{(m)}$, respectively. In the following, we show that the MPC delays and the delay gradients with respect to both agents and the floorplan features can be calculated irrespective of which agent is transmitting or receiving. To give a general proof, we show that the measurement equation (20) complies with

$$d(\mathbf{p}^{(m')}, \mathbf{p}^{(m)}, \mathbf{s}_k^{(m', m)}) = d(\mathbf{p}^{(m)}, \mathbf{p}^{(m')}, \mathbf{s}_k^{(m, m')}). \quad (21)$$

The ordering of reflected wall segments is different and needs to be considered. Let $\mathbf{s}_k^{(m', m)}$ consist of the indices of bounced walls of the traveling wave in chronological order (i.e. the i th element $[\mathbf{s}_k^{(m', m)}]_i$ denotes the i th bounced wall) from agent m' to m . Then $\mathbf{s}_k^{(m, m')}$ contains the bounced wall segments in reversed order of $\mathbf{s}_k^{(m', m)}$

$$[\mathbf{s}_k^{(m', m)}]_i = [\mathbf{s}_k^{(m, m')}]_{I-i+1} \quad \text{for all } i = 1, \dots, I. \quad (22)$$

We abbreviate $s_i^\triangleright = [s_k^{(m',m)}]_i$, $s_i^\triangleleft = [s_k^{(m,m')}]_i$ and omit the MPC index k for a shorter notation. Plugging (19) in (21) and tacking the square yields

$$\begin{aligned} \frac{1}{c} \left\| \underbrace{\mathbf{p}^{(m)}}_a - \underbrace{\prod_{i=1}^I \mathbf{A}_{s_i^\triangleright}}_{-b} \mathbf{p}^{(m')} - \underbrace{\sum_{i=1}^I \prod_{j=i+1}^I \mathbf{A}_{s_j^\triangleright}}_{-c} \mathbf{b}_{s_i^\triangleright} \right\|^2 = \\ \frac{1}{c} \left\| \underbrace{\mathbf{p}^{(m')}}_d - \underbrace{\prod_{i=1}^I \mathbf{A}_{s_i^\triangleleft}}_{-e} \mathbf{p}^{(m)} - \underbrace{\sum_{i=1}^I \prod_{j=i+1}^I \mathbf{A}_{s_j^\triangleleft}}_{-f} \mathbf{b}_{s_i^\triangleleft} \right\|^2 \end{aligned} \quad (23)$$

with the Householder matrix $\mathbf{A}_{s_i^\triangleright} = (\mathbf{I} - 2\mathbf{T}_{s_i^\triangleright})$ and $\mathbf{b}_{s_i^\triangleright} = 2\mathbf{T}_{s_i^\triangleright} \mathbf{p}_{s_i^\triangleright}$. Rewriting (23) and omitting c results in

$$\|\mathbf{a} + \mathbf{b} + \mathbf{c}\|^2 = \|\mathbf{d} + \mathbf{e} + \mathbf{f}\|^2$$

$$\begin{aligned} \mathbf{a}^\top \mathbf{a} + \mathbf{b}^\top \mathbf{b} + \mathbf{c}^\top \mathbf{c} + 2\mathbf{a}^\top \mathbf{b} + 2\mathbf{a}^\top \mathbf{c} + 2\mathbf{b}^\top \mathbf{c} = \\ \mathbf{d}^\top \mathbf{d} + \mathbf{e}^\top \mathbf{e} + \mathbf{f}^\top \mathbf{f} + 2\mathbf{d}^\top \mathbf{e} + 2\mathbf{d}^\top \mathbf{f} + 2\mathbf{e}^\top \mathbf{f}. \end{aligned}$$

The Householder matrix has the property

$$\begin{aligned} \mathbf{A}_{s_i^\triangleright}^\top \mathbf{A}_{s_i^\triangleright} &= (\mathbf{I} - 2\mathbf{U}_{\frac{\pi}{2}} \mathbf{e}_{s_i^\triangleright} \mathbf{e}_{s_i^\triangleright}^\top \mathbf{U}_{\frac{\pi}{2}}^\top)^\top (\mathbf{I} - 2\mathbf{U}_{\frac{\pi}{2}} \mathbf{e}_{s_i^\triangleright} \mathbf{e}_{s_i^\triangleright}^\top \mathbf{U}_{\frac{\pi}{2}}^\top) \\ &= (\mathbf{I} - 4\mathbf{U}_{\frac{\pi}{2}} \mathbf{e}_{s_i^\triangleright} \mathbf{e}_{s_i^\triangleright}^\top \mathbf{U}_{\frac{\pi}{2}}^\top + 4\mathbf{U}_{\frac{\pi}{2}} \mathbf{e}_{s_i^\triangleright} \mathbf{e}_{s_i^\triangleright}^\top \mathbf{e}_{s_i^\triangleright} \mathbf{e}_{s_i^\triangleright}^\top \mathbf{U}_{\frac{\pi}{2}}^\top) \\ &= \mathbf{I} \end{aligned} \quad (24)$$

which results in $\mathbf{a}^\top \mathbf{a} = \mathbf{e}^\top \mathbf{e} = (\mathbf{p}^{(m)})^\top \mathbf{p}^{(m)}$ and $\mathbf{b}^\top \mathbf{b} = \mathbf{d}^\top \mathbf{d} = (\mathbf{p}^{(m')})^\top \mathbf{p}^{(m')}$. Using the property

$$\begin{aligned} \mathbf{A}_{s_i^\triangleright} \mathbf{b}_{s_i^\triangleright} &= (\mathbf{I} - 2\mathbf{U}_{\frac{\pi}{2}} \mathbf{e}_{s_i^\triangleright} \mathbf{e}_{s_i^\triangleright}^\top \mathbf{U}_{\frac{\pi}{2}}^\top) 2\mathbf{U}_{\frac{\pi}{2}} \mathbf{e}_{s_i^\triangleright} \mathbf{e}_{s_i^\triangleright}^\top \mathbf{U}_{\frac{\pi}{2}}^\top \mathbf{p}_{s_i^\triangleright} \\ &= -2\mathbf{U}_{\frac{\pi}{2}} \mathbf{e}_{s_i^\triangleright} \mathbf{e}_{s_i^\triangleright}^\top \mathbf{U}_{\frac{\pi}{2}}^\top \mathbf{p}_{s_i^\triangleright} \\ &= -\mathbf{b}_{s_i^\triangleright} \end{aligned}$$

and (24), term $\mathbf{c}^\top \mathbf{c}$ results in

$$\begin{aligned} \mathbf{c}^\top \mathbf{c} &= \mathbf{b}_{s_1^\triangleright}^\top \mathbf{A}_{s_2^\triangleright}^\top \cdots \mathbf{A}_{s_I^\triangleright}^\top \mathbf{A}_{s_I^\triangleright} \cdots \mathbf{A}_{s_2^\triangleright} \mathbf{b}_{s_1^\triangleright} + \dots \\ &\quad + \mathbf{b}_{s_I^\triangleright}^\top \mathbf{A}_{s_I^\triangleright} \cdots \mathbf{A}_{s_2^\triangleright} \mathbf{b}_{s_1^\triangleright} + \dots + \mathbf{b}_{s_I^\triangleright}^\top \mathbf{b}_{s_I^\triangleright} \\ &= \mathbf{b}_{s_1^\triangleright}^\top \mathbf{b}_{s_1^\triangleright} + \dots - \mathbf{b}_{s_I^\triangleright}^\top \mathbf{A}_{s_{I-1}^\triangleright} \cdots \mathbf{A}_{s_2^\triangleright} \mathbf{b}_{s_1^\triangleright} + \dots + \mathbf{b}_{s_I^\triangleright}^\top \mathbf{b}_{s_I^\triangleright}. \end{aligned}$$

Since the first bounced wall in s_i^\triangleleft equals the last bounced wall in s_i^\triangleright , $s_i^\triangleleft = s_{I-i+1}^\triangleright$, the term $\mathbf{f}^\top \mathbf{f}$ follows as

$$\begin{aligned} \mathbf{f}^\top \mathbf{f} &= \mathbf{b}_{s_I^\triangleright}^\top \mathbf{A}_{s_{I-1}^\triangleright}^\top \cdots \mathbf{A}_{s_1^\triangleright}^\top \mathbf{A}_{s_1^\triangleright} \cdots \mathbf{A}_{s_{I-1}^\triangleright} \mathbf{b}_{s_I^\triangleright} + \dots \\ &\quad + \mathbf{b}_{s_I^\triangleright}^\top \mathbf{A}_{s_{I-1}^\triangleright} \cdots \mathbf{A}_{s_1^\triangleright} \mathbf{b}_{s_1^\triangleright} + \dots + \mathbf{b}_{s_I^\triangleright}^\top \mathbf{b}_{s_I^\triangleright} \\ &= \mathbf{b}_{s_I^\triangleright}^\top \mathbf{b}_{s_I^\triangleright} + \dots - \mathbf{b}_{s_I^\triangleright}^\top \mathbf{A}_{s_{I-1}^\triangleright} \cdots \mathbf{A}_{s_2^\triangleright} \mathbf{b}_{s_1^\triangleright} + \dots + \mathbf{b}_{s_1^\triangleright}^\top \mathbf{b}_{s_1^\triangleright} \end{aligned}$$

showing that $\mathbf{c}^\top \mathbf{c} = \mathbf{f}^\top \mathbf{f}$.

Rewriting the terms $\mathbf{a}^\top \mathbf{b}$ and $\mathbf{d}^\top \mathbf{e}$ results in

$$\begin{aligned}\mathbf{a}^\top \mathbf{b} &= -(\mathbf{p}^{(m)})^\top \prod_{i=1}^I \mathbf{A}_{s_i^\triangleright} \mathbf{p}^{(m')} \\ &= -(\mathbf{p}^{(m')})^\top \prod_{i=1}^I \mathbf{A}_{s_{I-i+1}^\triangleright}^\top \mathbf{p}^{(m)} \\ &= -(\mathbf{p}^{(m')})^\top \prod_{i=1}^I \mathbf{A}_{s_i^\triangleleft} \mathbf{p}^{(m)} = \mathbf{d}^\top \mathbf{e}\end{aligned}$$

applying (22) and the property of symmetry ($\mathbf{A}_{s_i^\triangleleft}^\top = \mathbf{A}_{s_i^\triangleleft}$). Finally, $\mathbf{b}^\top \mathbf{c}$ and $\mathbf{d}^\top \mathbf{f}$ follow as

$$\begin{aligned}\mathbf{b}^\top \mathbf{c} &= (\mathbf{p}^{(m)})^\top \left(\prod_{i=1}^I \mathbf{A}_{s_i^\triangleright} \right)^\top \sum_{i=1}^I \prod_{j=i+1}^I \mathbf{A}_{s_j^\triangleright} \mathbf{b}_{s_i^\triangleright} \\ &= (\mathbf{p}^{(m)})^\top \mathbf{A}_{s_1^\triangleright}^\top \cdots \mathbf{A}_{s_I^\triangleright}^\top \mathbf{A}_{s_I^\triangleright} \cdots \mathbf{A}_{s_2^\triangleright} \mathbf{b}_{s_1^\triangleright} + \dots \\ &\quad + (\mathbf{p}^{(m)})^\top \mathbf{A}_{s_1^\triangleright}^\top \cdots \mathbf{A}_{s_I^\triangleright}^\top \mathbf{b}_{s_I^\triangleright} \\ &= -(\mathbf{p}^{(m)})^\top \mathbf{b}_{s_1^\triangleright} - \dots - (\mathbf{p}^{(m)})^\top \mathbf{A}_{s_1^\triangleright}^\top \cdots \mathbf{A}_{s_{I-1}^\triangleright}^\top \mathbf{b}_{s_I^\triangleright} \\ &= -(\mathbf{p}^{(m)})^\top \mathbf{b}_{s_I^\triangleleft} - \dots - (\mathbf{p}^{(m)})^\top \mathbf{A}_{s_I^\triangleleft} \cdots \mathbf{A}_{s_2^\triangleleft} \mathbf{b}_{s_1^\triangleleft} \\ &= -(\mathbf{p}^{(m)})^\top \sum_{i=1}^I \prod_{j=i+1}^I \mathbf{A}_{s_j^\triangleleft} \mathbf{b}_{s_i^\triangleleft} = \mathbf{d}^\top \mathbf{f}\end{aligned}\tag{25}$$

and similarly to (25), $\mathbf{a}^\top \mathbf{c} = \mathbf{e}^\top \mathbf{f}$.

9 Gradient of self and relative measurements

9.0.1 Gradient of self measurements

Figure 9 illustrates the self measurement of agent m containing a single-bounce and two double-bounce reflections, one at parallel walls ($\mathbf{s}_{\text{parallel}}^{(m,m)} = [s_1, s_j]$) and one at a corner ($\mathbf{s}_{\text{corner}}^{(m,m)} = [s_i, s_j]$). Due to their regular occurrence in multipath propagation, these reflection are treated in more detail, in the following.

In case of the single-bounce reflection the vector of reflecting segments is $\mathbf{s}_{\text{single}}^{(m,m)} = [s_i]$ and (2) follows as

$$\tau_{\text{single}}^{(m,m)} = \frac{1}{c} d(\mathbf{p}^{(m)}, \mathbf{p}^{(m)}, \mathbf{s}_{\text{single}}^{(m,m)}) = \frac{1}{c} \|2\mathbf{T}_{s_i}(\mathbf{p}^{(m)} - \mathbf{p}_{s_i})\|.$$

The gradient with respect to the agent's position results in

$$\frac{\partial \tau_{\text{single}}^{(m,m)}}{\partial \mathbf{p}^{(m)}} = 2 \underbrace{\frac{2\mathbf{T}_{s_i}(\mathbf{p}^{(m)} - \mathbf{p}_{s_i})}{c \|2\mathbf{T}_{s_i}(\mathbf{p}^{(m)} - \mathbf{p}_{s_i})\|}}_{\boldsymbol{\xi}}\tag{26}$$

where $\boldsymbol{\xi}$ is the normalized direction of the incident multipath, scaled by $1/c$. The scaling factor of 2 indicates that an agent's position movement $\Delta \mathbf{p}$ towards the wall segment results in a doubled time lag of the MPC along the delay domain.

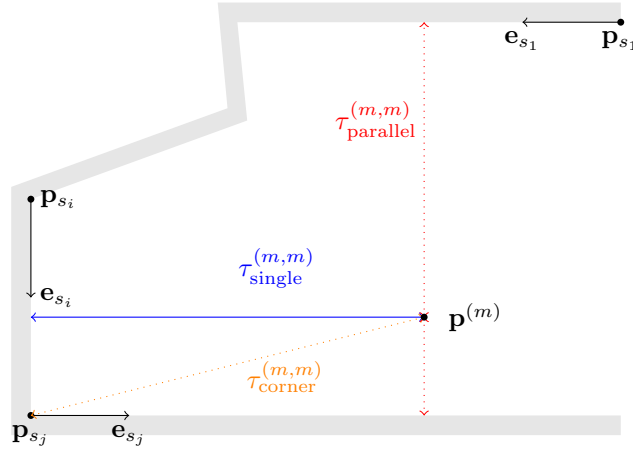


Figure 9: Illustration of multipath propagation originating from the self measurement of agent m at position $\mathbf{p}^{(m)}$. The wall segments are described by their location \mathbf{p}_s and direction \mathbf{e}_s . The single-bounce and corner reflection cover information about the agent's position whereas the double-bounce reflection between the parallel walls cannot be exploited for positioning.

The gradient with respect to the wall segment location \mathbf{p}_{s_i} follows equivalently to (26) as

$$\frac{\partial \tau_{\text{single}}^{(m,m)}}{\partial \mathbf{p}_{s_i}} = -2\xi = -\frac{\partial \tau_{\text{single}}^{(m,m)}}{\partial \mathbf{p}^{(m)}} \quad (27)$$

and demonstrates that the wall segment location's gradient is in opposite direction to the agent's position gradient.

In case of a double-bounce reflection, two wall segments are involved. If both wall segments are aligned in parallel (e.g. $\{s_1, s_j\}$), then $\mathbf{e}_{s_1} = \pm \mathbf{e}_{s_j}$ and (2) reduces to

$$\tau_{\text{parallel}}^{(m,m)} = \frac{1}{c} \|2\mathbf{T}_{s_1} \mathbf{p}_{s_1} - 2\mathbf{T}_{s_j} \mathbf{p}_{s_j}\|$$

showing that the MPC's delay $\tau_{\text{parallel}}^{(m,m)}$ is independent on the agent's position. Hence, double-bounce reflections originating from parallel walls convey information of wall segments only but cannot be used for positioning of the agents.

Finally, if the affected wall segments are aligned in orthogonal directions (e.g. $\{s_i, s_j\}$) then $\mathbf{e}_{s_i}^\top \mathbf{e}_{s_j} = 0$, $\mathbf{T}_{s_i} + \mathbf{T}_{s_j} = \mathbf{I}$ and the MPC's delay follows as

$$\tau_{\text{corner}}^{(m,m)} = \frac{1}{c} \|2\mathbf{p}^{(m)} - 2\mathbf{T}_{s_i} \mathbf{p}_{s_i} - 2\mathbf{T}_{s_j} \mathbf{p}_{s_j}\|$$

Its derivative with regard to the agent's position is

$$\frac{\partial \tau_{\text{corner}}^{(m,m)}}{\partial \mathbf{p}^{(m)}} = 2 \underbrace{\frac{2\mathbf{p}^{(m)} - 2\mathbf{T}_{s_i} \mathbf{p}_{s_i} - 2\mathbf{T}_{s_j} \mathbf{p}_{s_j}}{\|2\mathbf{p}^{(m)} - 2\mathbf{T}_{s_i} \mathbf{p}_{s_i} - 2\mathbf{T}_{s_j} \mathbf{p}_{s_j}\|}}_{\zeta}. \quad (28)$$

Similar to a single-bounce reflection (26) an agent's position movement towards the corner results in a doubled time lag of the MPC along the delay domain.

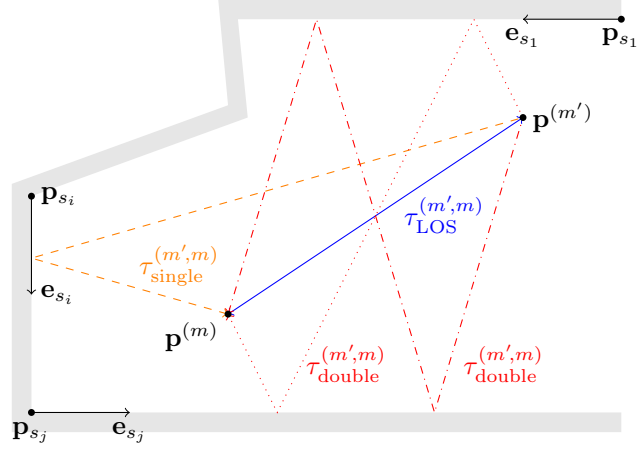


Figure 10: Illustration of multipath propagation of the relative measurement between the transmitting agent m' and receiving agent m .

The derivative with regard to the wall segment locations is

$$\frac{\partial \tau_{\text{corner}}^{(m,m)}}{\partial \mathbf{p}_{s_i}} = -2\mathbf{T}_{s_i}\boldsymbol{\zeta}, \quad \frac{\partial \tau_{\text{corner}}^{(m,m)}}{\partial \mathbf{p}_{s_j}} = -2\mathbf{T}_{s_j}\boldsymbol{\zeta}$$

showing that the MPC direction $\boldsymbol{\zeta}$ is decomposed in two components, $-2\mathbf{T}_{s_i}\boldsymbol{\zeta}$ and $-2\mathbf{T}_{s_j}\boldsymbol{\zeta}$. The sum of both gradients is equal to the agent's one (but in opposite direction)

$$\frac{\partial \tau_{\text{corner}}^{(m,m)}}{\partial \mathbf{p}_{s_i}} + \frac{\partial \tau_{\text{corner}}^{(m,m)}}{\partial \mathbf{p}_{s_j}} = -\frac{\partial \tau_{\text{corner}}^{(m,m)}}{\partial \mathbf{p}^{(m)}}.$$

In general, these gradients are always perpendicular to the wall segments enforced by matrices $\{\mathbf{T}_s\}$. The angle between the wall segment alignment and the bouncing MPC scales the magnitude of the gradient.

9.0.2 Gradient of relative measurements

Figure 10 exemplifies delays of deterministic MPCs obtained by a relative measurement between the transmitting agent m' and the receiving agent m consisting of an LOS and two additional reflections. The delay of the LOS $\tau_{\text{LOS}}^{(m',m)}$ is independent of wall segments and (2) follows as

$$\tau_{\text{LOS}}^{(m',m)} = \frac{1}{c} \|\mathbf{p}^{(m)} - \mathbf{p}^{(m')}\|$$

Its gradient with respect to both agents results in

$$\begin{aligned} \frac{\partial \tau_{\text{LOS}}^{(m',m)}}{\partial \mathbf{p}^{(m')}} &= \frac{\mathbf{p}^{(m)} - \mathbf{p}^{(m')}}{c \|\mathbf{p}^{(m)} - \mathbf{p}^{(m')}\|} \\ \frac{\partial \tau_{\text{LOS}}^{(m',m)}}{\partial \mathbf{p}^{(m)}} &= \frac{\mathbf{p}^{(m)} - \mathbf{p}^{(m')}}{c \|\mathbf{p}^{(m)} - \mathbf{p}^{(m')}\|} \end{aligned} \quad (29)$$

demonstrating that their gradient is in opposite directions $\partial\tau_{\text{LOS}}^{(m',m)}/\partial\mathbf{p}^{(m')} = -\partial\tau_{\text{LOS}}^{(m',m)}/\partial\mathbf{p}^{(m)}$. The gradient of the MPC delays $\tau_{\text{single}}^{(m',m)}$ and $\tau_{\text{double}}^{(m',m)}$ is obtained similarly to (29) by computing the derivative of (2) with regard to the agents' positions $\mathbf{p}^{(m)}$ and $\mathbf{p}^{(m')}$.

We can conclude that the gradient of agent m depends on the position of the cooperating agent m' . This is in contrast to the self measurements where the delays of the MPCs are independent of other agent positions. Furthermore the obtained delays of the relative measurements are less sensitive to agents' position movements compared to the self measurements (due to a missing factor of 2 which arises at (27) or (28)).

References

- [1] H. Wymeersch, J. Lien, and M. Z. Win, "Cooperative localization in wireless networks," *Proceedings of the IEEE*, 2009.
- [2] L. Cong and W. Zhuang, "Non-line-of-sight error mitigation in mobile location," in *INFOCOM 2004. Twenty-third Annual Joint Conference of the IEEE Computer and Communications Societies*, vol. 1, March 2004.
- [3] S. Marano, W. M. Gifford, H. Wymeersch, and M. Z. Win, "NLOS identification and mitigation for localization based on UWB experimental data," *IEEE Journal on Selected Areas in Communications*, vol. 28, no. 7, pp. 1026–1035, 2010.
- [4] H. Wymeersch, S. Marano, W. Gifford, and M. Win, "A machine learning approach to ranging error mitigation for UWB localization," *IEEE Transactions on Communications*, 2012.
- [5] A. Conti, D. Dardari, M. Guerra, L. Mucchi, and M. Win, "Experimental characterization of diversity navigation," *IEEE Systems Journal*, 2014.
- [6] Y. Shen, S. Mazuelas, and M. Win, "Network navigation: theory and interpretation," *IEEE Journal on Selected Areas in Communications*, 2012.
- [7] E. Leitinger, P. Meissner, C. Ruedisser, G. Dumphart, and K. Witrisal, "Evaluation of position-related information in multipath components for indoor positioning," *IEEE Journal on Selected Areas in Communications*, 2015.
- [8] E. Tsololikhin, I. Bilik, and N. Blaunstein, "A single-base-station localization approach using a statistical model of the NLOS propagation conditions in urban terrain," *IEEE Transactions on Vehicular Technology*, vol. 60, no. 3, 2011.
- [9] K. Witrisal, P. Meissner, E. Leitinger, Y. Shen, C. Gustafson, F. Tufvesson, K. Haneda, D. Dardari, A. F. Molisch, A. Conti, and M. Z. Win, "High-accuracy localization for assisted living," *IEEE Signal Processing Magazine*, 2016.
- [10] R. Parhizkar, I. Dokmanic, and M. Vetterli, "Single-channel indoor microphone localization," in *2014 IEEE International Conference on Acoustics, Speech and Signal Processing (ICASSP)*, May 2014.

- [11] S. V. de Velde and H. Steendam, "CUPID algorithm for cooperative indoor multipath-aided localization," in *2012 International Conference on Indoor Positioning and Indoor Navigation (IPIN)*, Nov 2012.
- [12] S. Van de Velde, H. Wymeersch, P. Meissner, K. Witrisal, and H. Steendam, "Cooperative multipath-aided indoor localization," in *2012 IEEE Wireless Communications and Networking Conference (WCNC)*. IEEE, 2012.
- [13] H. Naseri, M. Costa, and V. Koivunen, "Multipath-aided cooperative network localization using convex optimization," in *2014 48th Asilomar Conference on Signals, Systems and Computers*, Nov 2014.
- [14] M. Froehle, E. Leitinger, P. Meissner, and K. Witrisal, "Cooperative multipath-Assisted Indoor Navigation and Tracking (Co-MINT) Using UWB Signals," in *IEEE ICC Workshop on Advances in Network Localization and Navigation*, 2013.
- [15] J. Kulmer, E. Leitinger, P. Meissner, and K. Witrisal, "Cooperative Multipath-assisted Navigation and Tracking: A Low-Complexity Approach," in *1st EAI International Conference on Future access enablers of ubiquitous and intelligent infrastructures, 2015*. EAI, 2015.
- [16] J. Kulmer, E. Leitinger, P. Meissner, S. Hinteregger, and K. Witrisal, "Cooperative localization and tracking using multipath channel information," in *2016 International Conference on Localization and GNSS (ICL-GNSS)*, June 2016.
- [17] H. Miao, K. Yu, and M. J. Juntti, "Positioning for NLOS propagation: algorithm derivations and Cramer Rao bounds," *IEEE Transactions on Vehicular Technology*, vol. 56, no. 5, pp. 2568–2580, Sept 2007.
- [18] W. Xu, F. Quitin, M. Leng, W. P. Tay, and S. G. Razul, "Distributed localization of a RF target in NLOS environments," *IEEE Journal on Selected Areas in Communications*, vol. 33, no. 7, July 2015.
- [19] S. Thrun, W. Burgard, and D. Fox, *Probabilistic Robotics*. MIT, 2005.
- [20] C. Gentner, T. Jost, W. Wang, S. Zhang, A. Dammann, and U. C. Fiebig, "Multipath assisted positioning with simultaneous localization and mapping," *IEEE Transactions on Wireless Communications*, no. 99, 2016.
- [21] C. Gentner, B. Ma, M. Ulmschneider, T. Jost, and A. Dammann, "Simultaneous localization and mapping in multipath environments," in *2016 IEEE/ION Position, Location and Navigation Symposium (PLANS)*, April 2016, pp. 807–815.
- [22] P. Setlur, T. Negishi, N. Devroye, and D. Erricolo, "Multipath exploitation in non-LOS urban synthetic aperture radar," *IEEE Journal of Selected Topics in Signal Processing*, vol. 8, no. 1, pp. 137–152, Feb 2014.
- [23] Y. Shen and M. Win, "Fundamental limits of wideband localization; part I: a general framework," *IEEE Transactions on Information Theory*, 2010.

- [24] Y. Shen, H. Wymeersch, and M. Win, "Fundamental limits of wideband localization - part II: cooperative networks," *IEEE Transactions on Information Theory*, 2010.
- [25] M. Z. Win, A. Conti, S. Mazuelas, Y. Shen, W. M. Gifford, D. Dardari, and M. Chiani, "Network localization and navigation via cooperation," *IEEE Communications Magazine*, vol. 49, no. 5, pp. 56–62, May 2011.
- [26] K. Witrals and P. Meissner, "Performance bounds for multipath-assisted indoor navigation and tracking (MINT)," in *IEEE International Conference on Communications (ICC)*, 2012.
- [27] A. Molisch, "Ultra-wide-band propagation channels," *Proceedings of the IEEE*, 2009.
- [28] C. Falsi, D. Dardari, L. Mucchi, and M. Z. Win, "Time of arrival estimation for UWB localizers in realistic environments," *EURASIP Journal on Advances in Signal Processing*, vol. 2006, no. 1, 2006.
- [29] P. Meissner, E. Leitinger, and K. Witrals, "UWB for robust indoor tracking: weighting of multipath components for efficient estimation," *IEEE Wireless Communications Letters*, vol. 3, no. 5, pp. 501–504, Oct. 2014.
- [30] A. Molisch, *Wireless Communications*. Wiley, 2007.
- [31] J. Munkres, "Algorithms for the assignment and transportation problems," *Journal of the Society for Industrial and Applied Mathematics*, vol. 5, no. 1, pp. pp. 32–38, 1957.
- [32] D. Schuhmacher, B.-T. Vo, and B.-N. Vo, "A consistent metric for performance evaluation of multi-object filters," *IEEE Transactions on Signal Processing*, 2008.
- [33] Imsens Channel Sounder. [Online]. Available: <http://www.ilsens.com>
- [34] P. Meissner, E. Leitinger, M. Lafer, and K. Witrals, "MeasureMINT UWB database," 2013, Publicly available database of UWB indoor channel measurements.
- [35] C. Krall, "Signal processing for ultra wideband transceivers," Ph.D. dissertation, Graz University of Technology, Austria, 2008.
- [36] H. Schantz, "Planar elliptical element ultra-wideband dipole antennas," in *IEEE Antennas and Propagation Society International Symposium*, vol. 3. IEEE; 1999, 2002, pp. 44–47.
- [37] Mini Circuits, RC-4SPDT-A18 and RC-1SP4T-A18. [Online]. Available: <http://www.minicircuits.com>
- [38] P. Meissner and K. Witrals, "Multipath-Assisted Single-Anchor Indoor Localization in an Office Environment," in *19th International Conference on Systems, Signals and Image Processing (IWSSIP)*, Vienna, Austria, 2012, invited paper.

- [39] B. Etxzlinger, H. Wymeersch, and A. Springer, “Cooperative synchronization in wireless networks.” *IEEE Trans. Signal Processing*, vol. 62, no. 11, pp. 2837–2849, 2014.
- [40] J. Kulmer, S. Hinteregger, B. Großwindhager, M. Rath, M. Bakr, E. Leitinger, and K. Witrissal, “Using DecaWave UWB Transceivers for High-accuracy Multipath-assisted Indoor Positioning,” in *IEEE ICC 2017 Workshop on Advances in Network Localization and Navigation (ANLN)*, 2017.
- [41] J. Borish, “Extension of the image model to arbitrary polyhedra,” *The Journal of the Acoustical Society of America*, vol. 75, no. 6, 1984.